POLITECNICO DI TORINO

DIPARTIMENTO DI INGEGNERIA STRUTTURALE, EDILE E GEOTECNICA (DISEG)

Corso di Laurea Magistrale in Ingegneria Civile

NUMERICAL INVESTIGATIONS ON THE BUCKLING BEHAVIOR OF STIFFENED PLATES OF A HOLLOW BOX SECTION WITH DIFFERENT LAUNCHING BEARINGS

Relatore:

Prof. Ing. Rosario Ceravolo, Politecnico di Torino

Correlatore:

Prof. Ing. Martin Mensinger, Technical University of Munich

Laureando:

Livio Lischio

ANNO ACCADEMICO 2017/2018

Statement:

I declare that the present Master's thesis was made by myself, and only the sources and tools listened were used. I agree that my Master's thesis may be kept for an indefinite period for academic purposes.

Munich, 9/10/2018

_____

Signature

Summary

Abstract

The master thesis aim is to investigate, through a finite element model, how the presence of the bottom flange affects the stability of the steel section, during the process of the incremental launching of steel bridges. In particular, two types of bearings have been analyzed (one rigid and the other elastomeric) on two different types of launching bearings (one with a spherical node and the other with a simple discharge). Additionally, this thesis investigates the effect of a possible eccentricity of the load, due to the imperfect alignment of the constraint with respect to the section.

The realization of the model, and therefore the application of the boundary conditions, are based on laboratory tests carried out at the Chair of Metal Structures of the TU of Munich during the period January/February 2018.

The numerical surveys have been carried out using the $Ansys\ Workbench$ 18.0 finite element calculation software, and because of the possibility of modifying the $Workbench$ content by writing a $Java\ Script$, the entire model has been created within a $Python\ Script$, reducing not only the dimension of the entire project, but also optimizing the entire process by entering parameters.

The choice to analyze the overall behavior of the section stems from the desire to compare the results of this model with the experimental data extrapolated during the tests.

1.   INTRODUCTION

The following chapter describes the incremental launching and the reasons why it is necessary to perform a stability analysis on the bridge section components that could become unstable; it also briefly describes the laboratory test, on which the numerical model is based, and it introduces the reference normative for the stability verification of steel plates.

1.1   Incremental launching

The incremental launching is a method of bridge construction (Figure 1.1) whose first application dates back to 1964, when it was used for the first time during the construction of the Caroni River Bridge [1].

Figure 1.1: incremental launching example [18]

This principle, basically used for the construction of bridges with very high pillars, such as the Millau viaduct, makes it possible to construct and prestress the segments of the superstructure in a square located behind the abutment of the bridge, so directly in *situ*, and to lift it forward

by a distance equal to the length of the single component [2]. The process is repeated until the bridge is in its final position (Figure 1.2).

The sliding of the deck above the constraints is facilitated by the presence of teflon sheets, which have a low coefficient of friction.
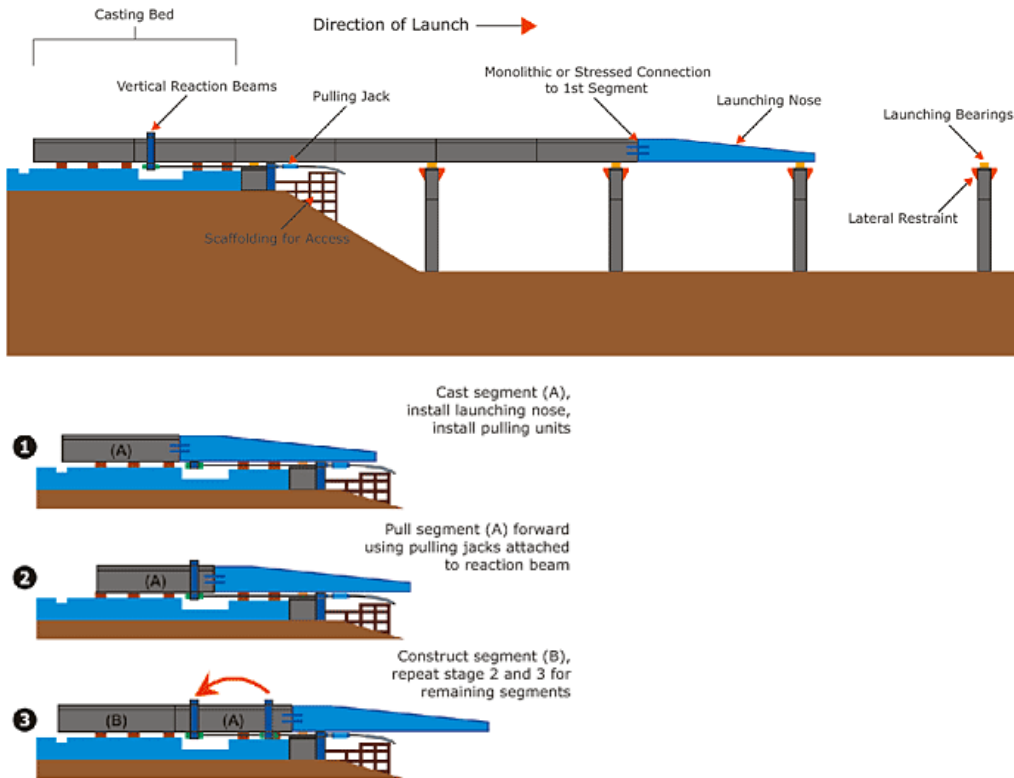
Figure 1.2: incremental launching construction technique [20], [21]

Of course, during the construction process, until the launching nose, which has left the adjacent pillar, reaches the next one, the bridge is in the condition of a cantilever beam (Figure 1.3).
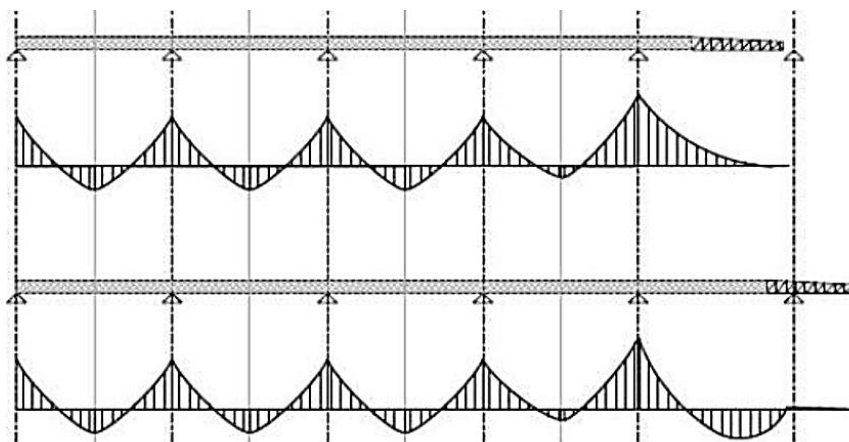
Figure 1.3: variable bending moment due to the different static schemes [19]

Temporary pillars can be erected during the construction process to reduce the moment and the consequent internal stresses (Figure 1.4).

Figure 1.4: incremental launching using temporary pillars [22]

The load-bearing forces in combination with the moments of support generate biaxial pressure conditions σ_x, σ_z, which have a negative effect on the instability tests (Figure 1.5). In the case of thin steel sections with webs inclined outwards, biaxial stresses also occur in the bottom plate [3].
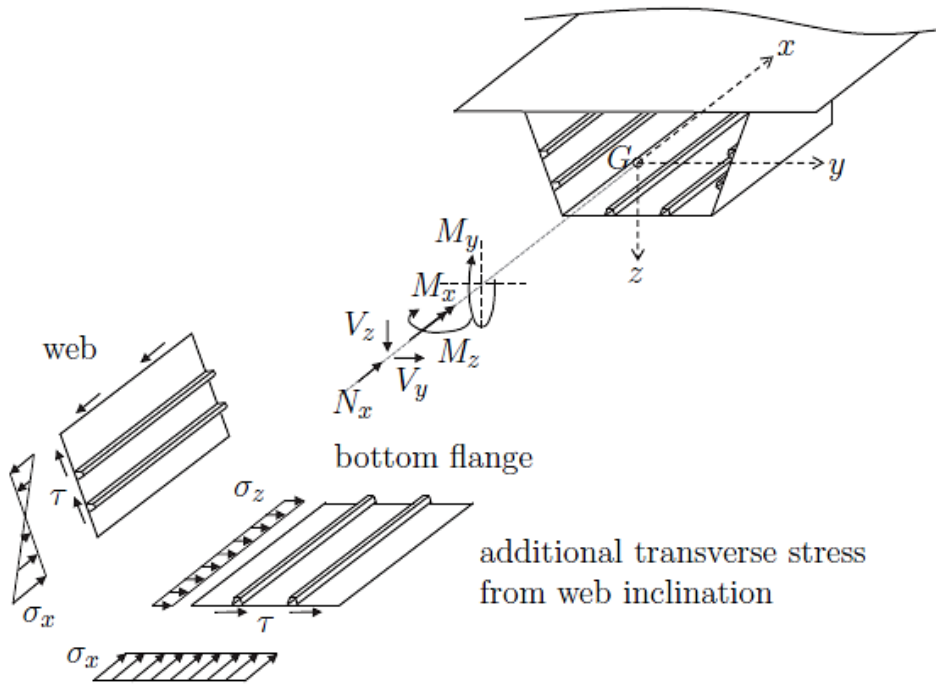
Figure 1.5: biaxial pressure condition [23]

1.2   Laboratory test

The laboratory test (Figure 1.6) carried out at the Chair of Metal Structures of TUM in January/February 2018 was commissioned during the planning of the Thulba viaduct [3], which has a composite steel-concrete section, 7 spans with distance between the columns that can reach up to 90m and a total length of $460m$.

The viaduct will be built using the incremental launching method.

Due to the limited force of the hydraulic presses in the laboratory, it was not possible to maintain the original scale of the project; for this reason, thickness of the web and the stiffeners were reduced [3].

Figure 1.6: laboratory test [3]

The load was applied in two directions in order to simulate the biaxial load condition to which the section core is subjected. The following is a schematisation of the test (Figure 1.7).
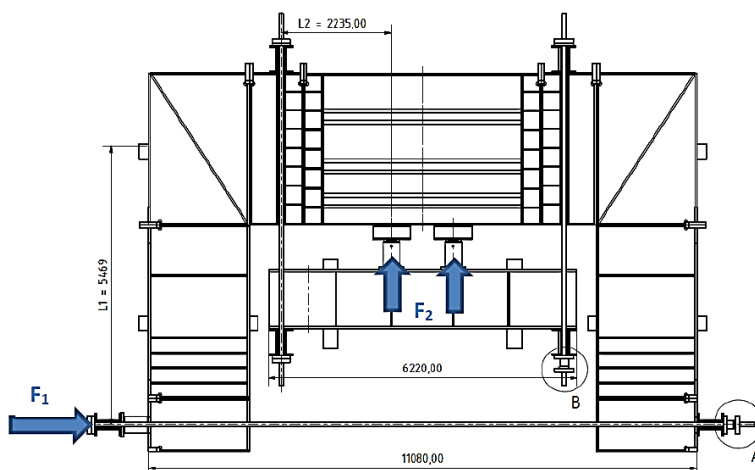
Figure 1.7: laboratory test scheme [3]

The load F1, applied to the legs of the frame, is placed at a distance L1 from the centre of gravity of the section and is exerted by means of a hydraulic press with a nominal capacity of

4.3 MN and two tension rods [4]. This eccentric force makes it possible to generate a bending moment and a normal force at the end sections, which simulates the thrust pushing suffered by the bridge during the launching.

The transverse load F2 is applied by means of two hydraulic presses with a nominal capacity of 4.3 MN, located on a rigid crossbeam connected to the frame by means of tension rods. The F2 force is then transferred to the bearings by means of thrust bearings type $GE80 - AW$ (Figure 1.8) or with a simple discharge, which have a cross sectional area type $HEM260$ (Figure 1.9).
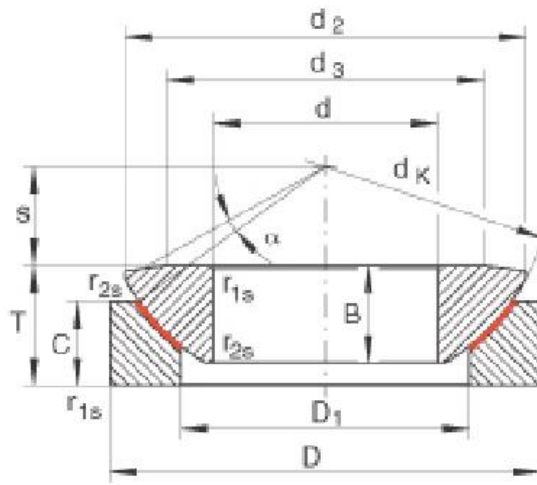
Figure 1.8: thrust bearings type GE$80 - AW$ [17]
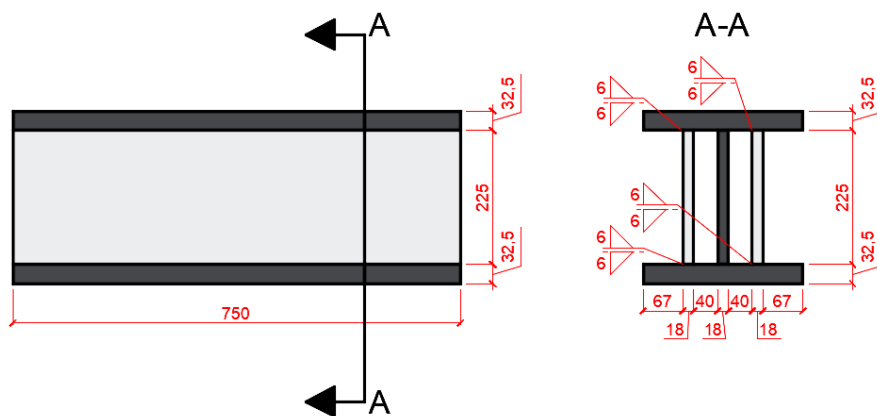
Figure 1.9: rigid support with a cross sectional area HEM260

The following illustration shows the connection thrust bearings – bearing, section – bearing (Figure 1.10).
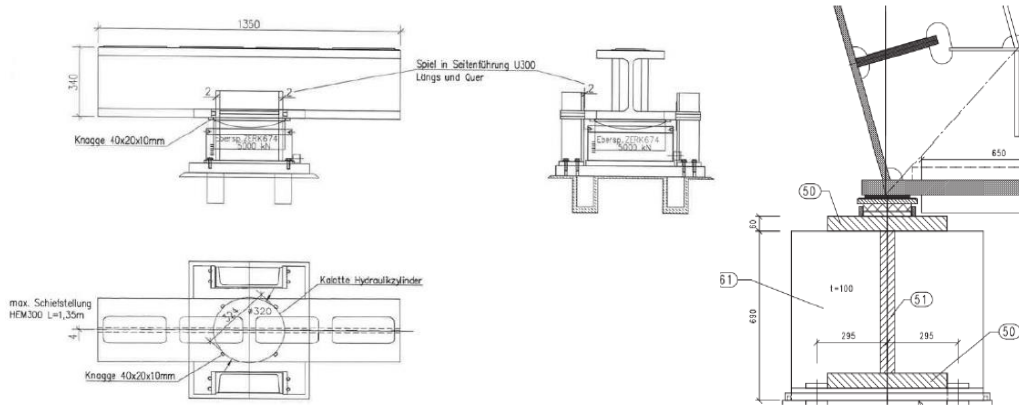
Figure 1.10: connection launching bearings – bearing, section – bearing. Principle of the hydraulic bearings of the company Max Bögl Stahl- und Anlagenbau GmbH & Co. KG [3]

A total of 6 tests were carried out with different $\beta = \sigma_Z/\sigma_X$ stress ratios above the constraint, pusher type, heights and stiffening arrangements (Figure 1.11).

1. Test1: geometry shown in fig (a); $\beta = 0.5$; spherical node thrust bearing;
2. Test2: geometry shown in fig(a); $\beta = 1$; spherical node thrust bearing, only at the beginning;
3. Test3: geometry shown in fig(b); $\beta = 1$; thrust bearing with single exhaust;
4. Test4: geometry shown in fig(b); $\beta = 0.5$; thrust bearing with single exhaust;
5. Test5: geometry shown in fig(c); $\beta = 0.5$; thrust bearing with single exhaust;
6. Test6: geometry shown in fig(d); $\beta = 0.5$; thrust bearing with single exhaust;
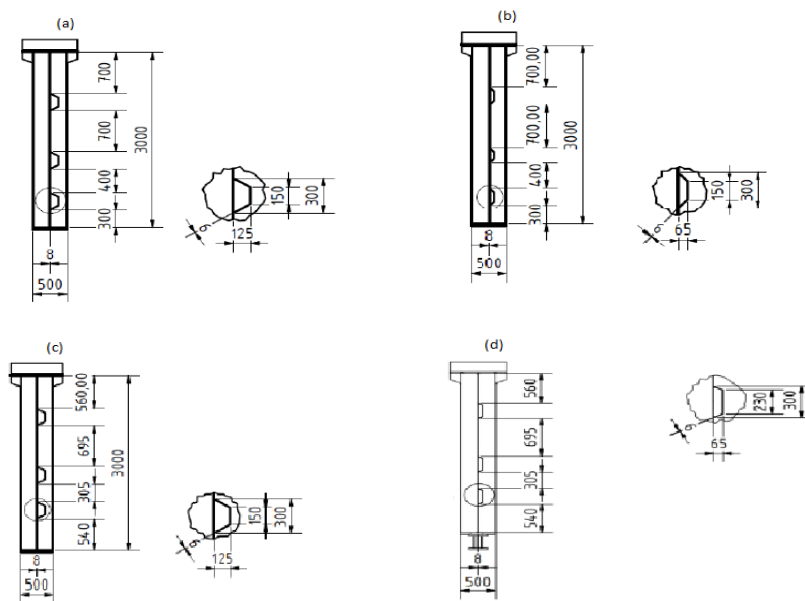
Figure 1.11: web section studied during the different tests [3]

The loads were recorded with the help of load cells and strain gauges; 3D scans were also performed on the test bodies before and during the experiments, in order to define their geometric imperfections and deformation state [3]. As it is possible to see from Figure 1.11, laboratory tests involved only the core of the section, hence the need to create a model able to capture how much influence the bottom flange has on the overall behaviour.

1.3   Normative

The reference standard for stability checks on steel plates is the EC3 part $1 - 5$ [5], which provides requirements for the design of orthotropic plates with and without stiffenings affected by buckling. This gives the designer the opportunity to adopt, in addition to the finite element method in accordance with $Annex\ C$, two different types of analysis:

- The $effective\ width\ approach$, which consists of determining the resistance of the section from the "effective widths" of its various compression components, resulting in redistribution of stresses. The reduction of rigidity and resistance due to the deformation of the plate is obtained by adopting a reduced cross section [6].

  The method is described in sections $4, 5, 6$ and 7. Within $Chapters\ 4, 5,$ and 6 the plate element is studied respectively under the effect of direct forces, shear and transverse force, while in Section 7 the interaction forces are introduced to analyze the effects simultaneously; however because of the high computational complexity, i.e. the close dependence on the load cases, and the low application flexibility (it cannot be applied to analyze the buckling of non-rectangular sections), in Germany this method is not used for plates with stiffeners [7];

- The $reduced\ stress\ method$ consists in limiting the stresses in the various components using a criterion similar to that of von-Mises.

$$\left(\frac{\sigma_{x,Ed}}{\rho_x f_y/\gamma_{M1}}\right)^2 + \left(\frac{\sigma_{z,Ed}}{\rho_z f_y/\gamma_{M1}}\right)^2 - V\left(\frac{\sigma_{x,Ed}}{\rho_x f_y/\gamma_{M1}}\right)\left(\frac{\sigma_{z,Ed}}{\rho_z f_y/\gamma_{M1}}\right) + 3\left(\frac{\tau_{Ed}}{\chi_w f_y/\gamma_{M1}}\right)^2 \leq 1$$

  Where the factor V is present only in case of biaxial compression ($\rho_x \cdot \rho_z$) and it is equal to 1 in all the other cases [7].

  The reduction factors ρ_x, ρ_z and χ_w can be determined as specified in chapter 10 of EN-1993-1-5, and are determined from a single slenderness (see equation 2 in [7]).

The most prudent solution would be to limit the linear distribution of stresses in the cross-section to the limit of the element that first deforms. Less conservative approaches for the "reduced stress method" are to consider additional cross section stress after the first collapse of the weaker part plate until the "stress limit" of the stronger plate element or even the soft deformation is reached. These approaches are not yet explicitly specified in EN 1993-1-5, however they can be used where appropriate [6].

This method is specified within section 10 and since it uses the full voltage range it is suitable for FE calculations.

2. MODEL: FROM ANSYS WORKBENCH TO PYTHON

This chapter contains the description of the model and the steps that led to its realization, from the writing in *Python* of the geometric model, to the application of mesh, materials, loads and boundary conditions.

2.1   Software

The calculation software adopted during this thesis was *Ansys Workbench* 18.0 (which represents one of *Ansys'* central simulation environments) and *Python* 2.7. The present software have been used in parallel, that is, at first the geometry and the boundary conditions have been realized respectively in *DesignModeler* (one of the *Workbench* drawing editors) and *Mechanical*, and once the truthfulness of the model has been verified, the whole has been reported in the form of *JScript* in *Python*. In fact, as shown in the following figure (Figure 2.1), it is possible to launch commands inside *Mechanical* and *DesignModeler* by writing them inside *SendCommand* [8].

Data Integrated Applications	Native Scripting Language	Support Journaling with SendCommand	Support Scripting with SendCommand
Mechanical APDL	APDL		Yes
Mechanical	JScript		Yes
DesignModeler	JScript		Yes
Meshing	JScript		Yes
FE Molder	JScript		Yes
AQWA	JScript		Yes
CFX	CCL	Yes	Yes
CFD Post	CCL	Yes	Yes
FLUENT	Scheme	Yes	Yes
PolyFlow	N/A		
IcePak	N/A		
AUTODYN	N/A		

You can insert the 'SendCommand' call into your ANSYS Workbench scripts to drive these data-integrated applications.

Recording WB journal will record the actions applied during the set up in theses data integrated apps.

Figure 2.1: customizing Ansys with Python [8]

2.2   Structure of the problem

2.2.1   General

One of the problems encountered during the design of a structure is the verification of instability, in which a structural component collapses under high compressive loads [9].

In fact, in many symmetrical structures, loaded symmetrically, the form of instability may not be as expected, since nothing activates the expected form of instability. To solve this problem, many FE programs, such as *Ansys*, allow you to apply pre-deformation to the perfect model geometry in the area where linear instability would occur [10].

For example, consider the case of a column under compression load (Figure 2.2):
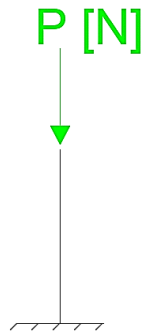
Figure 2.2: cantilever beam loaded with a tip load

In a linear analysis of large displacements, where the applied force acts as a follower force, the cantilever beam would not become unstable due to the perfect geometric symmetry and load. To solve the problem it's possible to perform a linear instability analysis of the eigenvalue based on the applied loads, and then apply a slight distortion to the unloaded surface. This distortion would be generated in the area where the linear instability occurred. Once the geometry has been deformed, it is possible to proceed with the analysis of nonlinear instability at large displacements [10].

The following image (Figure 2.3) shows a classic scheme for a model that needs to undergo nonlinear instability analysis. First, a static structural analysis linear to small displacements is performed. As will be better explained later, the forces applied during this phase do not coincide with those of the test, but allow to obtain the desired tension ratio (chapter 1.2).
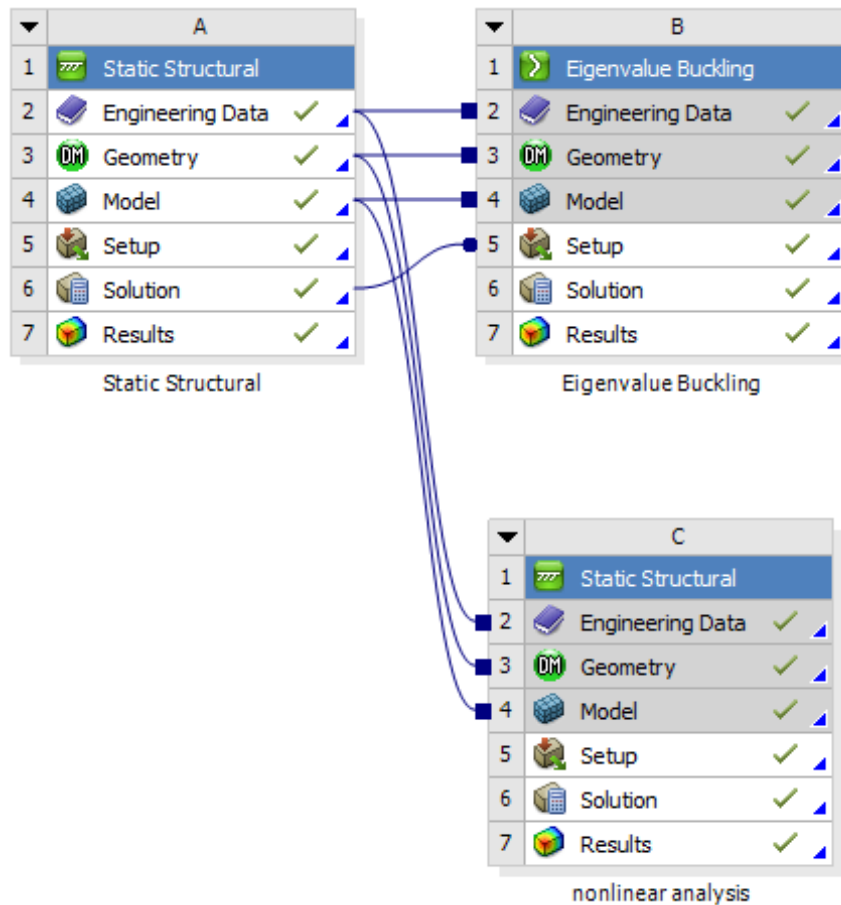
Figure 2.3: scheme for a nonlinear analysis

The *linear static analysis* is followed by linear instability analysis. During this phase the forms of instability and the load multiplication factors are determined; multiplying this factor by the applied loads return the ideal critical load, beyond which the structure becomes unstable (Figure 2.4).
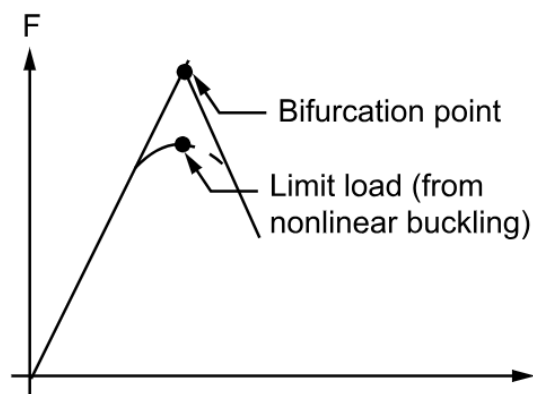
Figure 2.4: linear buckling behaviour [11]

Once determined the instability forms, it is possible to save them in $file.rst$ using the following *APDL* commands [10]:

```
/copy,file,rst,,..\..\Buckling,rst
```

Attention should be paid to the fact that *Ansys Mechanic*al performs an instability analysis of nonlinear-based eigenvalues as a linear instability analysis [3]. This is not a true nonlinear instability analysis, but a linear analysis that also applies to non-linear contacts.

It's worth noting from the figure below (Figure 2.5) that the linear load does not change, however in the case of Nonlinear Base Analysis the value must be increased by one [11].
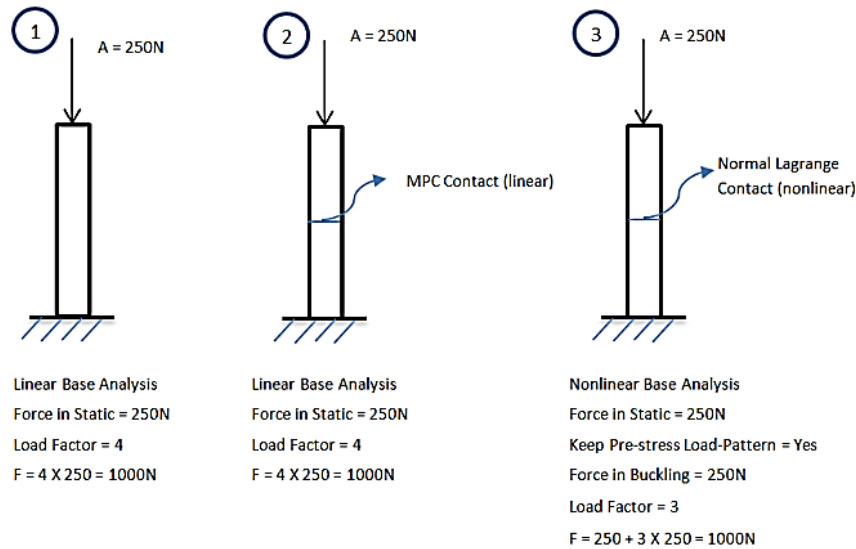
Figure 2.5: linear buckling analysis according to Ansys [11]

The analysis of linear instability is followed by the analysis of non-linear instability, which is basically nothing more than a static nonlinear analysis with large displacements. By entering the following *APDL* commands:

```
fini
/prep7
upgeom,15,1,1,..\..\Buckling,rst
fini
/solu
```

It is possible to recall the instability forms previously saved in the $file.rst$ and apply distortion of a certain factor to them. In this example, a distortion of a factor of 15 has been applied to the first form of instability, which means that if the largest displacement in the first form of instability has been normalized to $1\ mm$, then a distortion of $15mm$ is going to be applied.

Moreover, during this last phase, a load was no longer applied, but a displacement was applied, in order to trace the course of the reaction force F, determining the value beyond which the structure becomes unstable.

Applying the controlled deformation test also allows the force value to be mapped even during the $snap-through$ (Figure 2.6).
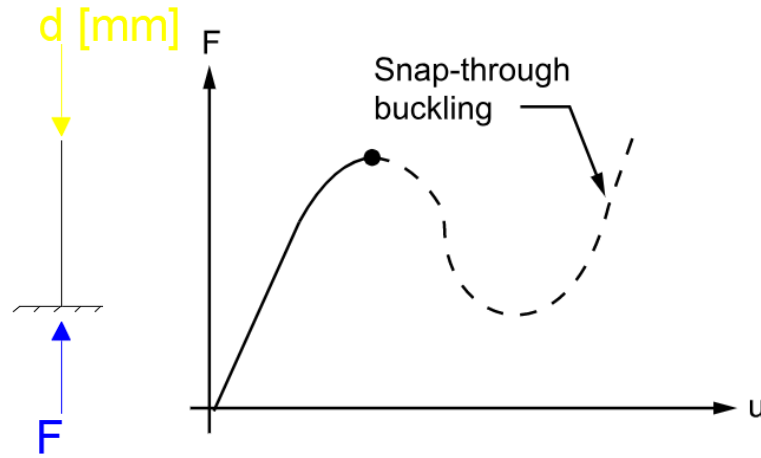
Figure 2.6: nonlinear buckling behavior [11]

2.2.2   Imperfections

As described in the previous section, nonlinear instability analysis involves the application of geometric imperfections within the model. This not only results in a much lower load than the critical one, but also allows to get closer to the real situation, where there are imperfections in the geometric components, for instance due to the manufacturing process of the component. Of course, these are very difficult to reproduce in a FE model, which is why the technique used in *Ansys* (see previous chapter) could be questioned and not lead to the expected result. According to Annex C of DIN EN 1993-1-5 [5], equivalent geometric imperfections are reproduced in FE models according to the table (Table 2.1) and figure (Figure 2.7), where a deflection with respect to the normal e_{0w} is applied.

Type of imperfection	Component	Shape	Magnitude
global	member with length ℓ	bow	see EN 1993-1-1, Table 5.1
global	longitudinal stiffener with length a	bow	min (a/400, b/400)
local	panel or subpanel with short span a or b	buckling shape	min (a/200, b/200)
local	stiffener or flange subject to twist	bow twist	1 / 50

Table 2.1: equivalent imperfection value according with the EC3 part 1-5 [5]
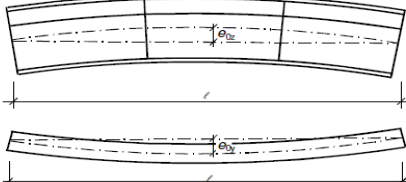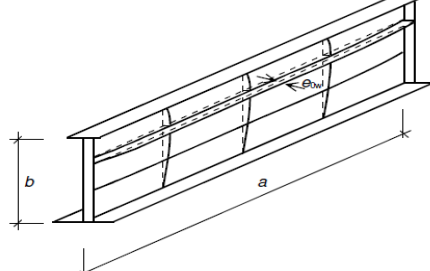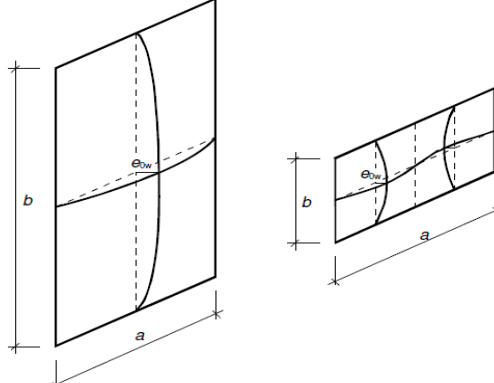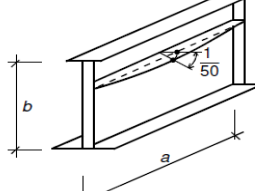
Type of imperfection	Component
global member with length ℓ	
global longitudinal stiffener with length a	
local panel or subpanel	
local stiffener or flange subject to twist	

Figure 2.7: equivalent imperfection as deflection with respect to the normal [5]

Of course, the interaction of different imperfections could also be considered. The leading imperfection should be taken with full magnitude and the accompanying imperfections may have their values reduced to 70% [5].

2.3   Geometrical model definition

The first step was the creation of the geometric model; this has been defined within the $hyton$ $Script$, which runs within $Workbench$ and interfaces with the design editor $DesignModeler$. Because of the low thickness of the components, each plate has been modelled as a surface, in order to assign shell elements as mesh.

Section and position of the constraints have been defined starting from a series of parameters contained in $file.txt$ then called inside the $Python\ Script$ through the introduction of the file path.

$$Math\_input = FilePath = "C:\backslash Users\backslash livio\backslash Desktop\backslash Section\backslash\ mat\_input.txt"$$

This has been done in order not to risk of modifying the $Script$ when the program is run using new parameters and also so as to have all the information necessary for the definition of a new model ordered within a single file.

Inside the $file.txt$ there is also a parameter called "$condition$" that allows to choice the number of stiffeners present on the bottom flange; that is, if half of the base is less than $condition$ then two stiffeners will be drawn (Figure 2.8), otherwise, if the condition is not respected three would be drawn (Figure 2.9).
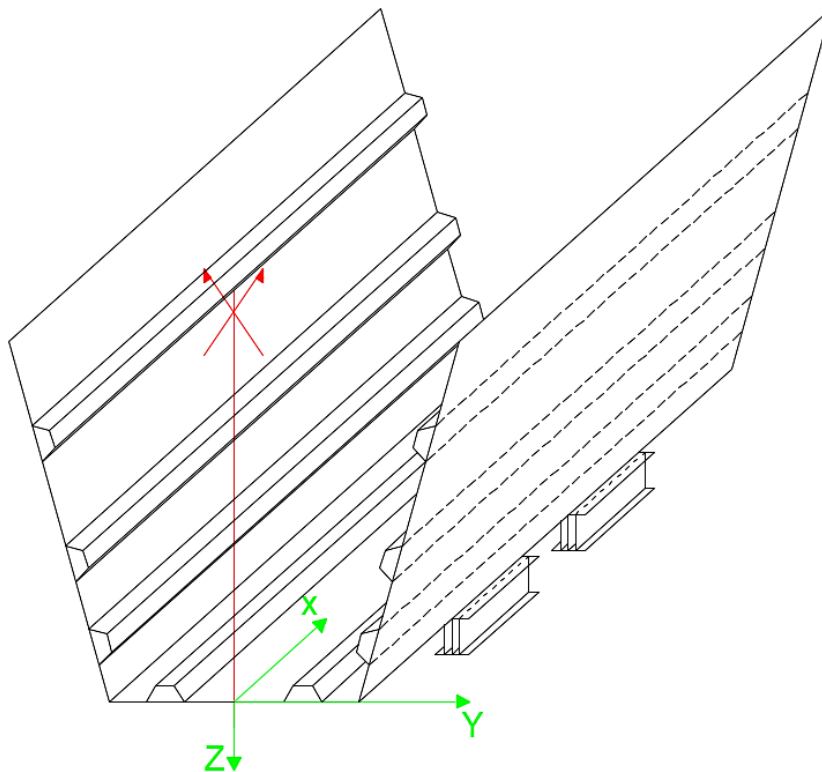
Figure 2.8: two stiffeners running along the bottom plate
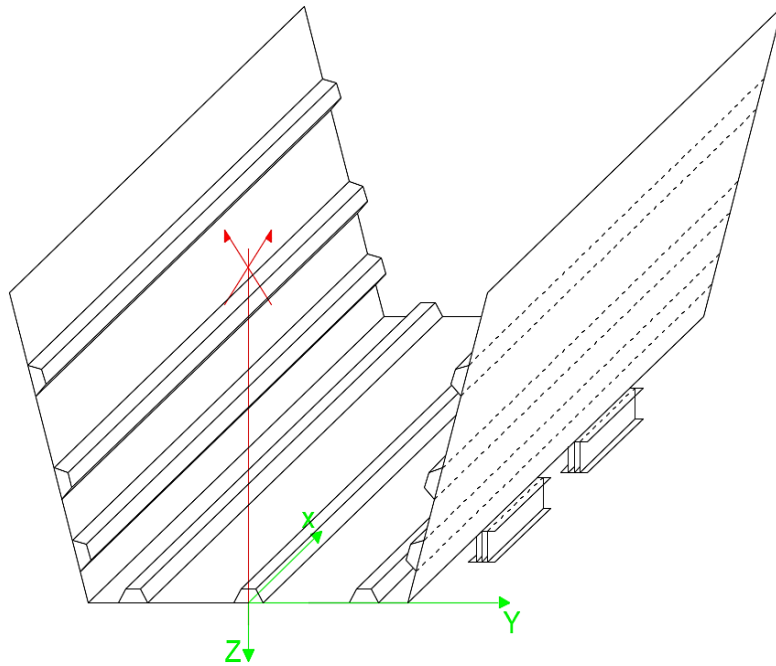
Figure 2.9: three stiffeners running along the bottom plate

In the present thesis, three longitudinal stiffeners have always been considered in order to make the bottom flange rigid enough to avoid instability.

The following images show the section with 2 and 3 stiffeners running longitudinally along the bottom plate and the respective parameters that define it (Figure 2.10, Figure 2.11).
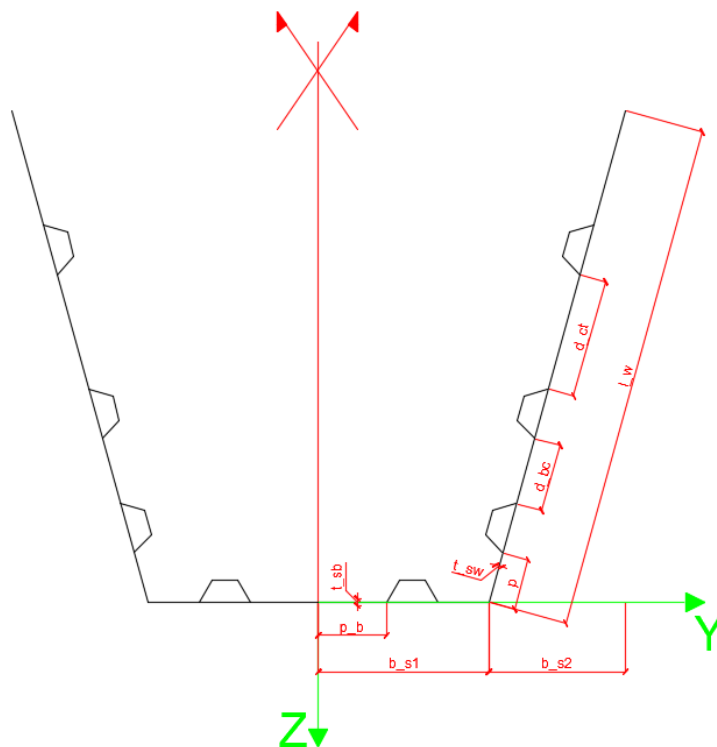
Figure 2.10: section of the body with two longitudinal stiffeners along the bottom plate
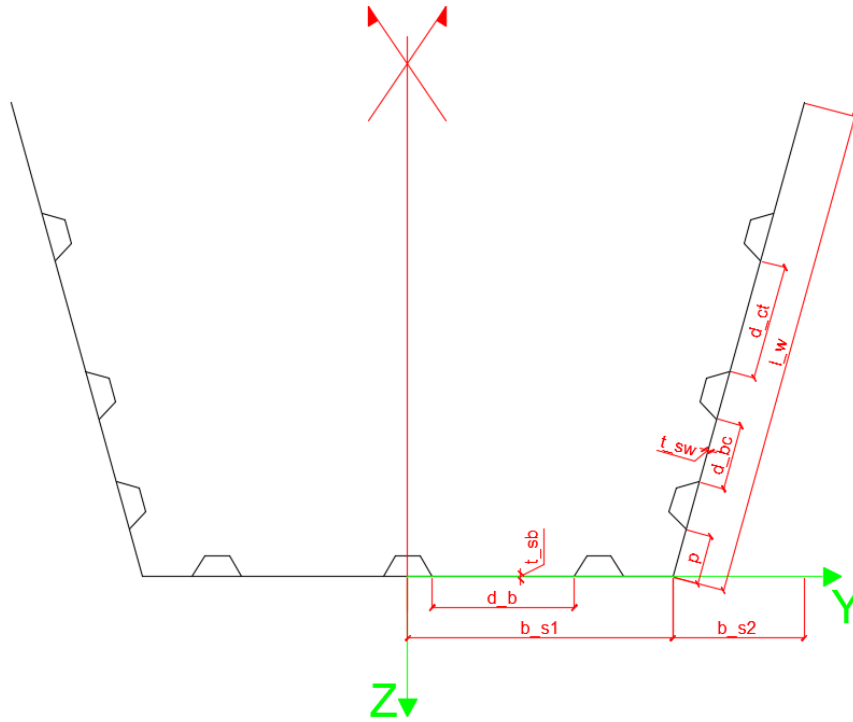
Figure 2.11: section of the body with three longitudinal stiffeners along the bottom plate
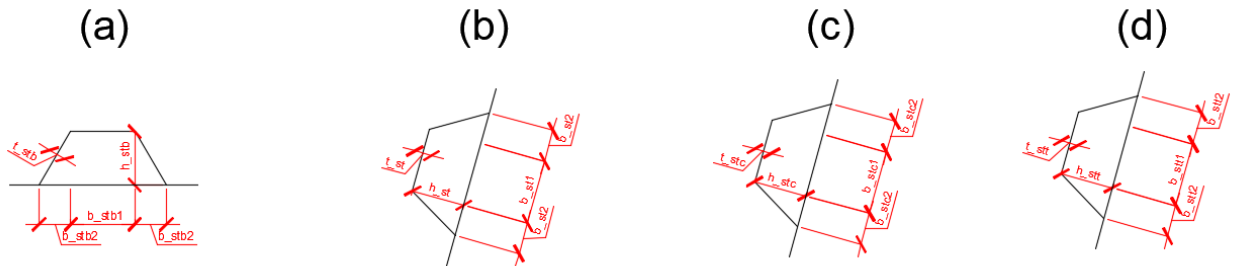
Figure 2.12: detail of the stiffeners - bottom plate stiffeners (a) - bottom web stiffeners (b) - central web stiffeners (c) - top web stiffeners (d)

The following values have been considered fixed for the simulation of the tests Figure 2.11:

- $d_b = 300mm$;
- $b_{s1} = 1000mm$;
- $b_{s2} = 800mm$;
- $l_w = 3000mm$;

The other parameters, such as the distance between the stiffeners and their geometry, vary according to the test (Figure 2.9, Figure 2.12).

Since *Python* is an object-oriented program, in order to make it as automatic as possible, the *Point*, *Side*, *Face* and *Body* classes have been created.

The Point class collects information regarding the coordinates (y, z, x) of the points that will form the section and constraints; moreover, since each coordinate has been defined starting from parameters, it is sufficient to modify these to obtain the new geometry.

```python
class Point:
    x = 0.0
    y = 0.0
    z = 0.0
    def __init__(self, y1, z1, x1):
        self.y = y1
        self.z = z1
        self.x = x1
    def GiveY(self):
        return self.y
    def GiveZ(self):
        return self.z
    def GiveX(self):
        return self.x
```

Since the whole section has been defined on the $Y - Z$ plane and then extruded along the x axis in order to create the volume (as will be explained in detail when talking about the *Face* class), the points would not need the coordinate x, however the addition of this additional information (which thus allows you to fully define the point in space) was necessary to define completely the position of the springs within the model (as will be explained below the springs are created in order to simulate as closely as possible the behavior of the elastomeric bearing). Within this class, functions have also been defined that allow the individual coordinate to be returned.

The *Side* class has been defined to connect two points, so it allows to draw the section in the plane "line by line". Within this class, functions have also been defined that allow to return the single point and since at the point it is possible to request the individual coordinates, the whole operation may be executed within a single command.

```python
class Side:
    point1 = (0.0, 0.0, 0.0)
    point2 = (0.0, 0.0, 0.0)
    def __init__(self, pointA, pointB):
        self.point1 = pointA
        self.point2 = pointB
    def length(self):
        self.l = (((self.point1.GiveY()-
self.point2.GiveY())**2)+((self.point1.GiveZ()-
self.point2.GiveZ())**2)+((self.point1.GiveX()-self.Point2.GiveX())**2))**(0.5)
        return self.l
    def GiveFirstPoint(self):
        return self.point1
    def GiveSecondPoint(self):
        return self.point2
```

The $Face$ class takes the side, which has been defined in the $Y - Z$ plane and extrudes it along the x axis, thus creates the surface; in fact it asks only the side and depth of extrusion (and example deep_s in Figure 2.13) as information. The latter represents an additional parameter contained within the $file.txt$, since the depth of the objects created depends on it (section and constraints).
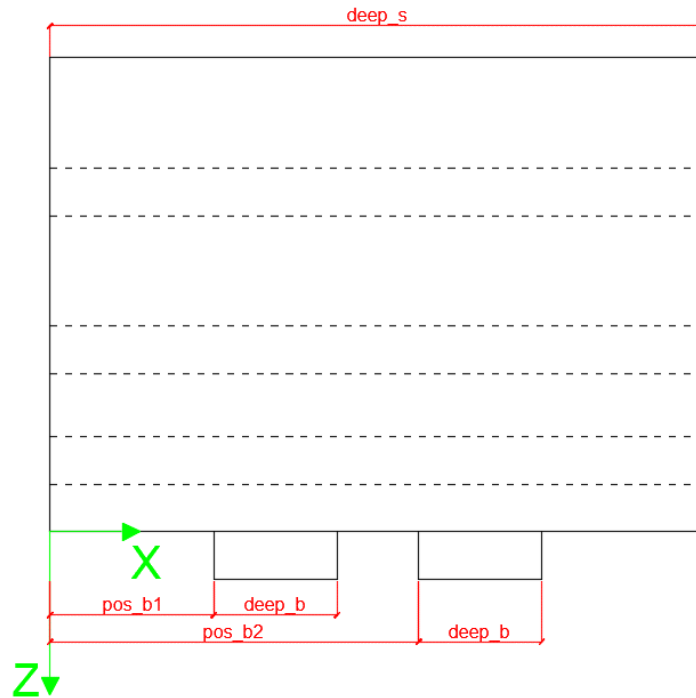
Figure 2.13: parameters contained in the file.txt that allow the definition of the position of the new plane and extrusion deep

However, within the $Face$ class several functions have been defined, each of them performs a specific task [12].

```python
class Face:
    def __init__(self, side1, ext):
        self.listSides={'first': side1}
        self._profiles = {}
        self._output = cStringIO.StringIO()
        self.extrusion = ext


    def addProfile(self, name, m, p, t, s=1.0, pos=1):
        '''
        Add a profile. This profile will compose the seciton at the given position. In addition, it
        can be scaled (up or down).

        :param name: profile name
        :param m: maximum chamber, relative to chord
        :param p: position (tenths) of maximum chamber
        :param t: thickness, relative to chord
        :param s: scale factor
        :param pos: profile position (from a reference plane)
```

```python
            '''
            self._profiles[name] = ((m, p, t, s), pos)

    def _writeNewPlane(self, planeName, offset=0.0):
        self._output.write("""
function do%s ()
{
    // Get the reference Plane (in this case, the YZ plane)
    var planeYZ = agb.GetYZPlane();
    var Yes = agc.Yes;
    var No  = agc.No;

    var newPlane = agb.PlaneFromPlane(planeYZ);
    if (newPlane)
    {
      newPlane.Name = "%s";
      newPlane.ReverseNormal = No;
      newPlane.ReverseAxes = No;
      newPlane.ExportCS = No;
      newPlane.AddTransform(agc.XformZOffset, %f);
    }

    agb.regen();

    return newPlane;
}
""" % (planeName, planeName, offset))


    def _writeSectionProfileOnPlane(self, planeName, SectionProfile=None):
        '''
        Writes the profile creation function.

        :param planeName: the plane name
        :param SectionProfile: the Section profile
        '''

    self._output.write("""function doSketches%s (plane)
            {
                    p = new Object();

                    //Plane
                    agb.SetActivePlane (plane);
                    p.Plane  = agb.GetActivePlane();
                    p.Origin = p.Plane.GetOrigin();
                    p.XAxis  = p.Plane.GetXAxis();
                    p.YAxis  = p.Plane.GetYAxis();

                    //Sketch
                    p.Sk1 = p.Plane.NewSketch();
                    p.Sk1.Name = "Sketch%s";

                    //Edges
                    with (p.Sk1)
              {""" % (planeName, planeName))

        for sides in self.listSides.keys():
            side = self.listSides[sides]
            point1 = side.GiveFirstPoint()
            yu = point1.GiveY()
            zu = point1.GiveZ()
            point2 = side.GiveSecondPoint()
            yl = point2.GiveY()
```

```python
            zl = point2.GiveZ()


            self._output.write("\t\tp.Ln7 = Line(%5.5f, %5.5f, %5.5f, %5.5f);\n"
% (yu, zu, yl, zl))

            self._output.write("""
        }
        """)

        agb.Regen();

        return p;
    }
    """)

    def _writeCreatePlaneFromSketch(self, planeName):
        '''
        Writes the commands for the plane creation (must be called after the
functions definition)

        :param planeName: the plane name
        '''
        self._output.write("pl%s = do%s ();\n" % (planeName, planeName))
        sketchName = "sk%s" % planeName
        self._output.write("%s = doSketches%s (pl%s);\n\n" % (sketchName,
planeName, planeName))

        return sketchName


    def _writeExtrudeOperation(self, skinName, sketches):
        '''
        Writes the commands for the Skin operation

        :param skinName: the skin name
        :param sketches: a list with the sketches which will form the wing
        '''

for sketchName in sketches:
        self._output.write("var Extrude1 = agb.Extrude(agc.Frozen, %s.Sk1,
        agc.DirNormal,     agc.ExtentFixed, %lf,0.0,0.0, agc.Yes, 0.0, 0.0);\n"
        % (sketchName, self.extrusion))
        self._output.write('Extrude1.Name = "%s";\n' % skinName)
        self._output.write("agb.Regen()



    def writeScript(self):
    '''
    Writes the JScript that builds the section to the output.
    '''


    profileNames = self._profiles.keys()
                profileNames.sort()
                sketches = []

                for profileName in profileNames:
                    profileData = self._profiles[profileName]
                    planeName = "Plane" + profileName
                    SectionProfile, position = profileData

                    self._writeNewPlane(planeName, offset=position)
                    self._writeSectionProfileOnPlane(planeName, SectionProfile)
```

```
                        sketchName = self._writeCreatePlaneFromSketch(planeName)
                        sketches.append(sketchName)

                    self._writeExtrudeOperation("Extrude", sketches)

                    contents = self._output.getvalue()
                    self._output.close()

                    return contents
```

In summary, without going into the details of each of them, the main steps to create the surface are explained:

- The side and the extrusion depth are assigned to the class *Face*:

  ```
  f32 = Face(l_22, deep_b)
  ```

- With the *addProfile* function, the section profile is drawn at a given position [12]:

  ```
  f32.addProfile("Face32", 0, 4, 12, 10.0, pos_b12)
  ```

  As explained above, the surface is created from one side drawn in the $Y - Z$ plane then extruded along the x axis; of course, not all sides must be drawn in the same plane, otherwise the freedom to draw a line at any position in space would have lost. This is why the *AddProfile* function was created. It allows drawing the line inside a local plane, generated as an offset along the x-axis with respect to the global reference system. This command is essential since it is true that the section is drawn inside the global reference system, or rather inside local systems that have zero offsets and therefore practically they coincide with the global system, however the constraints are drawn inside planes that have an offset along the x axis equal to pos_b1 and pos_b2 (Figure 2.13).

- With the *writeScript* function a *JavaScript* is written that will create the body [11]:

  ```
  jscript32 = f32.writeScript()
  ```

- Through the *SendCommand*() command it is possible to interface the *DM* drawing editor with *Python*, thus making it possible to run *JavaScript* within *Ansys*.

  ```
  geometryComponent.SendCommand(Command=jscript32)
  ```

However, in this way, many surfaces are created within *DM*, one adjacent to the other, apparently communicating; in reality, applying a generic force, the surfaces are not able to exchange tensions.

To overcome this problem an additional class has been defined: the *body* class.

```
class body:
    def __init__(self):

        self._output = cStringIO.StringIO()
```

```python
def join(self):
    self._output.write("var join1 = agb.FormNewPartFromAllBodies();\n")
    fix = self._output.getvalue()
    return fix
```

Naturally, whenever it is decided to change a parameter that modifies the geometry of the section, *Ansys* will continue to assign the same ID to each point, line or surface, since it is not a random process, but a sequence of well-defined operations. This aspect is of primary importance, since, for example, forces and constraints are assigned in precise points of the body that have a precise ID.

Through these simple steps a completely automated and versatile process has been created, valid not only for the present geometry, but for any solid obtained from lines extruded in the same direction, such as a box section; also, making a small change within the class Face would be possible to generate not surfaces, but solids. For example, assigning the class not just one line, but four, whose points form a closed surface, such as a simple square/rectangle, the program will create a beam element.

2.4   Material

The materials used have a non-linear bilinear behavioural law (Figure 2.14)
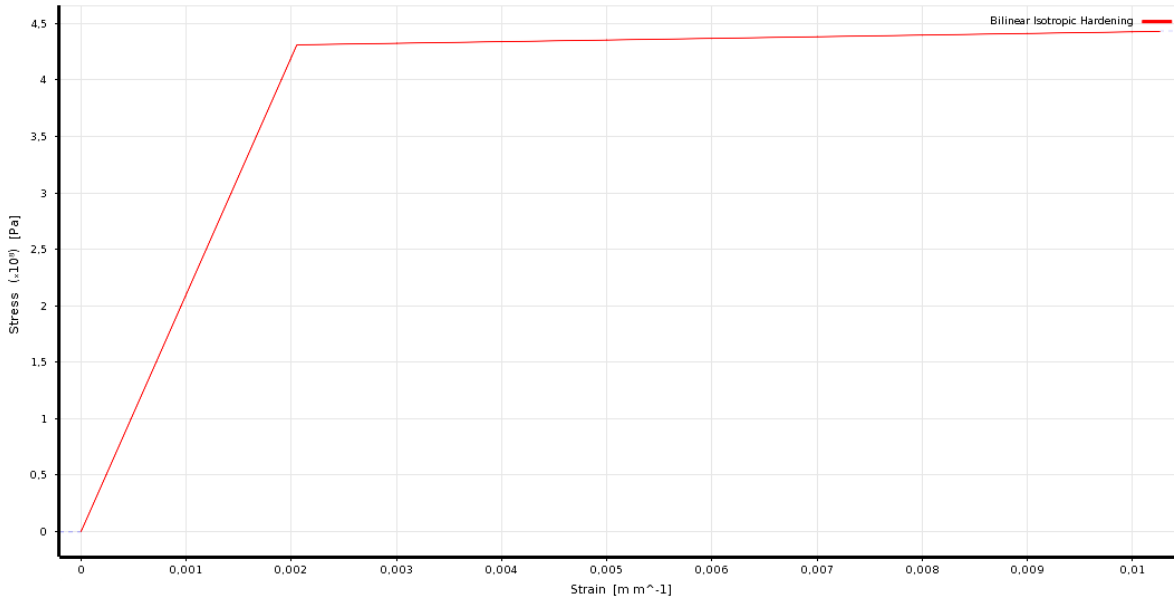
Figure 2.14: material behavior law

The properties are listed in the table below (Table 2.2).

	Stiffeners		Web		Flange	
Test	f_y [N/mm^2]	f_u [N/mm^2]	f_y [N/mm^2]	f_u [N/mm^2]	f_y [N/mm^2]	f_u [N/mm^2]
V1	431	541	435	558	428	567
V2	431	541	435	558	428	567
V3	431	541	435	558	428	567
V4	431	541	435	558	428	567
V5	383	541	409	537	400	543
V6	383	541	409	537	400	543

Table 2.2: material properties

All the tests have been studied starting from these materials, however inside the $file.txt$ containing the variables of the problem it is possible to modify elastic modulus, yield strength, ultimate tension and Poissont modulus of each of these. The definition of materials within the $Python\ Script$ has been facilitated by the presence of the Record Journal command within $Ansys$ (File-->Scripting-->RecordJournal), which records all the steps within a $file.wpjn$.

Below is an example of the definition of the material that will be assigned to the stiffeners:

```
system1 = GetSystem(Name="SYS")
engineeringData1 = system1.GetContainer(ComponentName="Engineering Data")
matl1 = engineeringData1.CreateMaterial(Name="Stiffener")
matlProp1 = matl1.CreateProperty(
    Name="Density",
    Qualifiers={"Definition": "", "Behavior": ""})
matlProp1.SetData(
    Index=-1,
    Variables=["Density"],
    Values=[["7850 [kg m^-3]"]])
matlProp2 = matl1.CreateProperty(
    Name="Elasticity",
    Behavior="Isotropic",
    Qualifiers={"Definition": "", "Behavior": "Isotropic"})
matlProp2.SetVariableProperty(
    VariableName="Young's Modulus",
    Property="Unit",
    Value="MPa")
matlProp2.SetData(
    Index=-1,
    Variables=["Young's Modulus"],
    Values=[["%s [MPa]"%E_s]])
matlProp2.SetData(
    Variables=["Poisson's Ratio"],
    Values=[["%s"%v_s]])
matlProp3 = matl1.CreateProperty(
    Name="Isotropic Hardening",
    Definition="Bilinear",
    Qualifiers={"Definition": "Bilinear", "Behavior": ""})
matlProp3.SetVariableProperty(
    VariableName="Yield Strength",
    Property="Unit",
    Value="MPa")
matlProp3.SetData(
    Index=-1,
    Variables=["Yield Strength"],
    Values=[["%s [MPa]"%F_ys]])
matlProp3.SetVariableProperty(
    VariableName="Tangent Modulus",
    Property="Unit",
    Value="MPa")
matlProp3.SetData(
    Variables=["Tangent Modulus"],
    Values=[["1450 [MPa]"]])
matlProp4 = matl1.CreateProperty(
    Name="Tensile Yield Strength",
    Qualifiers={"Definition": "", "Behavior": ""})
matlProp4.SetVariableProperty(
    VariableName="Tensile Yield Strength",
    Property="Unit",
    Value="MPa")
matlProp4.SetData(
    Index=-1,
    Variables=["Tensile Yield Strength"],
    Values=[["%s [MPa]"%F_ys]])
matlProp5 = matl1.CreateProperty(
    Name="Compressive Yield Strength",
    Qualifiers={"Definition": "", "Behavior": ""})
matlProp5.SetVariableProperty(
    VariableName="Compressive Yield Strength",
```

```python
        Property="Unit",
        Value="MPa")
    matlProp5.SetData(
        Index=-1,
        Variables=["Compressive Yield Strength"],
        Values=[["%s [MPa]"%F_ys]])
    matlProp6 = matl1.CreateProperty(
        Name="Tensile Ultimate Strength",
        Qualifiers={"Definition": "", "Behavior": ""})
    matlProp6.SetVariableProperty(
        VariableName="Tensile Ultimate Strength",
        Property="Unit",
        Value="MPa")
    matlProp6.SetData(
        Index=-1,
        Variables=["Tensile Ultimate Strength"],
        Values=[["%s [MPa]"%F_us]])
    matlProp7 = matl1.CreateProperty(
        Name="Compressive Ultimate Strength",
        Qualifiers={"Definition": "", "Behavior": ""})
    matlProp7.SetVariableProperty(
        VariableName="Compressive Ultimate Strength",
        Property="Unit",
        Value="MPa")
    matlProp7.SetData(
        Index=-1,
        Variables=["Compressive Ultimate Strength"],
        Values=[["%s [MPa]"%F_us]])
```

However, this command has only been used for defining materials, as it is impossible to capture operations within Mechanical [8].

2.5   Definition of the model

Once geometry and materials were defined, the mesh, boundary conditions, schematization and type of support-section interaction and loads were applied. As with geometry, the rest of the model was initially defined in *Mechanical*, and only after verifying its validity it was returned to *Python*.

2.5.1   Definition of the mesh

As specified in section 2.3, due to the high ratio of slenderness, the plates were reduced to surfaces, which are only then assigned the thickness.

Inside Mechanical the default element for the analysis of the plates is the shell element181 (Figure 2.15).
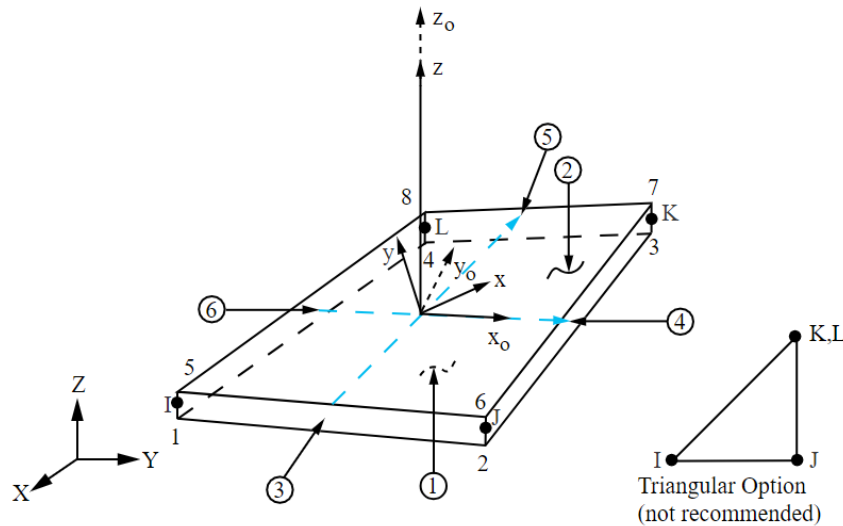
Figure 2.15: shell element 181 [13]

It is a four-node element with six degrees of freedom for each node (translations in the $x, y,$ and z directions and rotations around the $x, y,$ and z axes) suitable for linear, large rotation, and/or large strain applications [13].

The element takes the shear deformations into account according to Reissner-Mindlin's theory and applies by default a complete integration on the whole element (*APDL* command: *keyopt* (3) = 2). Due to the relatively large thinness of the web sheet of $L / t = 500$ in combination with the 4-knot element, there is a risk that the shear stiffness is overestimated due

to the "shear locking". One way to avoid the "shear locking" is the subintegration method ($APDL$ command: $keyopt\,(3) \;=\; 0$) [3], [13].

For this reason the model has been studied taking into consideration both types of integration, however, due to the difference in results of about 0.3% full integration has been used for all analyses.

The degenerated triangular option (Figure 2.15) is used as a filler element in mesh generation [13], however, as was found during the analysis, the presence of triangular and/or distorted elements causes the model to malfunction; for example, a perfect geometric symmetry and load application did not correspond to a symmetry in the deformed shape.

To avoid this unexpected behavior, changes have been added that have allowed to create a perfectly homogeneous mesh (Figure 2.16).
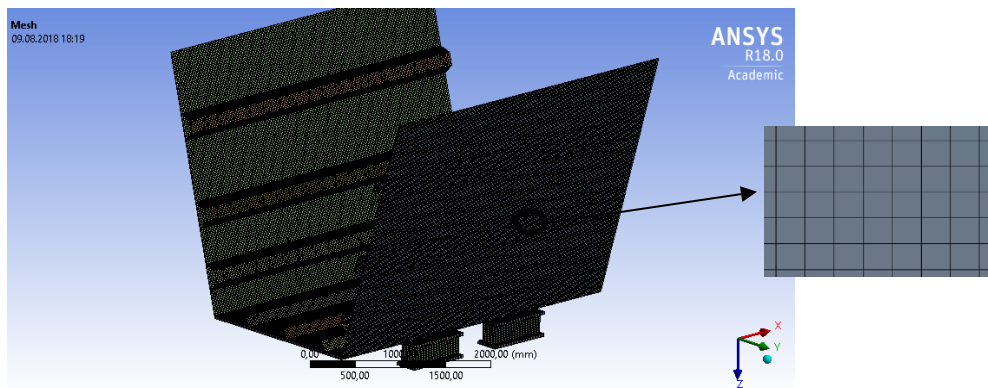
Figure 2.16: mesh of the Model

As far as the mesh size is concerned, a convergence analysis was carried out on the first value of the multiplier of the loads, until an asymptotic value was reached (Figure 2.17). From this analysis it emerged that beyond the value of 20mm the multiplier of the loads remained almost constant, for this reason, in order to avoid an excessive and useless computational effort, a dimension of the element equal to 20mm was chosen.
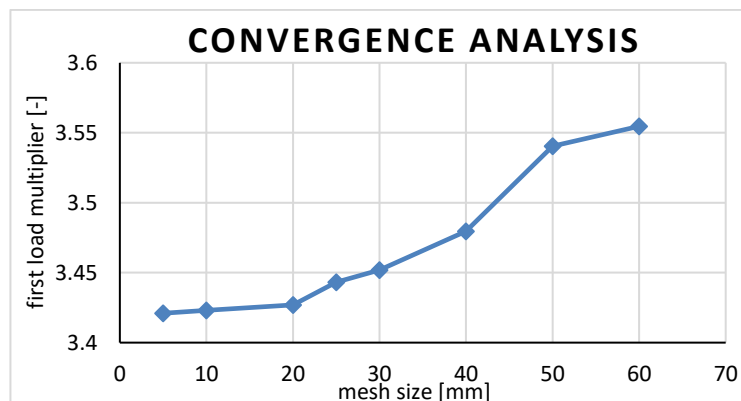
Figure 2.17: convergence analysis

The size of the element is a further parameter that is possible to change, because, given the opportunity to change the size of the body, probably a smaller body would require a finer mesh.

2.5.2   Bearings schematization

Two types of support have been defined: one in steel and the other one elastomeric. The position along the x-axis and the depth have been defined from parameters (Figure 2.13). In order to define the position along the y axis, for each constraint a parameter called *eccentricity* has been defined, which if equal to zero aligns the axis of the constraint with the edge of the section, not inducing any additional moment (Figure 2.18).
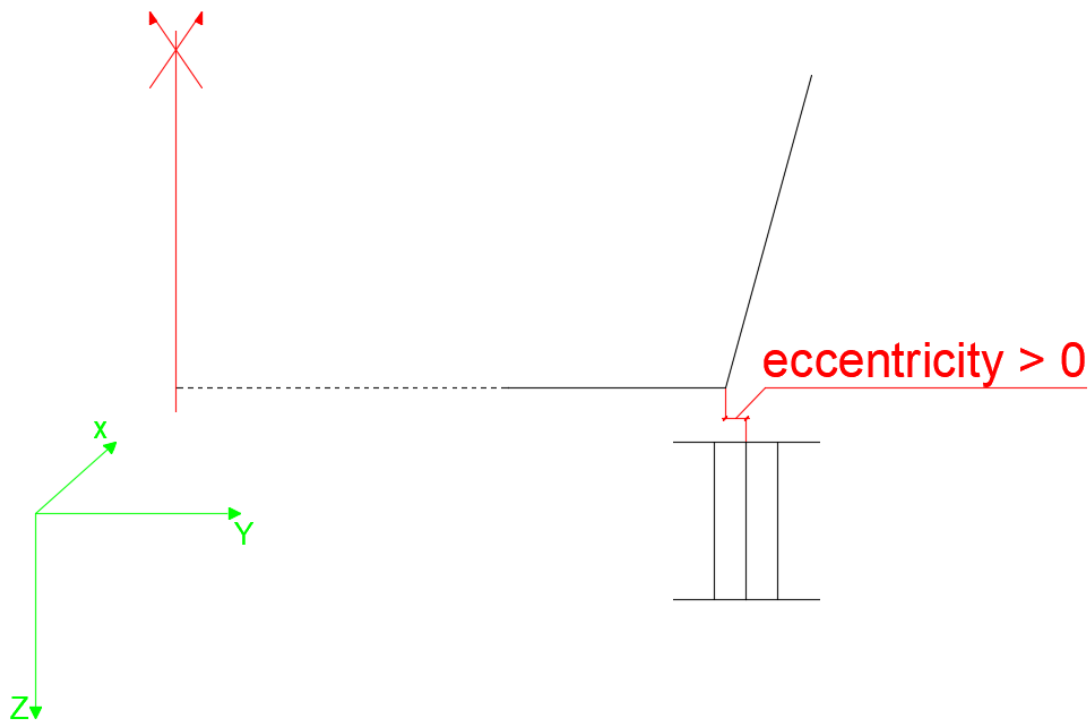
Figure 2.18: parameter that define the eccentricity of the bearing with respect to the section

As far as the schematization of the type of pusher adopted is concerned, see (chapter 2.5.3.2).

2.5.2.1 Rigid bearing

The rigid support (Figure 2.19) has a section of type $HEM260$ (Figure 1.9) and has been schematicated using shell elements (see paragraph 2.5.1).
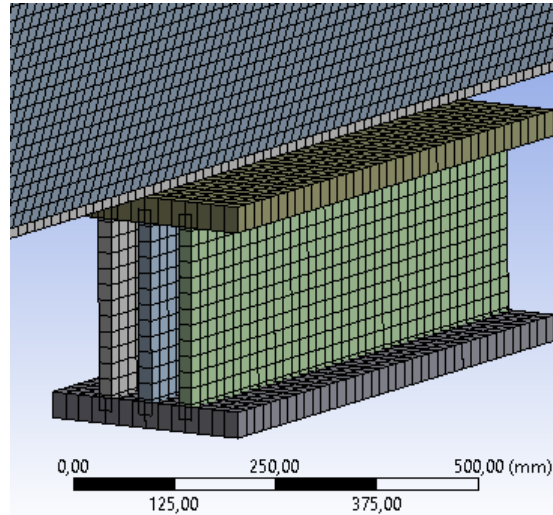
Figure 2.19: rigid support

2.5.2.2 Elastomeric bearing

The 32 mm elastomer layer has been modelled through 25 springs that have stiffness only in the z-direction (Figure 2.20) [3]. Horizontal forces are completely absorbed through the contact (see chapter 2.5.2.3; in addition, since horizontal loads are supposed to be significantly lower than the value that would produce shear deformations, a bounded type contact has been imposed between the steel plates that enclose the elastomer [3].
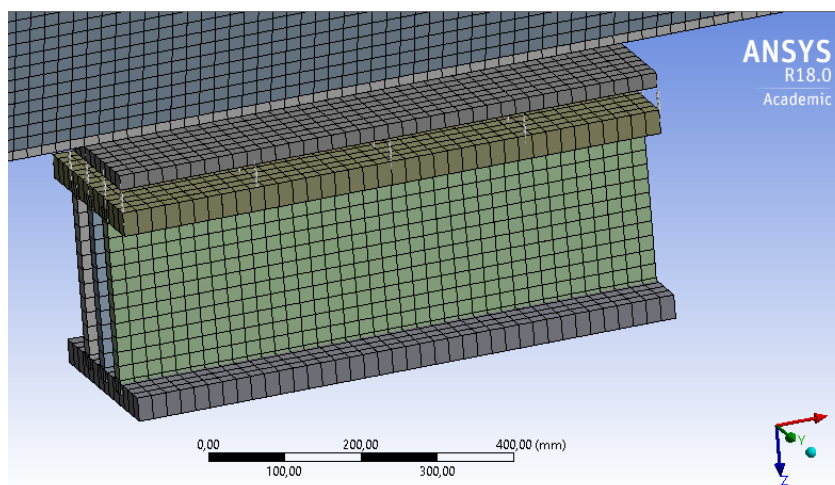
Figure 2.20: elastomear bearing modelled using springs

Each spring has stiffness equal to the overall stiffness k for the area of influence of each spring [3] (Figure 2.21).
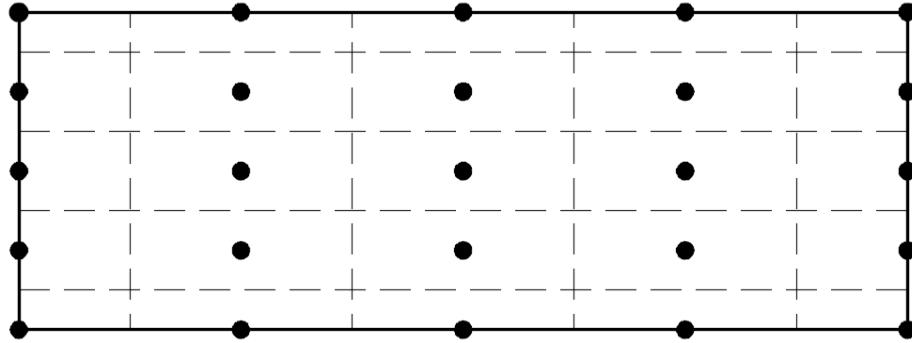
Figure 2.21: springs schematization

As can be seen from the Figure 2.20, three types of springs can be distinguished according to their location:

1) Edge springs, which individually cover an area $A_e = 1,5625\%$;
2) On-board springs, which individually cover an area $A_s = 3,125\%$;
3) On-board springs, which individually cover an area $A_c = 6,25\%$.

For the determination of the rigidity of the elastomeric layer, reference was made to DIN EN 1337-3 [14]. Considering an elastomeric $type\ B$ reinforcement with three layers of reinforcement (Figure 2.22), a shear modulus $G = 0.9MPa$ and a compression modulus $E_b = 2000MPa$, with the help of formula 20 of the standard [14] the lowering in each layer due to a unitary compression force has been determined.
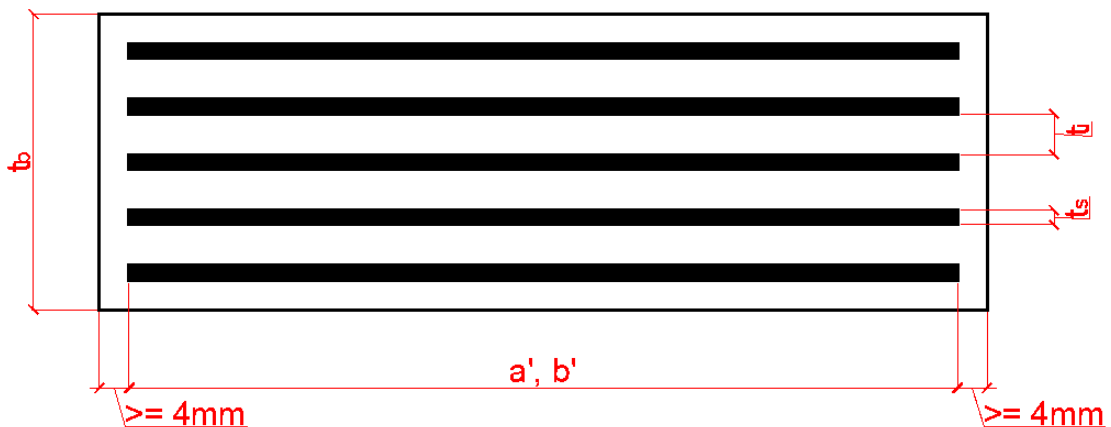
Figure 2.22: elastomer schematization with 5 steel reinforcements inside (according to [14])

$$v_c = \sum \frac{F_z \cdot t_i}{A'} \cdot \left(\frac{1}{5 \cdot G \cdot s_1^2} + \frac{1}{E_b} \right) = 1{,}61 \cdot 10^{-7} mm$$

Where:

$F_z = 1\ N$

$t_1 = 2{,}5\ mm;\ \ t_2 = 7{,}5\ mm;\ \ t_3 = 7{,}5\ mm;\ \ t_4 = 2{,}5\ mm$

$A' = a' \cdot b' = 260\ mm \cdot 742\ mm = 192920\ mm^2$

$G = 0{,}9\ MPa$

$E_b = 2000\ MPa$

$s_1 = Faktor\ form = \dfrac{A}{2 \cdot (a' + b') \cdot t_i}$

$$k = \frac{F}{v_c} = \frac{1}{1{,}61E - 07} \frac{N}{mm} = 6226943 \frac{N}{mm}$$

From which:

$$k_s = k \cdot A_e = 97259.98 \frac{N}{mm}$$

$$k_e = k \cdot A_s = 194592 \frac{N}{mm}$$

$$k_c = k \cdot A_c = 389183.9 \frac{N}{mm}$$

Inside the $file.txt$ it is possible to modify the k value, which will then be automatically distributed on each spring.

In order to verify the correctness of the model, the support has been studied separately before being coupled to the entire structure. Applying a compression force $F = 10000N$ and assuming the upper plate fixed, it was verified that in each spring the value of the reaction corresponded to that expected, that is:

$$R_s = F \cdot A_e = 156.25\ N \cong 156.23\ N = R_{s,FEM}$$

$$R_e = F \cdot A_s = 312.5\ N \cong 312.47\ N = R_{e,FEM}$$

$$R_c = F \cdot A_c = 625\ N \cong 624.93\ N = R_{c,FEM}$$

2.5.2.3 Structure bearings interaction

During the incremental launching, the structure slides over the supports, transferring both vertical and horizontal forces. The horizontal force is equal to the product of the vertical force and the coefficient of friction. In order to facilitate sliding, teflon sheets with a low friction coefficient are placed above the bearings. In the present thesis, as mentioned, two types of constraints have been analyzed that are based respectively on two types of pusher.

With regard to the rigid support-structure interaction, a coefficient of friction $\mu = 0.2$ was assumed, which is equal to the steel-steel coefficient of friction and corresponds to the value used during the tests.

As far as the interaction structure-elastomeric support is concerned, a friction coefficient $\mu = 0.02$ has been hypothesized, given the presence of teflon sheets placed above the constraint. This is because the coefficient of friction for PTFE and steel pair varies according to DIN EN 1337-2 [15] between the values of $\mu = 0.01$ and 0.15 for sliding friction [3]; however, higher coefficients of friction correspond to higher horizontal loads in the support, that's why a low value of $\mu = 0.02$ was chosen [3]. This means that only 2% of the vertical force can be transferred to the substrates in the case of elastomeric bonding.

The coefficient of friction is a further variable of the system inside the $file.txt$.

2.5.3   Boundary conditions

As for the application of boundary conditions, these have been assigned both directly to the geometric entities and to remote points connected to the body. Naturally, the boundary conditions applied to the supports change according to the type of pusher used during the incremental launching.

2.5.3.1   Geometry entities

Considering the reference system in the figure (Figure 2.9), the operating mechanism of the test and the figures (Figure 2.23), a prevented displacement of the end sections in the y direction was imposed.

Figure 2.23: picture of a steel section bridge

The same condition has been applied along the sides on which the top plate rests or will rest. This is because even if the upper plate were not present during the incremental launching of the bridge (Figure 2.24), there would still be a very rigid steel beam that connects the end sections.

Figure 2.24: picture of the top flange of a steel bridge section

Summarizing, along the sides highlighted (Figure 2.25) the displacement along y has been denied.
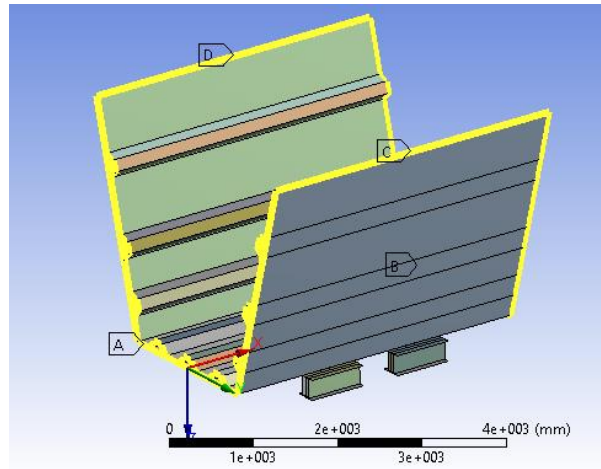
Figure 2.25: sides in which the y displacement has been denied

2.5.3.2   Remote points

The chapter will deal with the insertion of remote points where constraint conditions on displacements have been applied; for remote forces (paragraph 2.5.4).

Applying only the conditions of constraint as in the previous section is not sufficient to block the motion of the body in space, since to make the structure at least isostatic would need to impose conditions for the directions x and z.

Looking at the figure (Figure 1.7) one can well understand how the mechanism of operation of the tests is comparable to a beam on simple supports, where the supports are placed at a distance of $825mm$ from the end sections (this distance is another parameter that can be changed within the file.txt and is called x_{rp2}, however, given the geometry of the test was assumed a fixed value of $825mm$).

The remote points in A and B, connected to the section by very rigid beam elements [3] (Figure 2.26, Figure 2.27), were positioned at the barycentric level. For the constraint in A the prevented movement condition along z has been set, while for the constraint in B the prevented movement condition along x and along z has been set. As far as rotations are concerned, the end sections are left free to rotate.
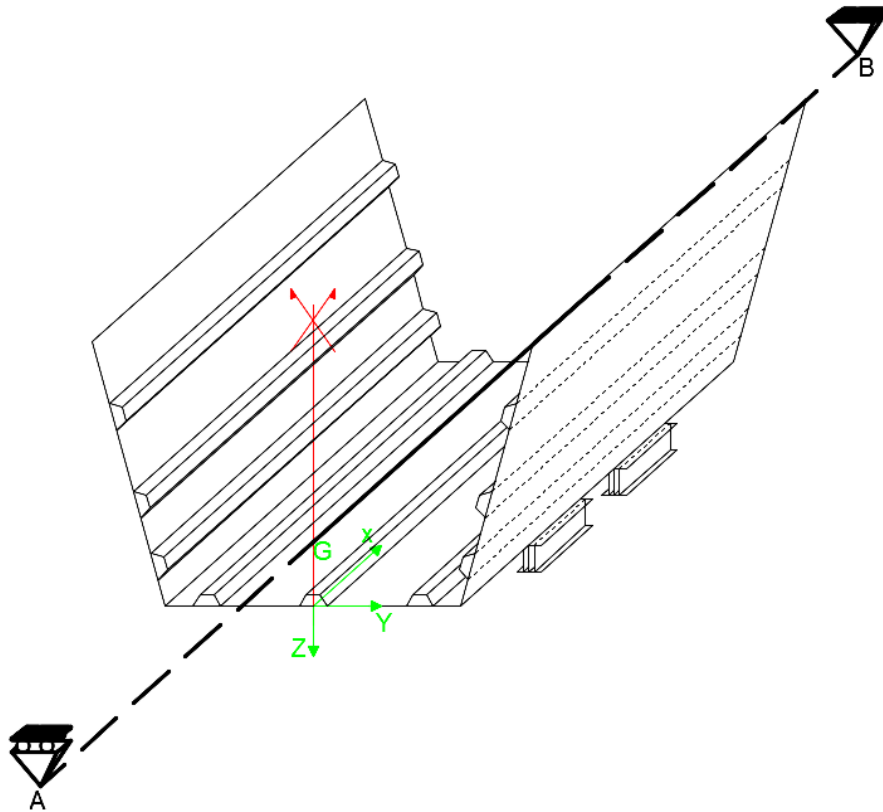
Figure 2.26: remote points connected with the extreme sectionns (3D)
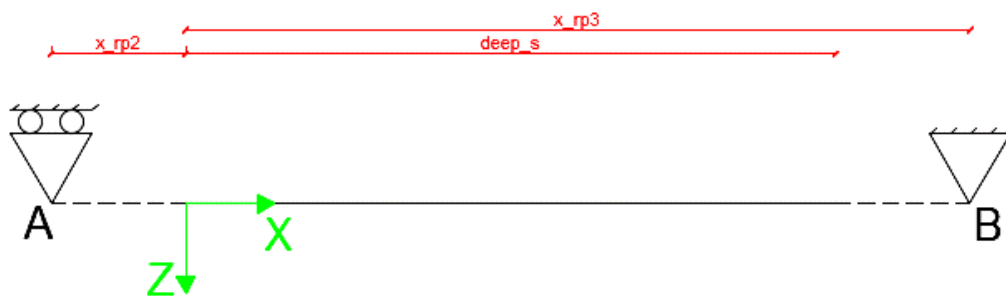
Figure 2.27: remote points connected with the extreme sections (2D)

In addition to the conditions of constraint in A and B, other remote points have been inserted, one at each support, whose positions and degrees of freedom depend on the type of pusher.

To simulate the spherical node pusher (Figure 2.28), on which the rigid $HEM260$ section constraint rests, the remote point has been placed at a height s with respect to the base of the constraint, a height where the centre of rotation of the pusher lies (Figure 1.8). With regard to the constraint conditions, the translation along the x and y directions and the rotation around the z axis have been blocked [3].
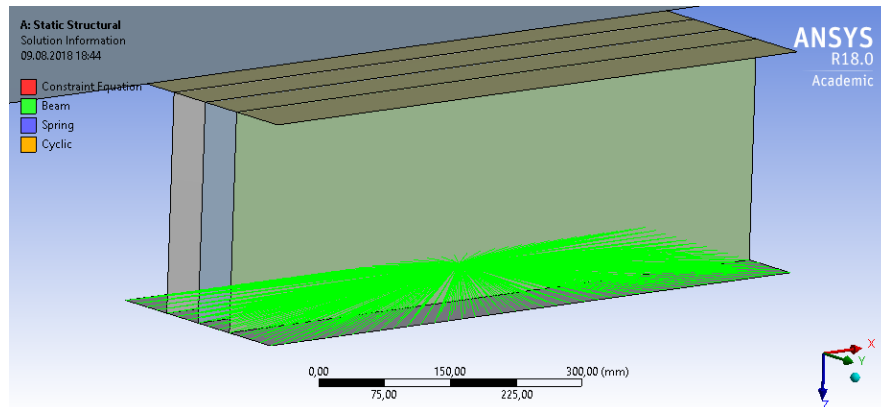
Figure 2.28: spherical node pusher simulation

To simulate the pusher with simple discharge (Figure 2.29), on which the elastomeric bearing rests, the remote point has been placed at a height coinciding with the base of the constraint. With regard to constraint conditions, translation along the x and y directions and rotation around the x and z axes have been blocked [3].
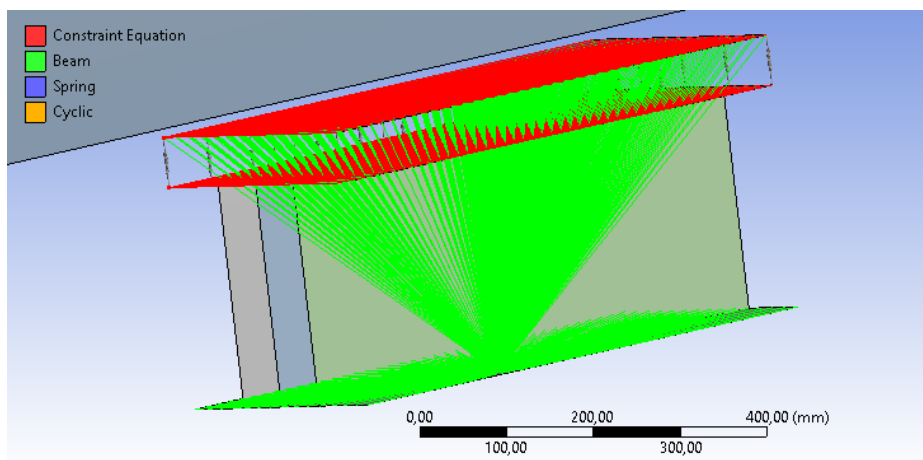
Figure 2.29: pusher with simple discharge simulation

2.5.4 Load application

As it is possible to observe from the Figure 1.7 also for the application of the forces it has been necessary to introduce remote points connected to the section through very rigid beam elements (Figure 2.30) [3].

The horizontal forces F1 and F2 have been applied in correspondence of remote points placed at the z_{rp} and z_{rp1} dimensions, measured starting from the center of gravity of the section (these quantities represent an additional parameter present inside the $file.txt$). The application of remote force allows not only to generate a bending moment, but also to apply a normal barycentric force that simulates the thrust effect during the incremental process.

As for the forces F3 and F4, these were applied at the remote points already discussed in the previous section. The self-weight P is applied as distributed load.
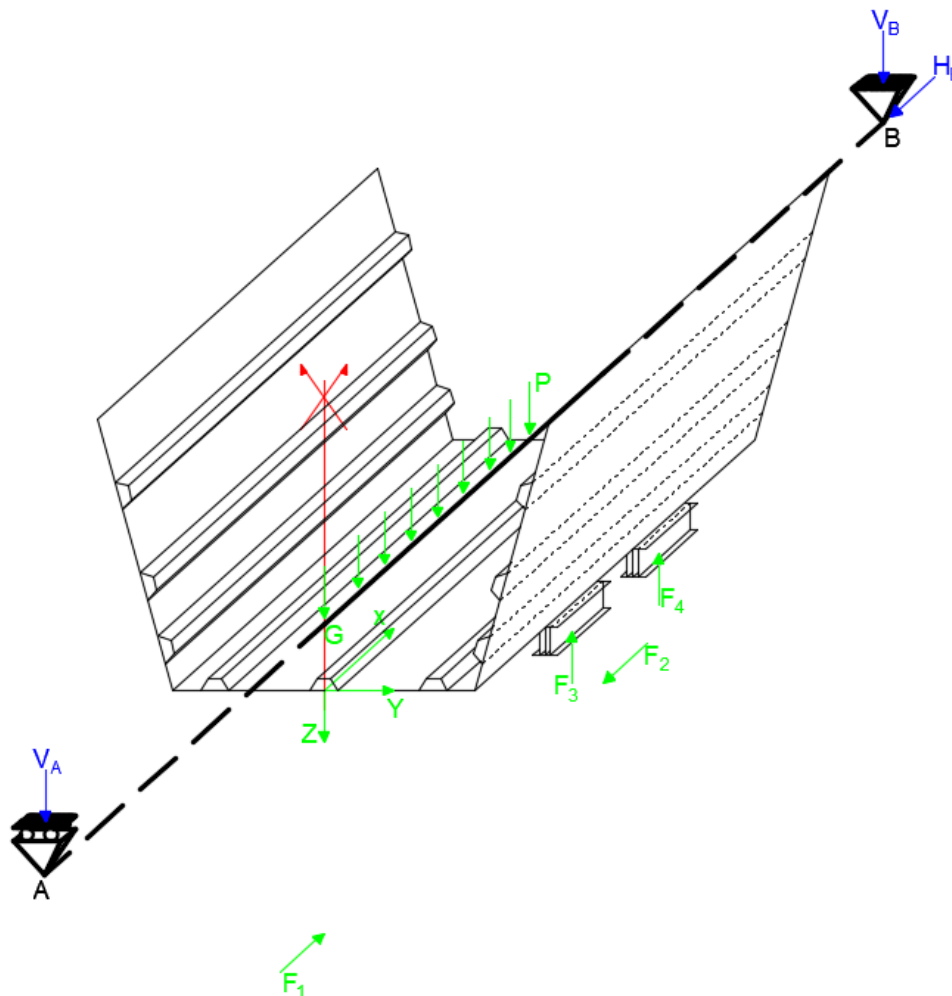
Figure 2.30: model scheme (3D)
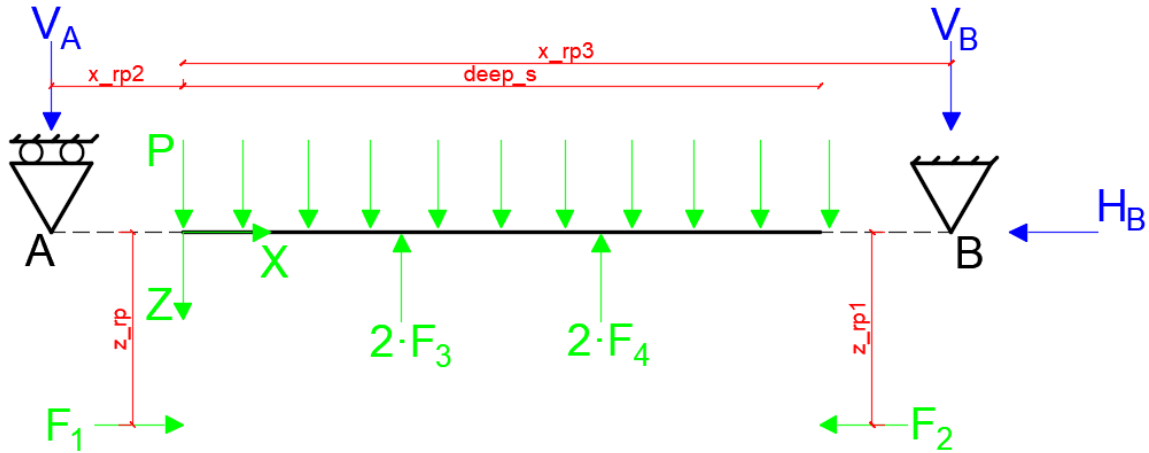
Figure 2.31: model scheme (2D)

The forces F3 and F4 are applied only in case of static analysis that precedes the linear buckling (see chapter 2.2.1), in order to obtain the desired β value, which varies according to six tests (Figure 1.11). In the case of non-linear analysis, forces are no longer applied, but displacements are applied, so that the test is performed not with force control, but with displacement (see paragraph 2.2).

In the case of geometrical symmetry and loading, a second *Script* was created in which the load nomenclature is shown as follows (Figure 2.32):
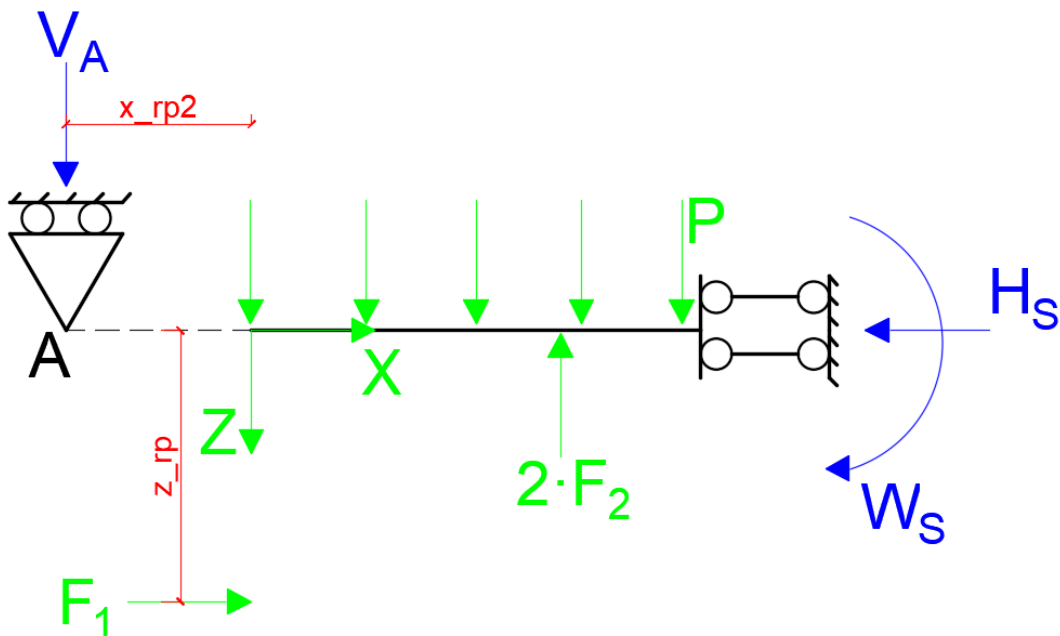
Figure 2.32: Symmetryc Model (2D)

Of course, it has been demonstrated that both models give identical results under the same loading conditions.

2.5.5   Validation of the Model

Once the model in *Mechanical* was completed, its truthfulness was evaluated. The values obtained by hand calculation were compared with those obtained from the program.

The comparison of the results obtained for test 1 at different points in the body is given as an example. In order to verify the correctness of the model, the own weight P of the section has been neglected (Figure 2.31).

In the case of the first test a stress ratio $\beta = 0.5$ was applied above the bearing (Figure 1.11), obtained in this model by applying $F_1 = F_2 = 3.0 \; MN$ and an $F_3 = F_4 = 0.43MN$.

Checking the tension state in the center section:

$$M = F_1 \cdot z_{rp} + 2F_3 \cdot \left(x_{rp2} + pos_{b1} + \frac{deep_b}{2} \right)$$

$$= 3000000N \cdot 5{,}469m + 430473{,}06N \cdot (0{,}825m + 1m + 0{,}375m)$$

$$= 1{,}83 \cdot 10^7 \; Nm$$

From which:

$$\sigma_{x,top} = -\frac{N}{A} + \frac{M}{I} z = \frac{\left(-\dfrac{3000000}{0{,}124} \dfrac{N}{m^2} + \dfrac{1{,}83E \cdot 10^7}{0{,}1042} \dfrac{Nm}{m^4} \cdot 2{,}21m \right)}{10^6} = 364{,}19 MPa$$

$$\sigma_{x,bottom} = -\frac{N}{A} - \frac{M}{I} z = \frac{\left(-\dfrac{3000000}{0{,}124} \dfrac{N}{m^2} + \dfrac{1{,}83E \cdot 10^7}{0{,}1042} \dfrac{Nm}{m^4} \cdot 0{,}679m \right)}{10^6} = -143{,}49 MPa$$

$$\Delta\sigma_{top} = 1 - \frac{\sigma_{x,top}}{\sigma_{x,top,FEM}} = \left(1 - \frac{364{,}19}{368} \right) \cdot 100 = 1{,}03\%$$

$$\Delta\sigma_{bottom} = 1 - \frac{\sigma_{x,bottom,FEM}}{\sigma_{x,bottom}} = \left(1 - \frac{-139}{-143{,}49} \right) \cdot 100 = 3{,}13\%$$

Where $\sigma_{x,top,FEM}$ and $\sigma_{x,bottom,FEM}$ are shown in Figure 2.33.
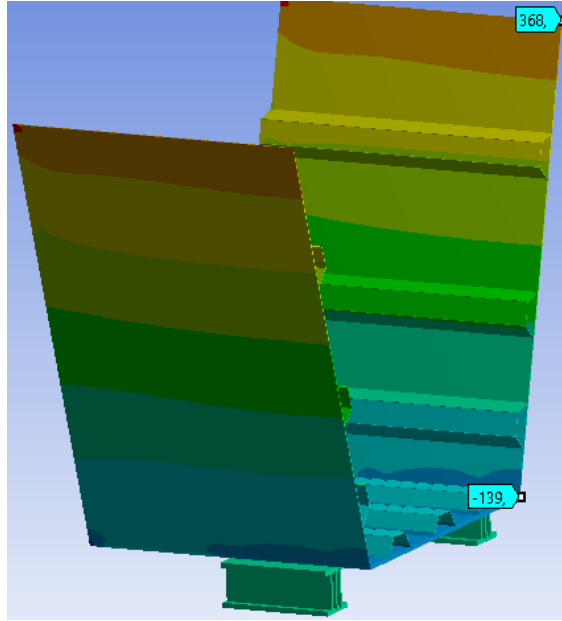
Figure 2.33: test 1 - $\sigma_{x,top,FEM}$ and $\sigma_{x,bottom,FEM}$ in the middle section

$$\sigma_z = -\frac{F_2}{A_1} = -\frac{430473,06}{6000} \, MPa = -71,75 MPa$$

$$\Delta\sigma_z = 1 - \frac{\sigma_{z,FEM}}{\sigma_z} = \left(1 - \frac{-71}{-71,75}\right) \cdot 100 = 1,05\%$$

Where $\sigma_{z,FEM}$ was taken as the average value between the minimum and the centerline value (Figure 2.34).
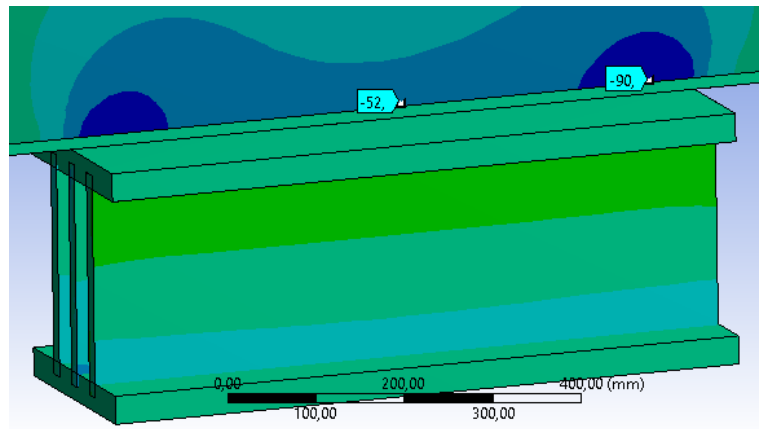
Figure 2.34: σ_z above the bearing (test 1 modelling)

The slight difference in the results is due to the presence of friction between the section and the support, which affects the distribution of tensions.

2.5.6 ACT Console

The ACT console is a tool in Workbench that allows you to write *IronPython* language commands directly within the program and display their outputs [16]. For example, by typing in the command:

```
geometry = ExtAPI.DataModel.Project.Model.Geometry
surface = geometry.Children[0].Children[37]
surface.Thickness = Quantity('18[mm]')
surface.Assignment = 'Web'
```

a thickness of 18mm will automatically be assigned to one of the surfaces that are part of the first body of the entire geometry. In doing so, the complete model was first created manually, and only after verifying its veracity, it was brought back into *IronPython* language inside the console.

At this point the last step was to recall the commands from the outside inserting them into the same *Script* in which the geometry was defined. To do this, simply rewrite the commands in the following way:

```
mySystems = GetAllSystems()
myContModel = mySystems[0].GetContainer(ComponentName = "Model")
myContModel.Edit(Hidden=True)

myCmd=""
myCmd+="geometry = ExtAPI.DataModel.Project.Model.Geometry\n"
myCmd+="surface = geometry.Children[0].Children[37]\n"
myCmd+="surface.Thickness = Quantity('18[mm]')\n"
myCmd+="surface.Assignment = 'Web'\n"
myContModel.SendCommand(Language="Python",Command=myCmd)
```

Where with the first three lines it has asked the program to open the "container" Model and make it possible to modify it by inserting the next lines. As shown inside Figure 2.1 the code lines written in *Python* can be reported in *Ansys* through the *SendCommand*() command.

3. TEST SIMULATION: THRUST BEARINGS TYPE GE80-AW

This chapter reports and comments on the results of the model, compared both with the tests results and with those contained in [3], which consists in modelling the real geometry of the first three tests and which provided reliable results, in particular for the test 3, then studied again using the elastomeric bearings. For this reason, the same boundary conditions as in [3] have been used, and therefore a comparison with its results is necessary.

In addition, the comparison with the real results is reported, because of the need to make a comparison with the tests that have not been studied in [3]. So doing it is possible to provide a better overview of the whole problem.

As explained in the paragraph 2.2.1, the calculation consists of three steps: linear mechanical analysis, linear eigenvalue analysis and nonlinear analysis (Figure 2.3).

The first two are used to determine a form of instability which is then used as a pre-strain for nonlinear analysis [10]. As regards the application of the conditions of constraint, the launching bearing with the spherical knot (amply discussed in chapter 2.5.3.2) has always been adopted (Figure 1.8). In chapter 4 the tests are remodeled using the elastomer bearing and the thrust bearing with single exhaust.

3.1 Test 1

As shown in Figure 1.11 the β stress ratio adopted during the test is 0.5. Due to the symmetry of the load, the symmetrical model was used (Figure 2.32, Figure 3.1).
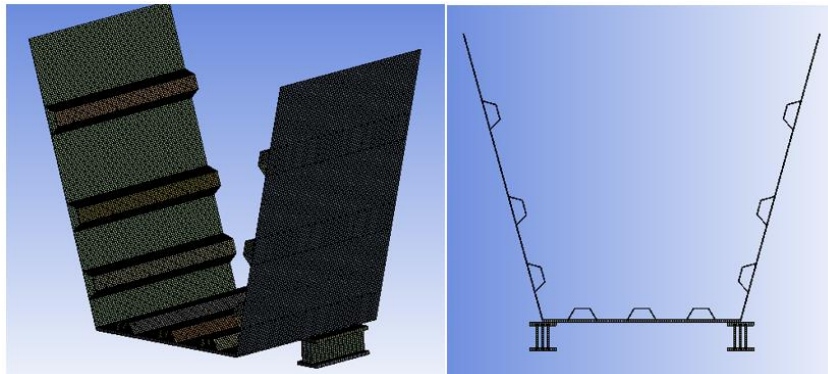
Figure 3.1: test 1 schematization using the symmetric model

In order to obtain the desired stress ratio, a load $F1 = 3000000$ N was imposed, to which corresponds, for inverse resolution, a value of $F2 = 430473.06$ N. To obtain the value F2, an *Excel* worksheet was simply created.

3.1.1   Test 1: static analysis

The linear static analysis for the first test has already been analyzed in paragraph 2.5.5 where the congruence between the values obtained by hand calculation and those obtained from the programme was demonstrated. As already mentioned several times, linear static analysis requires a lower load to be applied than that applied during the tests. This is done with the intention of obtaining the desired β stress ratio and to check whether buckling occurs at the lower stiffening.

This last aspect has been determinant in the choice of the number of the stiffeners that run along the bottom flange; in fact, a number equal to 3 longitudinal stiffeners has been chosen because it is the minimum requirement to avoid the instability of the bottom plate already in the first forms of instability.

3.1.2   Test 1: linear buckling

The linear static analysis is followed by linear instability analysis. During this phase, the forms of instability and the corresponding load multiplication factors are determined.

As explained in the paragraph 2.2.1, linear instability analysis returns an ideal critical load (Figure 2.4) due to the lack of imperfections within the geometry.

The following figures show the first form of instability (Figure 3.2). Worth noting is that the multiplication factor of the loads is practically the same ($3.4301 \cong 3.4304$).
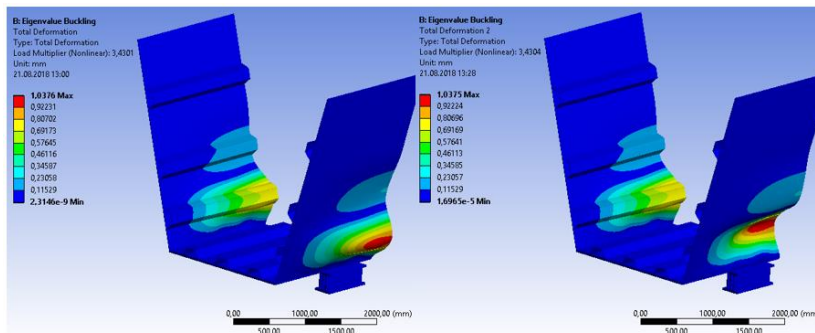
Figure 3.2: first buckling mode (test 1 modelling)

This is because, given the symmetry of the problem, instability occurs in both webs at the same time; however, since *Ansys* offers the opportunity to assign imperfections in the area where buckling occurred (to perform a nonlinear analysis), to which then a sign is applied (*plus* if an imperfection in the same direction of the buckling is applied and *minus* if an imperfection in the opposite direction is applied), each buckling mode is repeated twice so that it is possible to consider all 4 cases (*plus* or *minus* for both webs or alternate signs).

From Figure 3.2 is evident how instability involves the lower stiffeners, just like in the test (Figure 3.3).
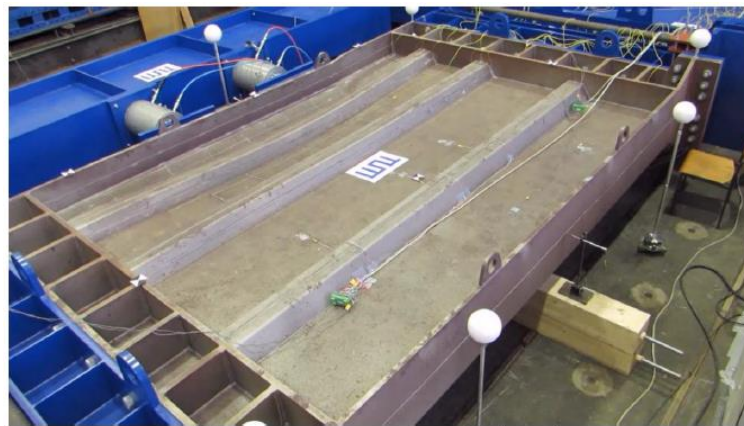
Figure 3.3: test 1 picture [3]

In Figure 3.4 forms of instability 2, 3, 4 and 5 are shown, showing how only in correspondence of the fifth buckling mode and for a very high value of the multiplication factor of the loads (5,7301) also the botttom plate becomes unstable.
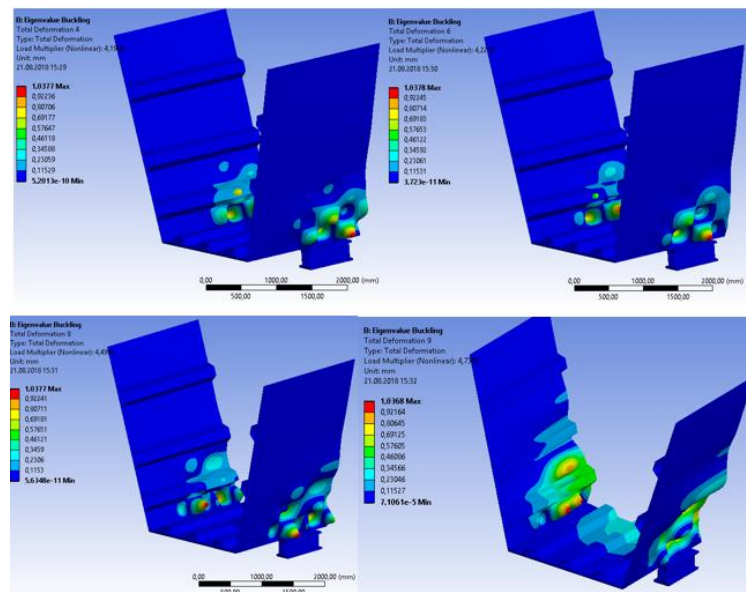
Figure 3.4: buckling modes 2, 3, 4 and 5 (test 1 modelling)

3.1.3 Test 1: nonlinear analysis

For an estimation of the final load, the linear instability analysis alone is not suitable, however it can be used as a starting point for a nonlinear instability analysis, using the forms of instability as imperfections [10]. On the basis of Table 2.1, the normative prescribes the application of an equivalent imperfection of:

$$e_{0w} = \min\left(\frac{a}{200}; \frac{b}{200}\right) = \frac{3000}{200}mm = 15mm$$

Applicable through APDL commands to any form of instability (paragraph 2.2.1). The value of the imperfection has been adopted not only to be on the security side, but also to allow a more faithful comparison with the results contained in [3].

Observing the direction of instabilization of the lower stiffener in Figure 3.3 it was decided to apply an imperfection to the first form of instability indicated as total deformation 2 (Figure 3.2). As already mentioned previously, a negative imperfection has been applied because the instability is turned inwards, however, a deflection with respect to the normal has to be applied outwards.

```
fini
/prep7
upgeom,-15/1.0375,1,2,..\..\Buckling,rst
fini
/solu
```

The distortion factor 15 has been divided by 1.0375 because the maximum displacement has been normalized to this value (see paragraph 2.2.1 and Figure 3.2). In this way a maximum imperfection of 15 mm will be applied.

Since the purpose of the nonlinear analysis is to trace the trend of the F2 force and obtain the maximum value beyond which the section becomes unstable (Figure 2.6), a force was no longer applied to the supports but a displacement of 20 mm [3] (Figure 3.5 and paragraph 2.2.1), instead F1 was assigned a value of 3.1296 MN, coinciding with that of the test.
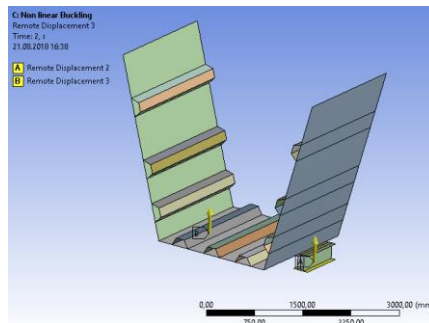
Figure 3.5: remote displacement applied to the bearings

The following picture (Figure 3.6) shows a perfect symmetry in the deformed, demonstrating that the first form of instability previously evaluated is identical in the two webs.
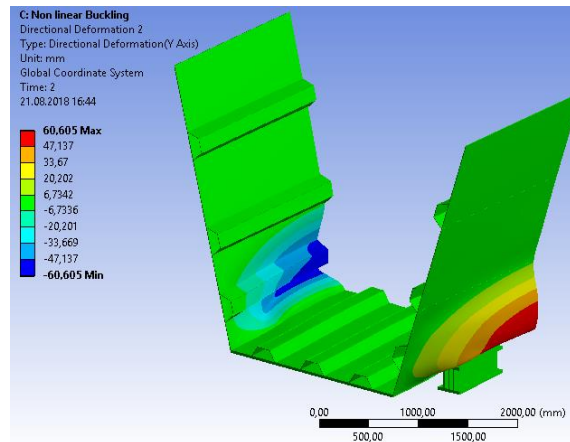
Figure 3.6: nonlinear deformed shape (test1 modelling)

While the force F2 trend shows a peak equal to 1.367 MN (Figure 3.7); in addition, performing the deformation control test it was possible to trace the trend of the force during $snap-through$. The force F2 regards the single bearing.

Displacement [mm]	F$_2$ [MN]
0	0
0,91321	0,11
1,8921	0,23
3,4805	0,38
5,2111	0,53
11,968	1,00
19,347	1,31
27,265	1,37
31,042	1,33
34,491	1,28
39,103	1,21
44,227	1,15
48,748	1,10
52,824	1,05
56,549	1,02
58,611	1,00
60,606	0,98
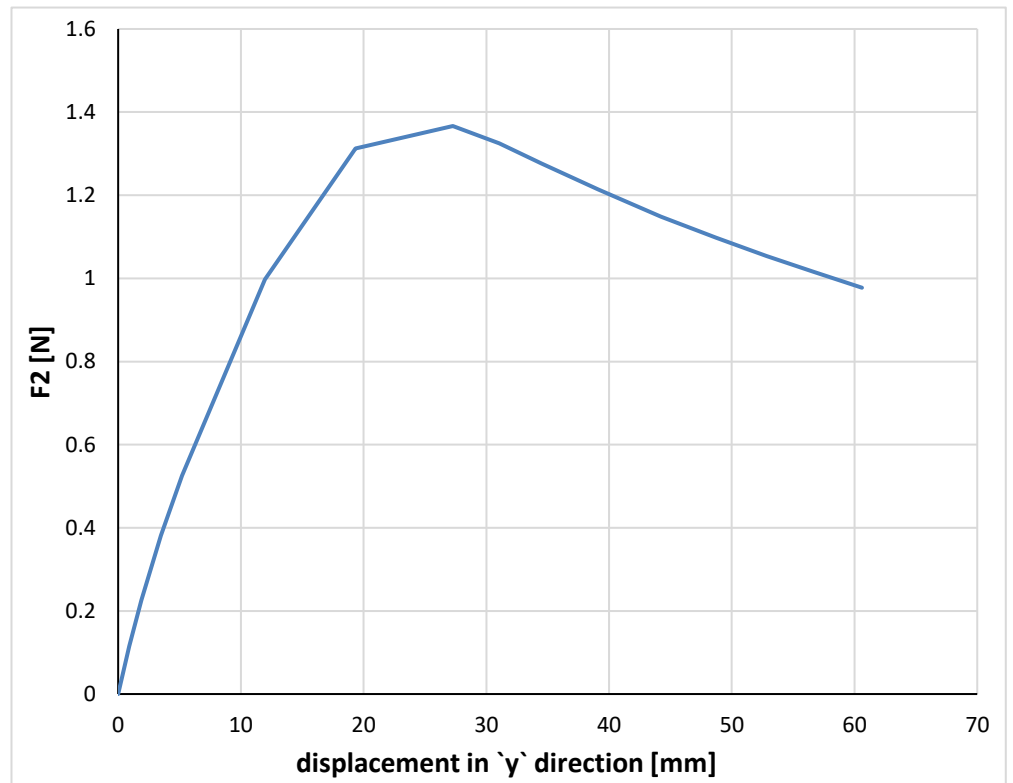
Figure 3.7: F2 trend (test 1 modelling)

The difference in percentage between the nonlinear model results and the test ones is shown in Table 3.1, however, it is too high despite 15 mm is a high imperfection. The force F2 refers to the single bearing.

F$_{1,FEM}$ [MN]	F$_{1, Test}$ [MN]	ΔF$_1$ [%]	F$_{2,FEM}$ [MN]	F$_{2, Test}$ [MN]	ΔF$_2$ [%]
3,1296	3,1296	0	1,367	0,83	64,56

Table 3.1: test 1 - difference in percentage between the nonlinear model results and the test 1 ones

Where: $\Delta F_2 = \frac{F_{2,FEM} - F_{2,test}}{F_{2,test}} \cdot 100$

Probably this is due to the different distribution of the imperfections compared to reality, in fact, from the 3D scans made on the body of the first test shows a greater presence of the imperfections in the lower part of the flange (Figure 3.8) which led to the premature plasticization of the part adjacent to the front constraint, also favored by the possibility of the constraint to rotate around the x-axis (Figure 3.9).
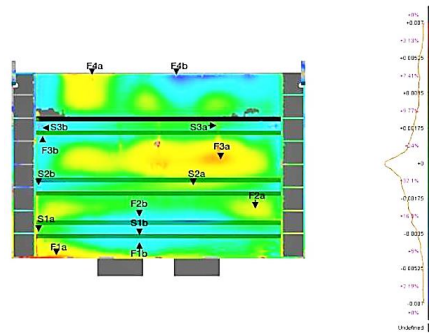
Figure 3.8: 3D scans made on the body of the first test [4]

Figure 3.9: premature plasticization of the part adjacent to the front constraint [4]

With respect to the model studied in [3] there is a difference of more or less the 26,67 % Table 3.2.

F$_{1,FEM}$ [MN]	F$_{1, JS}$ [MN]	ΔF$_1$ [%]	F$_{2,FEM}$ [MN]	F$_{2, JS}$ [MN]	ΔF$_2$ [%]
3,1296	3,1296	0	1,367	1,0788	26,67

Table 3.2: test 1 - difference in percentage between the nonlinear model results and the [3] ones

3.2   Test 2

As shown in Figure 1.11 the β stress ratio adopted during the test is equal to 1, while the geometry is unchanged compared to the previous test (Figure 3.1). Due to the symmetry of the load, the symmetrical model was used (Figure 2.32).

In order to obtain the desired stress ratio, a load $F1 = 1500000$ N was imposed, to which corresponds, for inverse resolution, a value of $F2 = 474203.41$ N. An Excel worksheet has simply been created to obtain the F2 value.

3.2.1   Test 2: static analysis

During the linear static analysis a lower load than that applied during the tests is applied. This is done with the intention of obtaining the desired β stress ratio and to check whether buckling occurs at the bottom flange.

This last aspect has been determinant in the choice of the number of the stiffeners that run along the bottom flange; in fact, a number equal to 3 longitudinal stiffeners has been chosen because it is the minimum requirement to avoid the instability of the bottom flange already in the first buckling modes.

Checking the tension state in the center section and imposing $P = 0$ (Figure 2.31):

$$M = F_1 \cdot z_{rp} + 2F_3 \cdot \left(x_{rp2} + pos_{b1} + \frac{deep_b}{2} \right)$$

$$= 1500000N \cdot 5,469m + 474203,41N \cdot (0,825m + 1m + 0,375m)$$

$$= 1,03 \cdot 10^7 Nm$$

From which:

$$\sigma_{x,top} = -\frac{N}{A} + \frac{M}{I}z = \frac{\left(-\dfrac{1500000}{0,124}\dfrac{N}{m^2} + \dfrac{1,03 \cdot 10^7}{0,1042}\dfrac{Nm}{m^4} \cdot 2,21m \right)}{10^6} = 206,37 \ MPa$$

$$\sigma_{x,bottom} = -\frac{N}{A} - \frac{M}{I}z = \frac{\left(-\dfrac{1500000}{0,124}\dfrac{N}{m^2} + \dfrac{1,03 \cdot 10^7}{0,1042}\dfrac{Nm}{m^4} \cdot 0,679m \right)}{10^6} = 79,20 \ MPa$$

$$\Delta\sigma_{top} = 1 - \frac{\sigma_{x,top}}{\sigma_{x,top,FEM}} = \left(1 - \frac{206,37}{214}\right) \cdot 100 = 3,57\%$$

$$\Delta\sigma_{bottom} = 1 - \frac{\sigma_{x,bottom,FEM}}{\sigma_{x,bottom}} = \left(1 - \frac{-76}{-79,2}\right) \cdot 100 = 4,0\%$$

Where $\sigma_{x,top,FEM}$ and $\sigma_{x,bottom,FEM}$ are shown in Figure 3.10.
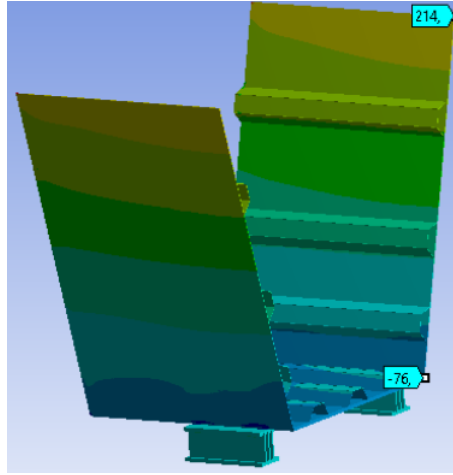
Figure 3.10: test 2 - $\sigma_{x,top,FEM}$ and $\sigma_{x,bottom,FEM}$ in the middle section

$$\sigma_z = -\frac{F_2}{A_1} = -\frac{474203,41}{6000} \, MPa = -79,2 MPa$$

$$\Delta\sigma_z = 1 - \frac{\sigma_{z,FEM}}{\sigma_z} = \left(1 - \frac{-81,5}{-79,2}\right) \cdot 100 = 1,05\%$$

Where $\sigma_{z,FEM}$ was taken as the average value between the minimum and the centerline value (Figure 3.11).

Figure 3.11: σ_z above the bearing (test 2 modelling)

The slight difference in the results is due to the presence of friction between the section and the support, which affects the distribution of tensions.

3.2.2   Test 2: linear buckling

The linear static analysis is followed by linear instability analysis. During this phase, the forms of instability and the corresponding load multiplication factors are determined.

As explained in the paragraph 2.2.1, linear instability analysis returns an ideal critical load (Figure 2.4) due to the lack of imperfections within the geometry.

Figure 3.12 shows the first form of instability. Worth noting is that the multiplication factor of the loads is practically the same ($3.1651 \cong 3.1661$).
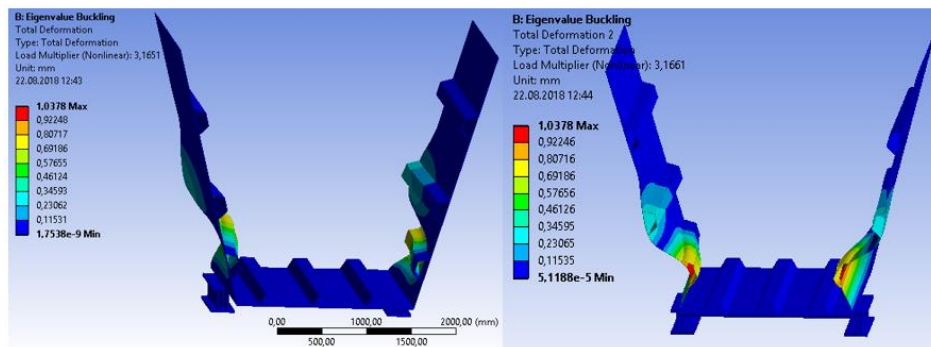
Figure 3.12: first buckling mode (test 2 modelling)

This is because, given the symmetry of the problem, instability occurs in both webs at the same time; however, since *Ansys* offers the opportunity to assign imperfections in the area where buckling occurred (to perform a nonlinear analysis), to which then a sign is applied (*plus* if an imperfection in the same direction of the buckling is applied and *minus* if an imperfection in the opposite direction is applied), each buckling mode is repeated twice so that it is possible to consider all 4 cases (*plus* or *minus* for both webs or alternate signs).

From Figure 3.12 is evident how instability involves the lower stiffeners, just like in the test [3] (Figure 3.13).
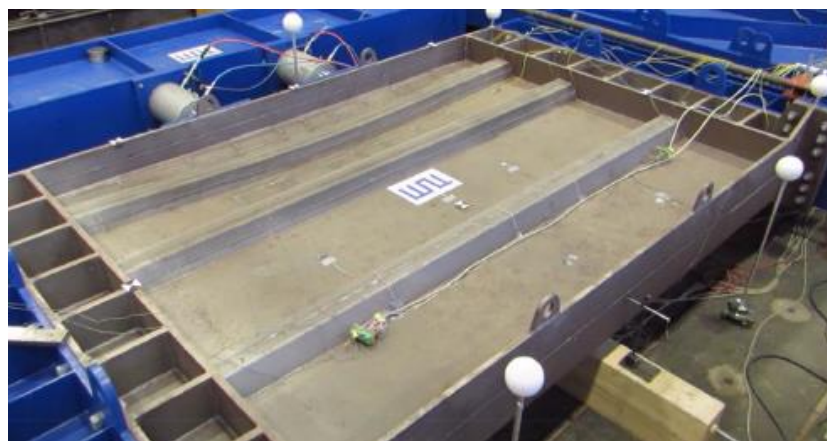
Figure 3.13: test 2 picture [3]

Figure 3.14 shows the forms of instability 2, 3, 4 and 5, showing how the instability occurs mainly at the lower stiffening and above the constraint, in fact only for high values of the multiplication factor of the loads the instability moves up. However, this was to be expected as the compression state is much higher at the bottom of the webs.
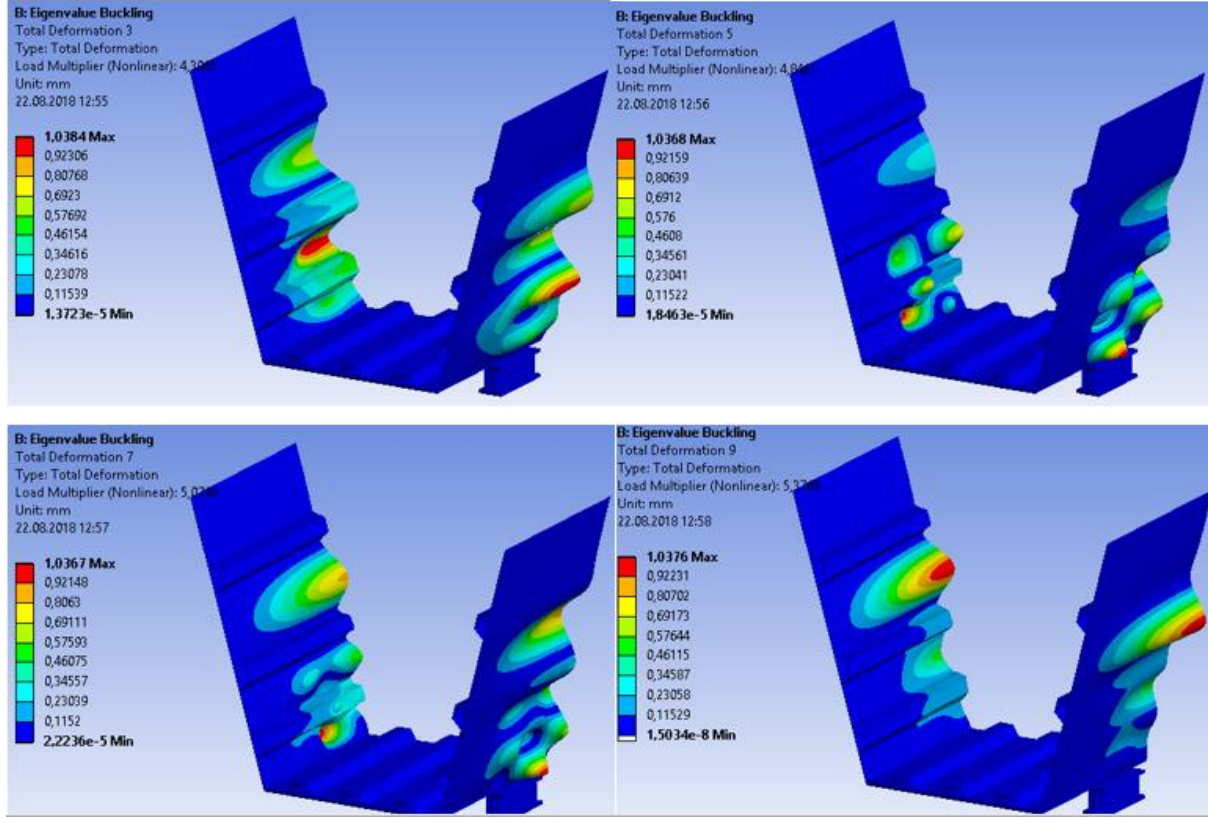
Figure 3.14: buckling modes 2, 3, 4 and 5 (test 2 modelling)

3.2.3   Test 2: nonlinear analysis

For an estimation of the final load, the linear instability analysis alone is not suitable, however it can be used as a starting point for a nonlinear instability analysis, using the forms of instability as imperfections [10]. On the basis of Table 2.1, the normative prescribes the application of an equivalent imperfection of:

$$e_{0w} = \min\left(\frac{a}{200}; \frac{b}{200}\right) = \frac{3000}{200} mm = 15mm$$

Applicable through APDL commands to any form of instability (paragraph 2.2.1). The value of the imperfection has been adopted not only to be on the security side, but also to allow a more faithful comparison with the results contained in [3].

Observing the direction of instabilization of the lower stiffener in Figure 3.13 it was decided to apply an imperfection to the first form of instability indicated as total deformation 2 (Figure 3.12). As already mentioned previously, a negative imperfection has been applied because the instability is turned inwards, however, a deflection with respect to the normal has to be applied outwards.

```
fini
/prep7
upgeom,-15/1.0378,1,2,..\..\Buckling,rst
fini
/solu
```

The distortion factor 15 has been divided by 1.0378 because the maximum displacement has been normalized to this value (see paragraph 2.2.1 and Figure 3.12). In this way a maximum imperfection of 15 mm will be applied. Since the purpose of the nonlinear analysis is to trace the trend of the F2 force and obtain the maximum value beyond which the section becomes unstable (Figure 2.6), a force was no longer applied to the supports but a displacement of 20 mm [3] (Figure 3.5 and paragraph 2.2.1), instead F1 was assigned a value of 1,609 MN, coinciding with that of the test. The following picture (Figure 3.15) shows a perfect symmetry in the deformed, demonstrating that the first form of instability previously evaluated is identical in the two webs.
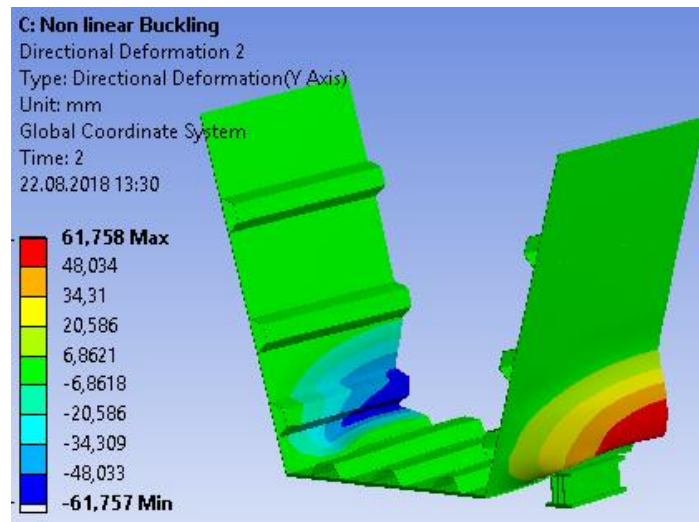
Figure 3.15: nonlinear deformed shape (test2 modelling)

While the force F2 trend shows a peak equal to 1.39 MN (Figure 3.16); in addition, performing the deformation control test it was possible to trace the trend of the force during $snap-through$..

Displacement [mm]	F$_2$ [MN]
0	0
1,6754	0,21
3,5475	0,41
6,687	0,68
10,14	0,91
17,296	1,27
25,076	1,39
32,18	1,33
35,283	1,29
38,178	1,26
42,088	1,21
46,76	1,16
50,903	1,12
54,665	1,08
58,006	1,04
59,953	1,02
61,757	1,00
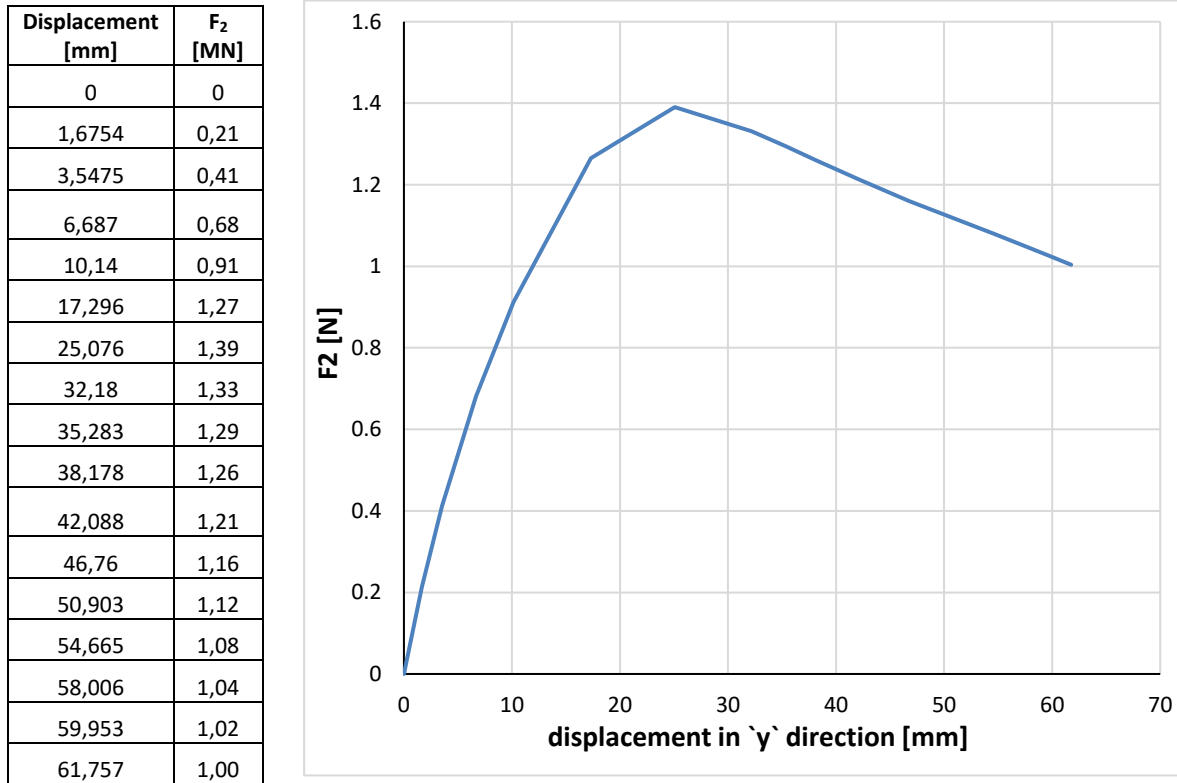
Figure 3.16: F2 trend (test 2 modelling)

The difference in percentage between the nonlinear model results and the test ones is shown in (Table 3.3). The force F2 refers to the single bearing.

F$_{1,FEM}$ [MN]	F$_{1, Test}$ [MN]	ΔF$_1$ [%]	F$_{2,FEM}$ [MN]	F$_{2, Test}$ [MN]	ΔF$_2$ [%]
1,61	1,61	0,00	1,39	1,12	**24,08**

Table 3.3: test 2 - difference in percentage between the nonlinear model results and the test2 ones

With respect to the model studied in [3] there is a difference of more or less the 8,5%, showing how the presence of the bottom plate provides a significant benefit on the overall behavior of the section.

F$_{1,FEM}$ [MN]	F$_{1, JS}$ [MN]	ΔF$_1$ [%]	F$_{2,FEM}$ [MN]	F$_{2, JS}$ [MN]	ΔF$_2$ [%]
1,61	1,61	0	1,39	1,28	**8,49**

Table 3.4: test 2 - difference in percentage between the nonlinear model results and the [3] ones

In addition, as can be seen from the Figure 3.17, the distribution of imperfections is much more uniform than in the previous test (Figure 3.8).
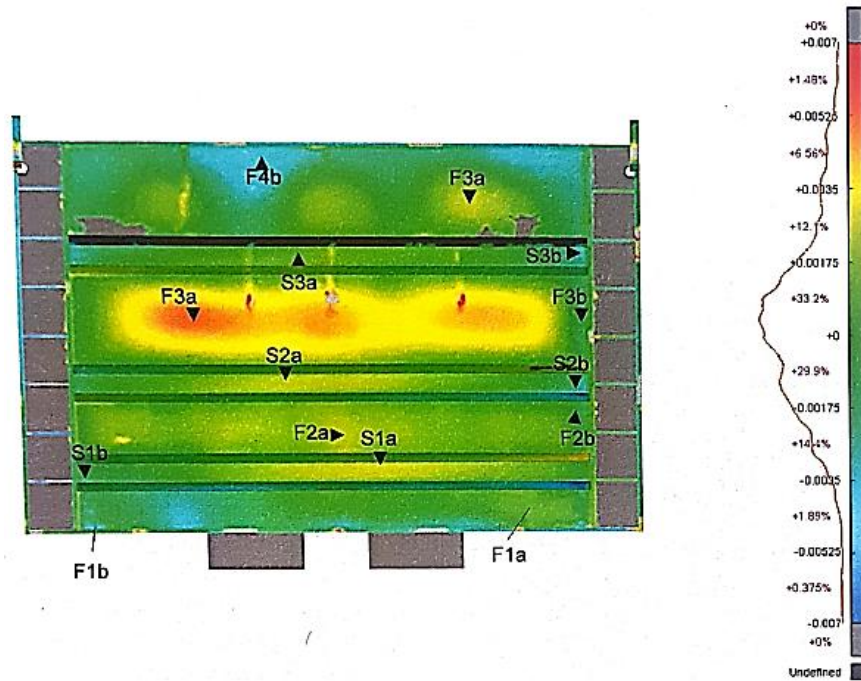
Figure 3.17: 3D scans made on the body of the second test [4]

3.3 Test 3

Compared to previous cases, the geometry has been modified, in particular the height of the stiffeners has changed, which is no longer 125 mm, but 65 mm (Figure 1.11). However, in order to verify the influence of the lower plate, two cases were studied: one in which the height of the stiffeners running along the bottom flange was also changed to 65 mm; one in which the height of these stiffeners was maintained at 125 mm.

The β stress ratio adopted during the test is equal to 1 and, as in previous cases, given the symmetry of the load, the symmetrical model was adopted (Figure 2.32).

In order to obtain the desired stress ratio, a load of F1 $= 1500000$ N was imposed, to which corresponds, for inverse resolution, a value of F2 $= 485226.58$ N. An *Excel* worksheet has simply been created to obtain the F2 value.

3.3.1 Test 3: static analysis with h$_{stb}$ = 65 mm

First the section with $h_{stb} = 65mm$ is analysed (Figure 2.12 (a), Figure 3.18).
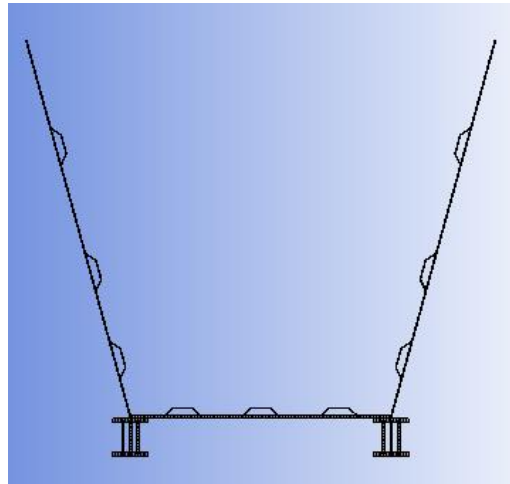
Figure 3.18: section with $h_{stb} = 65\ mm$ (test 3 modelling)

Checking the tension state in the center section and imposing $P = 0$ (Figure 2.31):

$$M = F_1 \cdot z_{rp} + 2F_3 \cdot \left(x_{rp2} + pos_{b1} + \frac{deep_b}{2} \right)$$

$$= 1500000N \cdot 5,469m + 485226,58N \cdot (0,825m + 1m + 0,375m)$$

$$= 1,03 \cdot 10^7 Nm$$

From which:

$$\sigma_{x,top} = -\frac{N}{A} + \frac{M}{I}z = \frac{\left(-\frac{1500000}{0,121}\frac{N}{m^2} + \frac{1,03 \cdot 10^7}{0,1012}\frac{Nm}{m^4} \cdot 2,21m\right)}{10^6} = 214,48\ MPa$$

$$\sigma_{x,bottom} = -\frac{N}{A} - \frac{M}{I}z = \frac{\left(-\frac{1500000}{0,121}\frac{N}{m^2} + \frac{1,03 \cdot 10^7}{0,1012}\frac{Nm}{m^4} \cdot 0,679m\right)}{10^6} = 80,87\ MPa$$

$$\Delta\sigma_{top} = 1 - \frac{\sigma_{x,top}}{\sigma_{x,top,FEM}} = \left(1 - \frac{214,48}{220}\right) \cdot 100 = 2,51\%$$

$$\Delta\sigma_{bottom} = 1 - \frac{\sigma_{bottom,top,FEM}}{\sigma_{bottom,top}} = \left(1 - \frac{-78}{-80,87}\right) \cdot 100 = 3,55\ \%$$

Where $\sigma_{x,top,FEM}$ and $\sigma_{x,bottom,FEM}$ are shown in Figure 3.19.
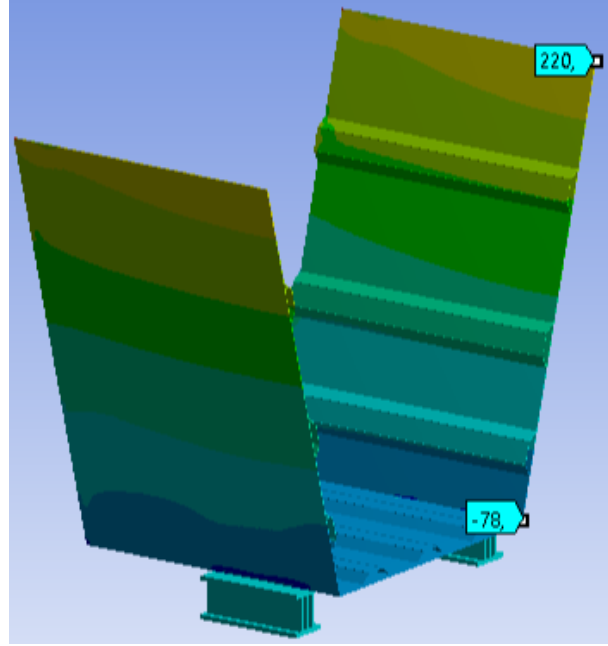
Figure 3.19: $\sigma_{x,top,FEM}$ and $\sigma_{x,bottom,FEM}$ in the middle section (test3 modelling with $h_{stb} = 65\ mm$)

$$\sigma_z = -\frac{F_2}{A_1} = -\frac{485226,58}{6000}\ MPa = -80,87 MPa$$

$$\Delta\sigma_z = 1 - \frac{\sigma_z}{\sigma_{z,FEM}} = \left(1 - \frac{-80,87}{-86}\right) \cdot 100 = 6,97\%$$

Where $\sigma_{z,FEM}$ was taken as the average value between the minimum and the centerline value (Figure 3.20).
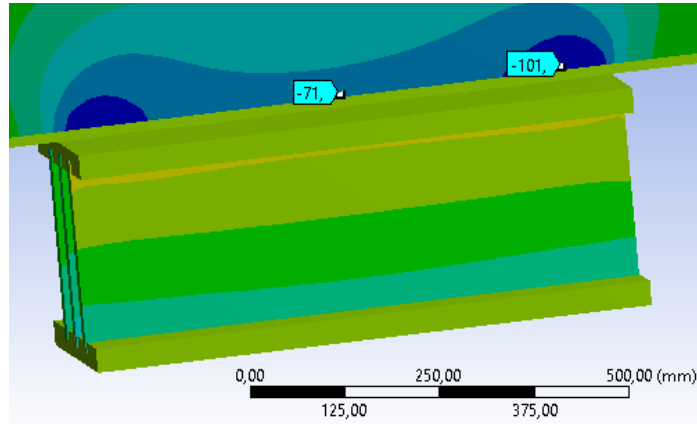
Figure 3.20: σ_z above the bearing (test 3 modelling with $h_{stb} = 65$ mm)

The slight difference in the results is due to the presence of friction between the section and the support, which affects the distribution of tensions.

3.3.2   Test 3: linear buckling with h$_{stb}$ = 65 mm

The linear static analysis is followed by linear instability analysis. During this phase, the forms of instability and the corresponding load multiplication factors are determined.

As explained in the paragraph 2.2.1, linear instability analysis returns an ideal critical load (Figure 2.4) due to the lack of imperfections within the geometry.

Figure 3.21 shows the first form of instability. Worth noting is that the multiplication factor of the loads is practically the same ($1.4503 \cong 1,4632$).
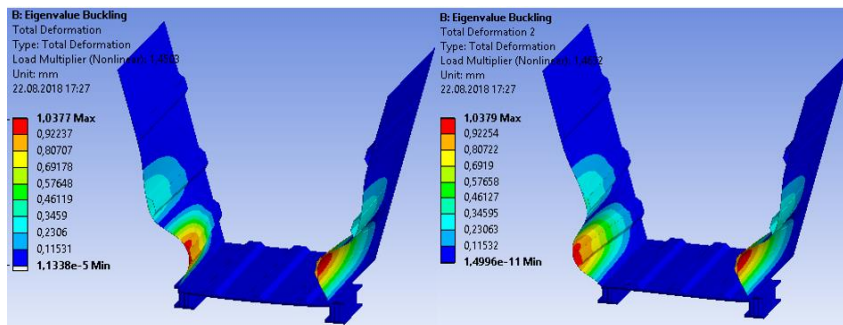
Figure 3.21: first buckling mode (test 3 with $h_{stb} = 65$ mm modelling)

This is because, given the symmetry of the problem, instability occurs in both webs at the same time; however, since *Ansys* offers the opportunity to assign imperfections in the area where

58

buckling occurred (to perform a nonlinear analysis), to which then a sign is applied (*plus* if an imperfection in the same direction of the buckling is applied and *minus* if an imperfection in the opposite direction is applied), each buckling mode is repeated twice so that it is possible to consider all 4 cases (*plus* or *minus* for both webs or alternate signs). From Figure 3.21 is evident how instability involves the lower stiffeners, just like in the test [3] (Figure 3.22).
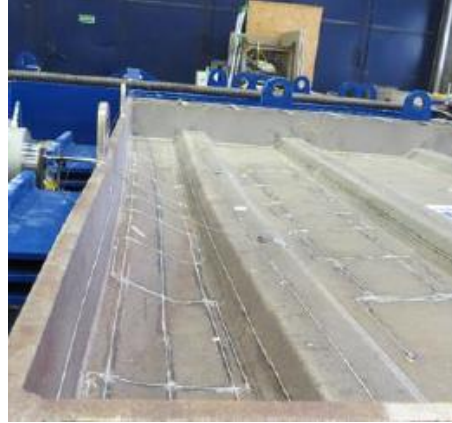
Figure 3.22: test 3 picture [4]

The Figure 3.23 shows the forms of instability 2, 3, 4 and 5, showing how the second form of instability already occurs at the central stiffeners and also involves part of the bottom flange; this is due to the low stiffness contribution of the stiffeners, being this practically halved compared to previous tests.
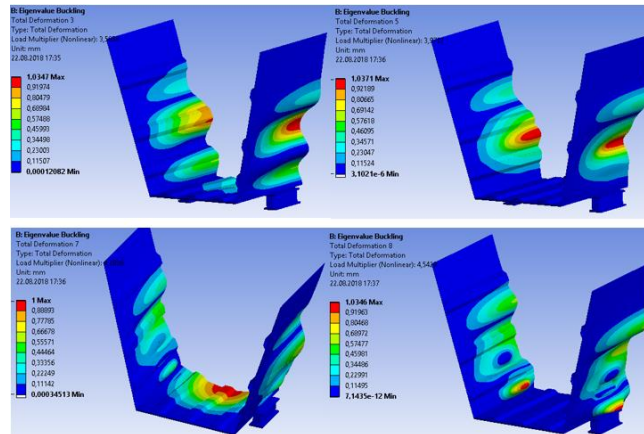
Figure 3.23: buckling modes 2, 3, 4 and 5 (test 3 modelling with $h_{stb} = 65\ mm$)

3.3.3   Test 3: nonlinear analysis with h$_{stb}$ = 65 mm

For an estimation of the final load, the linear instability analysis alone is not suitable, however it can be used as a starting point for a nonlinear instability analysis, using the forms of instability as imperfections [10].

On the basis of Table 2.1, the normative prescribes the application of an equivalent imperfection of:

$$e_{0w} = \min\left(\frac{a}{200}; \frac{b}{200}\right) = \frac{3000}{200}\,mm = 15mm$$

Applicable through APDL commands to any form of instability (paragraph 2.2.1). The value of the imperfection has been adopted not only to be on the security side, but also to allow a more faithful comparison with the results contained in [3].

Observing the direction of instabilization of the lower stiffener in Figure 3.22 it was decided to apply an imperfection to the first form of instability indicated as total deformation (Figure 3.21). As already mentioned previously, a negative imperfection has been applied because the instability is turned inwards, however, a deflection with respect to the normal has to be applied outwards.

```
fini
/prep7
upgeom,-15/1.0377,1,2,..\..\Buckling,rst
fini
/solu
```

The distortion factor 15 has been divided by 1.0377 because the maximum displacement has been normalized to this value (see paragraph 2.2.1 and Figure 3.21). In this way a maximum imperfection of $15\ mm$ will be applied. Since the purpose of the nonlinear analysis is to trace the trend of the F2 force and obtain the maximum value beyond which the section becomes unstable (Figure 2.6), a force was no longer applied to the supports but a displacement of $20\ mm$ [3] (Figure 3.5 and paragraph 2.2.1), instead F1 was assigned a value of 1,5753 MN, coinciding with that of the test. The following picture (Figure 3.24) shows a perfect symmetry in the deformed, demonstrating that the first form of instability previously evaluated is identical in the two webs.
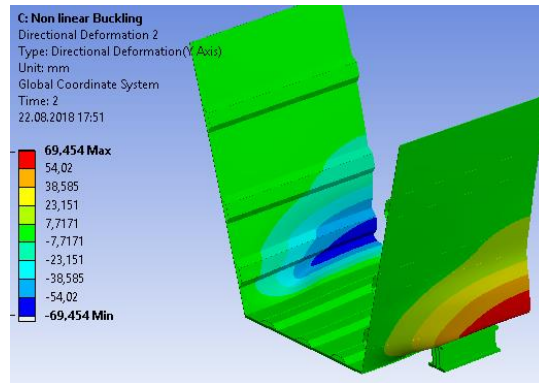
Figure 3.24: nonlinear deformed shape (test3 modelling with $h_{stb} = 65\ mm$)

While the force F2 trend shows a peak equal to $0,947\ MN$ (Figure 3.25); in addition, performing the deformation control test it was possible to trace the trend of the force during $snap - through.$

Displacement [mm]	F$_2$ [MN]
0	0
2,2753	0,19
4,8338	0,36
8,9974	0,57
13,307	0,74
21,966	0,94
30,462	0,95
37,833	0,90
44,041	0,85
49,402	0,82
54,166	0,79
58,471	0,76
62,418	0,74
66,066	0,72
69,454	0,71
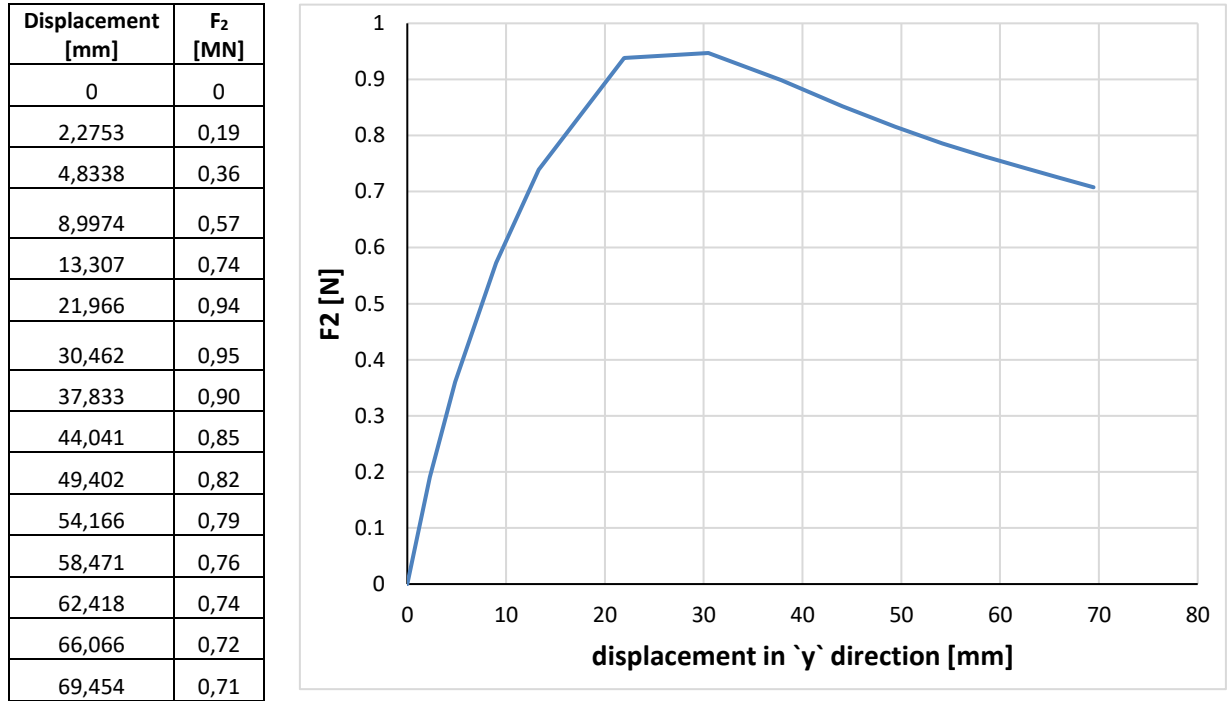
Figure 3.25: F2 trend (test 3 modelling with $h_{stb}\ =\ 65\ mm$)

The difference in percentage between the nonlinear model results and the test ones is shown in (Table 3.5). The force F2 refers to the single bearing.

F$_{1,FEM}$ [MN]	F$_{1, Test}$ [MN]	ΔF$_1$ [%]	F$_{2,FEM}$ [MN]	F$_{2, Test}$ [MN]	ΔF$_2$ [%]
1,58	1,58	0	0,947	0,89	**6,41**

Table 3.5: test 3 with h_{stb}=65mm - difference in percentage between the nonlinear model results and the test3[3] ones

With respect to the model studied in [3] there is a difference of more or less the $4,76\ \%$ (Table 3.6), showing how the presence of the bottom plate provides a benefit on the overall behavior of the section.

F$_{1,FEM}$ [MN]	F$_{1, JS}$ [MN]	ΔF$_1$ [%]	F$_{2,FEM}$ [MN]	F$_{2, JS}$ [MN]	ΔF$_2$ [%]
1,58	1,58	0	0,947	0,904	**4,76**

Table 3.6: test 3 with h_{stb}=65mm - difference in percentage between the nonlinear model results and the [3] ones

In addition, as can be seen from the Figure 3.26, the distribution of imperfections is much more uniform than in the test1 (Figure 3.8).
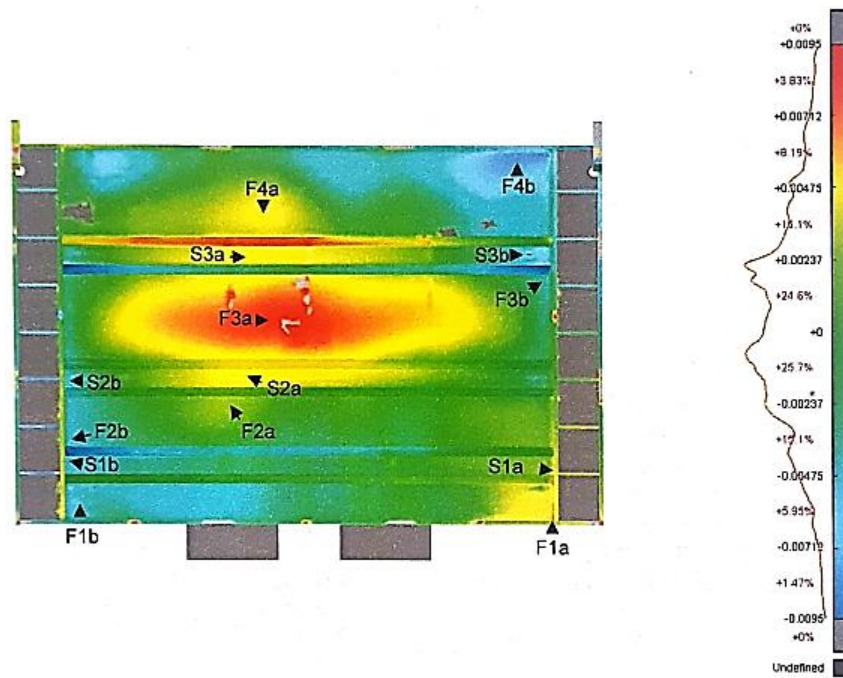
Figure 3.26: 3D scans made on the body of the third test [4]

3.3.4   Test 3: static analysis with h$_{stb}$ = 125 mm

It is analyzed now the section with $h_{stb} = 125mm$ (Figure 2.12 (a), Figure 3.27).
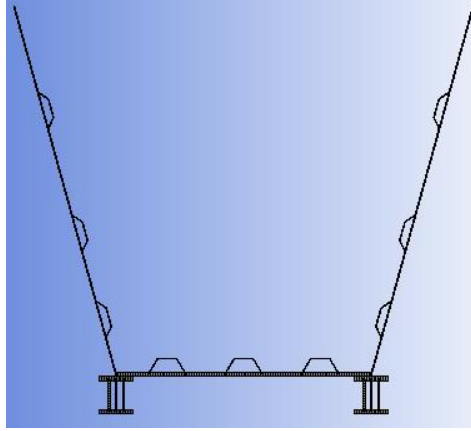
Figure 3.27: section with $h_{stb} = 125$ mm (test 3 modelling)

Checking the tension state in the center section and imposing $P = 0$ (Figure 2.31):

$$M = F_1 \cdot z_{rp} + 2F_3 \cdot \left(x_{rp2} + pos_{b1} + \frac{deep_b}{2} \right)$$

$$= 1500000N \cdot 5,469m + 485226,58N \cdot (0,825m + 1m + 0,375m)$$

$$= 1,03 \cdot 10^7 \, Nm$$

From which:

$$\sigma_{x,top} = -\frac{N}{A} + \frac{M}{I}z = \frac{\left(-\dfrac{1500000}{0,121} \dfrac{N}{m^2} + \dfrac{1,03 \cdot 10^7}{0,1012} \dfrac{Nm}{m^4} \cdot 2,21m \right)}{10^6} = 214,41 \, MPa$$

$$\sigma_{x,bottom} = -\frac{N}{A} - \frac{M}{I}z = \frac{\left(-\dfrac{1500000}{0,121} \dfrac{N}{m^2} + \dfrac{1,03 \cdot 10^7}{0,1015} \dfrac{Nm}{m^4} \cdot 0,679m \right)}{10^6} = 80,08 \, MPa$$

$$\Delta\sigma_{top} = 1 - \frac{\sigma_{x,top}}{\sigma_{x,top,FEM}} = \left(1 - \frac{214,41}{220} \right) \cdot 100 = 2,54\%$$

$$\Delta\sigma_{bottom} = 1 - \frac{\sigma_{x,bottom,FEM}}{\sigma_{bottom,top}} = \left(1 - \frac{-78}{-80,08} \right) \cdot 100 = 2,60 \, \%$$

Where $\sigma_{x,top,FEM}$ and $\sigma_{x,bottom,FEM}$ are shown in Figure 3.28.
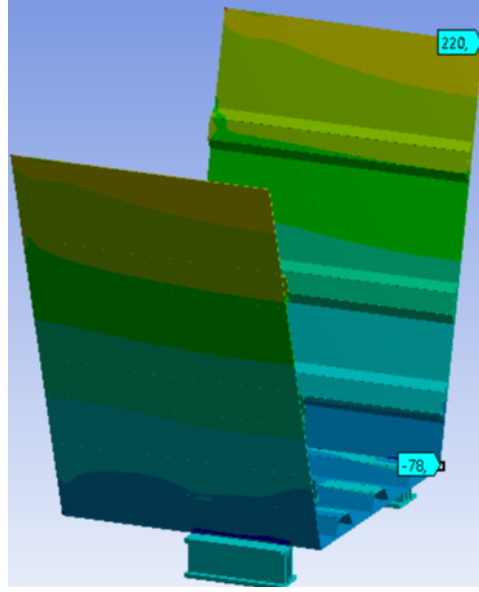
Figure 3.28: $\sigma_{x,top,FEM}$ and $\sigma_{x,bottom,FEM}$ in the middle section (test3 modelling with $h_{stb} = 125$ mm)

$$\sigma_z = -\frac{F_2}{A_1} = -\frac{485226,58}{6000} \, MPa = -80,87 MPa$$

$$\Delta\sigma_z = 1 - \frac{\sigma_z}{\sigma_{z,FEM}} = \left(1 - \frac{-80,87}{-88}\right) \cdot 100 = 8,1 \, \%$$

Where $\sigma_{z,FEM}$ was taken as the average value between the minimum and the centerline value (Figure 3.29).
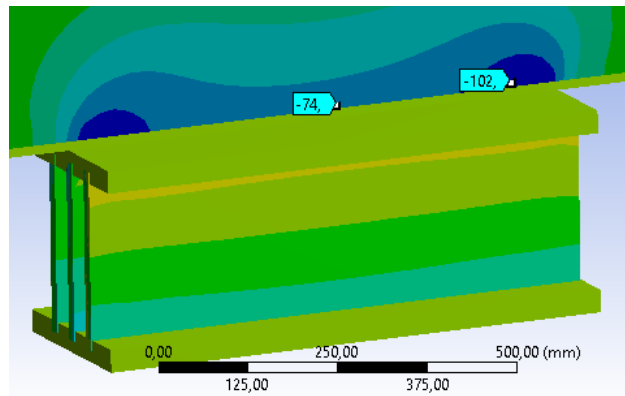
Figure 3.29: σ_z above the bearing (test 3 modelling with $h_{stb} = 125$ mm)

The slight difference in the results is due to the presence of friction between the section and the support, which affects the distribution of tensions.

3.3.5 Test 3: linear buckling with h$_{stb}$ = 125

The linear static analysis is followed by linear instability analysis. During this phase, the forms of instability and the corresponding load multiplication factors are determined. As explained in the paragraph 2.2.1, linear instability analysis returns an ideal critical load (Figure 2.4) due to the lack of imperfections within the geometry. Figure 3.30 shows the first form of instability. Worth noting is that the multiplication factor of the loads is practically the same (1.5016 $\cong$ 1,5028); in addition, at the same load as in the case of $h_{stb} = 65\ mm$, it is slightly higher due to the higher load-bearing capacity of the stiffeners.
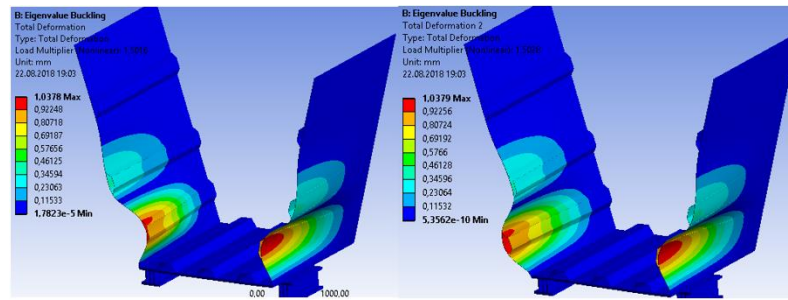
Figure 3.30: first buckling mode (test 3 with $h_{stb} = 125\ mm$ modelling)

This is because, given the symmetry of the problem, instability occurs in both webs at the same time; however, since *Ansys* offers the opportunity to assign imperfections in the area where buckling occurred (to perform a nonlinear analysis), to which then a sign is applied (*plus* if an imperfection in the same direction of the buckling is applied and *minus* if an imperfection in the opposite direction is applied), each buckling mode is repeated twice so that it is possible to consider all 4 cases (*plus* or *minus* for both webs or alternate signs). From Figure 3.30 is evident how instability involves the lower stiffeners, just like in the test (Figure 3.22). Figure 3.31 shows the forms of instability 2, 3, 4 and 5, showing how compared to the previous case (Figure 3.23) only in correspondence of the fourth form of instability occurs the instabilization of the bottom plate, thanks to the contribution of the stiffeners.
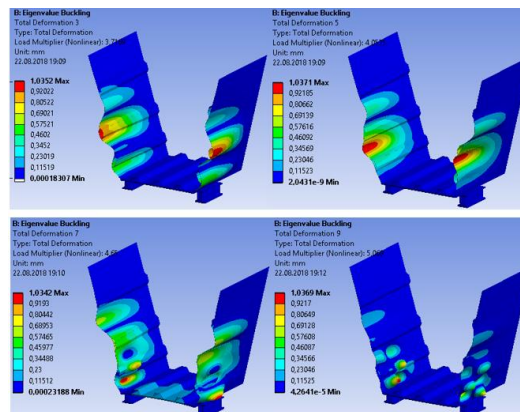
Figure 3.31: buckling modes 2, 3, 4 and 5 (test 3 modelling with $h_{stb} = 125\ mm$)

3.3.6 Test 3: nonlinear analysis h_{stb} = 125 mm

For an estimation of the final load, the linear instability analysis alone is not suitable, however it can be used as a starting point for a nonlinear instability analysis, using the forms of instability as imperfections [10]. On the basis of Table 2.1, the normative prescribes the application of an equivalent imperfection of:

$$e_{0w} = \min\left(\frac{a}{200}; \frac{b}{200}\right) = \frac{3000}{200} mm = 15 mm$$

Applicable through APDL commands to any form of instability (paragraph 2.2.1). The value of the imperfection has been adopted not only to be on the security side, but also to allow a more faithful comparison with the results contained in [3]. Observing the direction of instabilization of the lower stiffener in Figure 3.22 it was decided to apply an imperfection to the first form of instability indicated as total deformation (Figure 3.30). As already mentioned previously, a negative imperfection has been applied because the instability is turned inwards, however, a deflection with respect to the normal has to be applied outwards.

```
fini
/prep7
upgeom,-15/1.0378,1,2,..\..\Buckling,rst
fini
/solu
```

The distortion factor 15 has been divided by 1.0378 because the maximum displacement has been normalized to this value (see paragraph 2.2.1 and Figure 3.12). In this way a maximum imperfection of 15 mm will be applied. Since the purpose of the nonlinear analysis is to trace the trend of the F2 force and obtain the maximum value beyond which the section becomes unstable (Figure 2.6), a force was no longer applied to the supports but a displacement of 20 mm [3] (Figure 3.5 and paragraph 2.2.1), instead F1 was assigned a value of 1,5753 MN, coinciding with that of the test. The following picture (Figure 3.32) shows a perfect symmetry in the deformed, demonstrating that the first form of instability previously evaluated is identical in the two webs.
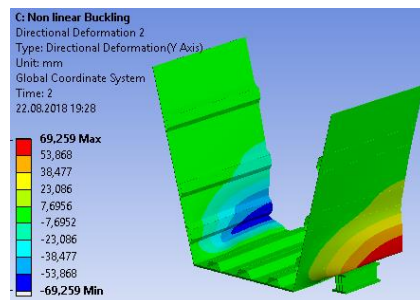
Figure 3.32: nonlinear deformed shape (test3 modelling with h_{stb} = 125 mm)

While the force F2 trend shows a peak equal to $0,996 \, MN$ (Figure 3.33); in addition, performing the deformation control test it was possible to trace the trend of the force during $snap - through$.

Displacement [mm]	F₂ [MN]
0	0
2,2549	0,20
4,7922	0,38
8,9292	0,60
13,235	0,78
22,104	0,98
30,621	1,00
37,939	0,95
44,086	0,92
49,413	0,89
54,143	0,87
58,414	0,85
62,323	0,84
65,918	0,82
69,259	0,81
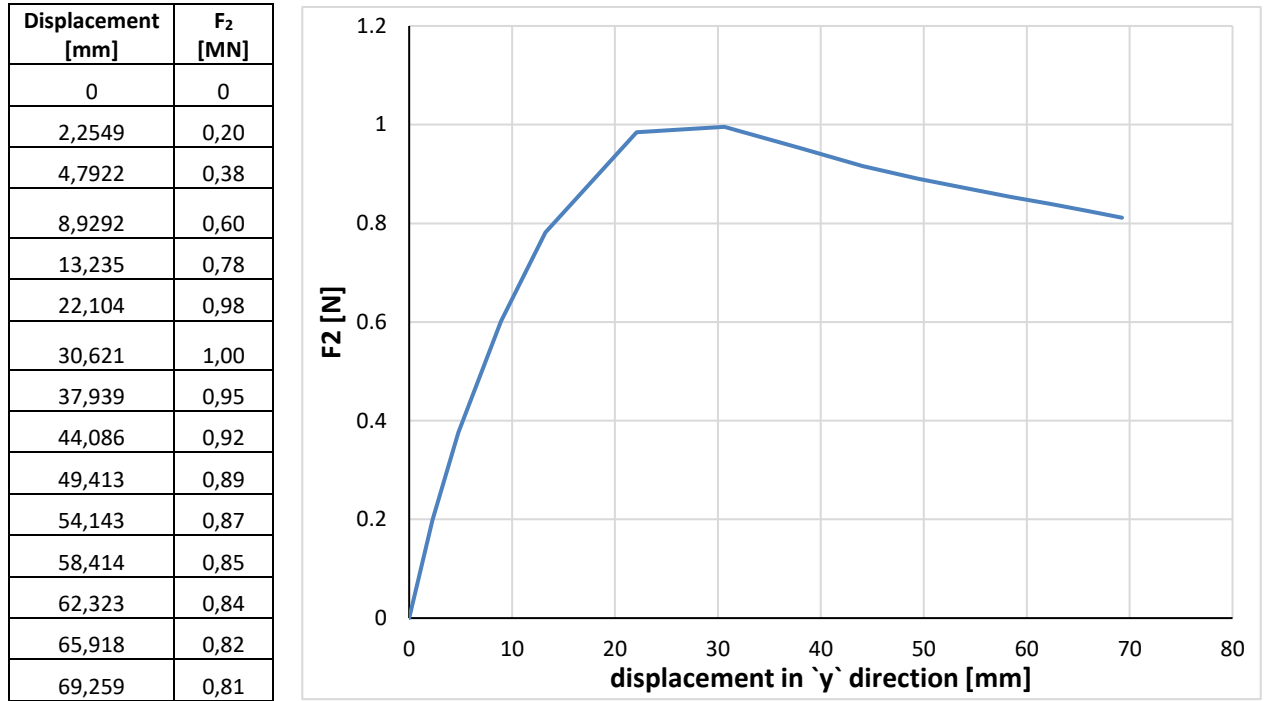
Figure 3.33: F2 trend (test 3 modelling with $h_{stb} = 125 \, mm$)

The difference in percentage between the nonlinear model results and the test ones is shown in (Table 3.7); it also follows that the presence of the bottom plate in this case leads to an increase of 11.85% of the final load, about twice the case of $h_{stb} = 65 \, mm$ (Table 3.5).

F₁,FEM [MN]	F₁, Test [MN]	ΔF₁ [%]	F₂,FEM [MN]	F₂, Test [MN]	ΔF₂ [%]
1,58	1,58	0	0,996	0,89	**11,85**

Table 3.7: test 3 with h_{stb}=125mm - difference in percentage between the nonlinear model results and the test 3 ones

With respect to the model studied in [3] there is a difference of more or less the 10%, showing how the presence of the bottom plate provides a significant benefit on the overall behavior of the section.

F₁,FEM [MN]	F₁, JS [MN]	ΔF₁ [%]	F₂,FEM [MN]	F₂, JS [MN]	ΔF₂ [%]
1,58	1,58	0	0,996	0,904	**10,18**

Table 3.8: test 3 with h_{stb}=65mm - difference in percentage between the nonlinear model results and the [3] ones

3.4   Test 4

Compared to the *test* 3 the geometry has not been modified (Figure 3.27). The β stress ratio adopted during the test is equal to 0,5 and as in previous cases, given the symmetry of the load, the symmetrical model was adopted (Figure 2.32).

In order to obtain the desired stress ratio, a load of $F1 = 2000000$ N was imposed, to which corresponds, for inverse resolution, a value of $F2 = 289445.06$ N. An *Excel* worksheet has simply been created to obtain the F2 value.

3.4.1   Test 4: static analysis

Checking the tension state in the center section and imposing $P = 0$ (Figure 2.31):

$$M = F_1 \cdot z_{rp} + 2F_3 \cdot \left(x_{rp2} + pos_{b1} + \frac{deep_b}{2}\right)$$

$$= 2000000N \cdot 5,469m + 289445,06N \cdot (0,825m + 1m + 0,375m)$$

$$= 1,22 \cdot 10^7 Nm$$

From which:

$$\sigma_{x,top} = -\frac{N}{A} + \frac{M}{I}z = \frac{\left(-\dfrac{2000000}{0,121}\dfrac{N}{m^2} + \dfrac{1,22 \cdot 10^7}{0,1012}\dfrac{Nm}{m^4} \cdot 2,21m\right)}{10^6} = 251,36\ MPa$$

$$\sigma_{x,bottom} = -\frac{N}{A} - \frac{M}{I}z = \frac{\left(-\dfrac{2000000}{0,121}\dfrac{N}{m^2} + \dfrac{1,22 \cdot 10^7}{0,1012}\dfrac{Nm}{m^4} \cdot 0,679m\right)}{10^6} = 96,48\ MPa$$

$$\Delta\sigma_{top} = 1 - \frac{\sigma_{x,top}}{\sigma_{x,top,FEM}} = \left(1 - \frac{251,46}{252}\right) \cdot 100 = 0,2\ \%$$

$$\Delta\sigma_{bottom} = 1 - \frac{\sigma_{bottom,top,FEM}}{\sigma_{bottom,top}} = \left(1 - \frac{-94}{-96,48}\right) \cdot 100 = 1,53\ \%$$

Where $\sigma_{x,top,FEM}$ and $\sigma_{x,bottom,FEM}$ are shown in Figure 3.34.
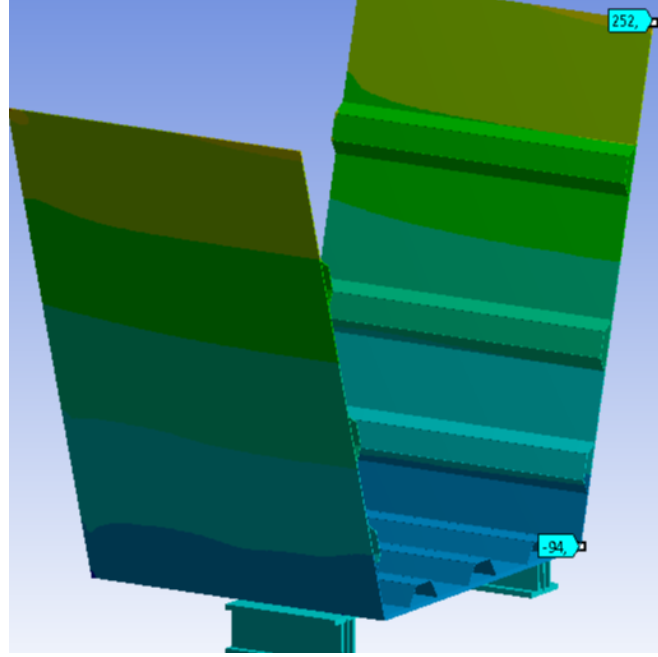
Figure 3.34: $\sigma_{x,top,FEM}$ and $\sigma_{x,bottom,FEM}$ in the middle section (test4)

$$\sigma_z = -\frac{F_2}{A_1} = -\frac{289445.06}{6000} \, MPa = -48,24 \, MPa$$

$$\Delta\sigma_z = 1 - \frac{\sigma_z}{\sigma_{z,FEM}} = \left(1 - \frac{-48,59}{-50}\right) \cdot 100 = 3,52\%$$

Where $\sigma_{z,FEM}$ was taken as the average value between the minimum and the centerline value (Figure 3.35).
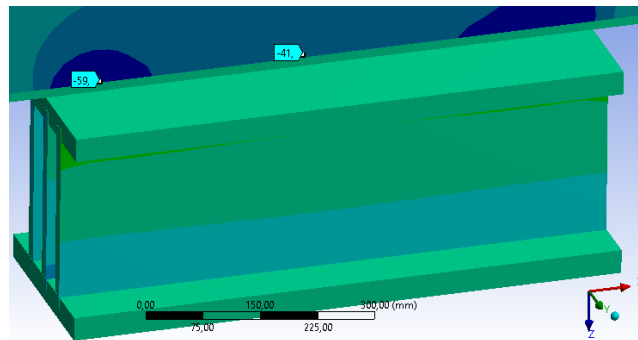
Figure 3.35: σ_z above the bearing (test 4 modelling)

The slight difference in the results is due to the presence of friction between the section and the support, which affects the distribution of tensions.

3.4.2 Test 4: linear buckling

The linear static analysis is followed by linear instability analysis. During this phase, the forms of instability and the corresponding load multiplication factors are determined. As explained in the paragraph 2.2.1, linear instability analysis returns an ideal critical load (Figure 2.4) due to the lack of imperfections within the geometry. Figure 3.36 shows the first form of instability. Worth noting is that the multiplication factor of the loads is practically the same (3,0446 $\cong$ 3,0486).
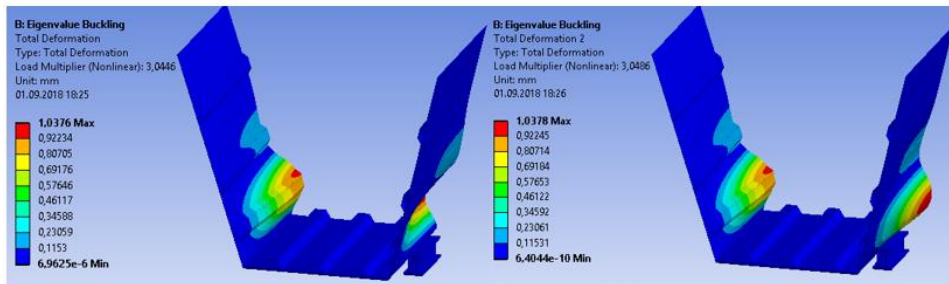
Figure 3.36: first buckling mode (test 4 modelling)

This is because, given the symmetry of the problem, instability occurs in both webs at the same time; however, since *Ansys* offers the opportunity to assign imperfections in the area where buckling occurred (to perform a nonlinear analysis), to which then a sign is applied (*plus* if an imperfection in the same direction of the buckling is applied and *minus* if an imperfection in the opposite direction is applied), each buckling mode is repeated twice so that it is possible to consider all 4 cases (*plus* or *minus* for both webs or alternate signs). Figure 3.37 shows the forms of instability 2, 3, 4 and 5. The instabilization of the bottom plate occurs only in the fourth form of instability thanks to the contribution of the stiffeners.
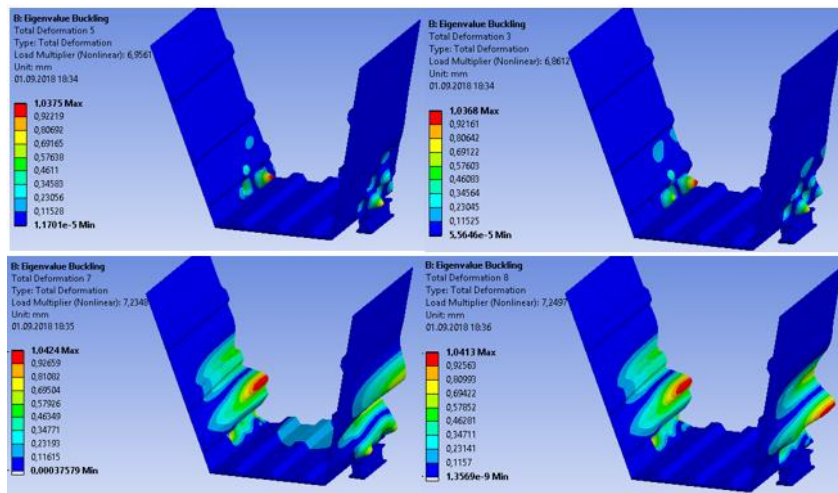
Figure 3.37: buckling modes 2, 3, 4 and 5 (test 4 modelling)

3.4.3   Test 4: nonlinear analysis

For an estimation of the final load, the linear instability analysis alone is not suitable, however it can be used as a starting point for a nonlinear instability analysis, using the forms of instability as imperfections [10]. On the basis of Table 2.1, the normative prescribes the application of an equivalent imperfection of:

$$e_{0w} = \min\left(\frac{a}{200}; \frac{b}{200}\right) = \frac{3000}{200} mm = 15mm$$

Applicable through APDL commands to any form of instability (paragraph 2.2.1). The value of the imperfection has been adopted not only to be on the security side, but also to allow a more faithful comparison with the results contained in [3].

```
fini
/prep7
upgeom,-15/1.0376,1,2,..\..\Buckling,rst
fini
/solu
```

The distortion factor 15 has been divided by 1.0376 because the maximum displacement has been normalized to this value (see paragraph 2.2.1 and Figure 3.36). In this way a maximum imperfection of 15 mm will be applied. Since the purpose of the nonlinear analysis is to trace the trend of the F2 force and obtain the maximum value beyond which the section becomes unstable (Figure 2.6), a force was no longer applied to the supports but a displacement of 20 mm [3] (Figure 3.5 and paragraph 2.2.1), instead F1 was assigned a value of 2,43854 MN, coinciding with that of the test. The following picture (Figure 3.38) shows a perfect symmetry in the deformed, demonstrating that the first form of instability previously evaluated is identical in the two webs.
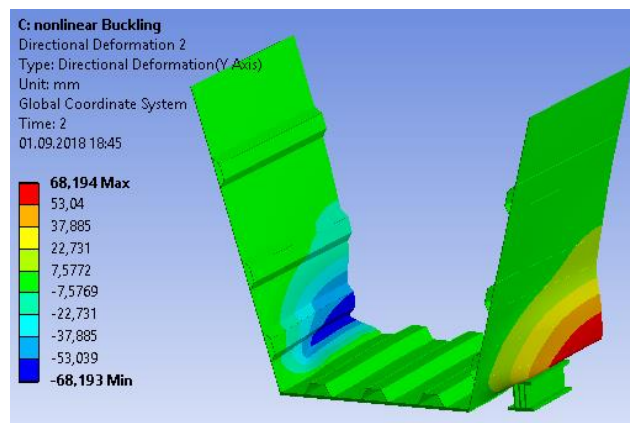
Figure 3.38: nonlinear deformed shape (test 4 modelling)

While the force F2 trend shows a peak equal to $0,981\ MN$ (Figure 3.39); in addition, performing the deformation control test it was possible to trace the trend of the force during $snap-through$. The force F2 refers to the single bearing.

Displacement [mm]	F$_2$ [MN]
0	0
1,6822	0,15
3,5516	0,28
6,6267	0,46
9,8992	0,61
18,52	0,92
27,582	0,98
35,369	0,95
41,933	0,91
47,57	0,88
52,519	0,86
56,966	0,84
61,017	0,82
64,746	0,80
68,194	0,79
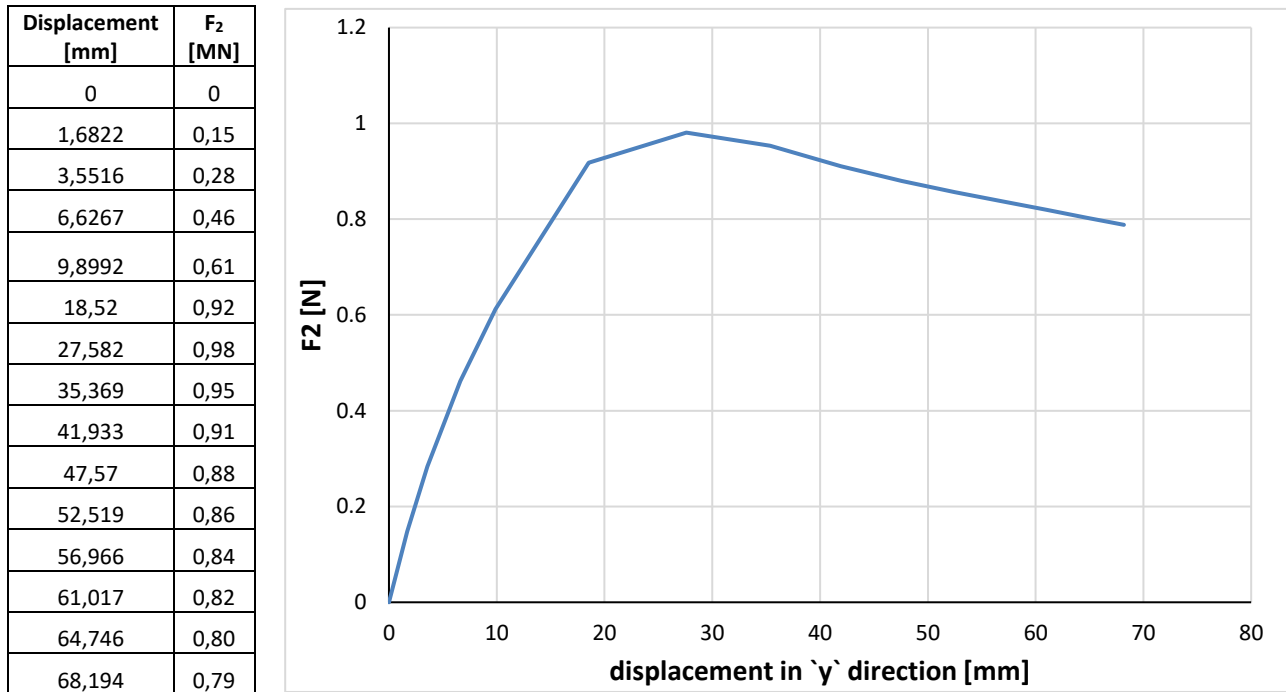
Figure 3.39: F2 trend (test 4 modelling)

The difference in percentage is much smaller than that resulting from the linear instability analysis, showing how the nonlinear instability analysis is much more accurate than the linear one; it also follows that the presence of the bottom plate in this case leads to an increase of 12,91% of the final load (Table 3.9).

F$_{1,FEM}$ [MN]	F$_{1,Test}$ [MN]	ΔF$_1$ [%]	F$_{2,FEM}$ [MN]	F$_{2,Test}$ [MN]	ΔF$_2$ [%]
2,44	2,44	0	0,981	0,87	**12,91**

Table 3.9: difference in percentage between the nonlinear model results and the test 4 ones

In addition, as can be seen from the Figure 3.40, the distribution of imperfections is concentrated above the top stiffeners (Figure 3.8).
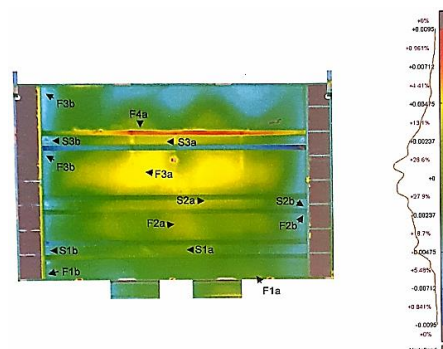
Figure 3.40: 3D scans made on the body of the fourth test [4]

3.5   Test 5 – 6

As far as the analysis of the last two tests is concerned, whose geometry is shown in Figure 1.11, the finite elements analysis did not show reliable results. Probably this is due to the boundary conditions applied, not suitable for the abrupt change of position of the lower stiffeners, placed no more at $300\ mm$ from the base of the bottom flange, but at $540\ mm$ Figure 3.41.
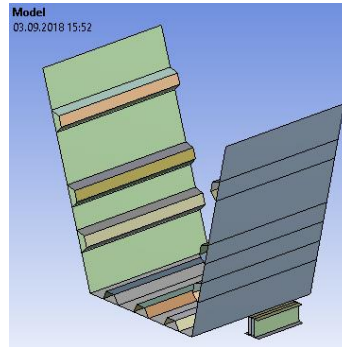
Figure 3.41: test 4 modelling

The linear instability is all concentrated in the lower part of the web (Figure 3.42, Figure 3.43), thus making the application of the imperfections unsuitable for nonlinear calculation. In test six alone, due to the small size of the stiffeners, instability seems to partly involve lower stiffeners (Figure 3.43); however, this still does not reflect what laboratory tests have shown. This situation occurs also for high value of β.
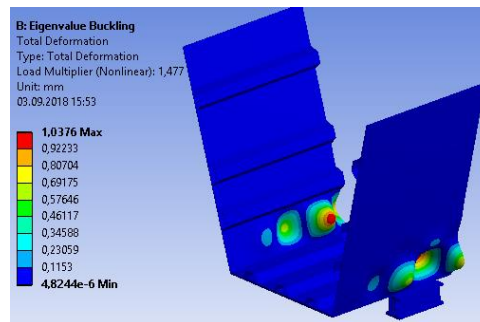
Figure 3.42: first buckling mode (test 5 modelling)
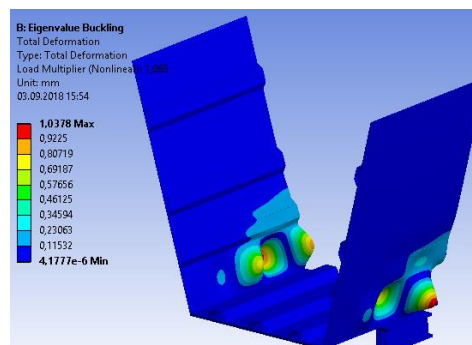
Figure 3.43: first buckling mode (test 6 modelling)

4. TEST SIMULATION: ELASTOMERIC BEARINGS

In the following chapter, the tests are modelled again but the elastomeric bearing is used (chapter 2.5.2.2). Compared to the previous case, the type of pusher used no longer allows rotation around the x-axis (Figure 2.9), the same condition adopted during tests three and four (chapter 1.2). As far as the theory at the base of the simulation is concerned, nothing has changed compared to what has already been widely explained in the chapter 3, in fact the problem has been divided again into three parts: linear static analysis, linear buckling analysis and nonlinear analysis with large displacements [10].

For this reason, in order to avoid an inappropriate repetition of the arguments, only the passages concerning the linear buckling analysis and the nonlinear analysis are reported.

Again, the results of the model have been compared both with the experimental data and with those contained in [3], for the same reason already explained in the beginning of the chapter 3.

4.1 Test 1: elastomeric bearings

On the basis of what has already been stated in chapter 3.1, the same forces have been adopted that allow therefore to obtain the desired stress ratio, $\beta = 0.5$. As it is possible to see in the Figure 4.1, the buckling occurs at the lower stiffeners, just like in the test (Figure 3.3). Furthermore, given the symmetry of the problem and the opportunity to assign the imperfections in the area where the buckling took place, each mode is repeated twice, in fact, the load multipliers are very similar.
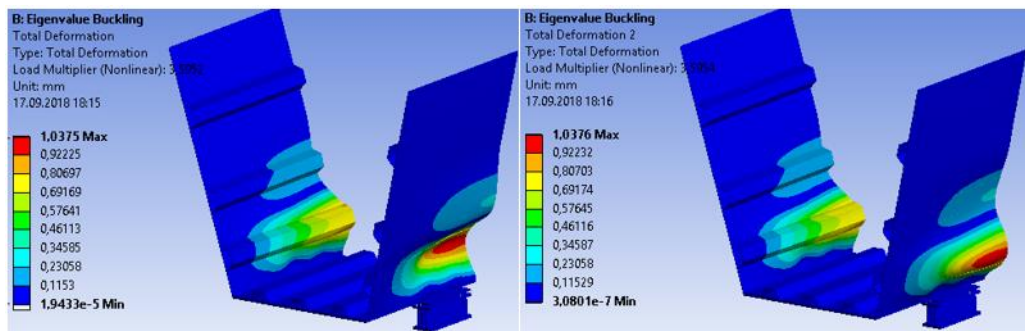
Figure 4.1: first buckling mode (test 1 modelling using the elastomeric bearings)

Figure 4.2 shows the buckling modes 2, 3, 4 and 5, showing how only in correspondence of the fifth mode the instability involves also the lower plate, just as in the case of a spherical node pusher (Figure 3.4).
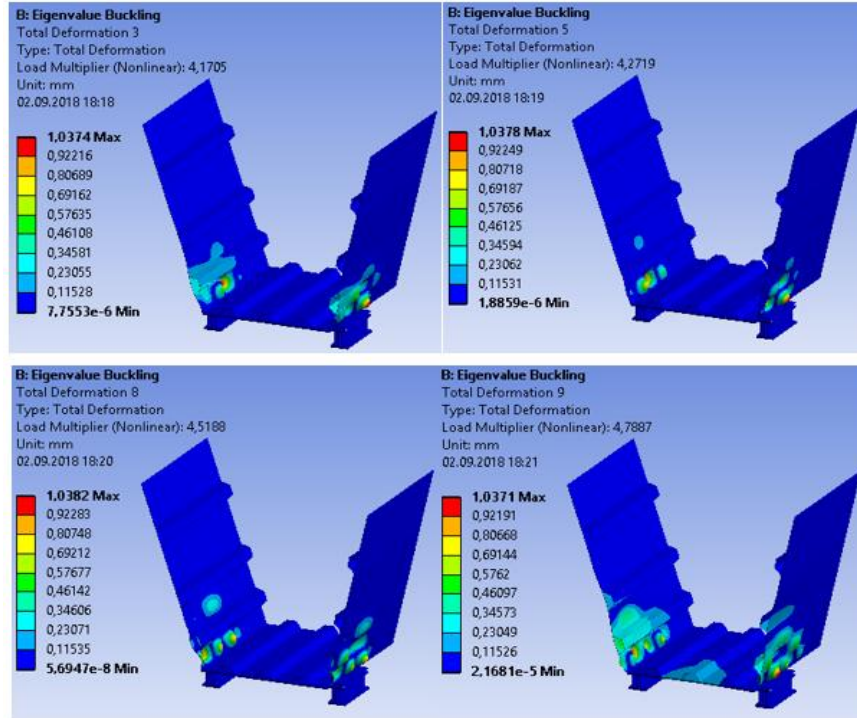
Figure 4.2: buckling modes 2, 3, 4 and 5 (test 1 modelling using the elastomeric bearings)

Linear buckling is followed by nonlinear analysis with large displacements. In this case, the equivalent imperfections are applied thanks to the use of the following APDL commands (chapter 3.1.3).

```
fini
/prep7
upgeom, -15/1.0375,1,1,..\..\Buckling,rst
fini
/solu
```

This results in a load end value that is much closer to the actual value (Table 4.1). However, although the applied imperfection is already very high, the value continues to be much higher than expected. The force F2 regards the single bearing.

$F_{1,FEM}$ [MN]	$F_{1, Test}$ [MN]	ΔF_1 [%]	$F_{2,FEM}$ [MN]	$F_{2, Test}$ [MN]	ΔF_2 [%]
3,1296	3,1296	0	1,345	0,83	**61,942**

Table 4.1: difference in percentage between the nonlinear model results and the test ones
(test 1 modelling using elastomeric bearings)

As mentioned in chapter 3.1, this is probably due to the concentration of imperfections (up to 6mm) in the area adjacent to the constraint (Figure 3.8).

Compared to the modelling with the spherical node pusher (chapter 3.1), there is a slight difference:

$$\left(1 - \frac{F_{2,FEM,CH4.1}}{F_{2,FEM,CH3.1}} - 1\right) \cdot 100 = \left(1 - \frac{1,345\ MN}{1,367\ MN}\right) \cdot 100 = 1,61\%$$

This shows that giving the constraint the opportunity to rotate around the x axis increases the ultimate load by 1.61%, thanks to the lower load rate absorbed by the core (Figure 4.3).
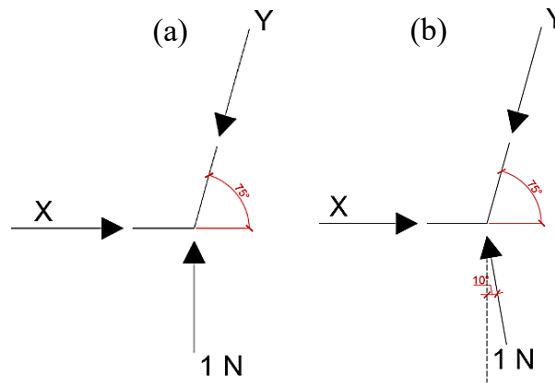
Figure 4.3: force system using the thrust bearing with single exhaust (a); force system using the spherical node thrust bearing (b)

$$(a)\ Y = \frac{1\ N}{sen75°} = 1,035\ N \qquad\qquad (b)\ Y = \frac{1\ N \cdot cos10°}{sen75°} = 1,020\ N$$

In addition, performing the deformation control test it was possible to trace the trend of the force during $snap - through$ (Figure 4.4).

Figure 4.4: F2 trend (test 1 modelling using elastomeric bearings)

4.2 Test 2: elastomeric bearings

On the basis of what has already been stated in chapter 3.2, the same forces have been adopted that allow therefore to obtain the desired stress ratio, $\beta = 0.5$.

As it is possible to see in the Figure 4.5, the buckling occurs at the lower stiffeners, just like in the test (Figure 3.13). Furthermore, given the symmetry of the problem and the opportunity to assign the imperfections in the area where the buckling occurs, each mode is repeated twice, in fact, the load multipliers are similar ($3.265 \cong 3.2658$).

Figure 4.5: first buckling mode (test 2 modelling using the elastomeric bearings)

Figure 4.6 shows the buckling modes 2, 3, 4 and 5:

Figure 4.6: buckling modes 2, 3, 4 and 5 (test 2 modelling using the elastomeric bearings)

Linear buckling is followed by nonlinear analysis with large displacements. In this case, the equivalent imperfections are applied thanks to the use of the following APDL commands (chapter 3.1.3).

```
fini
/prep7
upgeom, 15/1.0378,1,2,..\..\Buckling,rst
fini
/solu
```

This results in a load end value that is much closer to the actual one (Table 4.2).

$F_{1,FEM}$ [MN]	$F_{1, Test}$ [MN]	ΔF_1 [%]	$F_{2,FEM}$ [MN]	$F_{2, Test}$ [MN]	ΔF_2 [%]
1,61	1,61	0,00	1,364	1,12	**21,708**

Table 4.2: difference in percentage between the nonlinear model results and the test ones
(test 2 modelling using elastomeric bearings)

Moreover, as already found in *test* 1 (chapter 4.1), the rotational capacity of the constraint results in a higher ultimate load F2 than in the case of prevented rotation, thanks to the lower load rate absorbed by the web (Figure 4.3).

$$\left(1 - \frac{F_{2,FEM,CH4.2}}{F_{2,FEM,CH3.2}}\right) \cdot 100 = \left(1 - \frac{1{,}364 \; MN}{1{,}39 \; MN}\right) \cdot 100 = 1{,}87\%$$

In addition, performing the deformation control test it was possible to trace the trend of the force during *snap* − *through* (Figure 4.7).

Figure 4.7: F2 trend (test 2 modelling using elastomeric bearings)

4.3 Test 3: elastomeric bearings

As already done in chapter 3.3, two cases were analysed: one in which the height of the stiffeners running along the bottom flange was also changed to $65\ mm$; one in which the height of these stiffeners was maintained at $125\ mm$.

On the basis of what has already been stated in chapter 3.3, the same forces have been adopted that allow therefore to obtain the desired stress ratio, $\beta = 1$.

4.3.1 Test 3: elastomeric bearings with h_stb=65 mm

As it is possible to see in the Figure 4.8, the buckling occurs at the lower stiffeners, just like in the test (Figure 3.22). Furthermore, given the symmetry of the problem and the opportunity to assign the imperfections in the area where the buckling occurs, each mode is repeated twice, in fact, the load multipliers are similar ($1{,}5003 \cong 1{,}5124$).
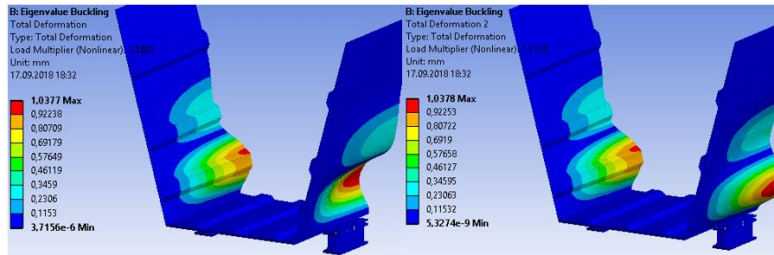
Figure 4.8: first buckling mode (test 3 modelling using the elastomeric bearings and considering $h_{stb} = 65mm$)

Figure 4.9 shows the buckling modes 2, 3, 4 and 5, showing how the second form of instability already involves the bottom plate (just like in the case of a spherical node pusher, Figure 3.23).
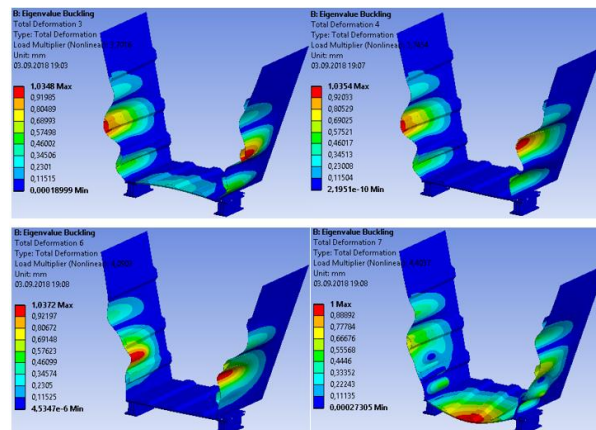
Figure 4.9: buckling modes 2, 3, 4 and 5 (test 3 modelling using the elastomeric bearings and considering $h_{stb} = 65mm$)

Linear buckling is followed by nonlinear analysis with large displacements. In this case, the equivalent imperfections are applied thanks to the use of the following APDL commands (chapter 3.1.3).

```
fini
/prep7
upgeom, -15/1.0377,1,1,..\..\Buckling,rst
fini
/solu
```

This results in a load end value that is much closer to the actual one (Table 4.3). In addition, the analysis shows that the presence of the bottom flange leads to an increase in section resistance of more or less the 4%. The force F2 regards the single bearing.

$F_{1,FEM}$ [MN]	$F_{1, Test}$ [MN]	ΔF_1 [%]	$F_{2,FEM}$ [MN]	$F_{2, Test}$ [MN]	ΔF_2 [%]
1,58	1,58	0	0,924	0,89	**3,80**

Table 4.3: difference in percentage between the nonlinear model results and the test ones
(test 3 modelling using elastomeric bearings and considering h_{stb} = 65mm)

With respect to the model studied in [3] there is a difference of more or less the 3,80 % (Table 4.4),

$F_{1,FEM}$ [MN]	$F_{1, JS}$ [MN]	ΔF_1 [%]	$F_{2,FEM}$ [MN]	$F_{2, JS}$ [MN]	ΔF_2 [%]
1,58	1,58	0	0,924	0,89	**3,80**

Table 4.4: difference in percentage between the nonlinear model results and the [3] ones
(test 3 modelling using elastomeric bearings and considering h_{stb} = 65mm)

This contribution is therefore not negligible, but it is not so high either. This is due to the reduced resistance contribution of the stiffeners running along the lower flange, whose size has been reduced compared to previous cases. Moreover, compared to the case of a spherical node pusher, there is a reduction in the final load of about 2.43%, given the higher rate of load absorbed by the web (Figure 4.3).

$$\left(1 - \frac{F_{2,FEM,CH4.3.1}}{F_{2,FEM,CH3.3.3}}\right) \cdot 100 = \left(1 - \frac{0,924 \ MN}{0,947 \ MN}\right) \cdot 100 = 2,43\%$$

In addition, performing the deformation control test it was possible to trace the trend of the force during $snap-through$.
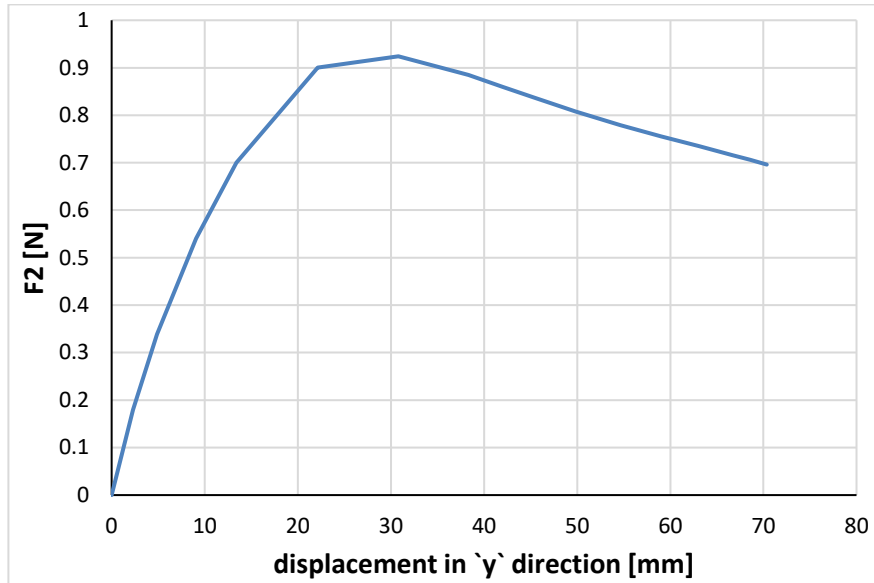
Figure 4.10: F2 trend (test 3 modelling using elastomeric bearings and considering hstb = 65mm)

4.3.2 Test 3: elastomeric bearings with h$_{stb}$=125 mm

As it is possible to see in the Figure 4.11, the buckling occurs at the lower stiffeners, just like in the test (Figure 3.22). Furthermore, given the symmetry of the problem and the opportunity to assign the imperfections in the area where the buckling occurs, each mode is repeated twice, in fact, the load multipliers are similar (1,5559 ≅ 1,5574).
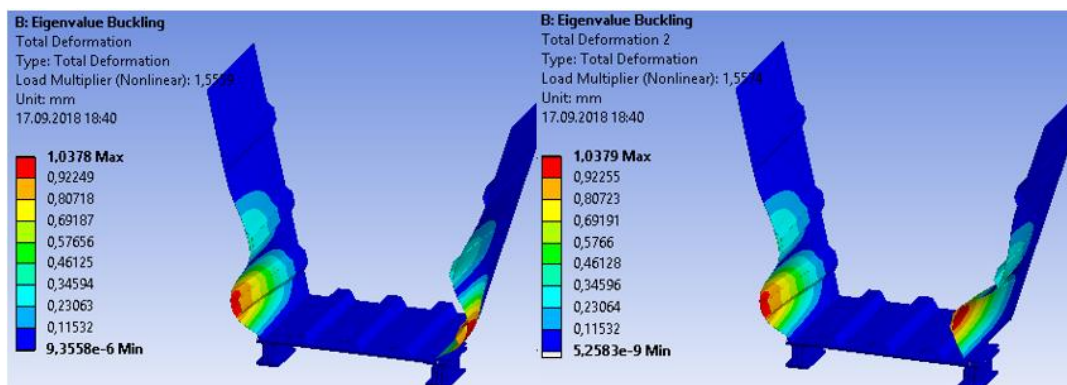
Figure 4.11: first buckling mode (test 3 modelling using the elastomeric bearings and considering hstb = 125mm)

Figure 4.12 shows the buckling modes 2, 3, 4 and 5, showing that only in correspondence of the fourth form of instability there is a slight deflection of the central stiffener which runs along

the bottom plate. This shows that the strong contribution of the stiffeners running along the bottom flange is a very important part of the overall section behaviour.
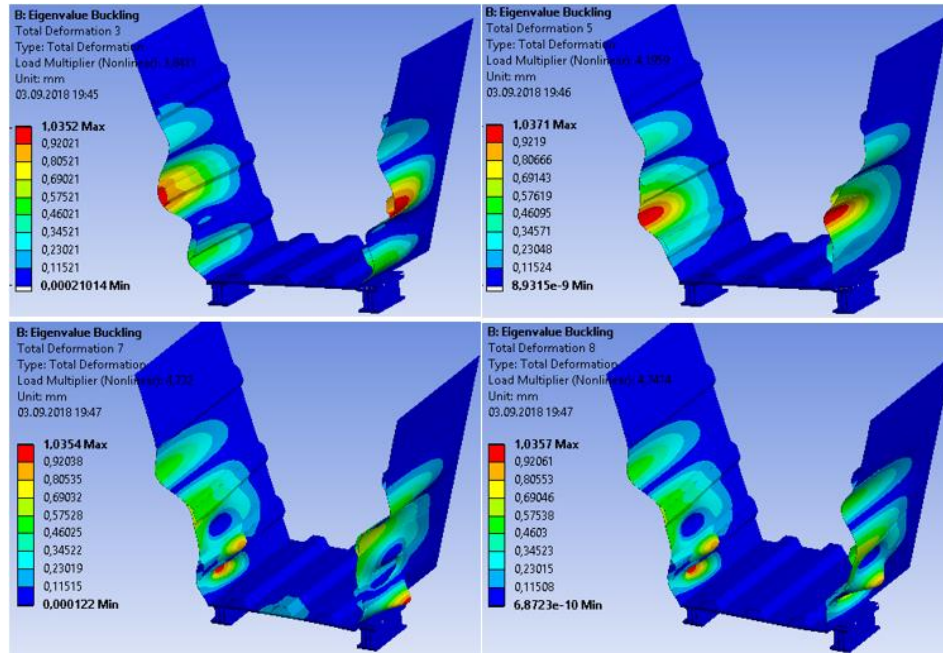
Figure 4.12: buckling modes 2, 3, 4 and 5 (test 3 modelling using the elastomeric bearings and considering hstb = 125mm)

Linear buckling is followed by nonlinear analysis with large displacements. In this case, the equivalent imperfections are applied thanks to the use of the following APDL commands (chapter 3.1.3).

```
fini
/prep7
upgeom, 15/1.0378,1,1,..\..\Buckling,rst
fini
/solu
```

This results in a load end value that is much closer to the actual one (Table 4.5). In addition, the analysis shows that the presence of the bottom flange leads to an increase in section resistance of more or less the 9,495%, more than twice the case of $h_{stb} = 65mm$ (Table 4.3, Table 4.4). The force F2 regards the single bearing.

$F_{1,FEM}$ [MN]	$F_{1, Test}$ [MN]	ΔF_1 [%]	$F_{2,FEM}$ [MN]	$F_{2, Test}$ [MN]	ΔF_2 [%]
1,58	1,58	0	0,975	0,89	9,495

Table 4.5: difference in percentage between the nonlinear model results and the test 3 ones (test 3 modelling using elastomeric bearings and considering hstb = 125mm)

With respect to the model studied in [3]   there is a difference of more or less the 9,5 % (Table 4.6), showing how the presence of the bottom plate provides a significant benefit on the overall behavior of the section.

$F_{1,FEM}$ [MN]	$F_{1, JS}$ [MN]	ΔF_1 [%]	$F_{2,FEM}$ [MN]	$F_{2, JS}$ [MN]	ΔF_2 [%]
1,58	1,58	0	0,975	0,89	**9,50**

Table 4.6: difference in percentage between the nonlinear model results and the [3] ones
(test 3 modelling using elastomeric bearings and considering hstb = 125mm)

Moreover, compared to the case of a spherical node pusher, there is a reduction in the final load of about 2.10%, given the higher rate of load absorbed by the web (Figure 4.3).

$$\left(1 - \frac{F_{2,FEM,CH4.3.2}}{F_{2,FEM,CH3.3.6}}\right) \cdot 100 = \left(1 - \frac{0,975\ MN}{0,996\ MN}\right) \cdot 100 = 2,10\%$$

In addition, performing the deformation control test it was possible to trace the trend of the force during $snap - through$ (Figure 4.13).
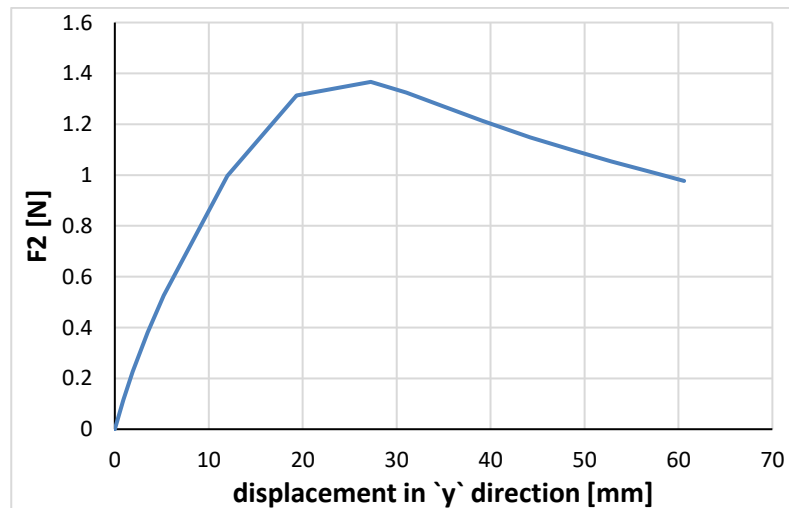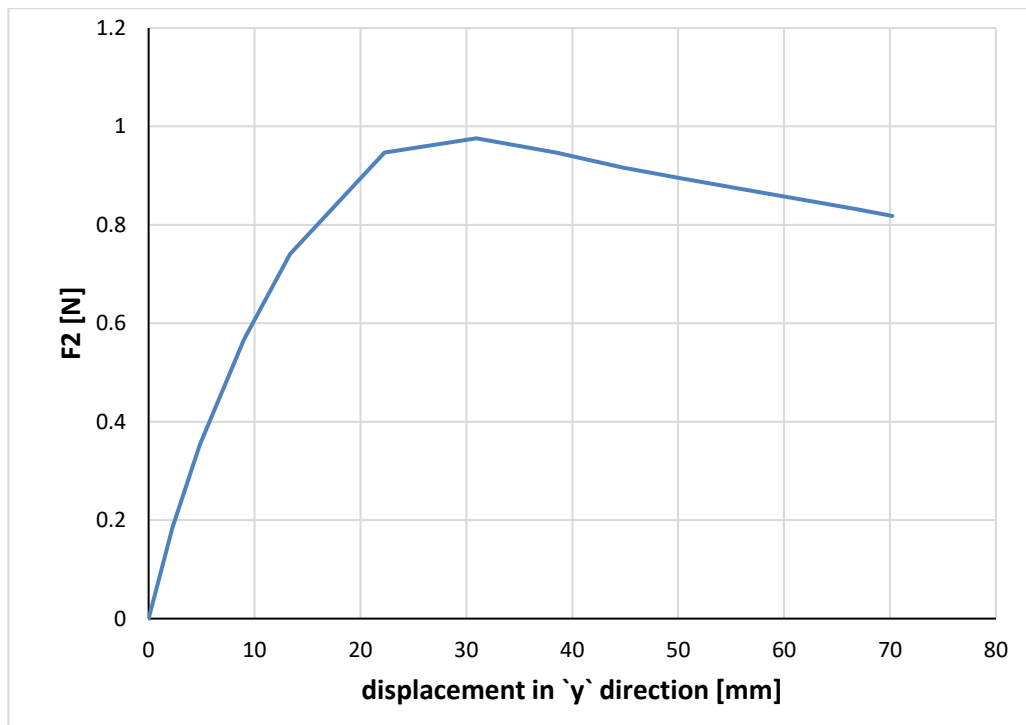

Figure 4.13: F2 trend (test 3 modelling using elastomeric bearings and considering hstb = 125mm)

4.4   Test 4: elastomeric bearings

On the basis of what has already been stated in chapter 3.4, the same forces have been adopted that allow therefore to obtain the desired stress ratio, $\beta = 0.5$. As it is possible to see in the Figure 4.14, the buckling occurs at the lower stiffeners. Furthermore, given the symmetry of the problem and the opportunity to assign the imperfections in the area where the buckling took place, each mode is repeated twice, in fact, the load multipliers are similar $(3,2009 \cong 3,2068)$.
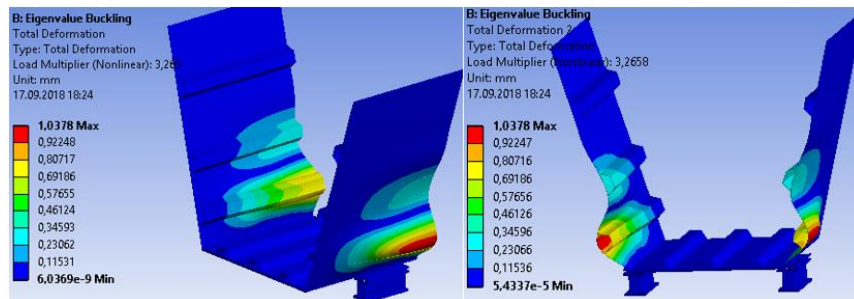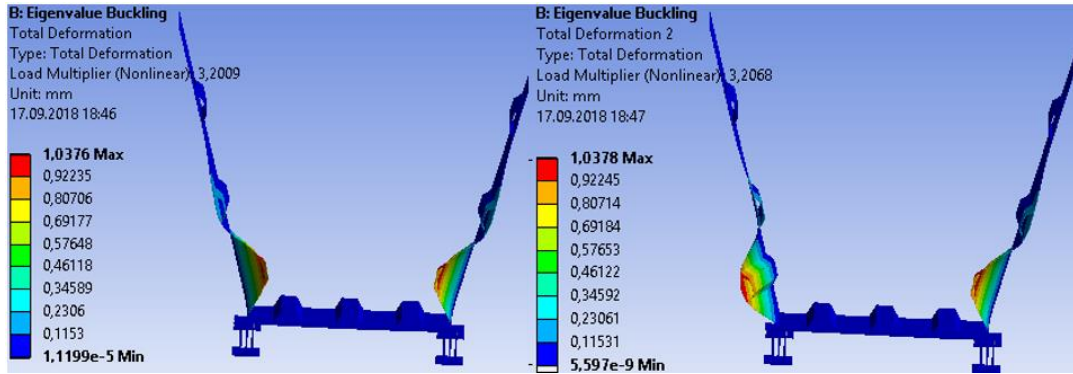

Figure 4.14: first buckling mode (test 4 modelling using the elastomeric bearings)

Figure 4.15 shows the buckling modes 2, 3, 4 and 5, showing that only the fifth form of instability involves the bottom plate as well.
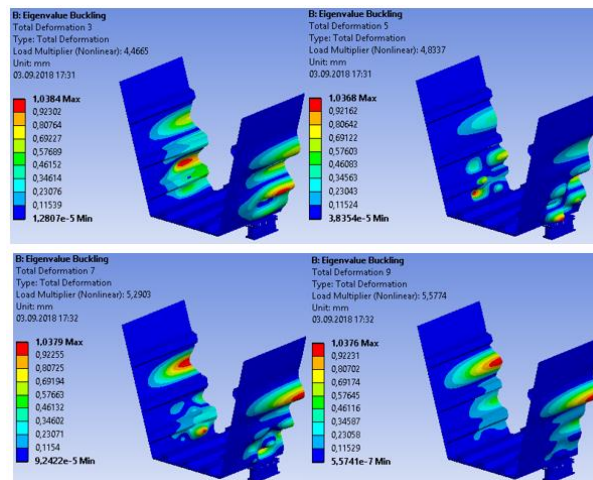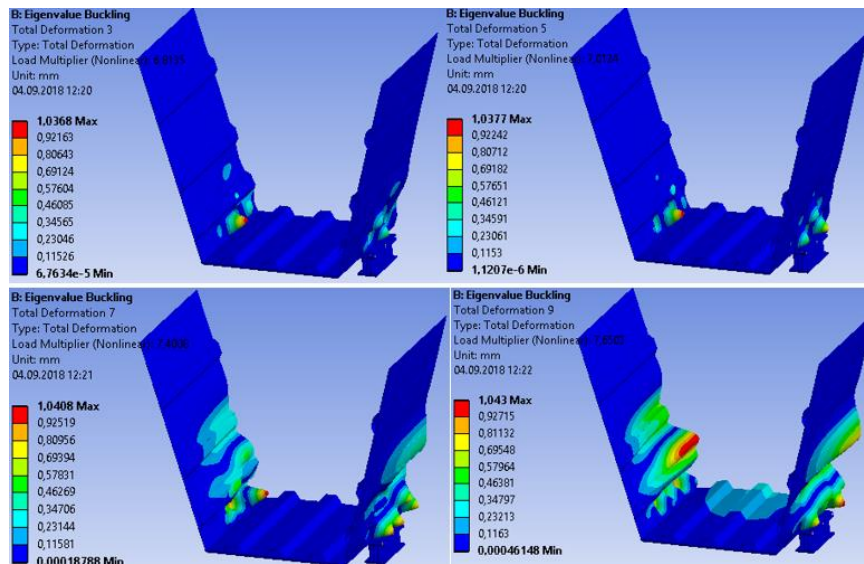

Figure 4.15: buckling modes 2, 3, 4 and 5 (test 4 modelling using the elastomeric bearings)

Linear buckling is followed by nonlinear analysis with large displacements. In this case, the equivalent imperfections are applied thanks to the use of the following APDL commands (chapter 3.1.3).

```
fini
/prep7
upgeom, -15/1.0376,1,1,..\..\Buckling,rst
fini
/solu
```

This results in a load end value that is much closer to the actual value (Table 4.7). In addition, the analysis shows that the presence of the bottom flange leads to an increase in section resistance of about 9,55%. The force F2 regards the single bearing.

$F_{1,FEM}$ [MN]	$F_{1, Test}$ [MN]	ΔF_1 [%]	$F_{2,FEM}$ [MN]	$F_{2, Test}$ [MN]	ΔF_2 [%]
2,44	2,44	0	0,951	0,87	**9,55**

Table 4.7: difference in percentage between the nonlinear model results and the test ones in case of nonlinear analysis (test 4 modelling using elastomeric bearings)

Moreover, as already found in $test$ 1 (chapter 4.1), the rotational capacity of the constraint results in a higher ultimate load $F2$ than in the case of prevented rotation, thanks to the lower load rate absorbed by the web (Figure 4.3).

$$\left(1 - \frac{F_{2,FEM,CH4.4}}{F_{2,FEM,CH3.4}}\right) \cdot 100 = \left(1 - \frac{0,951 \; MN}{0,981 \; MN}\right) \cdot 100 = 3,05\%$$

In addition, performing the deformation control test it was possible to trace the trend of the force during $snap - through$ (Figure 4.16).
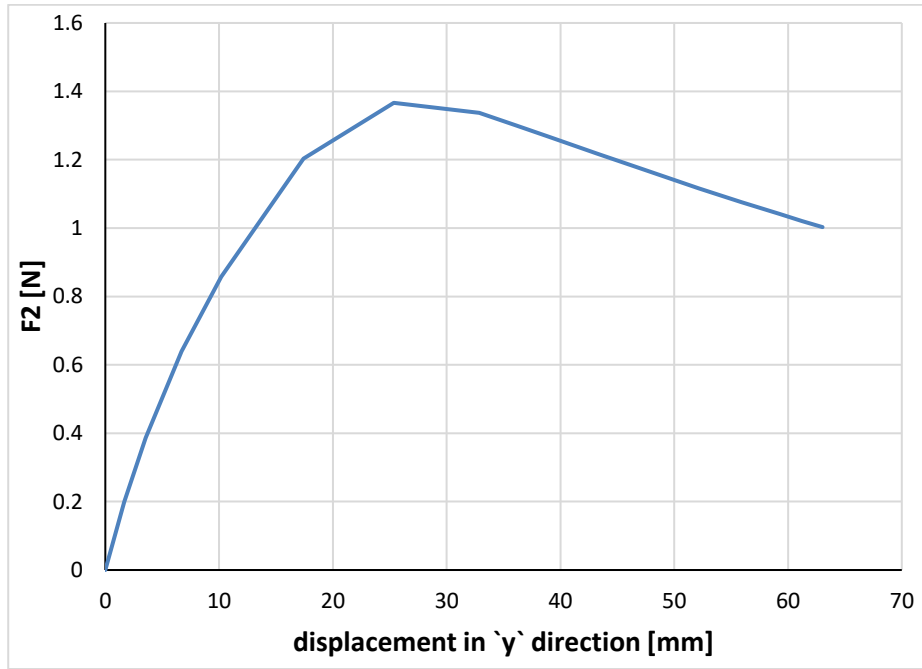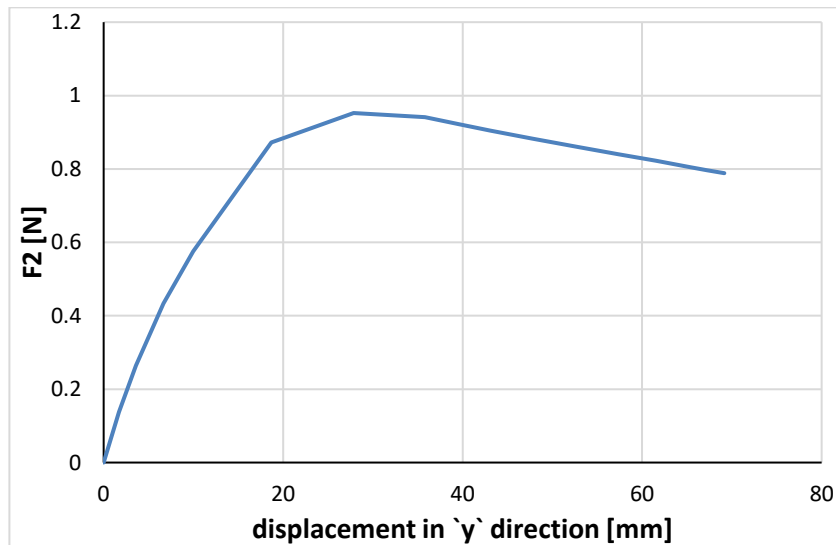

Figure 4.16: F2 trend (test 4 modelling using elastomeric bearings)

4.5 Test 5 – 6: elastomeric bearings

As far as the analysis of the last two tests is concerned, whose geometry is shown in Figure 1.11, the finite elements analysis did not show reliable results. Probably this is due to the boundary conditions applied, not suitable for the abrupt change of position of the lower stiffeners, placed no more at $300\,mm$ from the base of the bottom flange, but at $540\,mm$ Figure 3.41. The linear instability is all concentrated in the lower part of the web (Figure 4.17, Figure 4.18), thus making the application of the imperfections unsuitable for nonlinear calculation. In test six alone, due to the small size of the stiffeners, instability seems to partly involve lower stiffeners (Figure 4.18); however, this still does not reflect what laboratory tests have shown. This situation occurs also for high value of β.
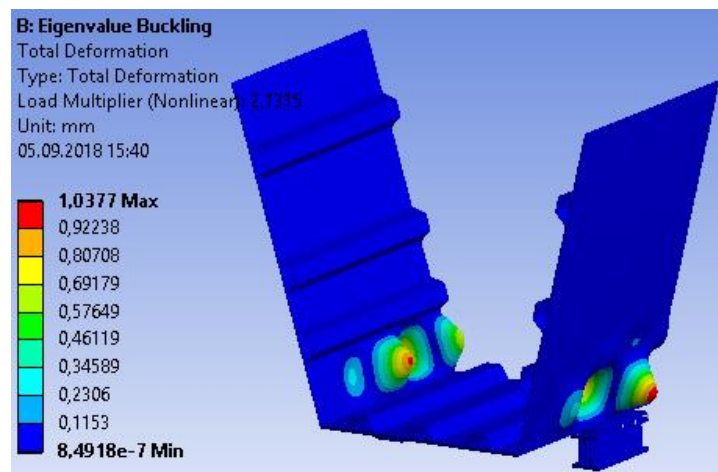
Figure 4.17: first buckling mode (test 5 modelling with the elastomeric bearings)
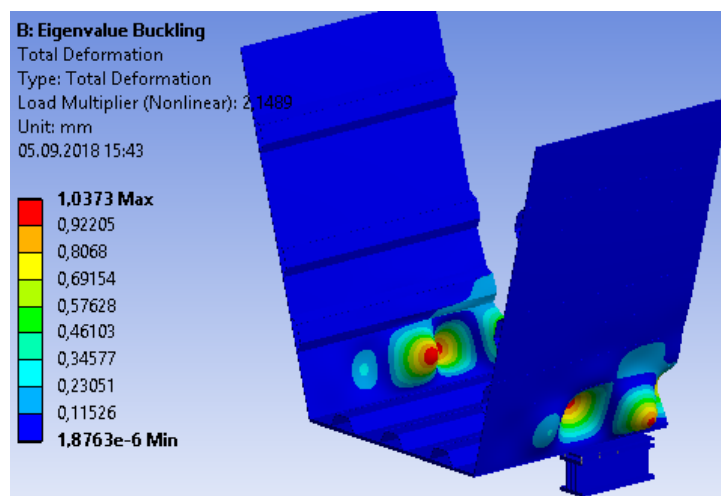
Figure 4.18: first buckling mode (test 6 modelling with the elastomeric bearings)

5. ECCENTRICITY INFLUENCE: THRUST BEARINGS TYPE GE80-AW

This chapter analyses the influence of load shifting on section instability. The type of pusher used is $GE\ 80 - AW$, for this reason, the results extrapolated from this analysis will be compared with those contained in chapter 3. Figure 2.18 shows the parameter (contained within the $file.txt$) that defines the position of the constraint along the y-axis (Figure 2.9). Inside chapters 3 and 4 the $eccentricity$ parameter is set to zero, in order to guarantee a perfect alignment between the center of gravity of the bearing and the section. Of course, during the incremental launching, since the bridge slides over the bearings, it can happen that they are in a staggered position with respect to the edge of the section. This results in a torque moment that must, therefore, be absorbed by the lower flange and the core of the section. The first 4 tests were then reanalyzed starting from a value of the $eccentricity$ parameter different from zero. In particular, this was placed at $\pm 30\ mm$. Naturally, since the analyzed bridge segment lies on 4 constraints, different constraints-section position combinations have been analyzed, that is to say:

- Positive/negative eccentricity for all the bearings (Figure 5.1):
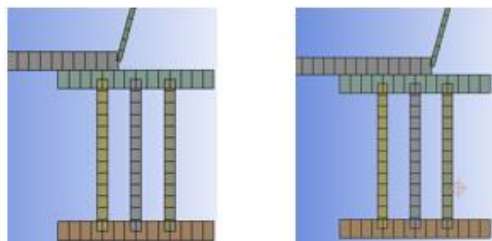
Figure 5.1: positive eccentricity of 30 mm (left); negative eccentricity of 30mm (right)

- positive eccentricity for the constraints placed in sector $y > 0$ and negative for those placed in sector $y < 0$ (Figure 5.2):

Figure 5.2: positive eccentricity for the right bearings and negative eccentricity for the left ones

- Positive eccentricity for the front bearings and negative eccentricity for the posteriors ones (Figure 5.3):
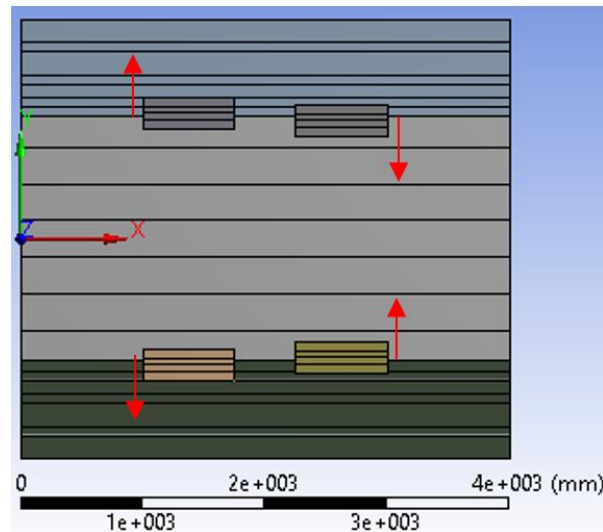
Figure 5.3: Positive eccentricity for the front bearings and negative eccentricity for the posteriors ones

- positive eccentricity for the front right bearing and the posterior left one, negative eccentricity for the front left bearing and posterior right one (Figure 5.4):
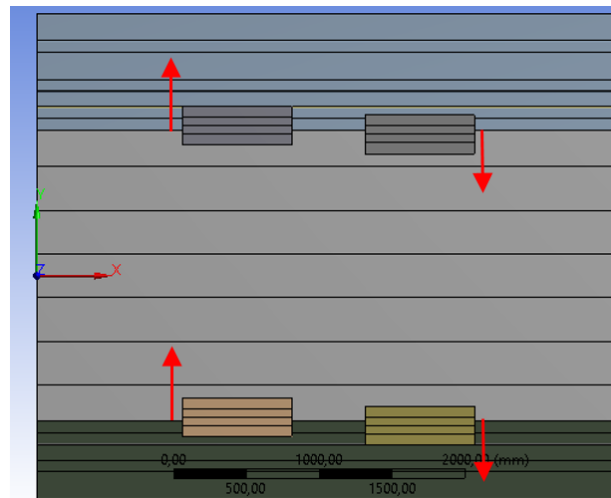
Figure 5.4: positive eccentricity for the front right bearing and the posterior left one, negative eccentricity for the front left bearing and posterior right one

As for the structure of the analysis, nothing has changed, in fact, the problem has been split into three parts: linear static analysis, linear buckling analysis, and nonlinear analysis at large displacements [10] (see chapters 2.2.1 and 3).

5.1   Test 1: analysis with eccentricity

Test 1 is re-analyzed by combining different types of eccentricity.

5.1.1   Test 1: positive/negative eccentricity for all the bearings

Considering the same system of forces already used in chapter 3.1, the influence of a possible decentralization of the bearings as in the Figure 5.1 has been analyzed.

As can be seen in Figure 5.5, even in the case of a positive eccentricity of $30\ mm$, the first buckling mode continues to affect the lower stiffeners, with a slightly lower load multiplication factor than in the case of zero eccentricity (chapter 3.1.2).
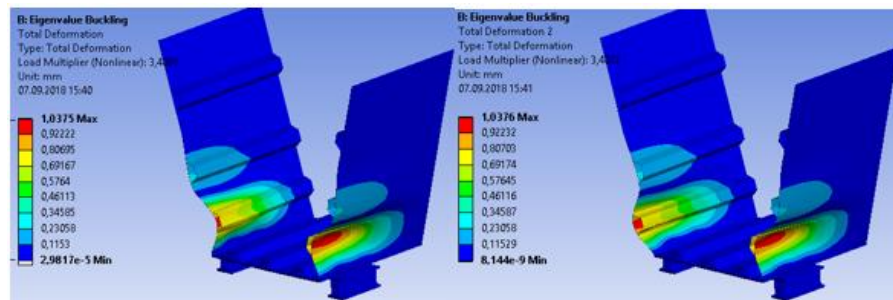
Figure 5.5: first buckling mode (test 1 modelling with positive eccentricity of 30 mm)

In addition, the instability of the bottom flange already occurs at the second buckling mode (Figure 5.6).
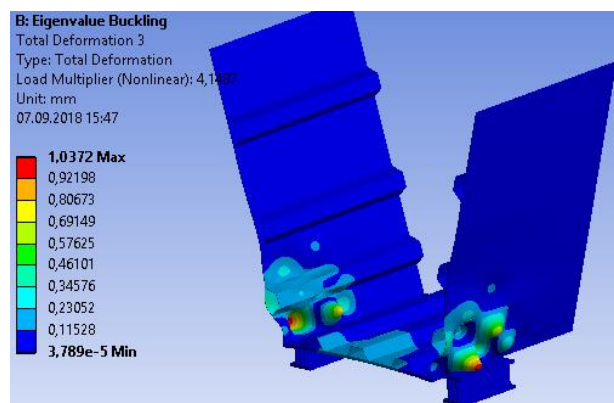
Figure 5.6: second buckling mode (test 1 modelling with positive eccentricity of 30 mm)

As far as the nonlinear analysis is concerned, the iteration of the F2 load led to a value equal to $1.342\ MN$, about 1.8% lower than in the case of absence of eccentricity ($1.367\ MN$).

This is due to the torque moment acting in the same direction of deformation of the web. For example, consider the constraint located in the sector of the negative y (Figure 5.7):
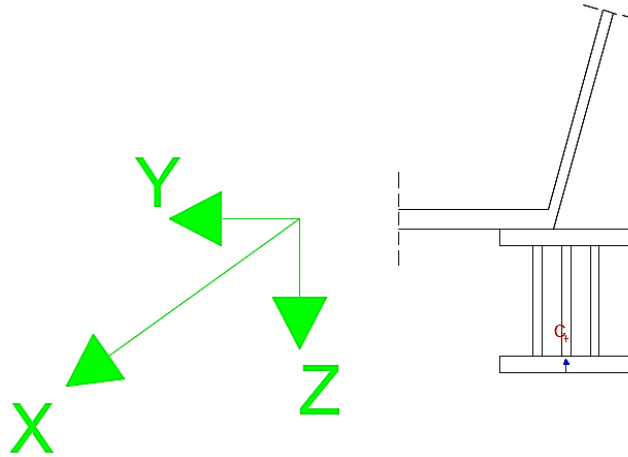
Figure 5.7: bearings located in the sector of the negative y with positive eccentricity

The displacement imposed along the z-direction of $20\ mm$ (blue arrow in Figure 5.7), tends to rotate the constraint around the center of rotation counterclockwise with displacements in y-direction of the upper part of the constraint up to $5mm$. The rotation center is placed at a height s with respect to the pusher (Figure 1.8) and coincides with the remote point analyzed in chapter 2.5.3.2. However, the system of forces equivalent to displacement tends to cause the component in y to generate a greater stabilizing moment than the unstable moment induced by the component in z (Figure 5.8).
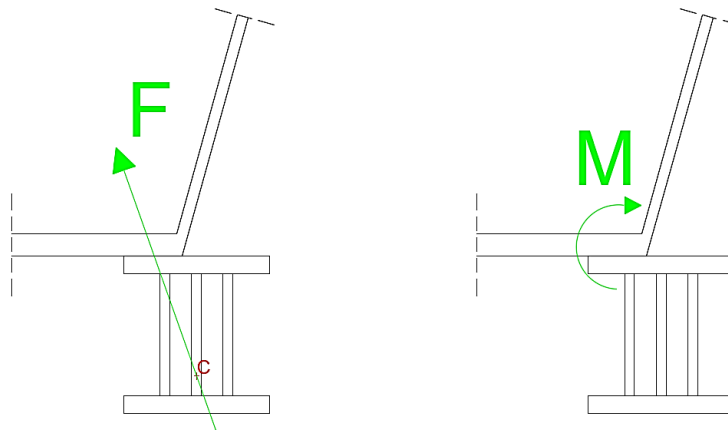
Figure 5.8: torque moment due to the positive eccentricity

In fact, by observing Figure 5.9, worth noting is how the deformation is consistent with the case of absence of eccentricity, and how it will be possible to see better later, even in the case of negative eccentricity.

The Table 5.1 shows the values of the components in x, y and z of the reaction induced by the imposed displacement; moreover, in the same table are reported the values of the stabilizing, destabilizing and total torque moment for each iteration.
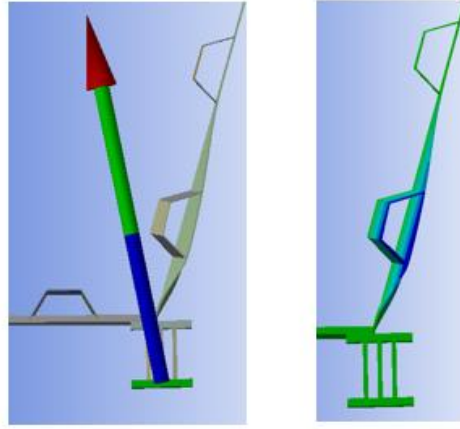
Figure 5.9: displacement in y direction (test 1 modelling with eccentricity of +30 mm)

F$_x$ [N]	F$_y$ [N]	F$_z$ [N]	F$_{tot}$ [N]	M$_i$ [Nmm]	M$_s$ [Nmm]	M [Nmm]
-10426	15690	-95413	97255	2,86E+06	4,12E+06	1,26E+06
-20528	30986	-1,88E+05	1,91E+05	5,63E+06	8,13E+06	2,50E+06
-35074	52812	-3,19E+05	3,25E+05	9,57E+06	1,39E+07	4,29E+06
-49079	73131	-4,42E+05	4,51E+05	1,33E+07	1,92E+07	5,94E+06
-96740	1,50E+05	-8,88E+05	9,06E+05	2,66E+07	3,95E+07	1,28E+07
-1,33E+05	2,07E+05	-1,21E+06	1,24E+06	3,63E+07	5,43E+07	1,80E+07
-1,47E+05	2,33E+05	**-1,34E+06**	1,37E+06	4,03E+07	6,12E+07	2,09E+07
-1,34E+05	2,27E+05	-1,27E+06	1,30E+06	3,82E+07	5,97E+07	2,15E+07
-1,28E+05	2,23E+05	-1,23E+06	1,26E+06	3,69E+07	5,86E+07	2,16E+07
-1,21E+05	2,19E+05	-1,19E+06	1,22E+06	3,58E+07	5,76E+07	2,18E+07
-1,11E+05	2,15E+05	-1,14E+06	1,17E+06	3,43E+07	5,64E+07	2,21E+07
-99314	2,10E+05	-1,09E+06	1,11E+06	3,27E+07	5,52E+07	2,25E+07
-90181	2,06E+05	-1,05E+06	1,07E+06	3,14E+07	5,42E+07	2,28E+07
-82709	2,03E+05	-1,01E+06	1,03E+06	3,03E+07	5,33E+07	2,30E+07
-79409	2,01E+05	-9,89E+05	1,01E+06	2,97E+07	5,27E+07	2,30E+07
-77099	1,98E+05	-9,69E+05	9,92E+05	2,91E+07	5,20E+07	2,30E+07

Table 5.1: reaction components and moments generated (test 1 modelling with eccentricity of +30 mm)

Where:

$$M_i = F_z \cdot 30 \ mm$$

$$M_s = F_y \cdot 262,5 \ mm$$

$$M = M_s - M_i$$

Therefore, it can be well understood that in the case of positive eccentricity, a high component in y-direction arise, then absorbed by the lower plate, which will be in a state of greater compression than in the case of the essence of eccentricity. For this reason, as mentioned above, the instability of the lower plate already occurs in correspondence to the second form of instability (Figure 5.6). However, at the expense of the high forces in y, the components in z are reduced, also given the absence of a resistant element that contrasts the unstable moment.

Now consider the case of negative eccentricity (Figure 5.10).
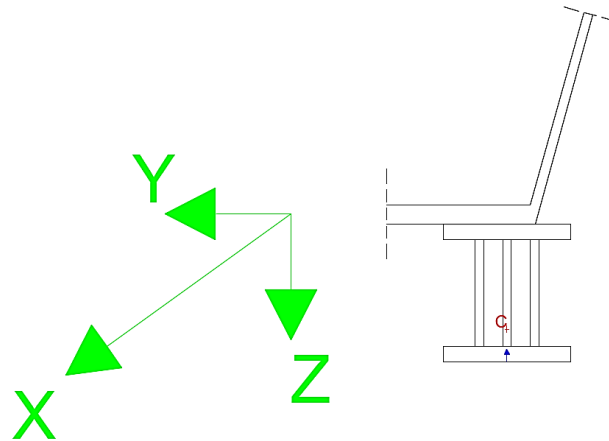
Figure 5.10: constraint located in the sector of the negative y with negative eccentricity

As can be seen in the Figure 5.11, even with a negative eccentricity of $30\ mm$, the first form of instability continues to affect the lower stiffeners, with a slightly higher load multiplication factor than in the case of zero eccentricity (chapter 3.1.2).
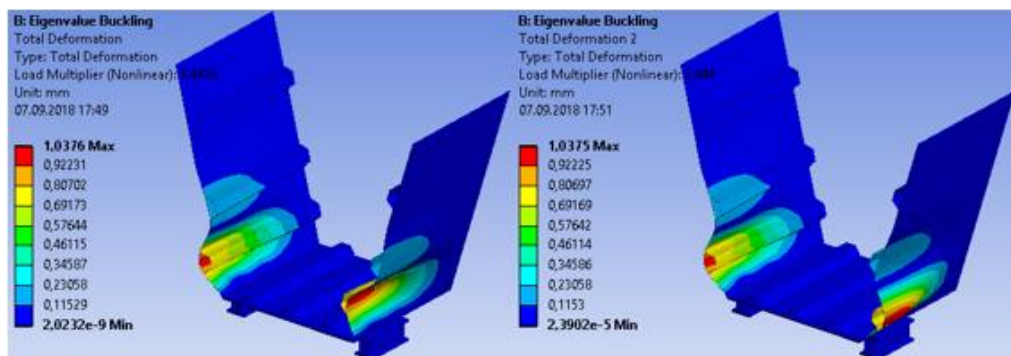
Figure 5.11: first buckling mode (test 1 modelling with negative eccentricity of 30 mm)

The Figure 5.12 shows the forms of instability $2, 3, 4$ and 5, showing how only the fifth involves the bottom plate, just as in the case of absence of eccentricity and with a slightly higher value of the load multiplier.
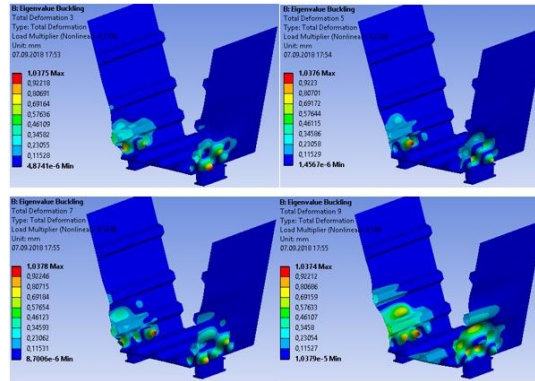
Figure 5.12: buckling modes 2, 3, 4 and 5 (test 1 modelling with negative eccentricity of 30 mm)

As far as the nonlinear analysis is concerned, it provided a value of F2 equal to $1.39\ MN$, about 1.8% higher than in the case of absence of eccentricity. This is probably due to the presence of the bottom flange, which allows minimum rotations to the constraint with the consequent birth of forces in y even of an order of magnitude smaller than in the case of positive eccentricity (Table 5.2).

| F_x [N]	F_y [N]	F_z [N]	F_{tot} [N]	M_s [N]	M_i [N]	M [N]
-22301	-4525,1	-1,14E+05	1,16E+05	3,42E+06	1,19E+06	2,23E+06
-43824	-8910,4	-2,23E+05	2,28E+05	6,70E+06	2,34E+06	4,37E+06
-74103	-15823	-3,78E+05	3,85E+05	1,13E+07	4,15E+06	7,18E+06
-1,02E+05	-23156	-5,20E+05	5,30E+05	1,56E+07	6,08E+06	9,51E+06
-1,96E+05	-4,97E+04	-9,95E+05	1,02E+06	2,99E+07	1,31E+07	1,68E+07
-2,62E+05	-6,50E+04	-1,32E+06	1,35E+06	3,96E+07	1,71E+07	2,25E+07
-2,80E+05	-5,35E+04	**-1,39E+06**	1,42E+06	4,18E+07	1,41E+07	2,77E+07
-2,65E+05	-2,60E+04	-1,30E+06	1,33E+06	3,90E+07	6,83E+06	3,21E+07
-2,57E+05	-1,37E+04	-1,25E+06	1,28E+06	3,76E+07	3,61E+06	3,40E+07
-2,50E+05	-2,89E+03	-1,22E+06	1,24E+06	3,65E+07	7,58E+05	3,57E+07
-2,39E+05	1,11E+04	-1,16E+06	1,19E+06	3,49E+07	-2,90E+06	3,78E+07
-2,27E+05	2,61E+04	-1,11E+06	1,13E+06	3,32E+07	-6,84E+06	4,01E+07
-2,17E+05	3,81E+04	-1,06E+06	1,09E+06	3,19E+07	-1,00E+07	4,19E+07
-2,07E+05	4,82E+04	-1,02E+06	1,05E+06	3,07E+07	-1,27E+07	4,34E+07
-2,02E+05	5,38E+04	-1,00E+06	1,02E+06	3,01E+07	-1,41E+07	4,42E+07
-1,97E+05	5,89E+04	-9,82E+05	1,00E+06	2,95E+07	-1,55E+07	4,49E+07

Table 5.2: reaction components and moments generated (test 1 modelling with eccentricity of -30 mm)

Where:

$$M_i = F_y \cdot 262,5 \; mm$$

$$M_s = F_z \cdot 30 \; mm$$

$$M = M_s - M_i$$

In the Table 5.2 we can also observe how the sign of the component F_y results to be always negative until after the attainment of the maximum value of F_z; therefore the force can be schematized as in figure (Figure 5.13).
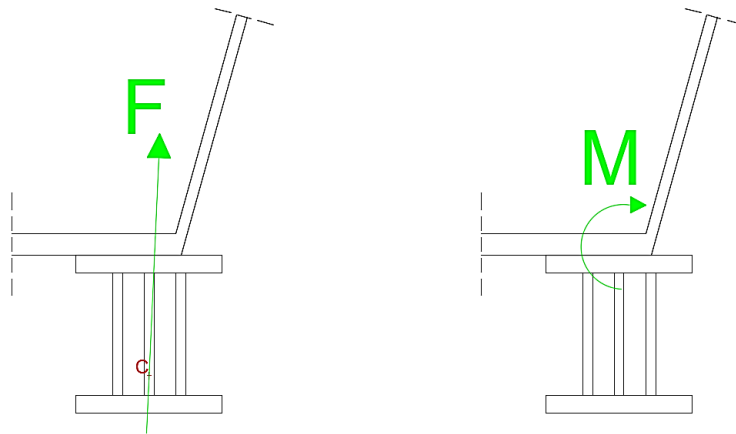
Figure 5.13: torque moment due to the negative eccentricity

The presence of the plate and the high value of torque lead to greater deformations of the web compared to both the case of negative eccentricity and the case of absence of eccentricity (Figure 5.14).
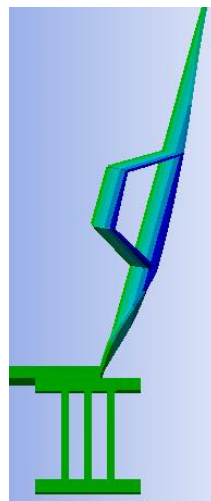
Figure 5.14: displacement in y direction due to the negative eccentricity

Therefore it can be well understood how in case of negative eccentricity the presence of the plate plays a very important role, not only because it absorbs the horizontal stresses (reduced compared to the case of positive eccentricity), but also because opposing the rotation of the constraint allows a growth of the ultimate value F2 of 1.8% higher than in the case of essence of eccentricity and a greater deformation before collapse.

The comparison between the various cases is shown below (Figure 5.15).
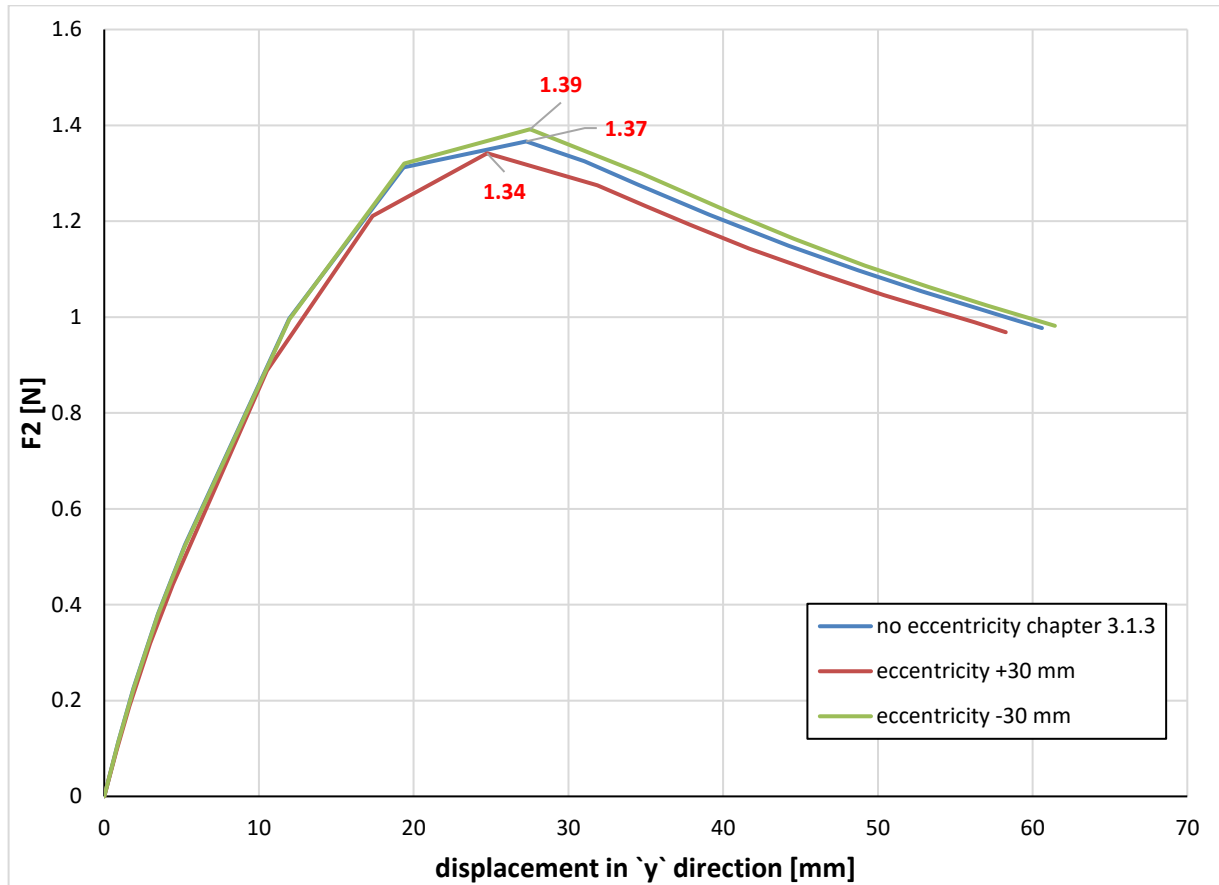
Figure 5.15: comparison between the various cases (test 1 modelling)

5.1.2 Test 1: positive eccentricity for the constraints placed in sector y > 0 and negative for those placed in sector y < 0

Considering the same system of forces already used in chapter 3.1, the influence of a possible decentralization of the constraints as in the figure (Figure 5.2) has been analyzed.

As can be seen in the Figure 5.16 the first two form of instabilities affect the lower stiffeners, but compared to the previous cases, the instability no longer occurs simultaneously in the two webs, but involves first the web that rests on the bearing that has positive eccentricity and after the web that rests on the bearing with negative eccentricity.
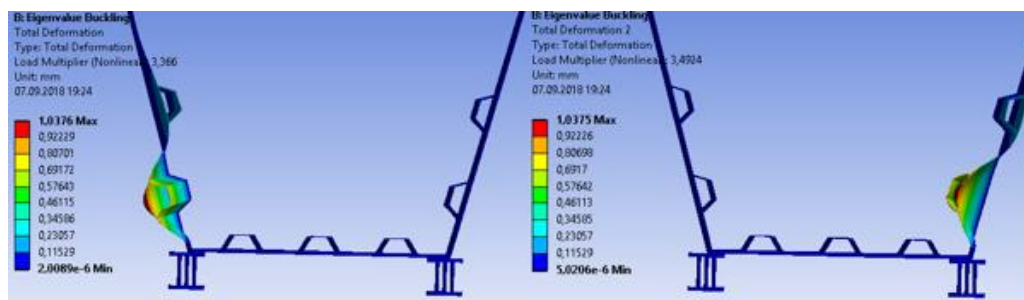
Figure 5.16: first and second buckling modes (test 1 modelling with positive eccentricity for the constraints placed in sector y>0 and negative for those placed in sector y<0)

The first two forms of instability were therefore considered as predeformations for nonlinear analysis in order to distribute the geometric imperfections on both webs.

The F2 values (Figure 5.17, Figure 5.18), as expected, are not very different from those obtained previously (chapter 5.1.1).
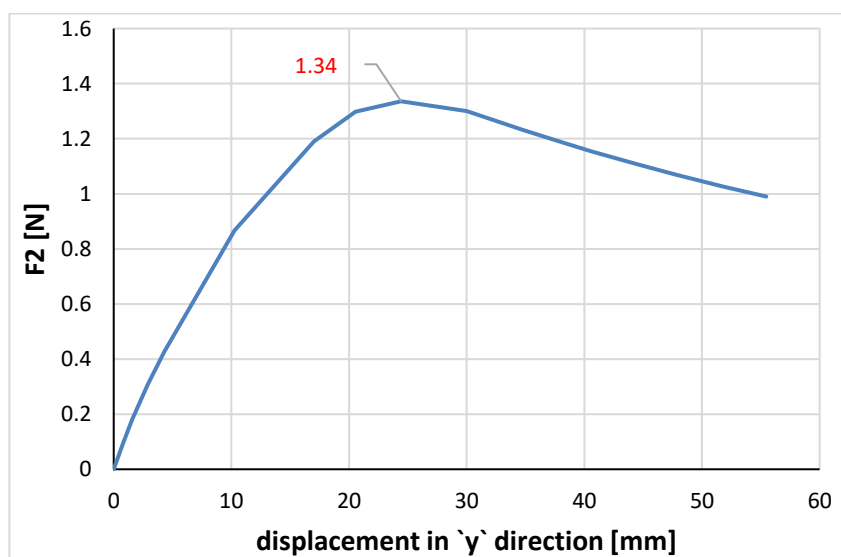
Figure 5.17: trend of the reaction F2 under the bearing with positive eccentricity (test 1 modelling)
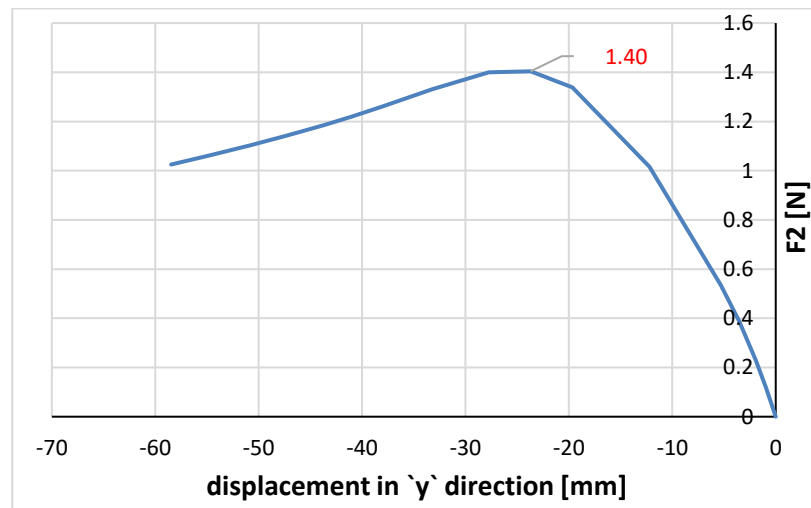
Figure 5.18: trend of the reaction F2 under the bearing with negative eccentricity (test 1 modelling)

Probably the slight difference is due to the combination of the two forms of instability to generate the imperfections.

5.1.3   Test 1: positive eccentricity for the front bearings and negative eccentricity for the posteriors ones

To analyze the case of positive eccentricity for the front bearings and negative for the posteriors ones (Figure 5.3) the complete model has been adopted, since there is no longer any geometric symmetry. As it is possible to observe in the Figure 5.19, the first form of instability continues to affect the lower stiffeners, involving both webs at the same time, given the symmetry with respect to the *z*-axis; however, the swelling is greater in the part above the bearing having positive eccentricity, since it would tend to become unstable first.
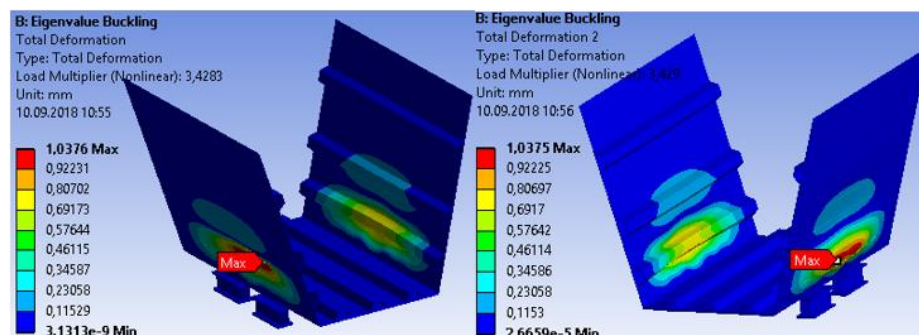
Figure 5.19: first buckling mode (test 1 modelling with positive eccentricity for the front bearings and negative eccentricity for the posteriors ones)

In fact, as a demonstration of this, one can appreciate in the Figure 5.20 how the second and third forms of instability almost exclusively concern the front constraints.
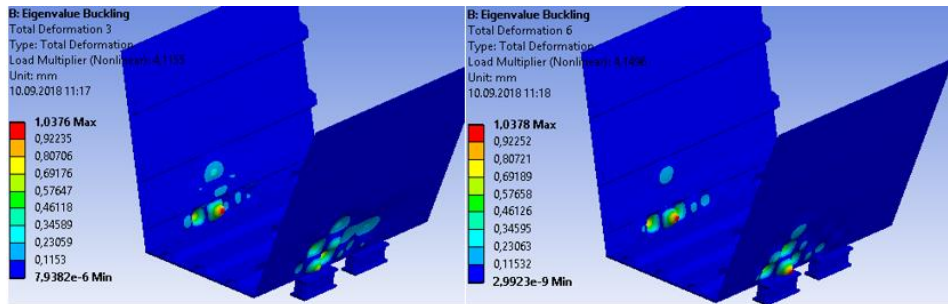
Figure 5.20: second and third buckling mode (test 1 modelling with positive eccentricity for the front bearings and negative eccentricity for the posteriors ones)

Having an uneven swelling in the form of instability means not assigning a homogeneous imperfection. In fact, the 15 mm imperfection would be assigned only in the part above the constraint having positive eccentricity, while in the part above the constraints having negative eccentricity would be assigned a reduced imperfection.

In terms of results (Figure 5.21), the nonlinear analysis led to an increase in the value of F2 below the constraints with negative eccentricity; however, the analysis led to a significant reduction in the value of F2 below the constraints with positive eccentricity. This could be explained by the fact that the major deformation work is carried out by the constraints with negative eccentricity, which are so more loaded, partially unloading the constraints with positive eccentricity.
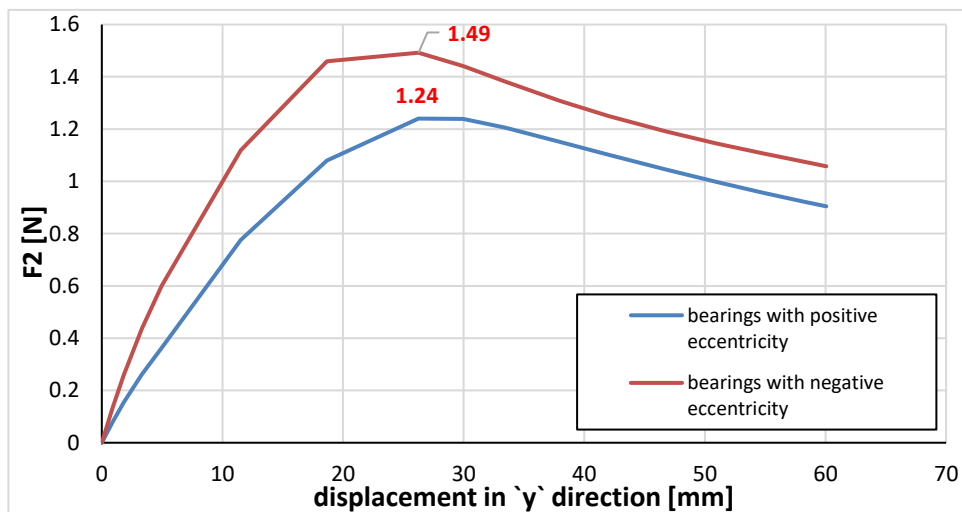
Figure 5.21: trend of the reaction F2 under the bearings (test 1 modelling with positive eccentricity for the front bearings and negative eccentricity for the posteriors ones)

This shows how the distribution of imperfections and the bearings position significantly influence the final values.

100

5.1.4 Test 1: positive eccentricity for the front right bearing and the posterior left one, negative eccentricity for the front left bearing and posterior right one

The last case analyzed is that of positive eccentricity assigned to the front right and posterior left bearings and negative eccentricity assigned to the front left and posterior right bearing (Figure 5.4). As can be seen in the Figure 5.22, the first form of instability continues to affect the lower stiffeners, involving both webs at the same time given the polar symmetry; however, the swelling is greater in the part above the bearing having positive eccentricity, since it would tend to get unstable first.
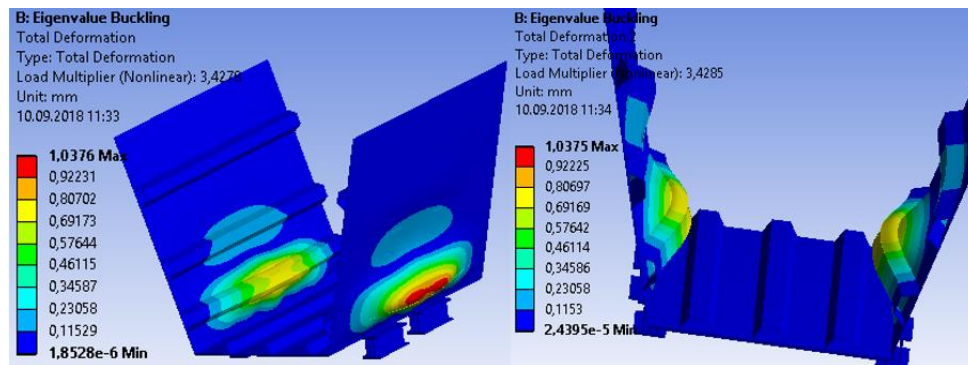
Figure 5.22: first buckling mode (test 1 modelling with positive eccentricity for the front right bearing and the posterior left one, negative eccentricity for the front left bearing and posterior right one)

In fact, as a demonstration of this, it can be appreciated in the Figure 5.23 how the second and third form of instability almost exclusively concerns the web above the bearings having a positive eccentricity.
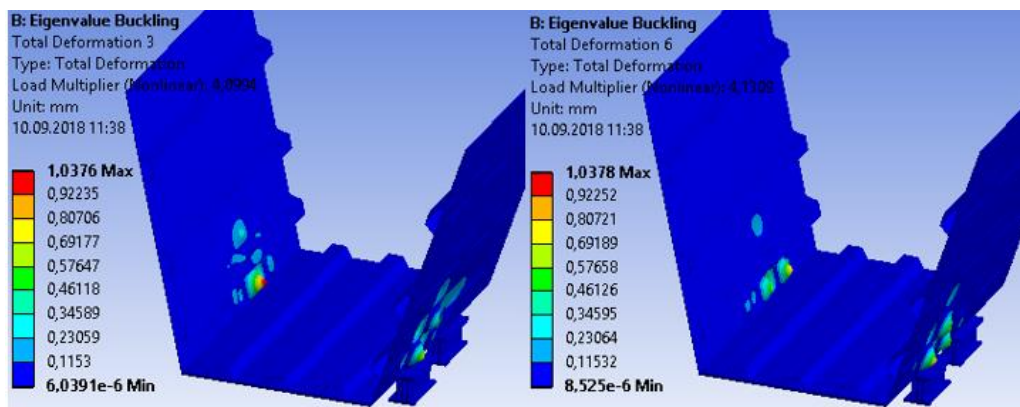
Figure 5.23: second and third buckling mode (test 1 modelling with positive eccentricity for the front right bearing and the posterior left one, negative eccentricity for the front left bearing and posterior right one)

Having an uneven swelling in the form of instability means not assigning a homogeneous imperfection. In fact, the 15 mm imperfection would be assigned only in the part above the bearings having positive eccentricity, while in the part above the bearings having negative eccentricity would be assigned a reduced imperfection.

In terms of results (Figure 5.24), the nonlinear analysis led to an increase in the value of F2 below the constraints with negative eccentricity; however, the analysis has also led to a significant reduction in the value of F2 below the constraints with positive eccentricity. This could be explained by the fact that the major deformation work is carried out by the constraints with negative eccentricity, which are so more loaded, partially unloading the constraints with positive eccentricity. For this reason the results are similar to those of the previous chapter (5.1.3).

Figure 5.24: trend of the reaction F2 under the bearings (test 1 modelling with positive eccentricity for the front right bearing and the posterior left one, negative eccentricity for the front left bearing and posterior right one)

5.2   Test 2: analysis with eccentricity

Test 2 is re-analyzed by combining different types of eccentricity.

5.2.1   Test 2: positive/negative eccentricity for all the bearings

Considering the same system of forces already used in chapter 3.2, the influence of a possible decentralization of the bearings as in the Figure 5.1 has been analyzed.

As can be seen in Figure 5.25, even in the case of a positive eccentricity of 30 mm, the first buckling mode continues to affect the lower stiffeners, with a slightly lower load multiplication factor than in the case of zero eccentricity (chapter 3.2.2).
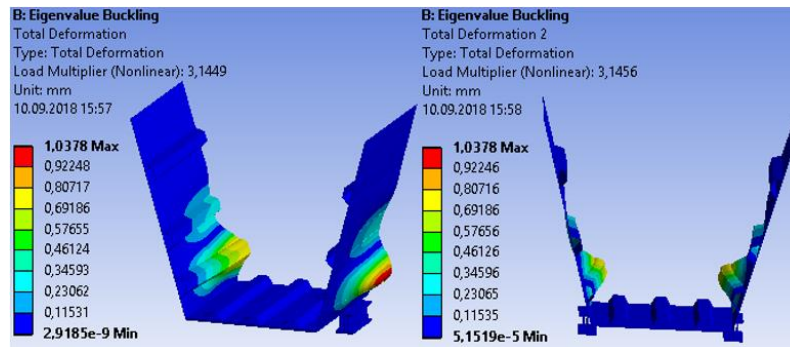
Figure 5.25: first buckling mode (test 2 modelling with positive eccentricity of 30 mm)

As far as the nonlinear analysis is concerned, the iteration of the F2 load led to a value equal to 1.351 MN, about 2.8% lower than in the case of absence of eccentricity (1.39 MN), for the same reasons already explained in chapter 5.1.1.

Considering the negative eccentricity, again the first buckling mode occurs in correspondence of the lower stiffeners (Figure 5.26), with a slightly higher load multiplication factor than in the case of zero eccentricity (chapter 3.2.2).
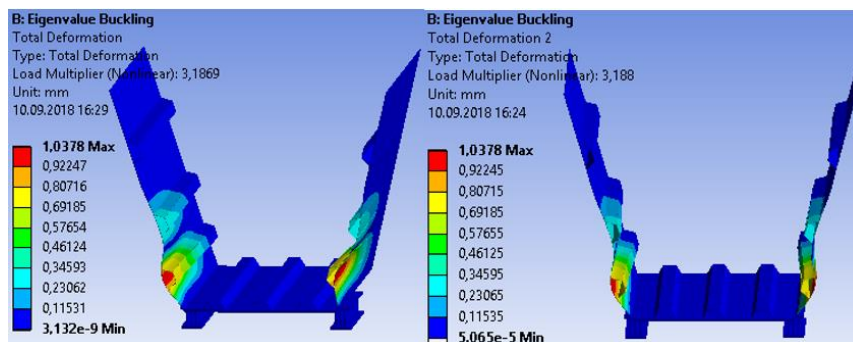
Figure 5.26: first buckling mode (test 2 modelling with negative eccentricity of 30 mm)

As far as the nonlinear analysis is concerned, it provided a value of F2 equal to 1.42 MN, about 2,11% higher than in the case of absence of eccentricity, for the same reasons already explained in chapter 5.1.1.

The comparison between the various cases is shown below (Figure 5.27).
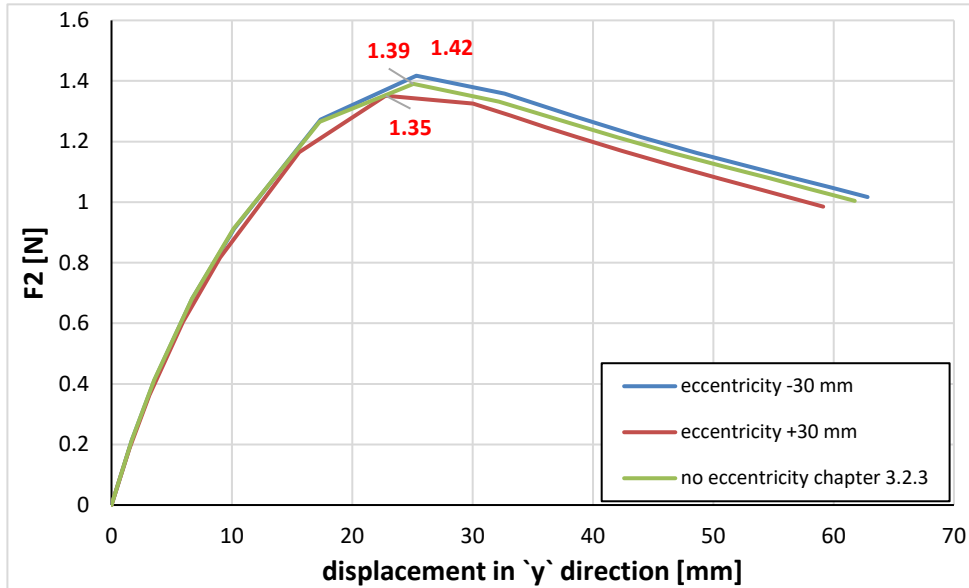
Figure 5.27: comparison between the various cases (test 2 modelling)

5.2.2   Test 2: positive eccentricity for the constraints placed in sector y > 0 and negative for those placed in sector y < 0

Considering the same system of forces already used in chapter 3.2, the influence of a possible decentralization of the constraints as in the figure (Figure 5.2) has been analyzed.

As can be seen in the Figure 5.28, the first two form of instabilities affect the lower stiffeners, but compared to the previous cases, the instability no longer occurs simultaneously in the two webs, but involves first the web that rests on the bearing that has positive eccentricity and after the web that rests on the bearing with negative eccentricity.
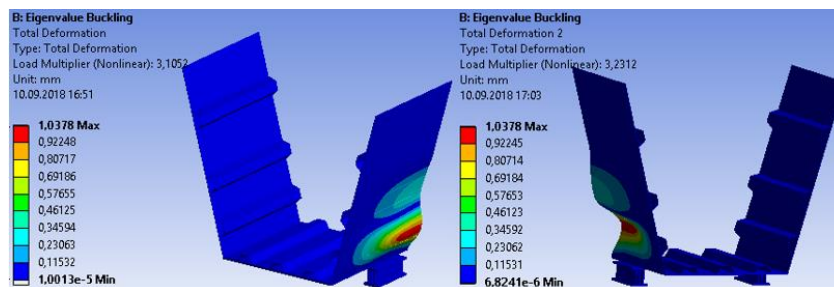
Figure 5.28: first and second buckling modes (test 2 modelling with positive eccentricity for the constraints placed in sector y>0 and negative for those placed in sector y<0)

The first two forms of instability were therefore considered as predeformations for nonlinear analysis in order to distribute the geometric imperfections on both webs.

The F2 values (Figure 5.29, Figure 5.30), as expected, are not very different from those obtained previously (chapter 5.2.1).
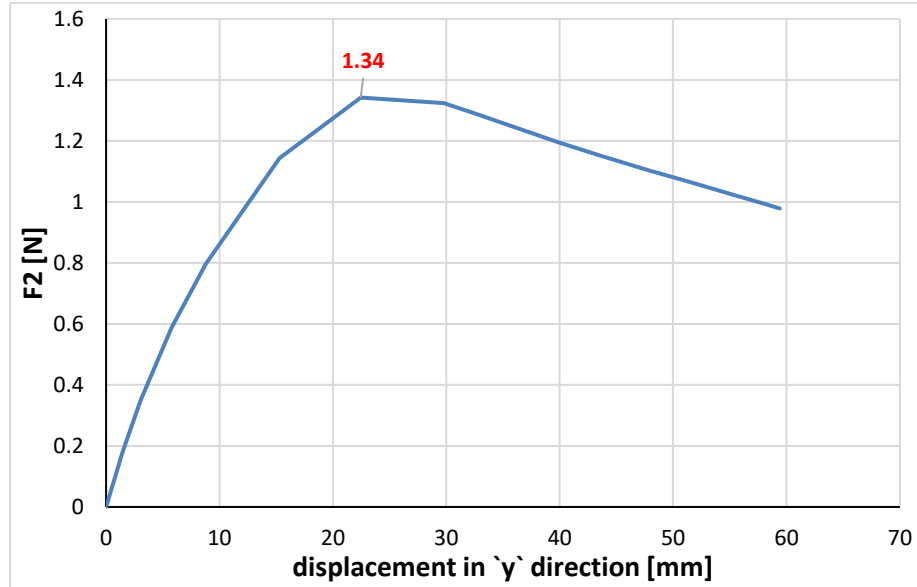
Figure 5.29: trend of the reaction F2 under the bearing with positive eccentricity (test 2 modelling)
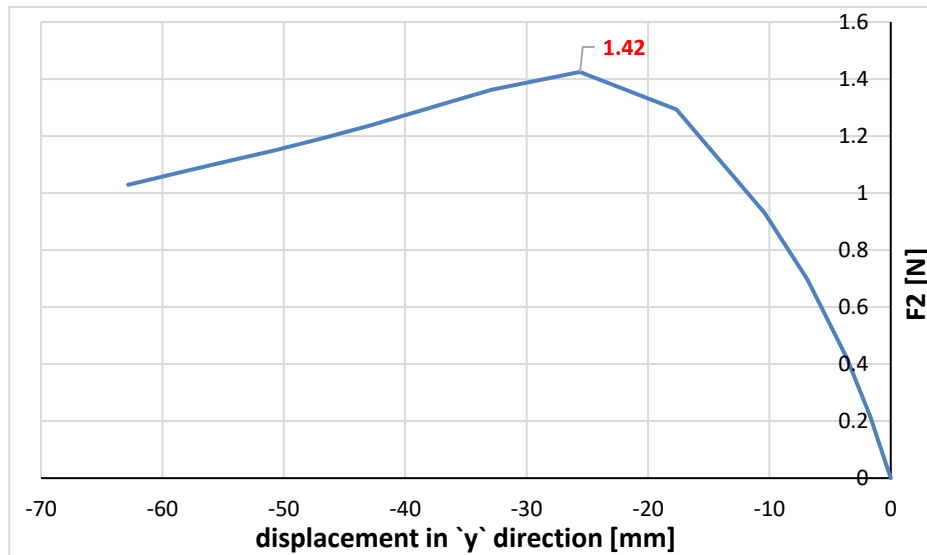
Figure 5.30: trend of the reaction F2 under the bearing with negative eccentricity (test 2 modelling)

Probably the slight difference is due to the combination of the two forms of instability to generate the imperfections.

5.2.3 Test 2: positive eccentricity for the front bearings and negative eccentricity for the posteriors ones

To analyze the case of positive eccentricity for the front bearings and negative for the posteriors ones (Figure 5.3) the complete model has been adopted, since there is no longer any geometric symmetry. As it is possible to observe in the Figure 5.31, the first form of instability continues to affect the lower stiffeners, involving both webs at the same time, given the symmetry with respect to the z-axis; however, the swelling is greater in the part above the bearing having positive eccentricity, since it would tend to become unstable first.
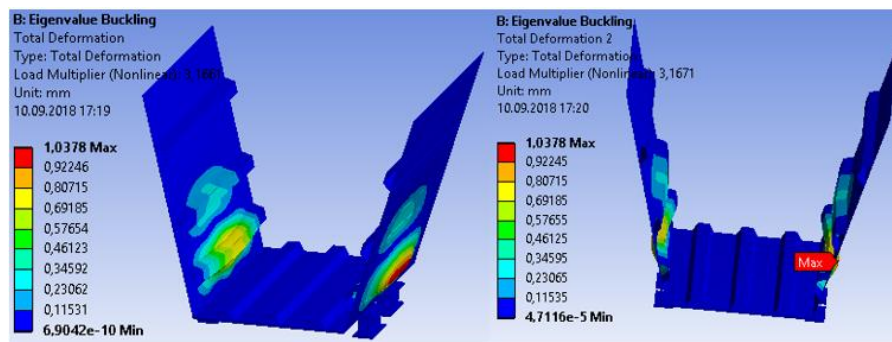
Figure 5.31: first buckling mode (test 2 modelling with positive eccentricity for the front bearings and negative eccentricity for the posteriors ones)

In fact, as a demonstration of this, one can appreciate in the Figure 5.32 how the second form of instability almost exclusively concerns the front constraints.
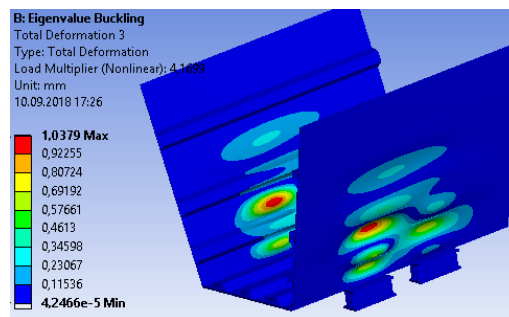
Figure 5.32: second buckling mode (test 2 modelling with positive eccentricity for the front bearings and negative eccentricity for the posteriors ones)

Having an uneven swelling in the form of instability means not assigning a homogeneous imperfection. In fact, the $15\ mm$ imperfection would be assigned only in the part above the constraint having positive eccentricity, while in the part above the constraints having negative eccentricity would be assigned a reduced imperfection.

In terms of results (Figure 5.33), the nonlinear analysis has lead to an increase in the value of F2 below the constraints with negative eccentricity; however, the analysis has led to a

significant reduction in the value of F2 below the constraints with positive eccentricity. This could be explained by the fact that the major deformation work is carried out by the constraints with negative eccentricity, which are so more loaded, partially unloading the constraints with positive eccentricity.
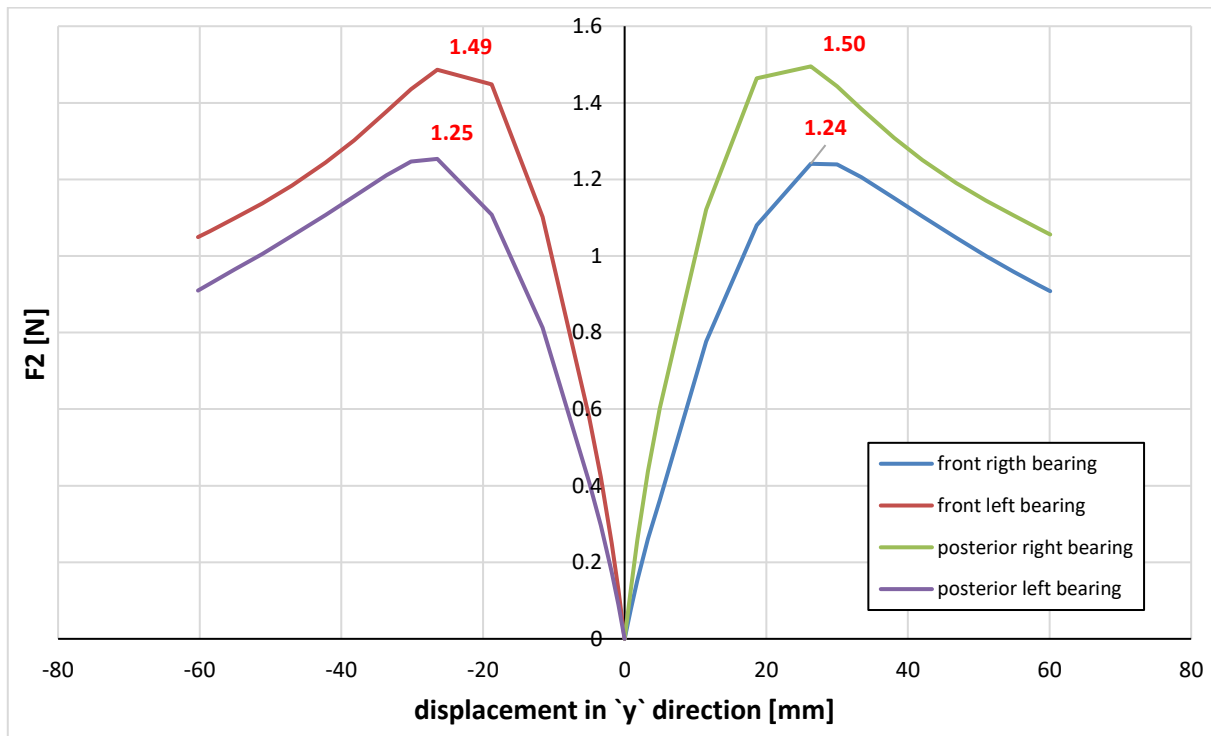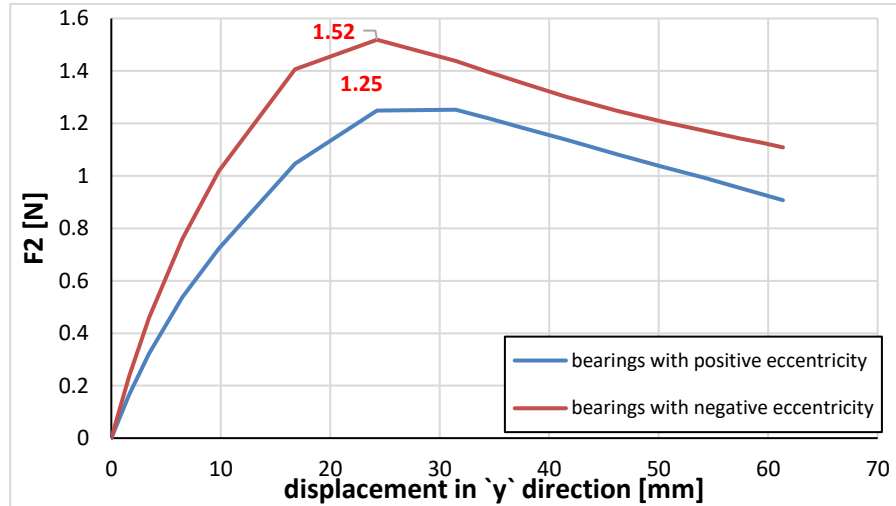

Figure 5.33: trend of the reaction F2 under the bearings (test 2 modelling with positive eccentricity for the front bearings and negative eccentricity for the posteriors ones)

5.2.4   Test 2: positive eccentricity for the front right bearing and the posterior left one, negative eccentricity for the front left bearing and posterior right one

The last case analyzed is that of positive eccentricity assigned to the anterior right and posterior left constraint and negative eccentricity assigned to the anterior left and posterior right bearing (Figure 5.4). As can be seen in the Figure 5.34, the first form of instability continues to affect the lower stiffeners, involving both webs at the same time given the polar symmetry; however, the swelling is greater in the part above the bearing having positive eccentricity, since it would tend to get unstable first.
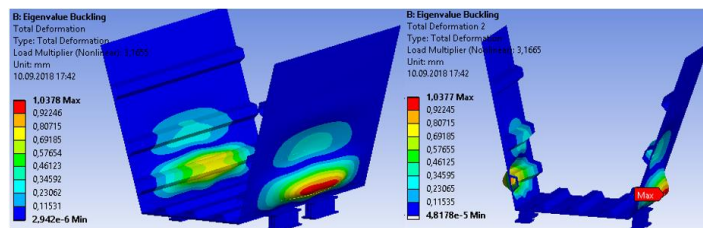
Figure 5.34: first buckling mode (test 2 modelling with positive eccentricity for the front right bearing and the posterior left one, negative eccentricity for the front left bearing and posterior right one)

In fact, as a demonstration of this, it can be appreciated in the Figure 5.35 how the second form of instability almost exclusively concerns the web above the bearings having a positive eccentricity.
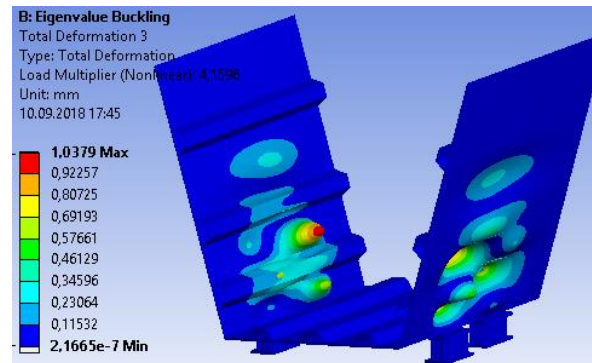
Figure 5.35: second buckling mode (test 1 modelling with positive eccentricity for the front right bearing and the posterior left one, negative eccentricity for the front left bearing and posterior right one)

Having an uneven swelling in the form of instability means not assigning a homogeneous imperfection. In fact, the 15 mm imperfection would be assigned only in the part above the bearings having positive eccentricity, while in the part above the bearings having negative eccentricity would be assigned a reduced imperfection.

The results extrapolated from the nonlinear analysis are very similar to those of the previous chapter (Figure 5.36) (5.2.3).
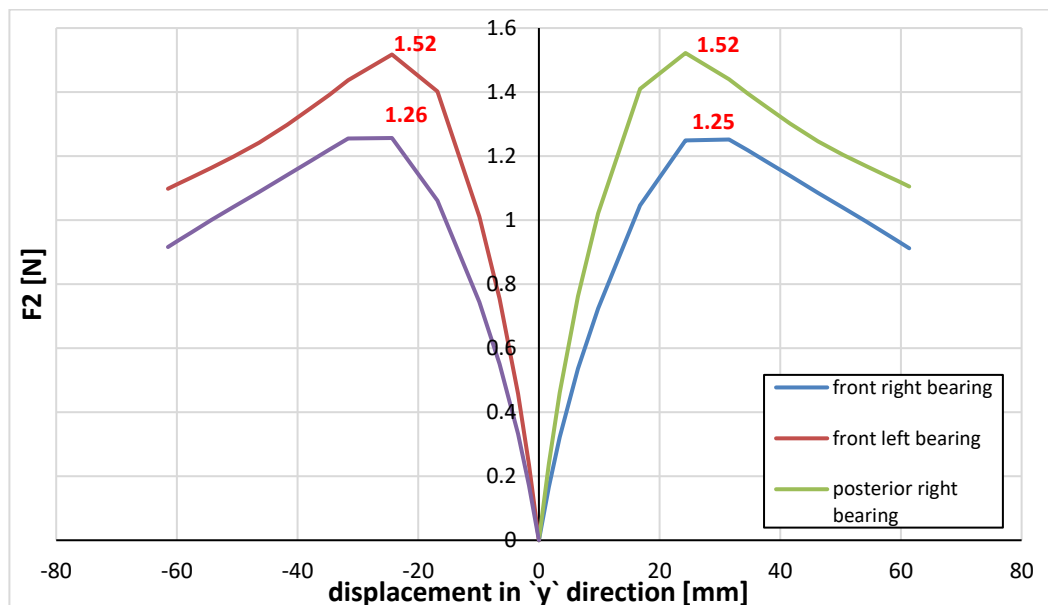
Figure 5.36: trend of the reaction F2 under the bearings (test 2 modelling with positive eccentricity for the front right bearing and the posterior left one, negative eccentricity for the front left bearing and posterior right one)

5.3 Test 3: analysis with eccentricity

Test 3 is re-analyzed by combining different types of eccentricity and as already done for the cases without eccentricity, two cases were analyzed: one in which the height of the stiffeners running along the bottom flange was also changed to 65 mm; one in which the height of these stiffeners was maintained at 125 mm.

5.3.1 Test 3: positive/negative eccentricity for all the bearings and h_{stb} = 65 mm

Considering the same system of forces already used in chapter 3.3.1, the influence of a possible decentralization of the bearings as in the Figure 5.1 has been analyzed.

As can be seen in Figure 5.36, even in the case of a positive eccentricity of 30 mm, the first buckling mode continues to affect the lower stiffeners, with a slightly lower load multiplication factor than in the case of zero eccentricity (chapter 3.3.2). Moreover, already in correspondence with the first buckling mode, part of the lower plate becomes unstable, due to the high compression induced by the rotation of the reaction (see chapter 5.1.1). The instability also occurs due to the reduced stiffness of the longitudinal stiffeners.
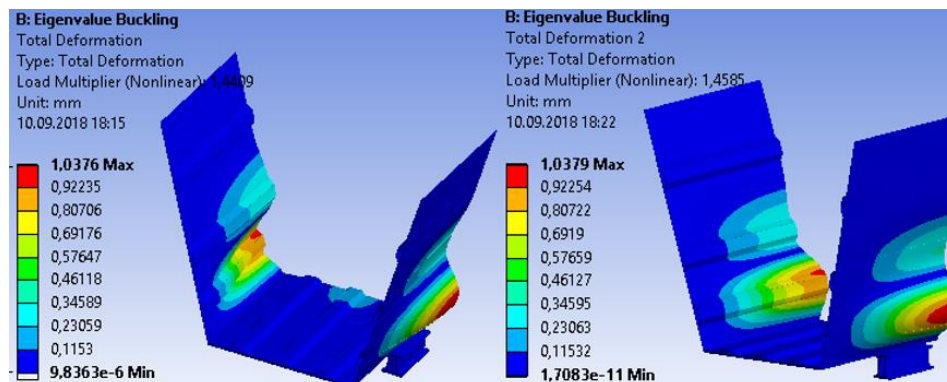
Figure 5.37: first buckling mode (test 3 modelling with positive eccentricity of 30 mm and with h_{stb} =65 mm)

As far as the nonlinear analysis is concerned, the iteration of the F2 load led to a value equal to 0,934 MN, about 1.4% lower than in the case of absence of eccentricity (0,947 MN), for the same reasons already explained in chapter 5.1.1.

Considering the negative eccentricity, again the first buckling mode occurs in correspondence of the lower stiffeners (Figure 5.38), with a slightly higher load multiplication factor than in the case of zero eccentricity (chapter 3.3.2).
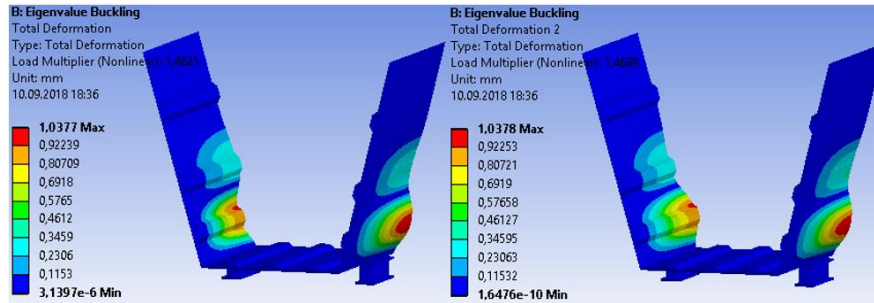
Figure 5.38: first buckling mode (test 3 modelling with negative eccentricity of 30 mm and with hstb =65 mm)

Moreover, compared to the case of positive eccentricity (Figure 5.37), the buckling of the bottom plate occurs at the second form of instability (Figure 5.39); this is due to the presence of the plate which, by reducing the rotation of the constraint and therefore also of the bonding reaction, is subject to a state of lesser compression (see chapter 5.1.1).
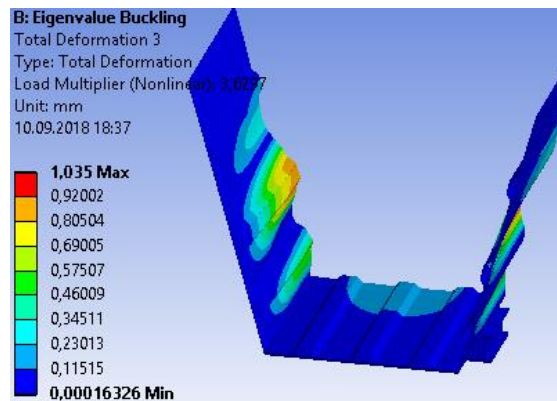
Figure 5.39: second buckling mode (test 3 modelling with negative eccentricity of 30 mm and with hstb =65 mm)

As far as the nonlinear analysis is concerned, it provided a value of F2 equal to $0,953 \, MN$, about 0,63% higher than in the case of absence of eccentricity, for the same reasons already explained in chapter 5.1.1.

The comparison between the various cases is shown below (Figure 5.40).
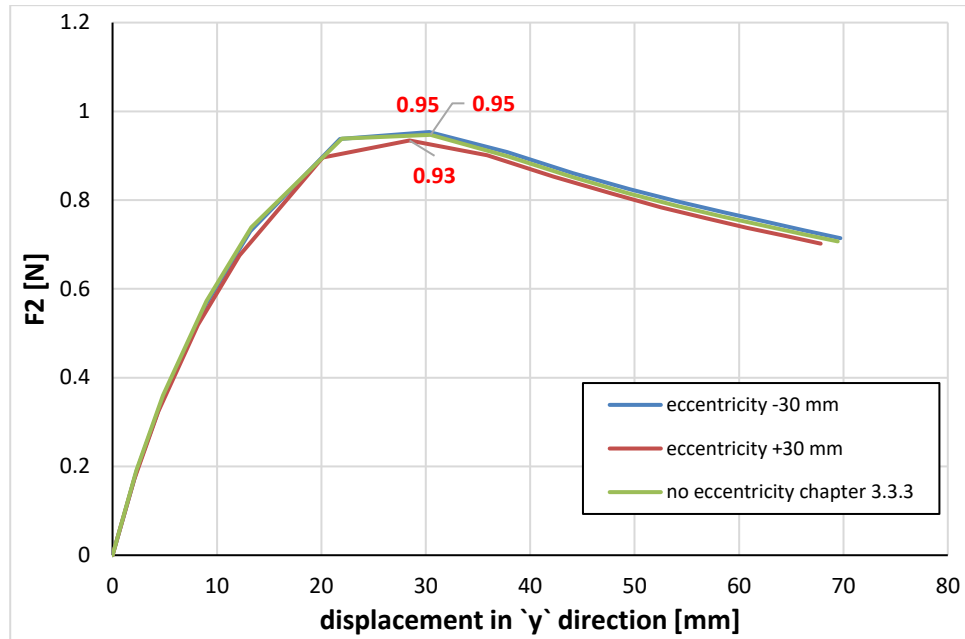
Figure 5.40: comparison between the various cases (test 3 modelling with hstb = 65mm)

5.3.2 Test 3: positive eccentricity for the constraints placed in sector y > 0 and negative for those placed in sector y < 0 and h$_{stb}$ = 65mm

Considering the same system of forces already used in chapter 3.3, the influence of a possible decentralization of the constraints as in the figure (Figure 5.2) has been analyzed.

As can be seen in the Figure 5.41, the first two form of instabilities affect the lower stiffeners, but compared to the previous cases, the instability no longer occurs simultaneously in the two webs, but involves first the web that rests on the bearing that has positive eccentricity and after the web that rests on the bearing with negative eccentricity.
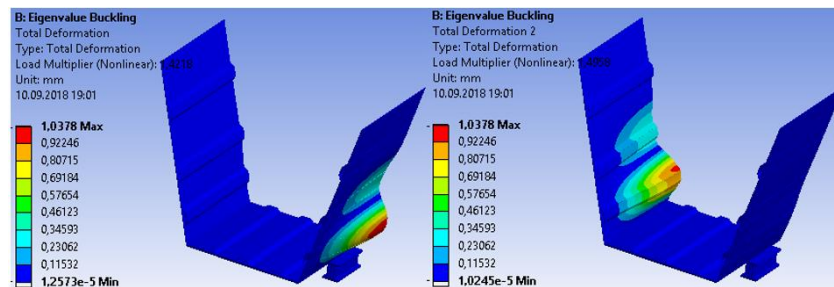
Figure 5.41: first and second buckling modes (test 3 modelling with positive eccentricity for the constraints placed in sector y>0 and negative for those placed in sector y<0 and h$_{stb}$ = 65mm)

111

The first two forms of instability were therefore considered as predeformations for nonlinear analysis in order to distribute the geometric imperfections on both webs.

The F2 values (Figure 5.42, Figure 5.43), as expected, are not very different from those obtained previously (chapter 5.3.1).
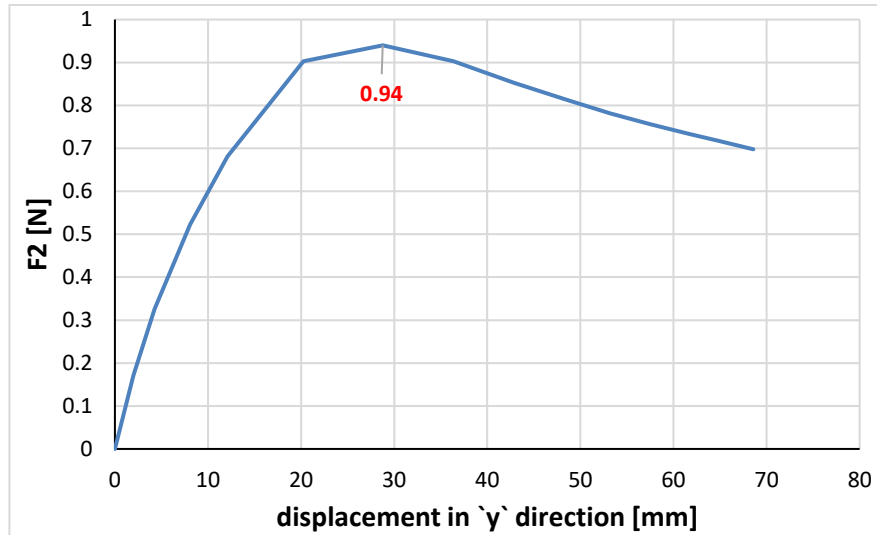
Figure 5.42: trend of the reaction F2 under the bearing with positive eccentricity (test 3 modelling with hstb = 65mm)
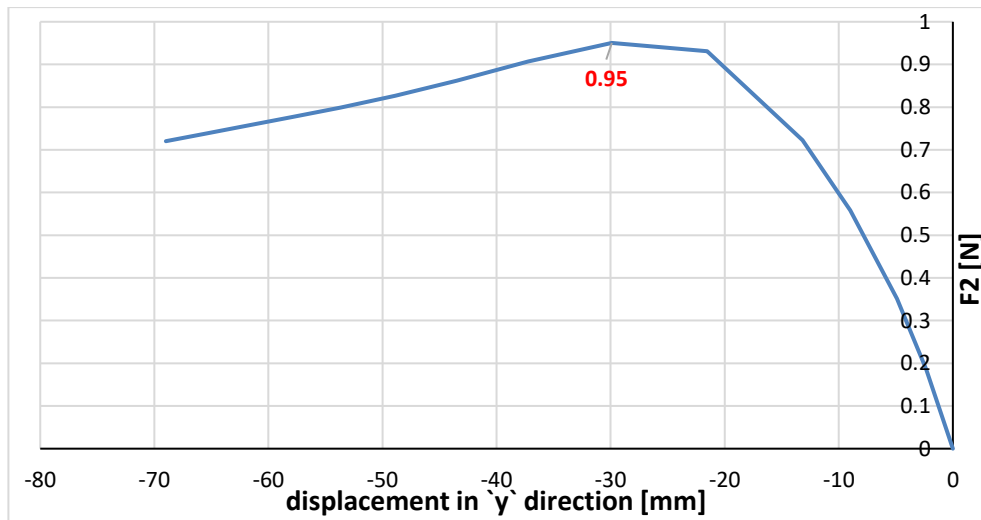
Figure 5.43: trend of the reaction F2 under the bearing with negative eccentricity (test 3 modelling with h_{stb} = 65mm)

Probably the slight difference is due to the combination of the two forms of instability to generate the imperfections.

5.3.3   Test 3: positive eccentricity for the front bearings and negative eccentricity for the posteriors ones and h$_{stb}$ = 65mm

To analyze the case of positive eccentricity for the front bearings and negative for the posteriors ones (Figure 5.3) the complete model has been adopted, since there is no longer any geometric symmetry. As it is possible to observe in the Figure 5.31, the first form of instability continues to affect the lower stiffeners, involving both webs at the same time, given the symmetry with respect to the *z*-axis; however, compared to what has been seen in paragraphs 5.1.3 and 5.2.3, the web is unstable especially in the central area of the lower stiffeners, due to their low resistance contribution.
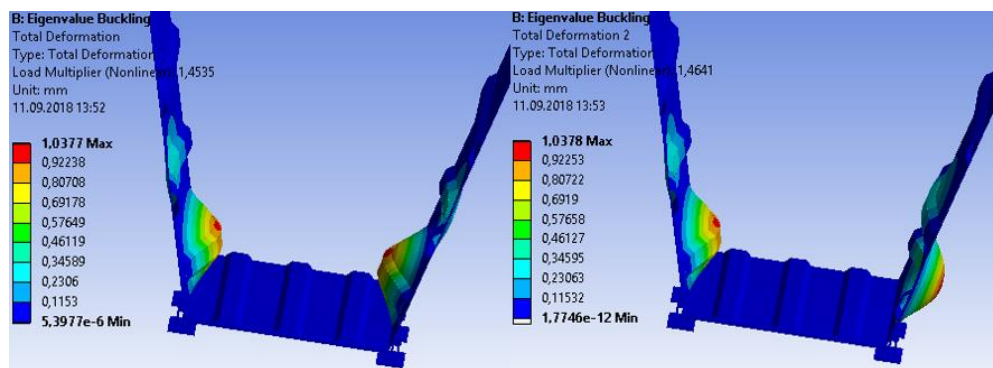
Figure 5.44: first buckling mode (test 3 modelling with positive eccentricity for the front bearings and negative eccentricity for the posteriors ones and h$_{stb}$ = 65mm)

The instability of the lower plate already occurs at the second form of instability and the affected area is shifted towards the constraints with positive eccentricity, since, as explained in chapter 5.1.1, the counterclockwise rotation of the reaction involves high compressive forces in the flange (Figure 5.45).
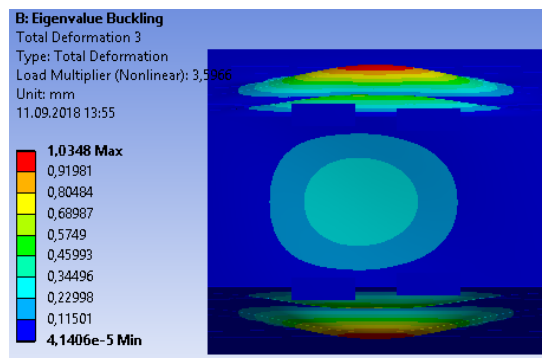
Figure 5.45: first buckling mode (test 3 modelling with positive eccentricity for the front bearings and negative eccentricity for the posteriors ones and h$_{stb}$ = 65mm)

In this case (Figure 5.46), compared to what has been seen in chapters 5.1.3 and 5.2.3, the distribution of imperfections would be uniform. However, the nonlinear analyses led to an increase of about 6% in the final value of F2 below the constraints with negative eccentricity

and a decrease of about 6% in the final value of F2 below the constraints with positive eccentricity. The percentages refer to the values reported in chapter 5.3.1.

This could be explained by the fact that the major deformation work is carried out by the constraints with negative eccentricity, which are so more loaded, partially unloading the constraints with positive eccentricity.
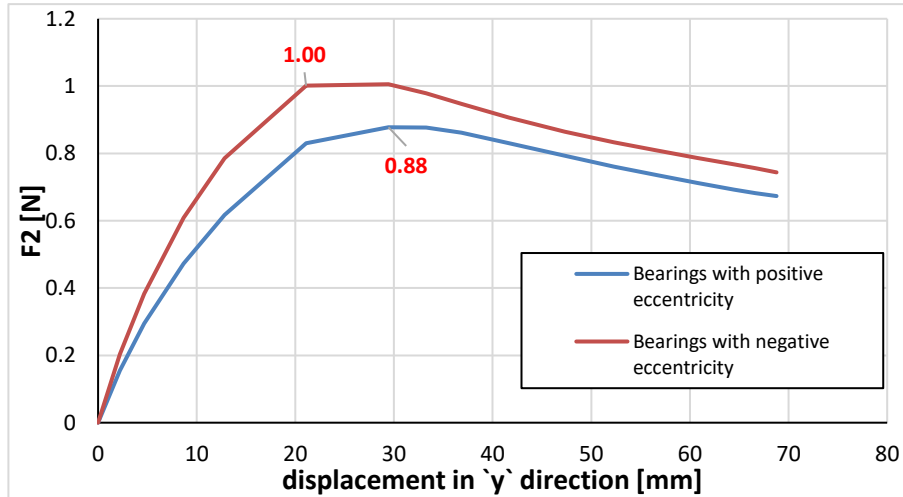
Figure 5.46: trend of the reaction F2 under the bearings (test 3 modelling with positive eccentricity for the front bearings and negative eccentricity for the posteriors ones and h_{stb} = 65mm)

This demonstrates that the spatial distribution of constraints has a significant impact on overall behaviour.

5.3.4 Test 3: positive eccentricity for the front right bearing and the posterior left one, negative eccentricity for the front left bearing and posterior right one and $h_{stb} = 65mm$

The last case analyzed is that of positive eccentricity assigned to the anterior right and posterior left constraint and negative eccentricity assigned to the anterior left and posterior right bearing (Figure 5.4). As can be seen in the Figure 5.47, the first form of instability continues to affect the lower stiffeners, involving both webs at the same time given the polar symmetry. However, compared to what has been seen in paragraphs 5.1.4 and 5.2.4, the web is unstable especially in the central area of the lower stiffeners, due to their low resistance contribution.
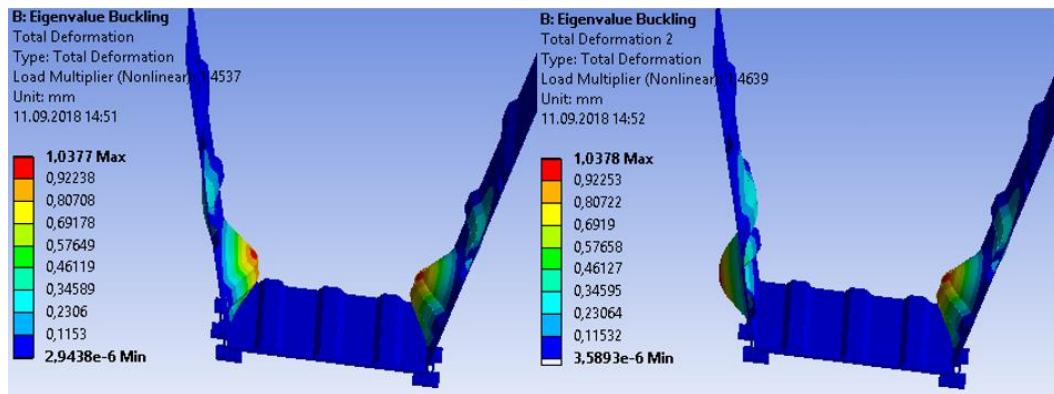
Figure 5.47: first buckling mode (test 3 modelling with positive eccentricity for the front right bearing and the posterior left one, negative eccentricity for the front left bearing and posterior right one and hstb = 65mm)

The instability of the lower plate already occurs at the second form of instability and the affected the central area, in particular along the direction of the bearings with positive eccentricity (Figure 5.48).
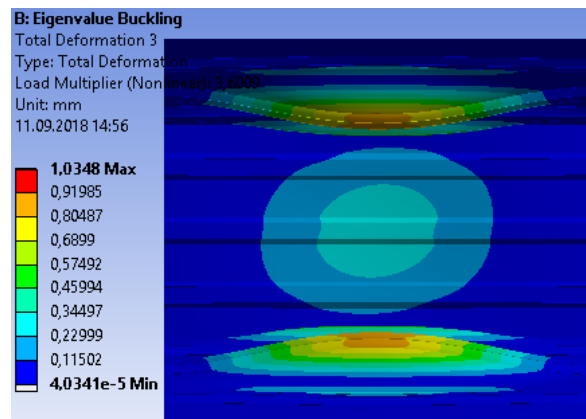
Figure 5.48: second buckling mode (test 3 modelling with positive eccentricity for the front right bearing and the posterior left one, negative eccentricity for the front left bearing and posterior right one and hstb = 65mm)

115

The nonlinear analysis has led to results very close to those of the chapter 5.3.3 (Figure 5.49).

Figure 5.49: trend of the reaction F2 under the bearings (test 3 modelling with positive eccentricity for the front right bearing and the posterior left one, negative eccentricity for the front left bearing and posterior right one and h_{stb} = 65mm)

5.3.5   Test 3: positive/negative eccentricity for all the bearings and h_{stb} = 125 mm

Considering the same system of forces already used in chapter 3.3.4, the influence of a possible decentralization of the bearings as in the Figure 5.1 has been analyzed.

As can be seen in Figure 5.50, even in the case of a positive eccentricity of 30 mm, the first buckling mode continues to affect the lower stiffeners, with a slightly lower load multiplication factor than in the case of zero eccentricity (chapter 3.3.5).
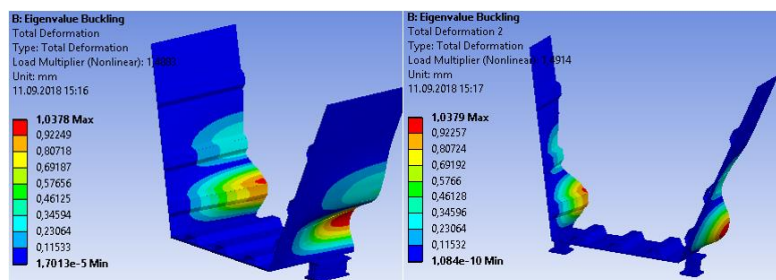
Figure 5.50: first buckling mode (test 3 modelling with positive eccentricity of 30 mm and with h_{stb} =125 mm)

In addition, the bottom flange only becomes unstable to the fourth buckling mode (Figure 5.51), given the greater resistant contribution of stiffeners compared to the previous case (see chapter 5.3.1).
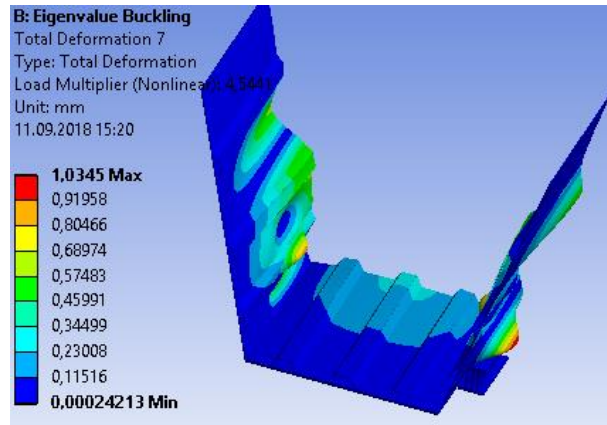
Figure 5.51: fourth buckling mode (test 3 modelling with positive eccentricity of 30 mm and with h_{stb} =125 mm)

As far as the nonlinear analysis is concerned, the iteration of the F2 load led to a value equal to 0,976 *MN*, about 2,0 % lower than in the case of absence of eccentricity (0,996 *MN*), for the same reasons already explained in chapter 5.1.1.

Considering the negative eccentricity, again the first buckling mode occurs in correspondence of the lower stiffeners (Figure 5.52), with a slightly higher load multiplication factor than in the case of zero eccentricity (chapter 3.3.5).
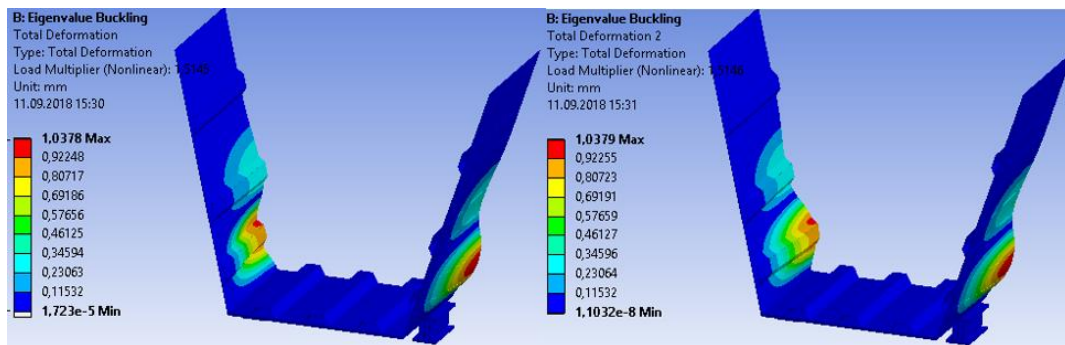
Figure 5.52: first buckling mode (test 3 modelling with negative eccentricity of 30 mm and with hstb =125 mm)

As far as the nonlinear analysis is concerned, it provided a value of F2 equal to 1,01 *MN*, about 1,8% higher than in the case of absence of eccentricity, for the same reasons already explained in chapter 5.1.1.

The comparison between the various cases is shown below (Figure 5.53).
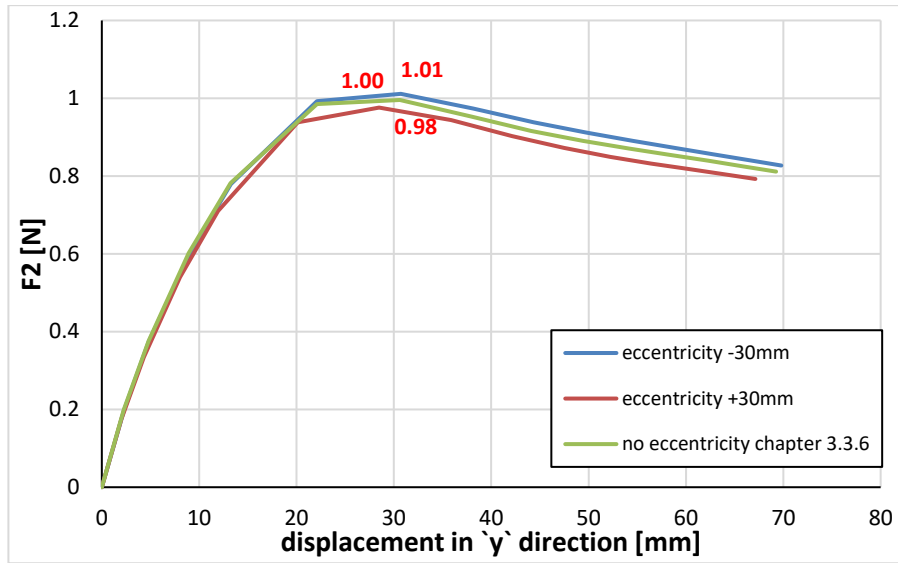
Figure 5.53: comparison between the various cases (test 3 modelling with hstb = 125mm)

5.3.6 Test 3: positive eccentricity for the constraints placed in sector y > 0 and negative for those placed in sector y < 0 and h_{stb} = 125mm

Considering the same system of forces already used in chapter 3.3, the influence of a possible decentralization of the constraints as in the figure (Figure 5.2) has been analyzed.

As can be seen in the Figure 5.54, the first two form of instabilities affect the lower stiffeners, but compared to the previous cases, the instability no longer occurs simultaneously in the two webs, but involves first the web that rests on the bearing that has positive eccentricity and after the web that rests on the bearing with negative eccentricity.
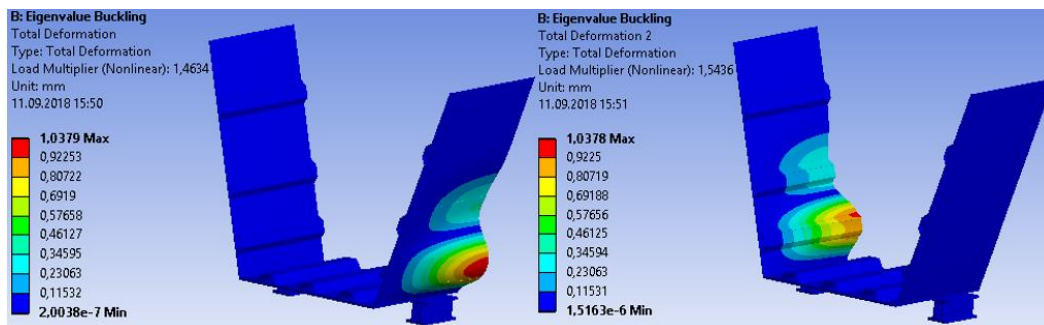
Figure 5.54: first and second buckling modes (test 3 modelling with positive eccentricity for the constraints placed in sector y>0 and negative for those placed in sector y<0 and h_{stb} = 125mm)

The first two forms of instability were therefore considered as predeformations for nonlinear analysis in order to distribute the geometric imperfections on both webs.

The F2 values (Figure 5.55, Figure 5.56), as expected, are not very different from those obtained previously (chapter 5.3.5).
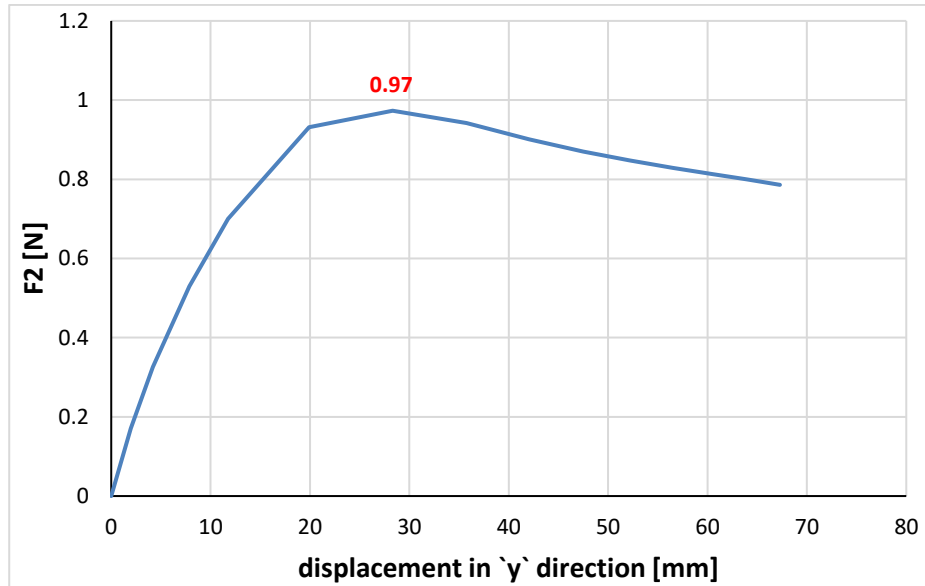
Figure 5.55: trend of the reaction F2 under the bearing with positive eccentricity (test 3 modelling with $h_{stb} = 125mm$)
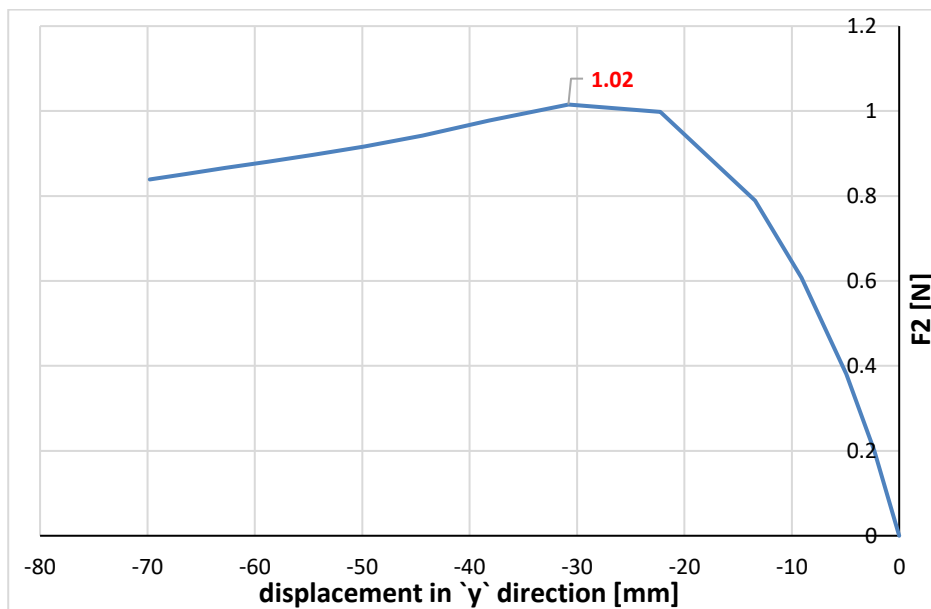
Figure 5.56: trend of the reaction F2 under the bearing with negative eccentricity (test 3 modelling with $h_{stb} = 125mm$)

5.3.7 Test 3: positive eccentricity for the front bearings and negative eccentricity for the posteriors ones and h_{stb} = 125mm

To analyze the case of positive eccentricity for the front bearings and negative for the posteriors ones (Figure 5.3) the complete model has been adopted, since there is no longer any geometric symmetry. As it is possible to observe in the Figure 5.57, the first form of instability continues to affect the lower stiffeners, involving both webs at the same time, given the symmetry with respect to the z-axis; however, compared to what has been seen in paragraphs 5.1.3 and 5.2.3, the web is unstable especially in the central area of the lower stiffeners, due to their low resistance contribution.
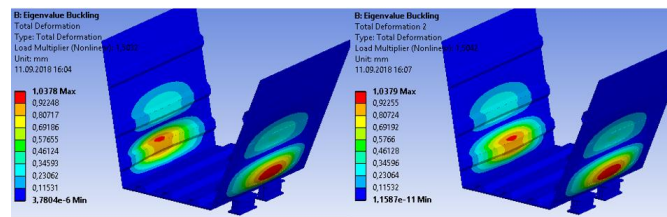
Figure 5.57: first buckling mode (test 3 modelling with positive eccentricity for the front bearings and negative eccentricity for the posteriors ones and h_{stb} = 125mm)

The nonlinear analyses led to an increase of about 6,5% in the final value of F2 below the constraints with negative eccentricity and a decrease of about 7,8% in the final value of F2 below the constraints with positive eccentricity (Figure 5.58). The percentages refer to the values reported in chapter 5.3.5. This could be explained by the fact that the major deformation work is carried out by the constraints with negative eccentricity, which are so more loaded, partially unloading the constraints with positive eccentricity.
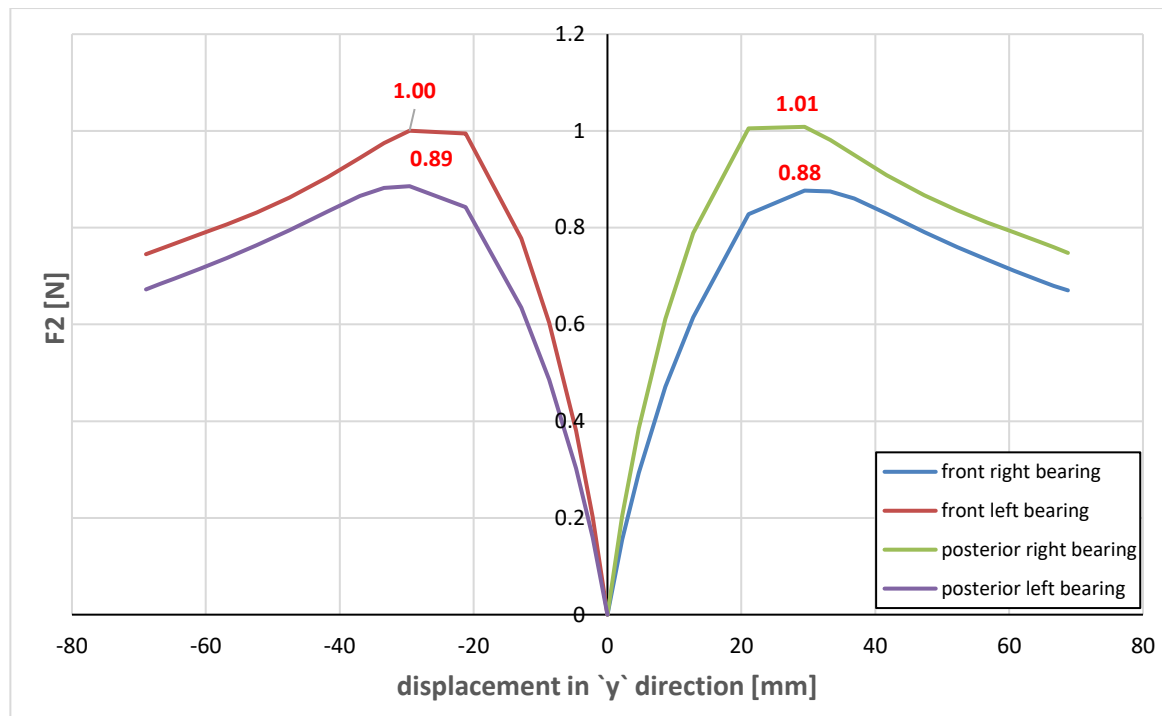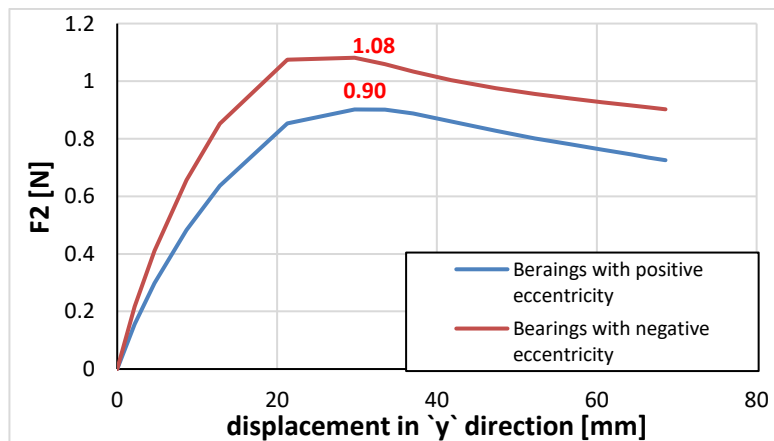

Figure 5.58: trend of the reaction F2 under the bearings (test 3 modelling with positive eccentricity for the front bearings and negative eccentricity for the posteriors ones and h_{stb} = 125mm)

5.3.8 Test 3: positive eccentricity for the front right bearing and the posterior left one, negative eccentricity for the front left bearing and posterior right one and $h_{stb} = 125mm$

The last case analyzed is that of positive eccentricity assigned to the anterior right and posterior left constraint and negative eccentricity assigned to the anterior left and posterior right bearing (Figure 5.4). As can be seen in the Figure 5.59, the first form of instability continues to affect the lower stiffeners, involving both webs at the same time given the polar symmetry. However, compared to what has been seen in paragraphs 5.1.4 and 5.2.4, the web is unstable especially in the central area of the lower stiffeners, due to their low resistance contribution.

Figure 5.59: first buckling mode (test 3 modelling with positive eccentricity for the front right bearing and the posterior left one, negative eccentricity for the front left bearing and posterior right one and hstb = 125mm)

The nonlinear analysis led to results very close to those of the chapter 5.3.7 (Figure 5.60).

Figure 5.60: trend of the reaction F2 under the bearings (test 3 modelling with positive eccentricity for the front right bearing and the posterior left one, negative eccentricity for the front left bearing and posterior right one and $h_{stb} = 125mm$)

5.4 Test 4: analysis with eccentricity

Test 2 is re-analyzed by combining different types of eccentricity.

5.4.1 Test 4: positive/negative eccentricity for all the bearings

Considering the same system of forces already used in chapter 3.4, the influence of a possible decentralization of the bearings as in the Figure 5.1 has been analyzed.

As can be seen in Figure 5.61, even in the case of a positive eccentricity of 30 mm, the first buckling mode continues to affect the lower stiffeners, with a slightly lower load multiplication factor than in the case of zero eccentricity (chapter 3.4.2).
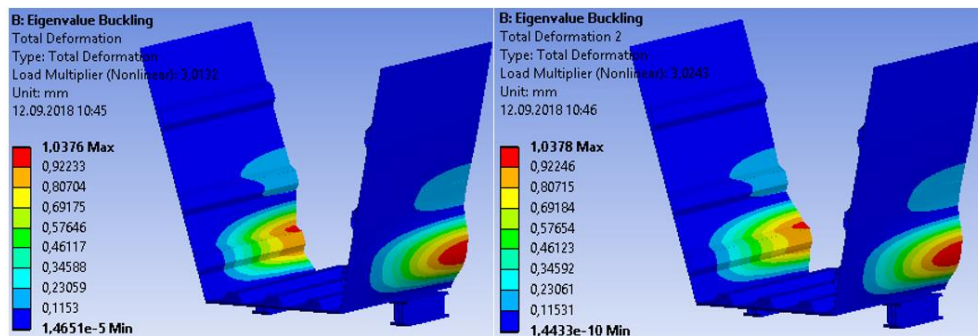
Figure 5.61: first buckling mode (test 4 modelling with positive eccentricity of 30 mm)

As far as the nonlinear analysis is concerned, the iteration of the F2 load led to a value equal to 0,953 MN, about 2,9% lower than in the case of absence of eccentricity (0,981 MN), for the same reasons already explained in chapter 5.1.1.

Considering the negative eccentricity, again the first buckling mode occurs in correspondence of the lower stiffeners (Figure 5.62), with a slightly higher load multiplication factor than in the case of zero eccentricity (chapter 3.4.2).
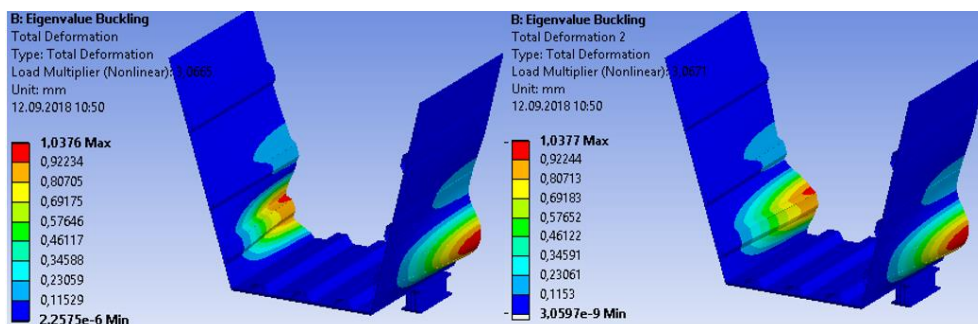
Figure 5.62: first buckling mode (test 4 modelling with negative eccentricity of 30 mm)

As far as the nonlinear analysis is concerned, it provided a value of F2 equal to 0,993 *MN*, about 1,2% higher than in the case of absence of eccentricity, for the same reasons already explained in chapter 5.1.1.

The comparison between the various cases is shown below (Figure 5.63).
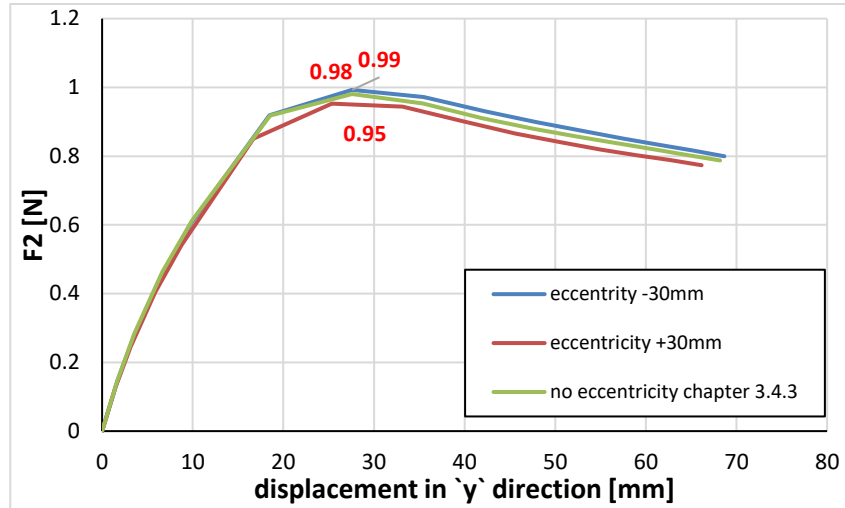
Figure 5.63: comparison between the various cases (test 4 modelling)

5.4.2   Test 4: positive eccentricity for the constraints placed in sector y > 0 and negative for those placed in sector y < 0

Considering the same system of forces already used in chapter 3.4, the influence of a possible decentralization of the constraints as in the figure (Figure 5.2) has been analyzed.

As can be seen in the Figure 5.64, the first two form of instabilities affect the lower stiffeners, but compared to the previous cases, the instability no longer occurs simultaneously in the two webs, but involves first the web that rests on the bearing that has positive eccentricity and after the web that rests on the bearing with negative eccentricity.
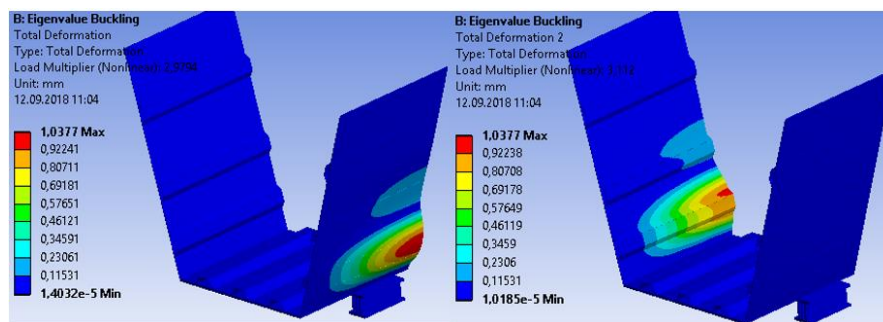
Figure 5.64: first and second buckling modes (test 2 modelling with positive eccentricity for the constraints placed in sector y>0 and negative for those placed in sector y<0)

The first two forms of instability were therefore considered as predeformations for nonlinear analysis in order to distribute the geometric imperfections on both webs.

The F2 values (Figure 5.65, Figure 5.66), as expected, are not very different from those obtained previously (chapter 5.4.1).
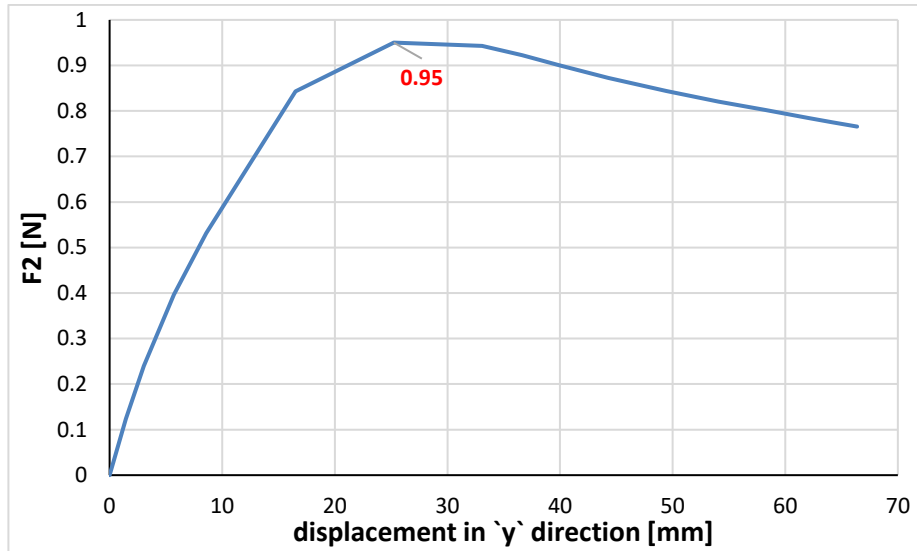
Figure 5.65: trend of the reaction F2 under the bearing with positive eccentricity (test 4 modelling)
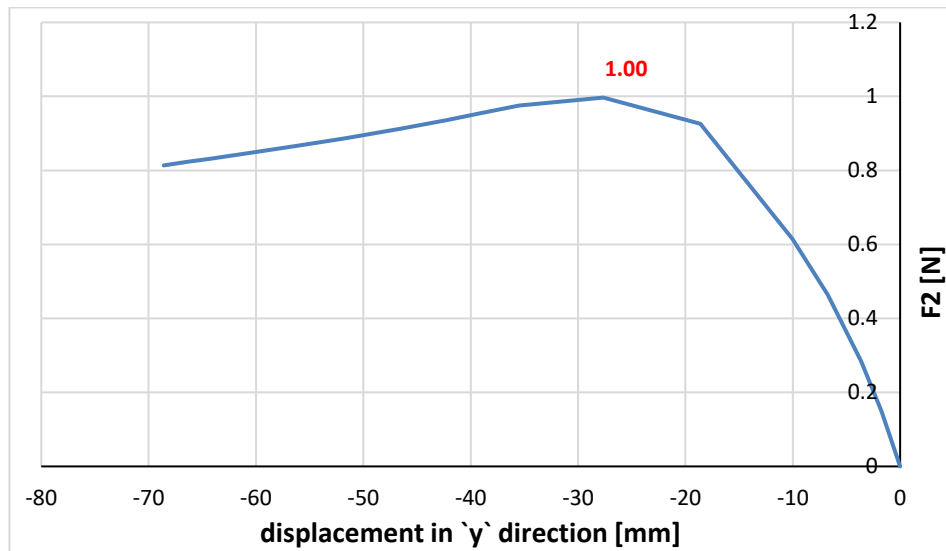
Figure 5.66: trend of the reaction F2 under the bearing with negative eccentricity (test 4 modelling)

5.4.3 Test 4: positive eccentricity for the front bearings and negative eccentricity for the posteriors ones

As it is possible to observe in the Figure 5.67, the first form of instability continues to affect the lower stiffeners, involving both webs at the same time, given the symmetry with respect to the z-axis; however, compared to what has been seen in paragraphs 5.1.3 and 5.2.3, the web is unstable especially in the central area of the lower stiffeners, due to their low resistance contribution.
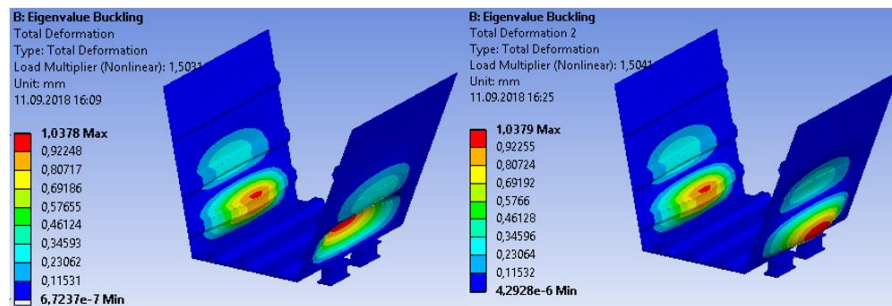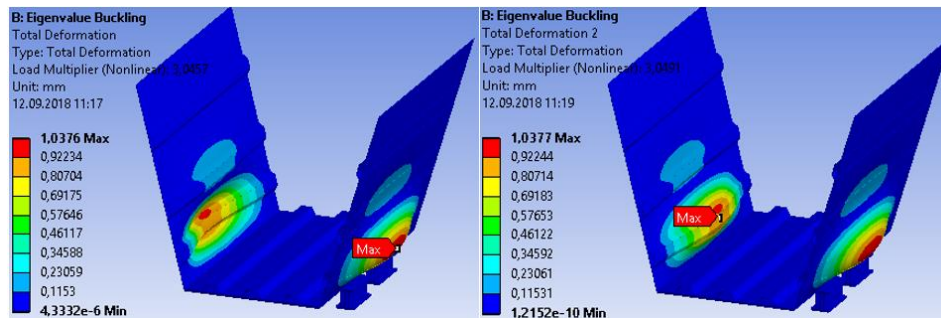

Figure 5.67: first buckling mode (test 4 modelling with positive eccentricity for the front bearings and negative eccentricity for the posteriors ones)

The nonlinear analyses led to an increase of about 7,5% in the final value of F2 below the constraints with negative eccentricity and a decrease of about 7,7% in the final value of F2 below the constraints with positive eccentricity Figure 5.68. The percentages refer to the values reported in chapter 5.4.1. This could be explained by the fact that the major deformation work is carried out by the constraints with negative eccentricity, which are so more loaded, partially unloading the constraints with positive eccentricity.
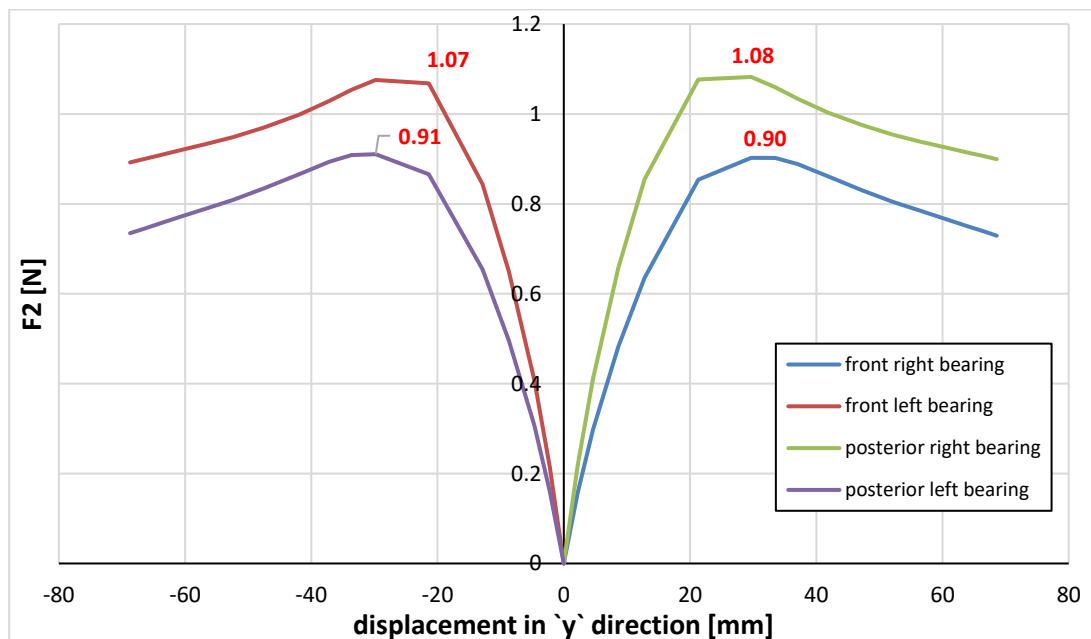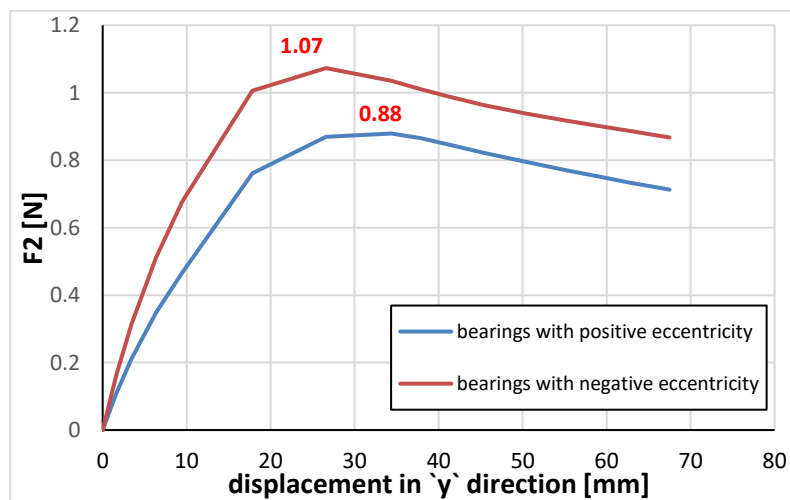

Figure 5.68: trend of the reaction F2 under the bearings (test 4 modelling with positive eccentricity for the front bearings and negative eccentricity for the posteriors ones)

5.4.4 Test 4: positive eccentricity for the front right bearing and the posterior left one, negative eccentricity for the front left bearing and posterior right one

The last case analyzed is that of positive eccentricity assigned to the anterior right and posterior left constraint and negative eccentricity assigned to the anterior left and posterior right bearing (Figure 5.4). As can be seen in the Figure 5.69, the first form of instability continues to affect the lower stiffeners, involving both webs at the same time given the polar symmetry. However, compared to what has been seen in paragraphs 5.1.4 and 5.2.4, the web is unstable especially in the central area of the lower stiffeners, due to their low resistance contribution.
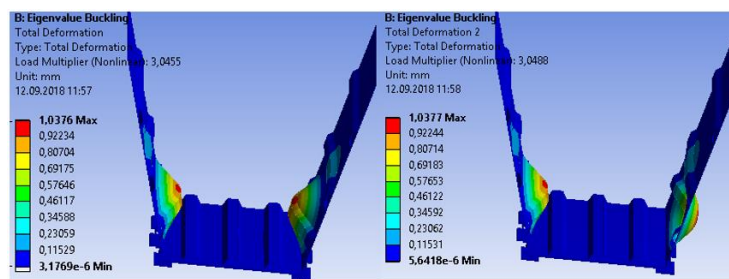
Figure 5.69: first buckling mode (test 4 modelling with positive eccentricity for the front right bearing and the posterior left one, negative eccentricity for the front left bearing and posterior right one)

The nonlinear analysis as expected led to results very close to those of the chapter 5.4.3 (Figure 5.70).
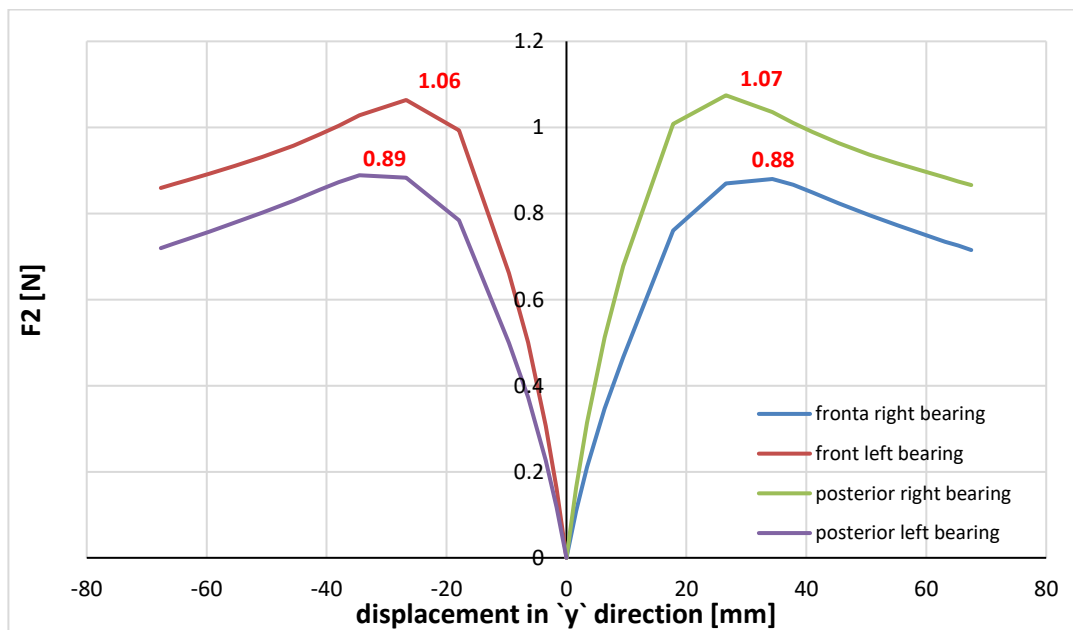
Figure 5.70: trend of the reaction F2 under the bearings (test 2 modelling with positive eccentricity for the front right bearing and the posterior left one, negative eccentricity for the front left bearing and posterior right one)

6. ECCENTRICITY INFLUENCE: ELASTOMERIC BEARINGS

As already discussed in the previous chapter, the following chapter deals with the influence of possible load shifting on section instability. The same combinations "position of the bearings - section" (Figure 5.1, Figure 5.2, Figure 5.3, Figure 5.4) have been adopted, considering however no longer the rigid constraint, but the elastomeric one (Figure 2.20), which rests on the thrust bearing with single exhaust.

As for the structure of the analysis, nothing has changed, in fact, the problem has been split into three parts: linear static analysis, linear buckling analysis, and nonlinear analysis at large displacements [10] (see chapters 2.2.1 and 3).

6.1 Test 1: analysis with eccentricity

Considering the different eccentricities of the constraints with respect to the section, the nonlinear analysis has led to results that are not very different with respect to the case of absence of eccentricities (chapter 4.1). This is probably due to the impossibility of the constraint to rotate around the x-axis, and to the high stiffness of the elastomer (schematized by springs); consequently, the torque moment generated by the eccentric load does not act on the web and on the bottom flange, but is absorbed directly by the bearing.

The trends of the force F2 in case of eccentricity are shown below (Figure 6.1, Figure 6.2, Figure 6.3, Figure 6.4). Worth noting is that, only in case of mixed eccentricities along the same web, there is an increment of the value F2 under the bearings with negative eccentricity and a decrement under the bearings with positive eccentricity (Figure 6.3, Figure 6.4). This is due to the possibility of the upper steel plate that closes the elastomer to rotate. In fact fixing the rotation of the top plate around the x and z axis, the same value as the case of no eccentricity is again obtained (Figure 6.5, Figure 6.6).

Figure 6.1: test 1 - positive/negative eccentricity for all the bearings

Figure 6.2: test 1 - positive eccentricity for the constraints placed in sector y > 0 and negative for those placed in sector y < 0

Figure 6.3: Test 1 - positive eccentricity for the front bearings and negative eccentricity for the posteriors ones

Figure 6.4: Test 1 - positive eccentricity for the front right bearing and the posterior left one, negative eccentricity for the front left bearing and posterior right one

Figure 6.5: Test 1 - positive eccentricity for the front bearings and negative eccentricity for the posteriors ones (no rotation of the of the upper plate around the x and z axis)

Figure 6.6: Test 1 - positive eccentricity for the front right bearing and the posterior left one, negative eccentricity for the front left bearing and posterior right one (no rotation of the of the upper plate around the x and z axis)

6.2   Test 2: analysis with eccentricity

Considering the different eccentricities of the constraints with respect to the section, the nonlinear analysis has led to results that are not very different with respect to the case of absence of eccentricities (chapter 4.2). This is probably due to the same reasons already explained in the chapter 6.1. Below are reported the trends of the force F2 in case of eccentricity (Figure 6.7, Figure 6.8, Figure 6.9, Figure 6.10). Worth noting is that, only in case of mixed eccentricities along the same web, there is an increment of the value F2 under the bearings with negative eccentricity and a decrement under the bearings with positive eccentricity (Figure 6.11, Figure 6.12). This is due to the possibility of the upper steel plate that closes the elastomer to rotate. In fact fixing the rotation of the top plate around the x and z axis, the same value as the case of no eccentricity is again obtained (Figure 6.9, Figure 6.10).

Figure 6.7: test 2 - positive/negative eccentricity for all the bearings

Figure 6.8: test 2 - positive eccentricity for the constraints placed in sector y > 0 and negative for those placed in sector y < 0

The difference is due to the combination of the two forms of instability to generate the imperfections.

Figure 6.9: Test 2 - positive eccentricity for the front bearings and negative eccentricity for the posteriors ones

Figure 6.10: Test 2 - positive eccentricity for the front right bearing and the posterior left one, negative eccentricity for the front left bearing and posterior right one

Figure 6.11: Test 2 - positive eccentricity for the front bearings and negative eccentricity for the posteriors ones (no rotation of the of the upper plate around the x and z axis)

Figure 6.12: Test 2 - positive eccentricity for the front right bearing and the posterior left one, negative eccentricity for the front left bearing and posterior right one (no rotation of the of the upper plate around the x and z axis)

6.3   Test 3: analysis with eccentricity and $h_{stb} = 65mm$

Considering the different eccentricities of the constraints with respect to the section, the nonlinear analysis has led to results that are not very different with respect to the case of absence of eccentricities (chapter 4.3.1). This is probably due to the same reasons already explained in the chapter 6.1. Below are reported the trends of the force F2 in case of eccentricity (Figure 6.13, Figure 6.14, Figure 6.15, Figure 6.16). Worth noting is that, only in case of mixed eccentricities along the same web, there is an increment of the value F2 under the bearings with negative eccentricity and a decrement under the bearings with positive eccentricity (Figure 6.15, Figure 6.16). This is due to the possibility of the upper steel plate that closes the elastomer to rotate. In fact fixing the rotation of the top plate around the x and z axis, the same value as the case of no eccentricity is again obtained (Figure 6.17, Figure 6.18).
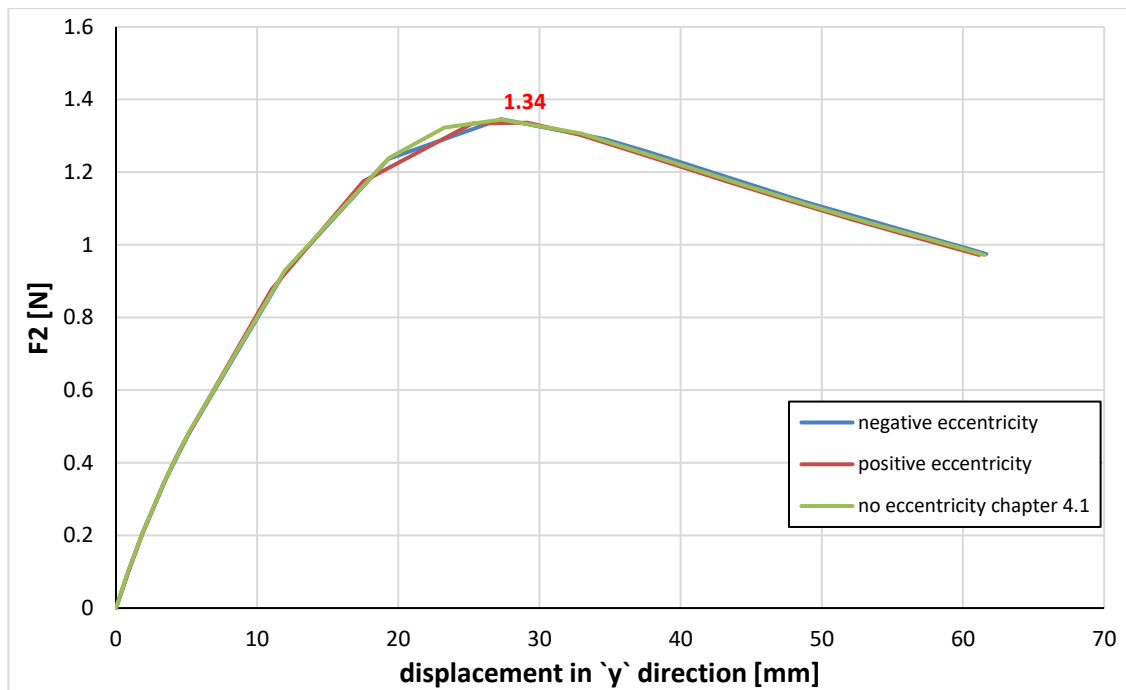
Figure 6.13: test 3 with h_{stb} = 65mm - positive/negative eccentricity for all the bearings

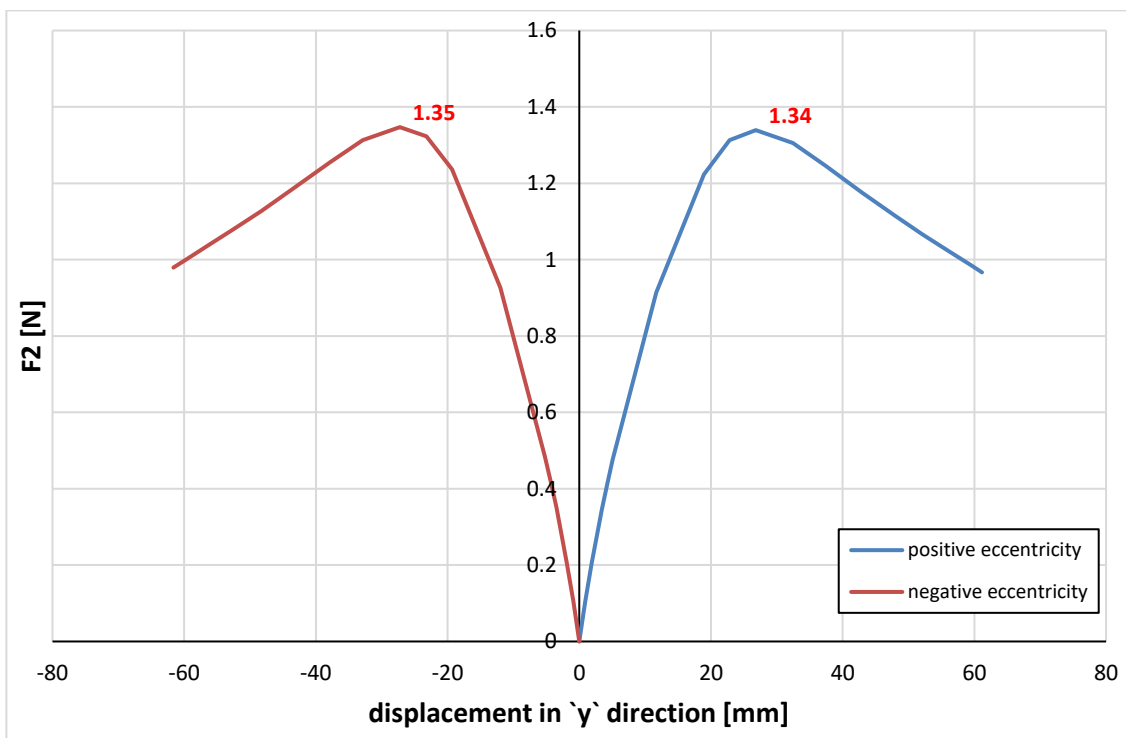*Figure 6.14: test 3 with h_{stb} = 65mm - positive eccentricity for the constraints placed in sector y > 0 and negative for those placed in sector y < 0*

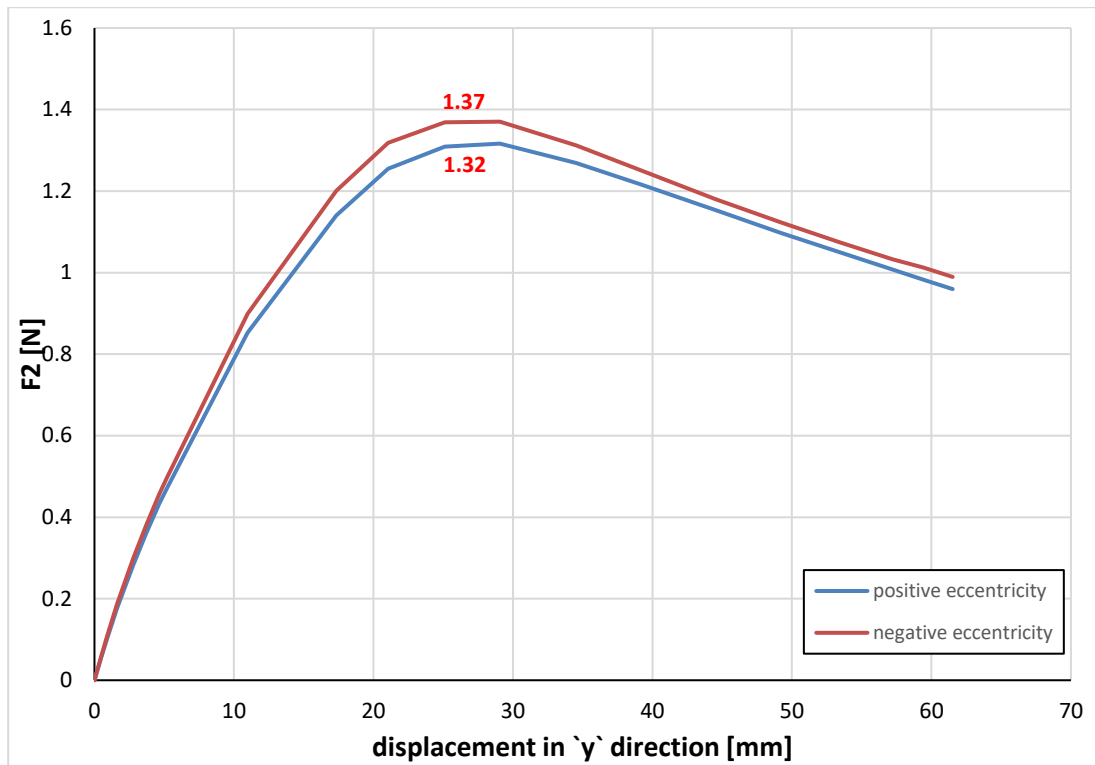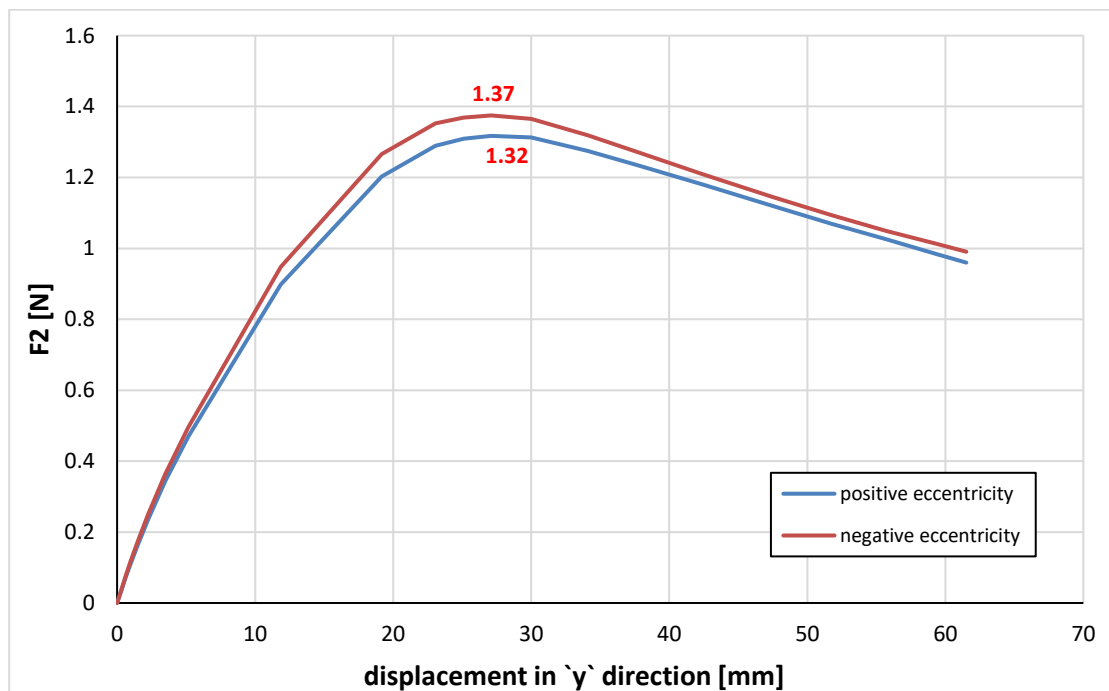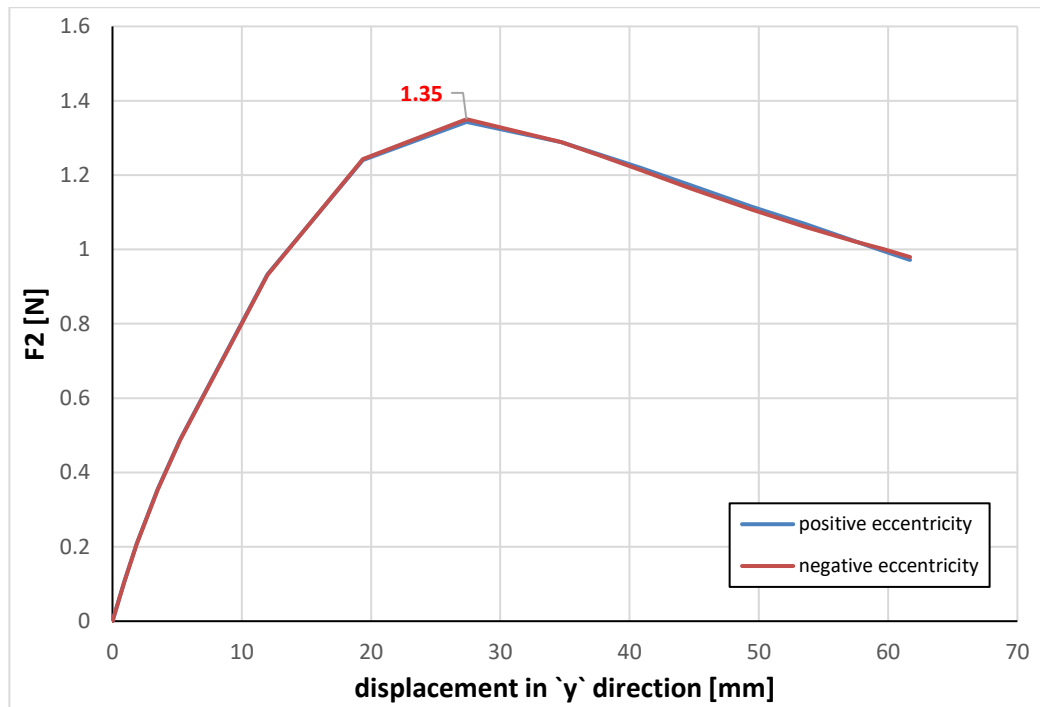*Figure 6.15: test 3 with h_{stb} = 65mm - positive eccentricity for the front bearings and negative eccentricity for the posteriors ones*

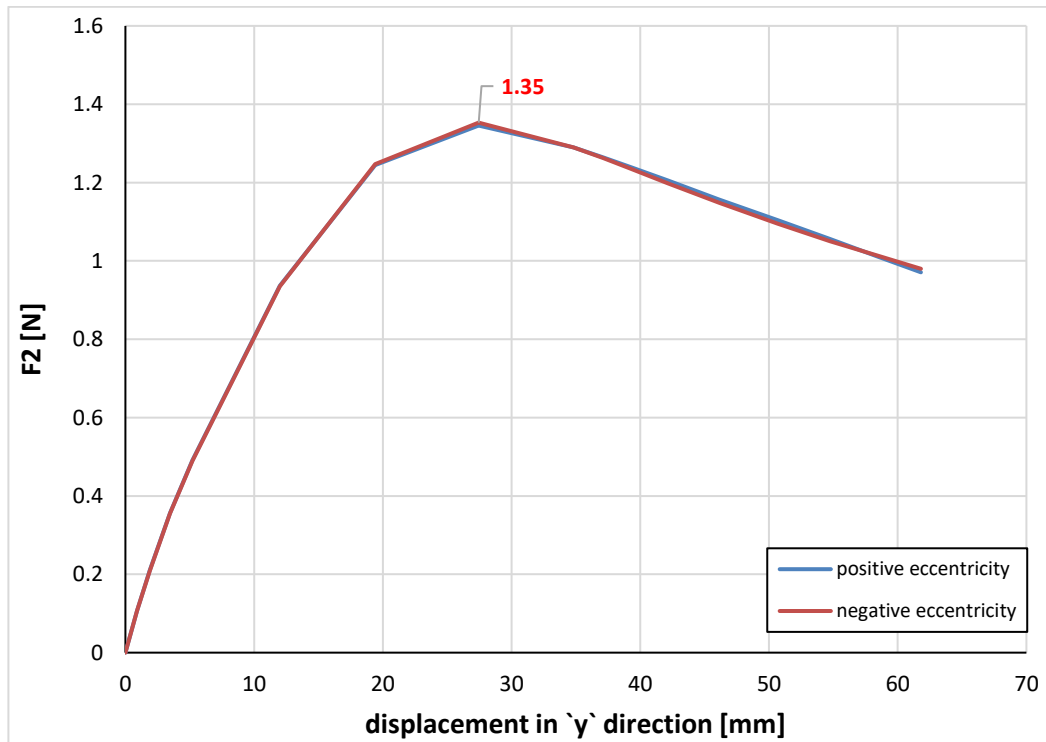*Figure 6.16: test 3 with h_{stb} = 65mm - positive eccentricity for the front right bearing and the posterior left one, negative eccentricity for the front left bearing and posterior right one*

Figure 6.17: test 3 with h_{stb} = 65mm - positive eccentricity for the front bearings and negative eccentricity for the posteriors ones (no rotation of the of the upper plate around the x and z axis)

Figure 6.18: test 3 with h_{stb} = 65mm - positive eccentricity for the front right bearing and the posterior left one, negative eccentricity for the front left bearing and posterior right one (no rotation of the of the upper plate around the x and z axis)

6.4   Test 3: analysis with eccentricity and $h_{stb} = 125$ mm

Considering the different eccentricities of the constraints with respect to the section, the nonlinear analysis has led to results that are not very different with respect to the case of absence of eccentricities (chapter 4.3.2). This is probably due to the same reasons already explained in the chapter 6.1. Below are reported the trends of the force F2 in case of eccentricity (Figure 6.19, Figure 6.20, Figure 6.21, Figure 6.22). Worth noting is that, only in case of mixed eccentricities along the same web, there is an increment of the value F2 under the bearings with negative eccentricity and a decrement under the bearings with positive eccentricity (Figure 6.21, Figure 6.22). This is due to the possibility of the upper steel plate that closes the elastomer to rotate. In fact fixing the rotation of the top plate around the x and z axis, the same value as the case of no eccentricity is again obtained (Figure 6.23, Figure 6.24).
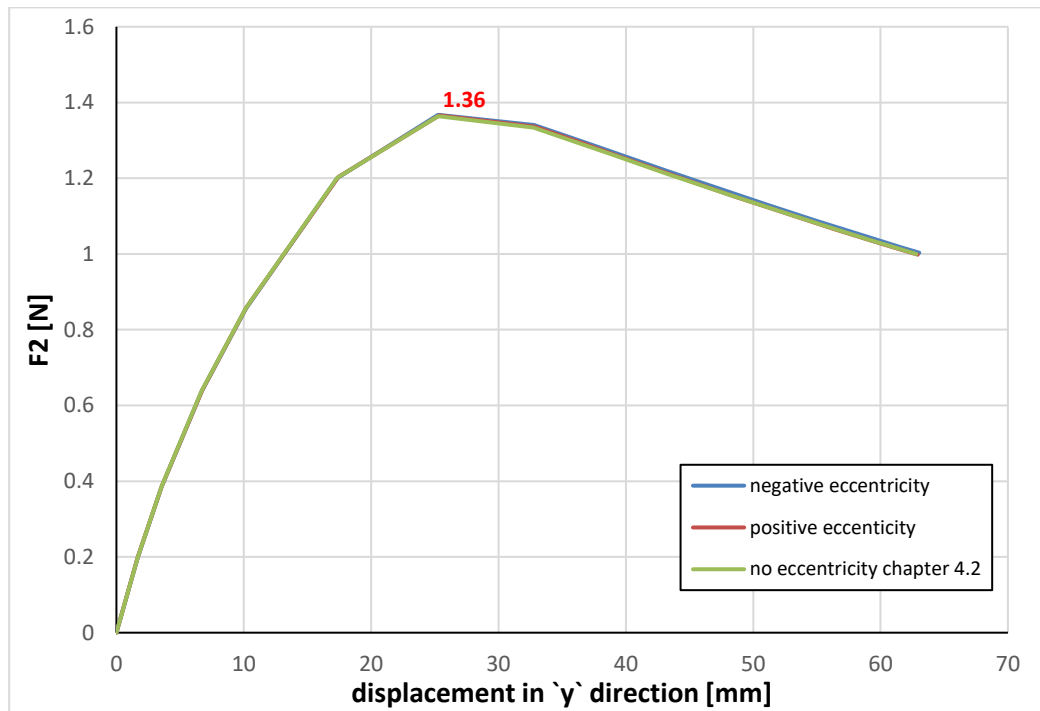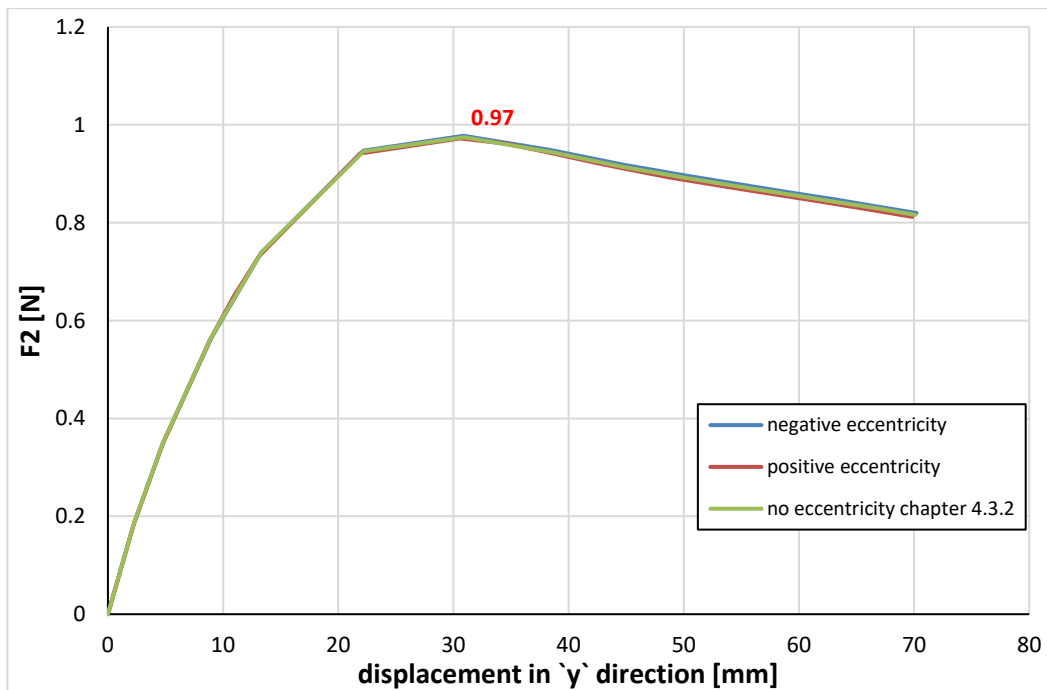

Figure 6.19: test 3 with $h_{stb} = 125mm$ - positive/negative eccentricity for all the bearings
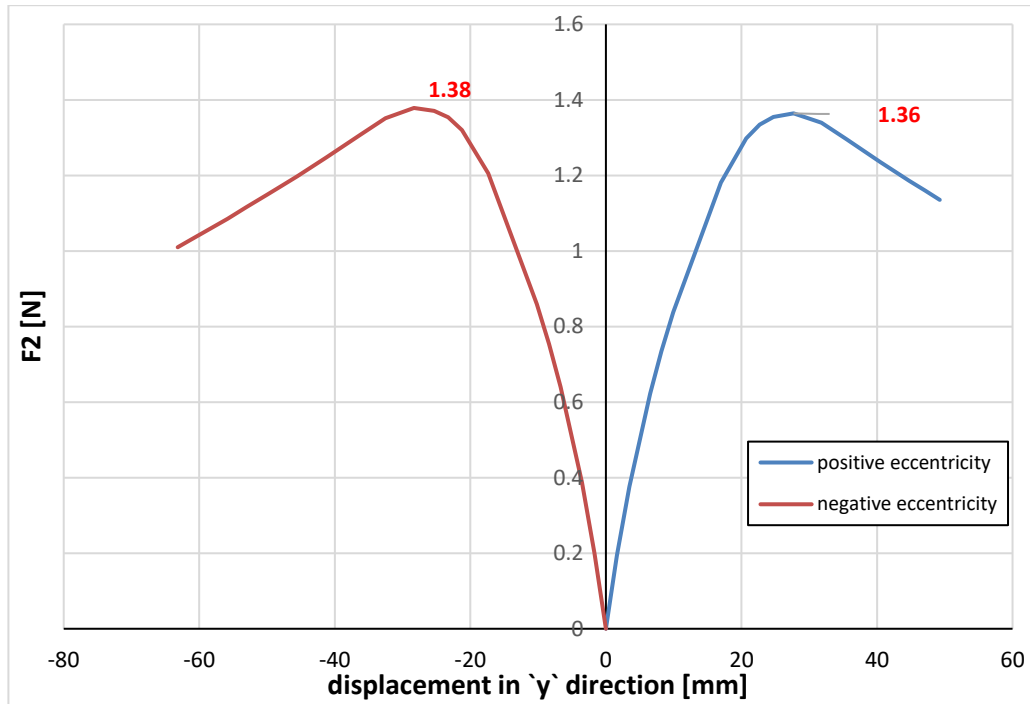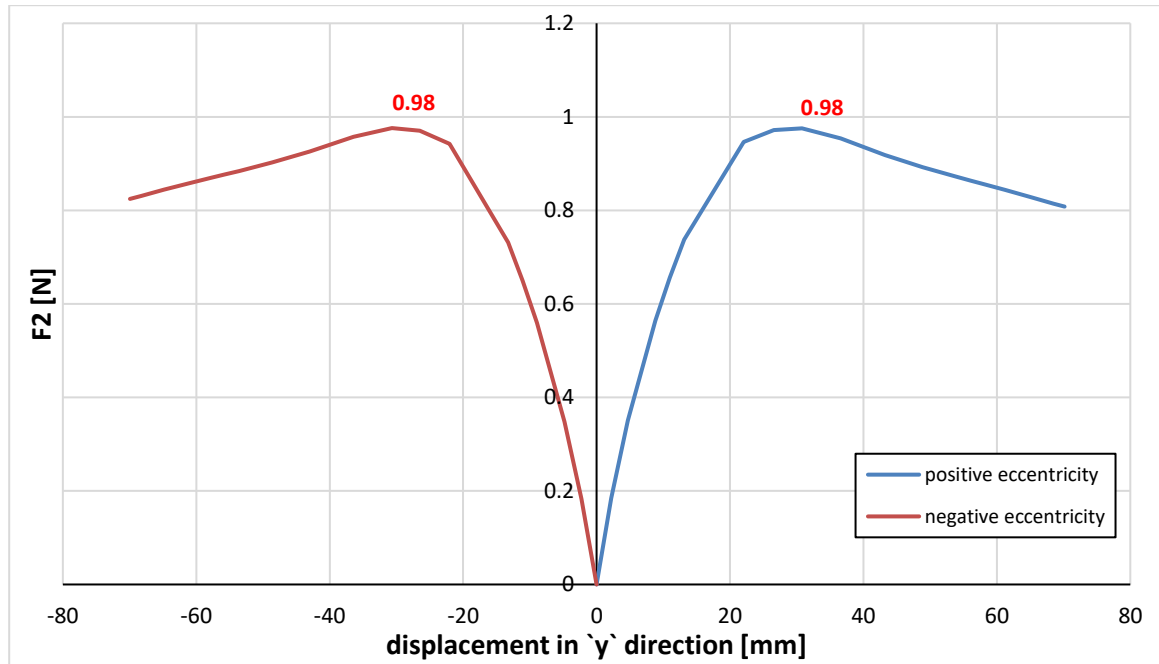
Figure 6.20: test 3 with h_{stb} = 125mm - positive eccentricity for the constraints placed in sector y > 0 and negative for those placed in sector y < 0
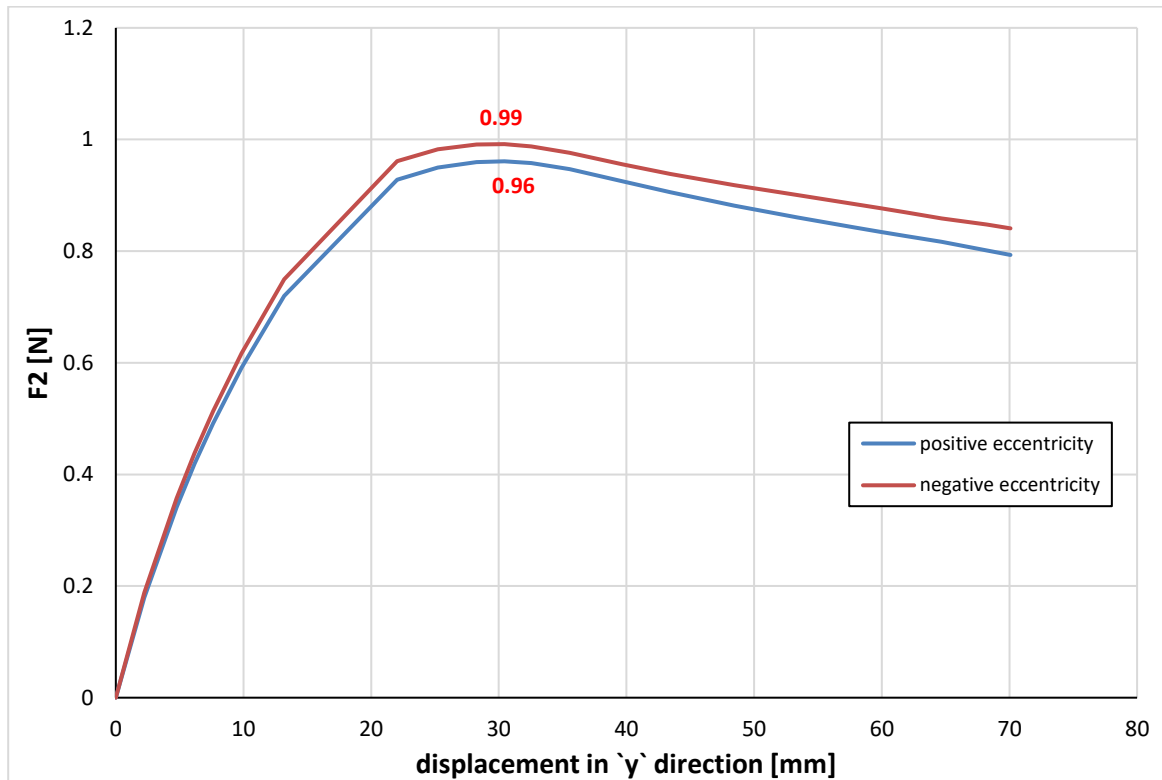
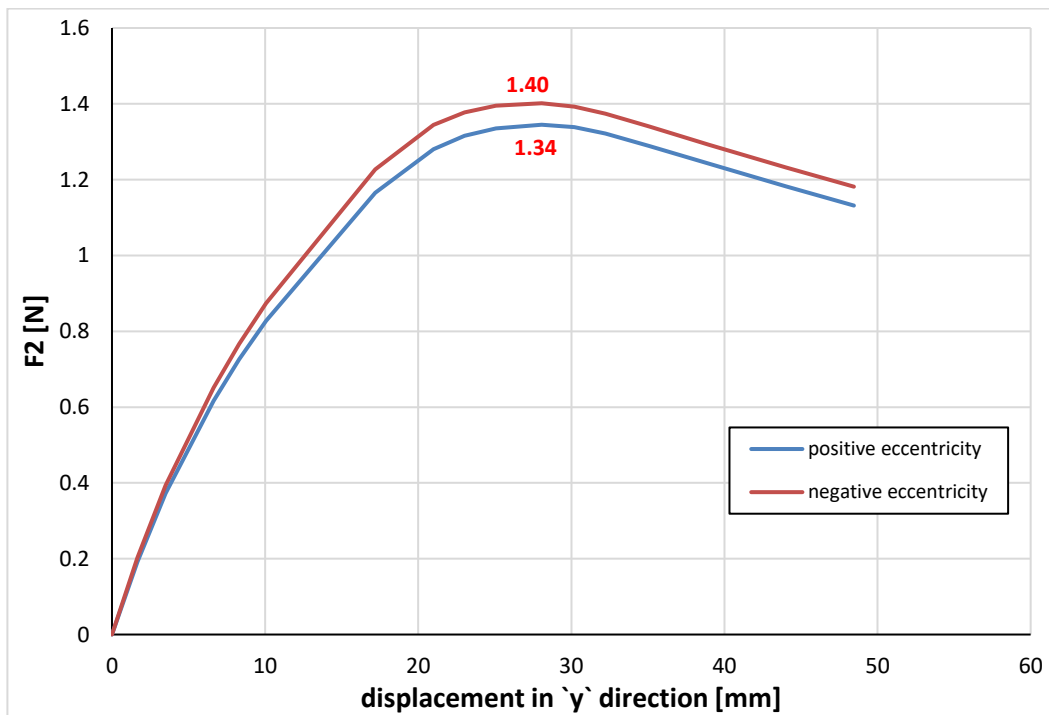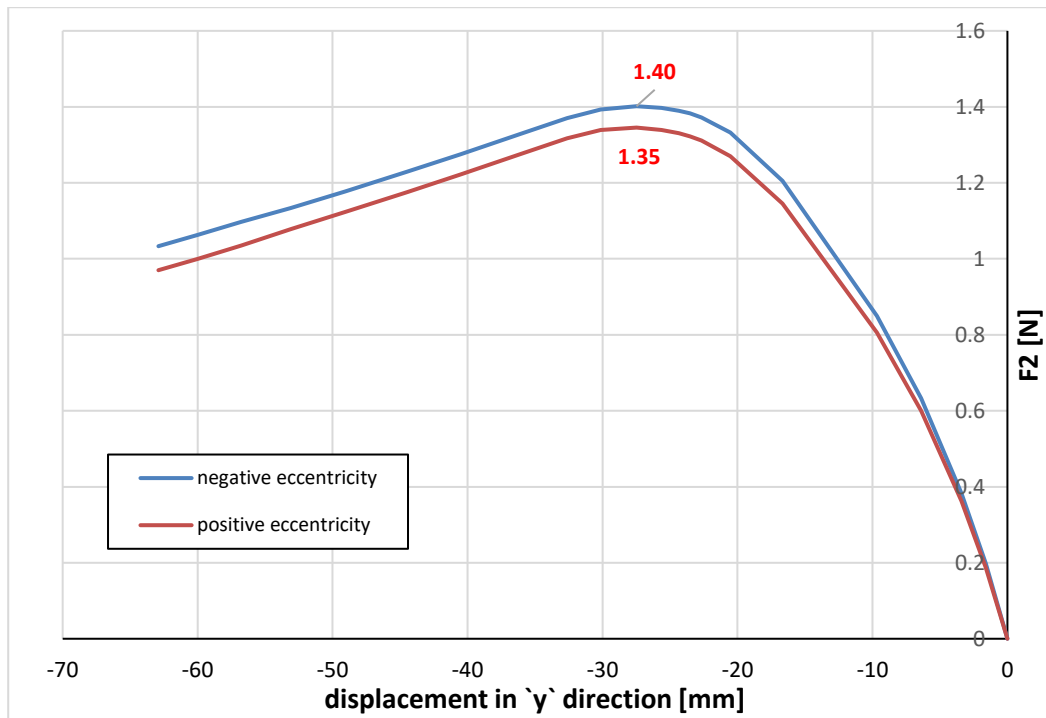*Figure 6.21: test 3 with h_{stb} = 125mm - positive eccentricity for the front bearings and negative eccentricity for the posteriors ones*
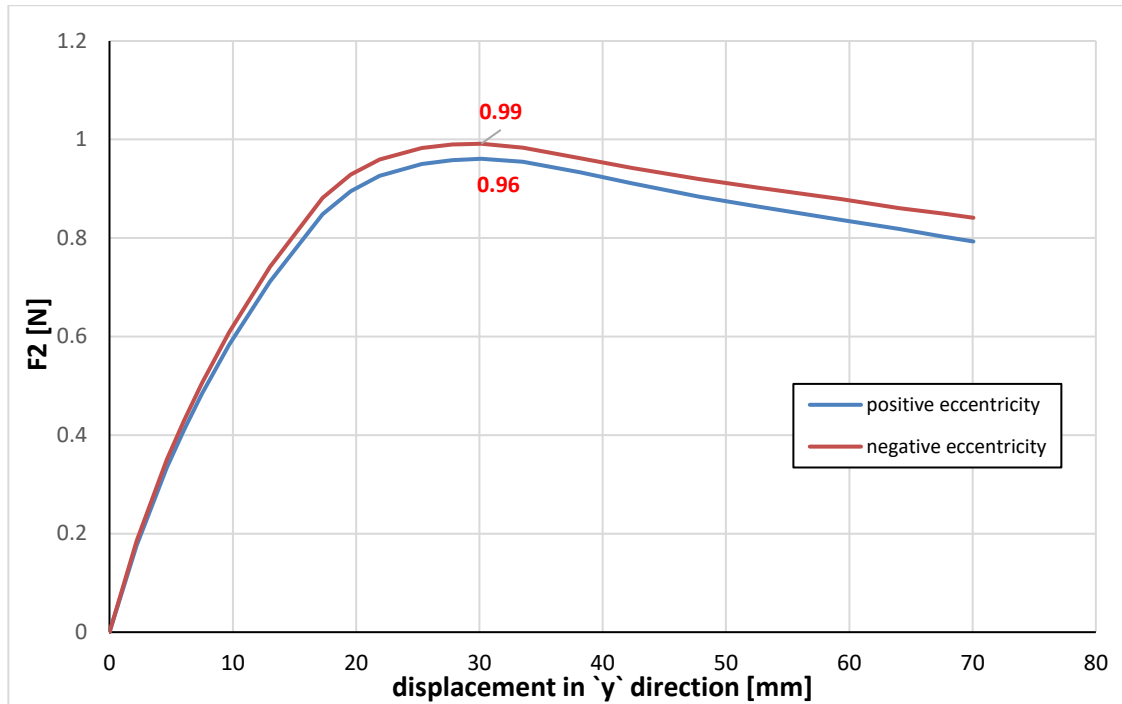
Figure 6.22: test 3 with h_{stb} = 125mm - positive eccentricity for the front right bearing and the posterior left one, negative eccentricity for the front left bearing and posterior right one
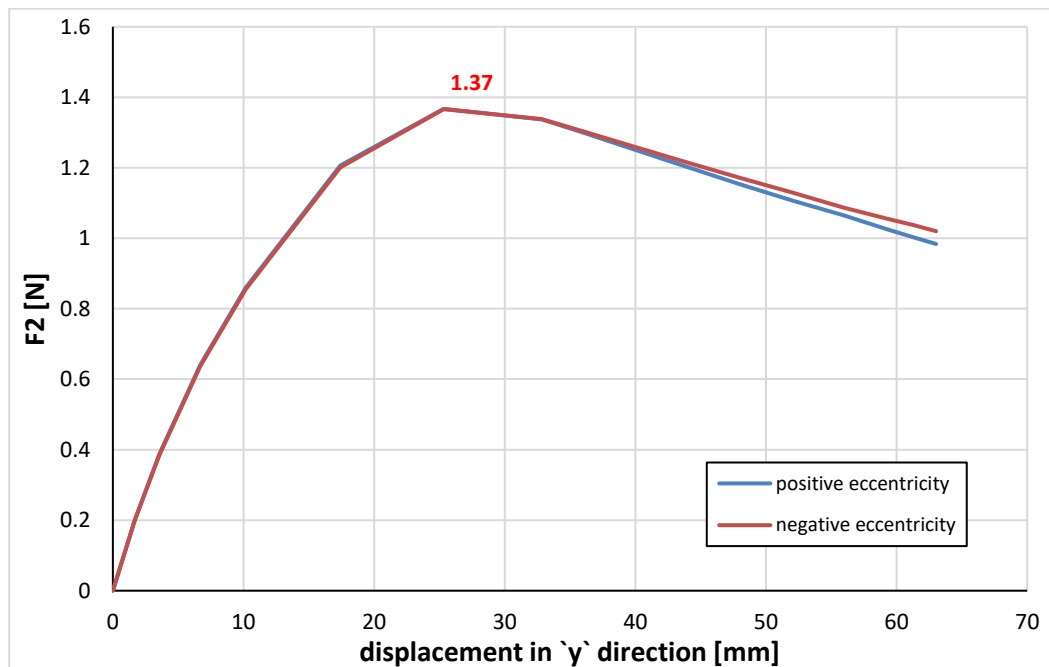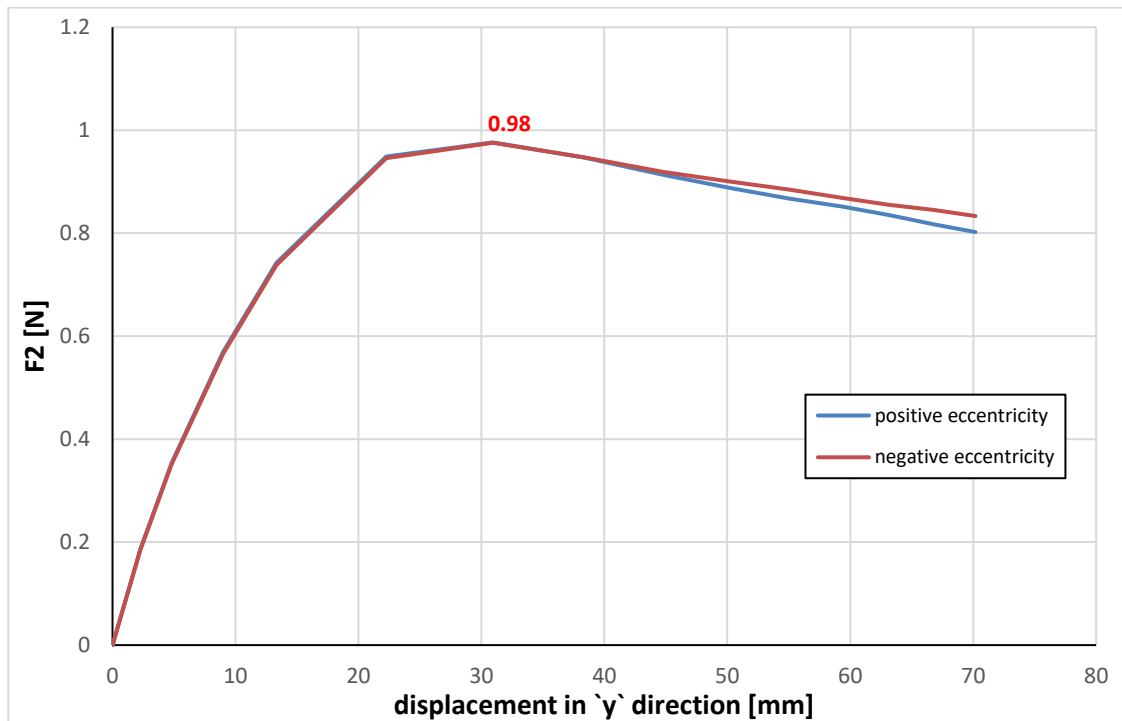

Figure 6.23: test 3 with h_{stb} = 125mm - positive eccentricity for the front bearings and negative eccentricity for the posteriors ones (no rotation of the of the upper plate around the x and z axis)
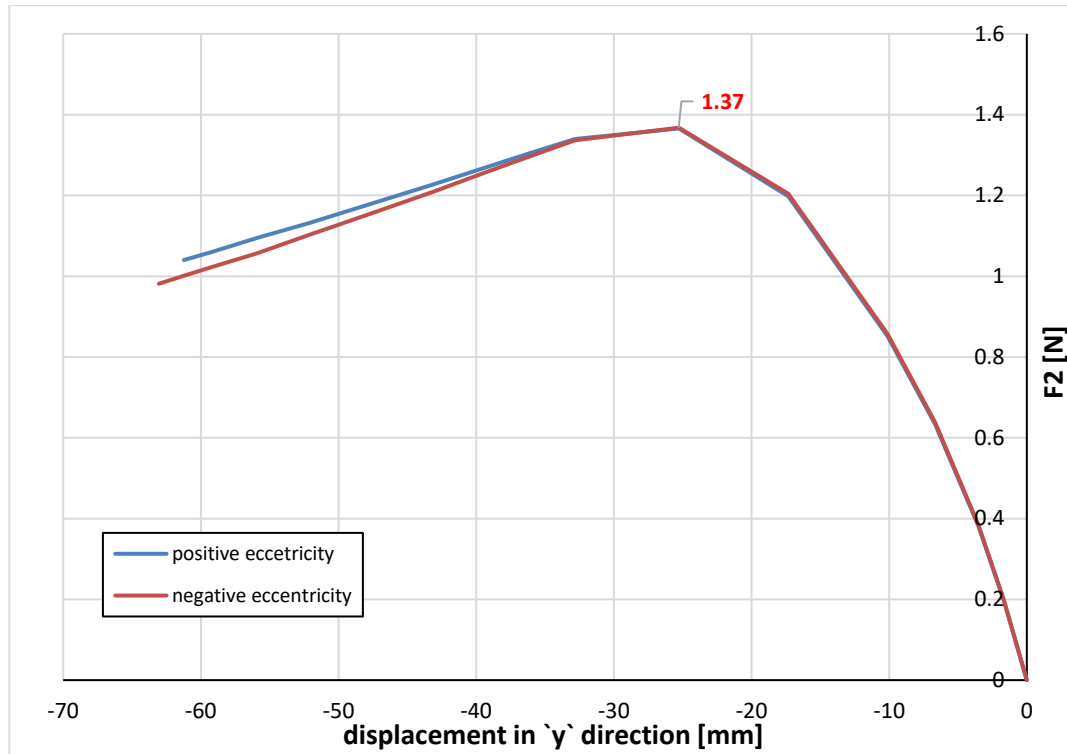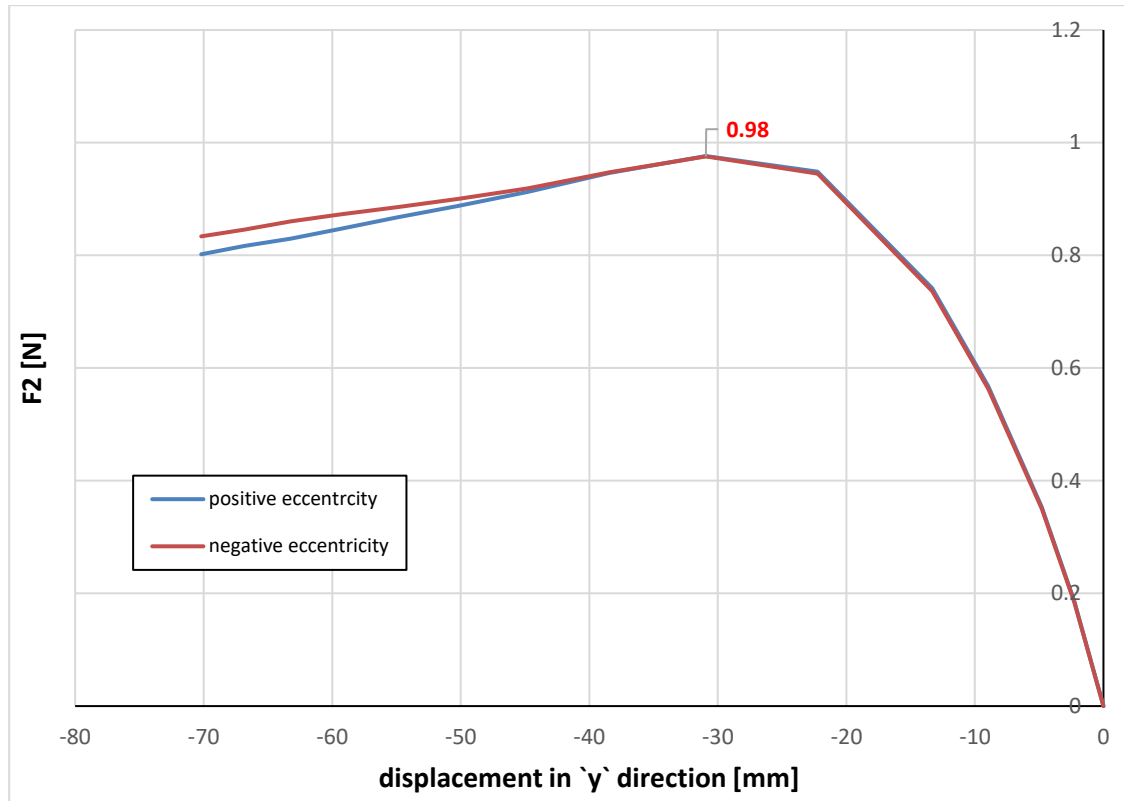
Figure 6.24: test 3 with h_{stb} = 125mm - positive eccentricity for the front right bearing and the posterior left one, negative eccentricity for the front left bearing and posterior right one (no rotation of the of the upper plate around the x and z axis)

6.5   Test 4: analysis with eccentricity

Considering the different eccentricities of the constraints with respect to the section, the nonlinear analysis has led to results that are not very different with respect to the case of absence of eccentricities (chapter 4.4). This is probably due to the same reasons already explained in the chapter 6.1. Below are reported the trends of the force F2 in case of eccentricity (Figure 6.25, Figure 6.26, Figure 6.27, Figure 6.28). Worth noting is that, only in case of mixed eccentricities along the same web, there is an increment of the value F2 under the bearings with negative eccentricity and a decrement under the bearings with positive eccentricity (Figure 6.27, Figure 6.28). This is due to the possibility of the upper steel plate that closes the elastomer to rotate. In fact fixing the rotation of the top plate around the x and z axis, the same value as the case of no eccentricity is again obtained (Figure 6.29, Figure 6.30).
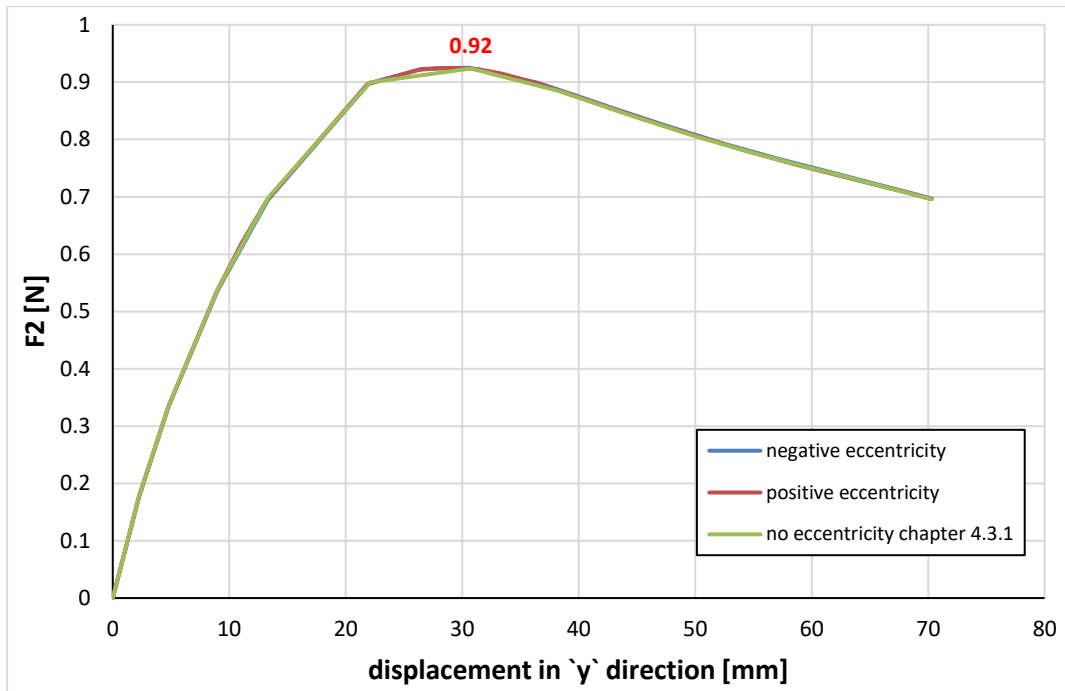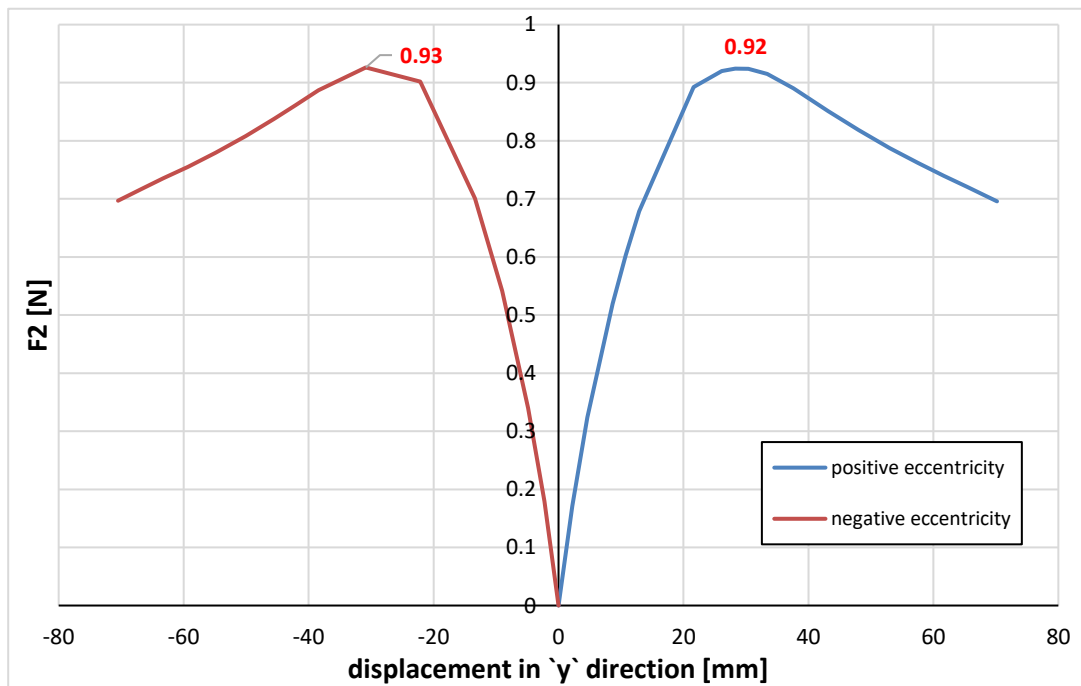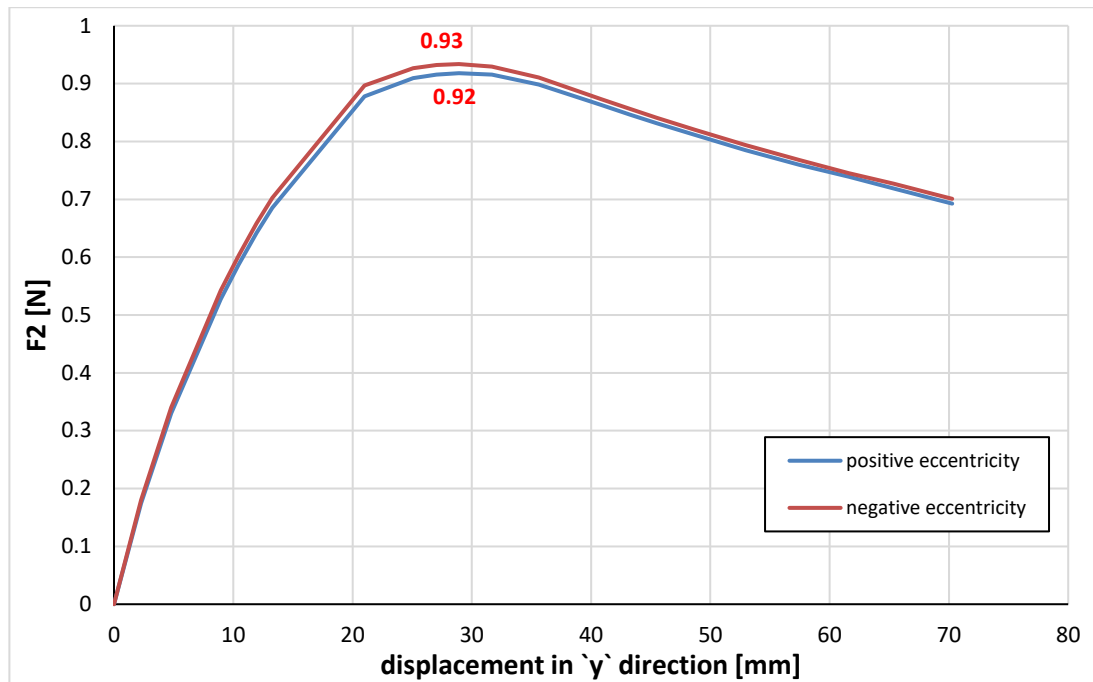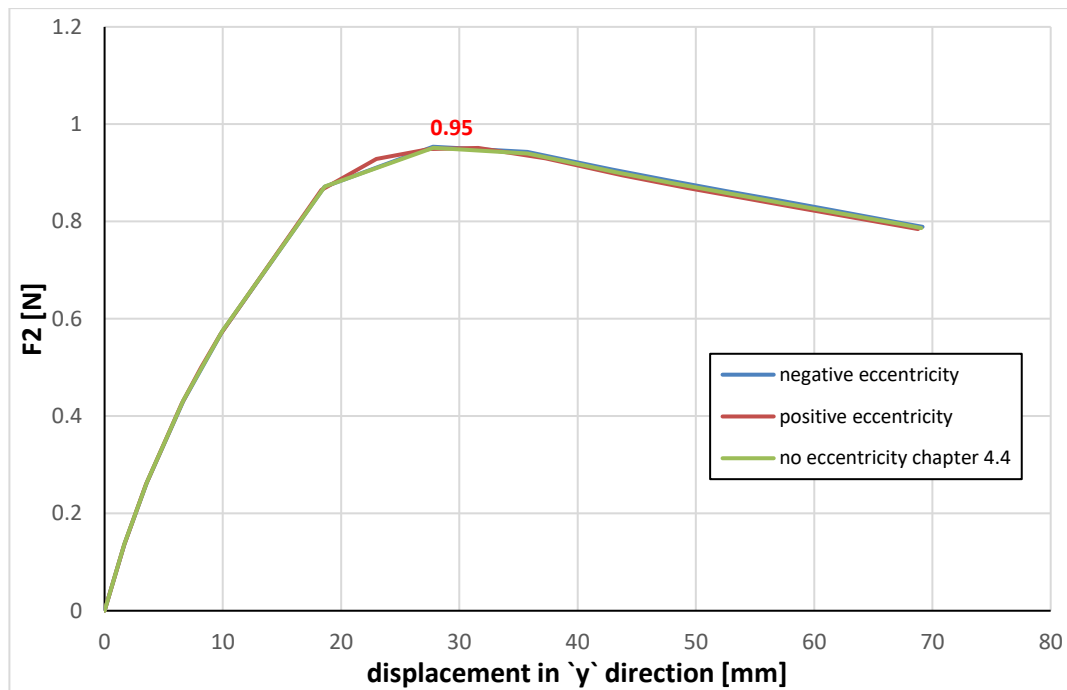
Figure 6.25: test 4 - positive/negative eccentricity for all the bearings

Figure 6.26: test 4 - positive eccentricity for the constraints placed in sector y > 0 and negative for those placed in sector y < 0

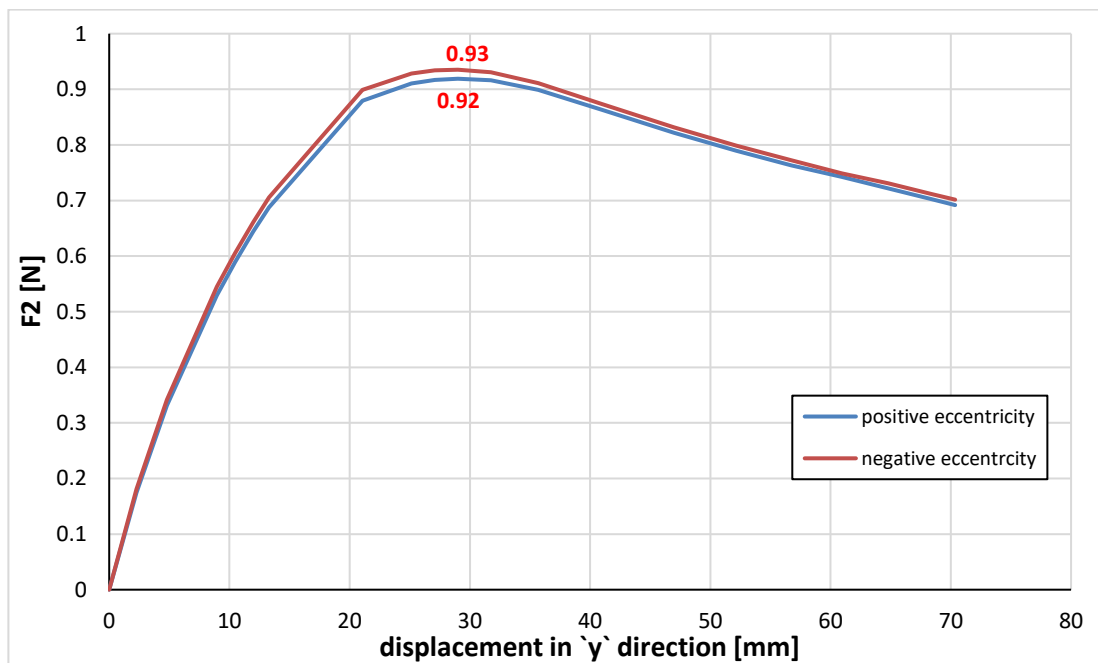*Figure 6.27: Test 4 - positive eccentricity for the front bearings and negative eccentricity for the posteriors ones*

Figure 6.28: Test 4 - positive eccentricity for the front right bearing and the posterior left one, negative eccentricity for the front left bearing and posterior right one
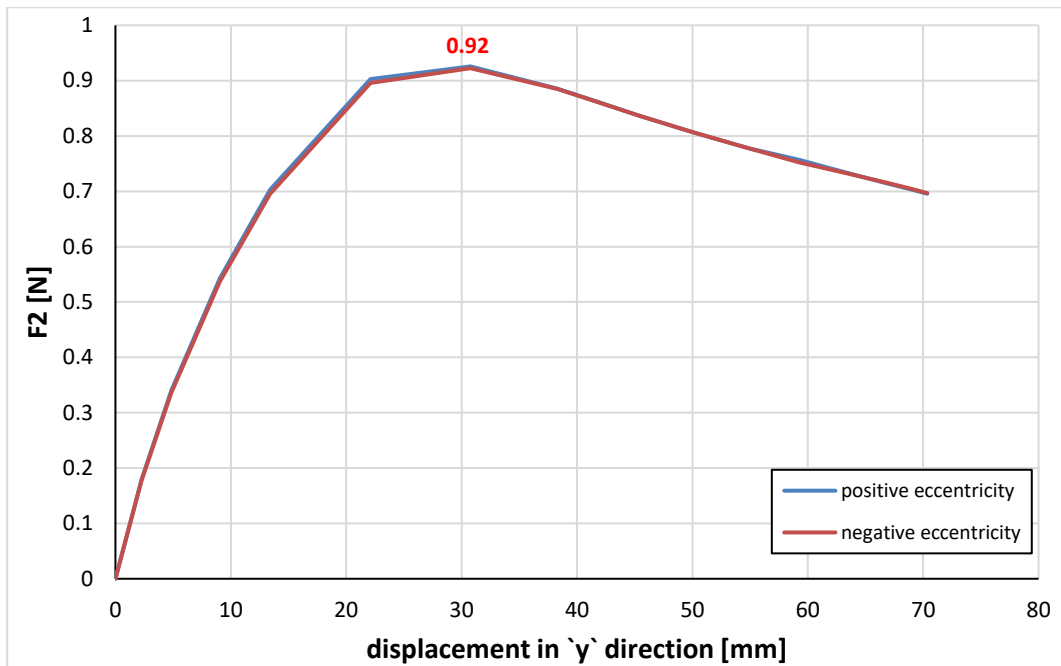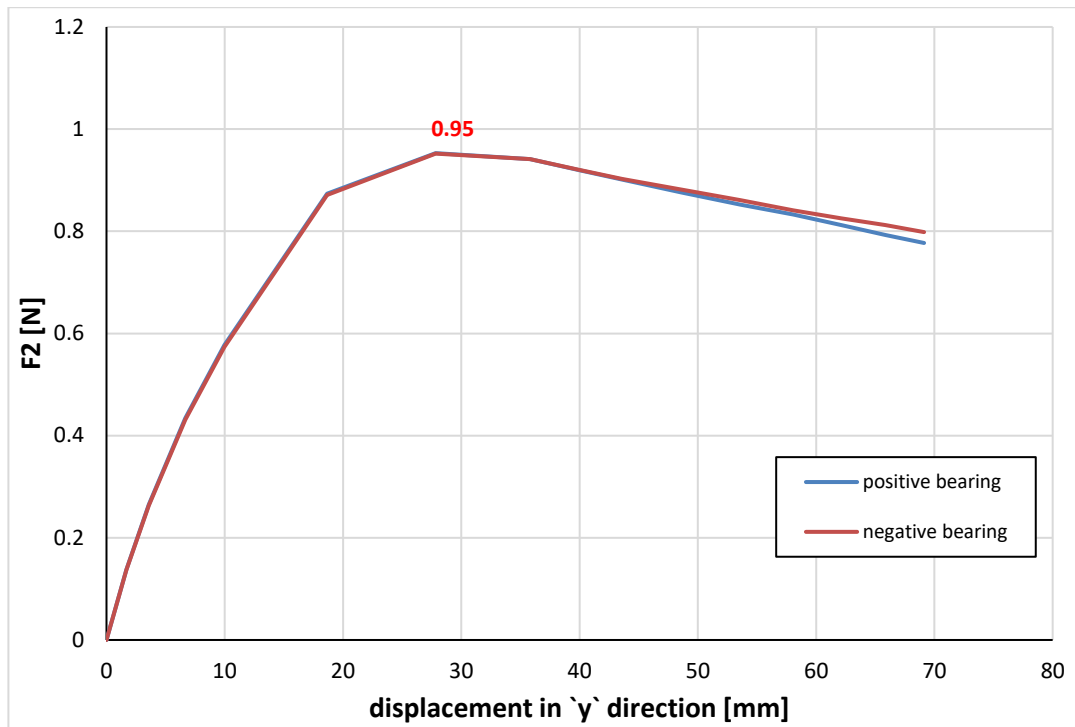
Figure 6.29: Test 4 - positive eccentricity for the front bearings and negative eccentricity
for the posteriors ones (no rotation of the of the upper plate around the x and z axis)
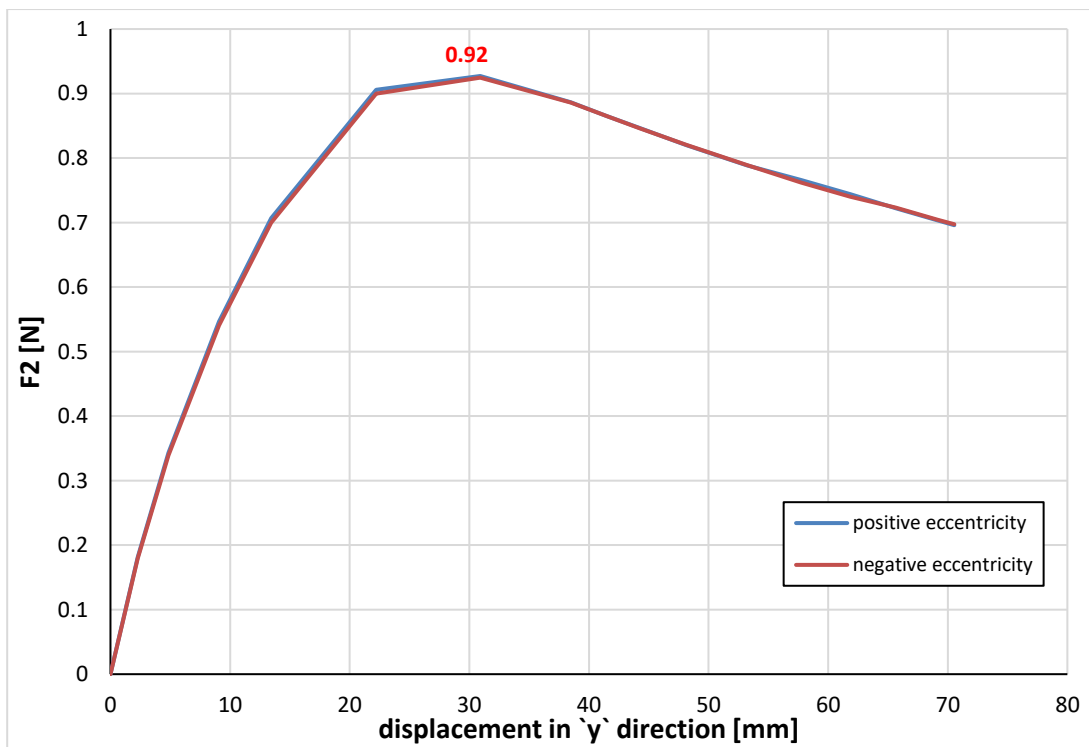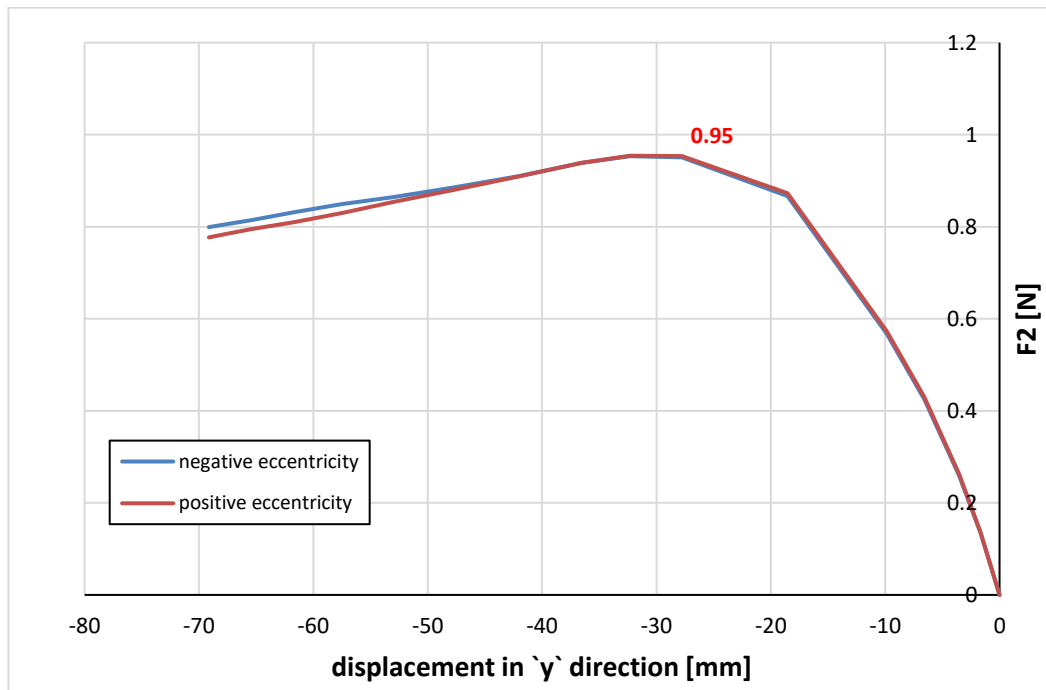

Figure 6.30: Test 4 - positive eccentricity for the front right bearing and the posterior left
one, negative eccentricity for the front left bearing and posterior right one (no rotation of
the of the upper plate around the x and z axis)

7. CONCLUSIONS

This study has attempted to provide a contribution to the analysis of instability phenomena that may affect the steel bridge box sections during the incremental launching. Therefore, a finite element model was created using *Ansys Workbench*. Once the truthfulness of the model had been verified, everything was written in the form of *Python* code and optimized through the introduction of parameters. In fact, in the end, it would be sufficient to modify the parameters of interest (geometric and/or mechanical) contained in a *file.txt* to obtain the new geometry and the new load conditions.

By setting the geometric parameters and the stress ratios to the values of the first four laboratory tests, it was analyzed how much the presence of the lower plate, stiffened longitudinally, influences the overall behavior of the section.

The transversal load F2 (concerning the single constraint) was introduced by means of two different types of bearings that rest respectively on two different types of launching bearings:

- steel bearings with a section HEM260, which rests on a spherical node pusher type $GE80 - AW$, which does not allow rotation with respect to the z-axis (Figure 2.9);
- type B elastomeric bearings with three sheets of reinforcement, resting on a pusher with simple discharge, which allows rotation only with respect to the y-axis (Figure 2.9).

The results extrapolated from the model (Table 7.2) were compared with the real results (first two columns of the Table 7.3) and with those contained in [3] (last two columns of theTable 7.3), which analyzes the real tests through a finite element modeling in *Ansys*, starting from the same boundary conditions used in this work. As it is possible to observe in the Table 7.1, the model realized in [3] reproduces quite faithfully the real results, in particular in the case of test 3, studied then again considering the elastomeric bearing.

TEST	Real value F2 [MN]	F2 [MN] [3]	F2$_{Elastomear}$ [3]	$\Delta F_{test-[3]}$ [%]	$\Delta F_{test-[3]\ elastomer}$ [%]
1	0.830	1.079	-	30.0	-
2	1.121	1.282	-	14.4	-
3	0.890	0.904	0.89	1.6	0

Table 7.1: comparison between real data and those reported in [3]

	F2 [MN]	
TEST	Calotte	Elastomear
1 (h_{stb} = 125mm)	1.367	1.345
2 (h_{stb} = 125mm)	1.39	1.364
3 (h_{stb} = 65mm)	0.947	0.924
3 (h_{stb} = 125mm)	0.996	0.975
4 (h_{stb} = 125mm)	0.981	0.951

Table 7.2: model results – GE80-AW (first column); elastomeric bearing (second column)

TEST	$\Delta F_{test-calotte}$ [%]	$\Delta F_{test-elastomer}$ [%]	$\Delta F_{calotte-[3]}$ [%]	$\Delta F_{elastomer-[3]}$ [%]
1 (h_{stb} = 125mm)	64.56	61.94	26.67	-
2 (h_{stb} = 125mm)	24.08	21.708	8.49	-
3 (h_{stb} = 65mm)	6.41	3.8	4.76	3.8
3 (h_{stb} = 125mm)	11.85	9.5	10.18	9.5
4 (h_{stb} = 125mm)	12.91	9.55	-	-

Table 7.3: comparison of the results of the models with the real ones and those contained in [3] without eccentricity

Looking at the last two columns of the Table 7.3, it is possible to see how the presence of the lower plate has led to an increase in the final load F2 of about $9 - 10\%$, considering the height of the stiffeners running along the lower plate equal to 125mm; while, to a reduction from 125mm to 65mm of the height of the stiffeners corresponds a reduction in the final value of F2 of more than 5%.

However, in the Table 7.2, it can also be observed that in the case of absence of eccentricity the spherical node pusher returns values about $2 - 3\%$ higher than in the case of the pusher with simple discharge. This is probably due to the possibility of the bearing to rotate around the x-axis (spherical node pusher). This result in a reduced introduction of the transverse load rate into the web, which can, therefore, withstand higher values of the F2 load before that it becomes unstable.

The behavior of the section subjected to an eccentric transverse load was very interesting. Again, the contribution of the bottom plate varied according to the type of pusher and the type of eccentricity used. The following eccentricities have been adopted:

- *case a*: positive eccentricity for all the bearings (Figure 5.1);
- *case b*: negative eccentricity for all the bearings (Figure 5.1);
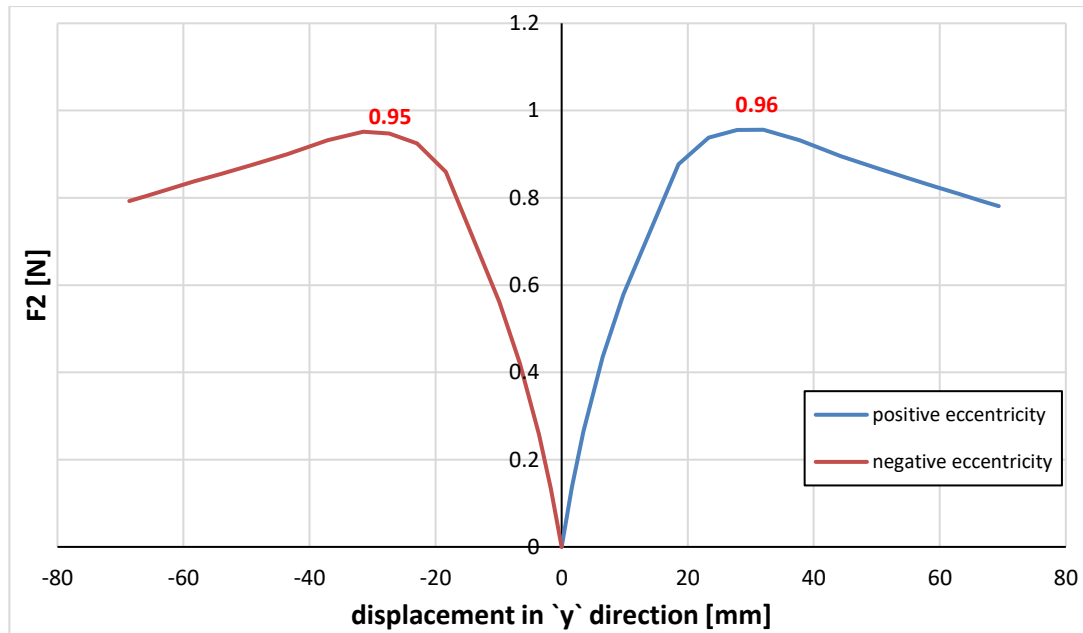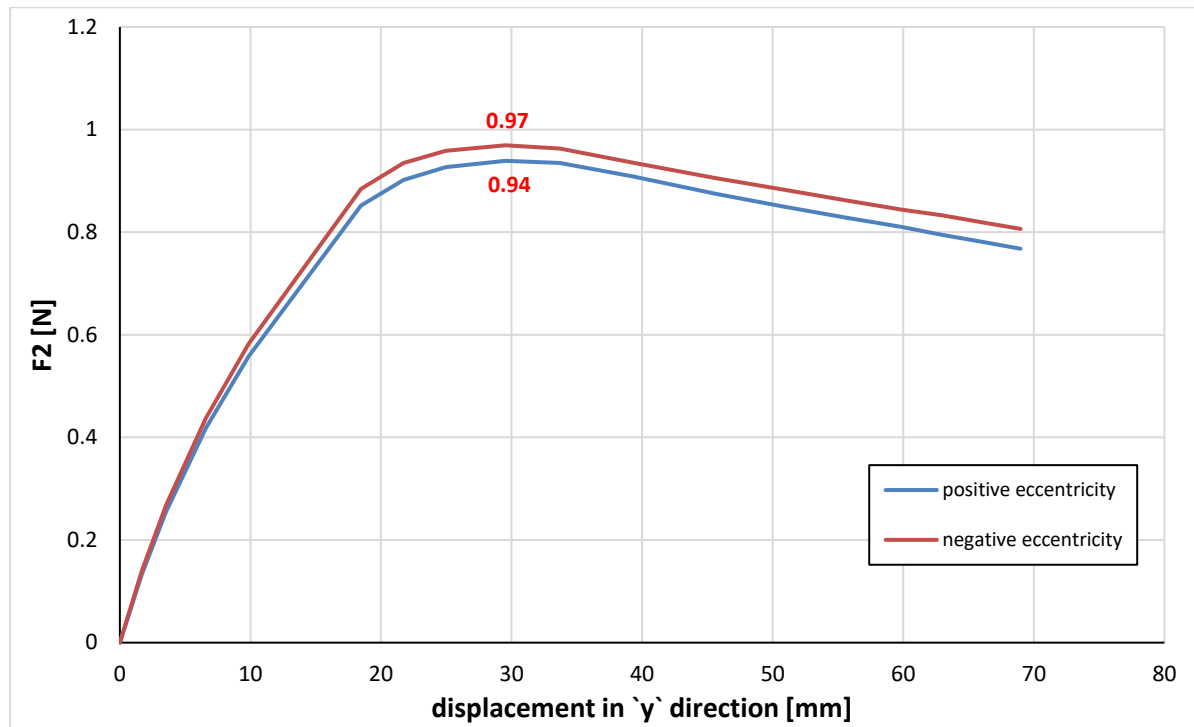- *case c*: positive eccentricity for the constraints placed in sector $y > 0$ and negative for those placed in sector $y < 0$ (Figure 5.2);

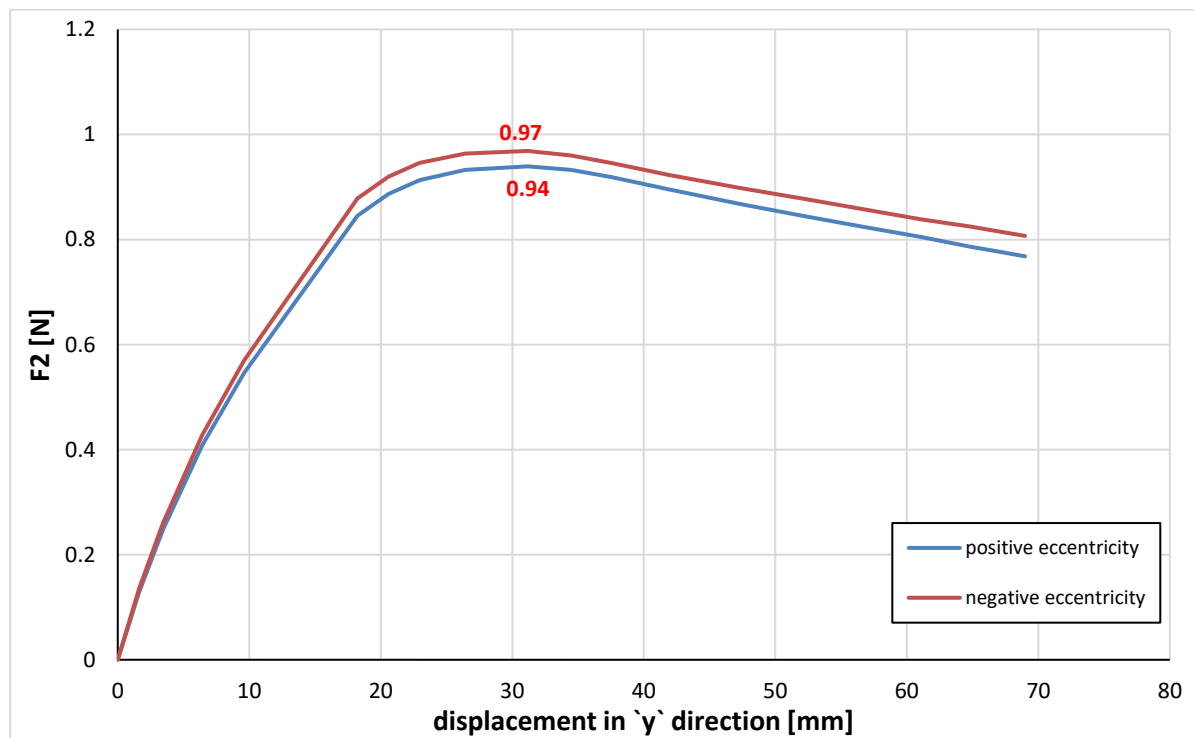- *case d*: positive eccentricity for the front bearings and negative eccentricity for the posteriors ones (Figure 5.3);

- *case e*: positive eccentricity for the front right bearing and the posterior left one, negative eccentricity for the front left bearing and posterior right one (Figure 5.4).

In case of rigid bearings and spherical node pusher, the *case a* led to a reduction in the final value of F2 compared to the case of absence of eccentricity (Table 7.4). This has been associated with the birth of high horizontal stresses (absorbed by the bottom flange) which have a stabilizing effect, to the detriment of reduced transversal unstable stresses. The *case b*, on the other hand, led to an increase in the final value of F2, given the presence of the lower plate, which opposes rotation (Table 7.5).

The mixed eccentricity along the same web (*case d* and *case e*), has instead led to a significant increase in the final value of the transversal load under the bearings having negative eccentricity (Table 7.5), and a significant reduction in the final load under the bearings having positive eccentricity (Table 7.4).

TEST	F2 [MN]					
	no eccentricity	case a	case b	case c	case d	case e
1 (h_{stb} = 125mm)	1.367	1.342	-	1.336	1.240	1.241
2 (h_{stb} = 125mm)	1.390	1.351	-	1.342	1.252	1.252
3 (h_{stb} = 65mm)	0.947	0.934	-	0.940	0.878	0.877
3 (h_{stb} = 125mm)	0.996	0.976	-	0.973	0.902	0.902
4 (h_{stb} = 125mm)	0.981	0.953	-	0.950	0.879	0.880

Table 7.4: eccentricity influence in case of steel bearings and spherical node pusher - reaction F2 under the bearings with positive eccentricity

TEST	F2 [MN]					
	no eccentricity	case a	case b	case c	case d	case e
1 (h_{stb} = 125mm)	1.367	-	1.392	1.404	1.492	1.495
2 (h_{stb} = 125mm)	1.390	-	1.417	1.425	1.519	1.522
3 (h_{stb} = 65mm)	0.947	-	0.953	0.950	1.006	1.008
3 (h_{stb} = 125mm)	0.996	-	1.011	1.015	1.081	1.082
4 (h_{stb} = 125mm)	0.981	-	0.993	0.997	1.073	1.075

Table 7.5: eccentricity influence in case of steel bearings and spherical node pusher - reaction F2 under the bearings with negative eccentricity

In case of elastomeric bearings and pusher with simple discharge, the only positive or negative eccentricity did not involve significant variations in the final value of F2 (*case a* and *case b* in Table 7.6 and Table 7.7). This has been associated with the impossibility of rotating around the x-axis, and with the high stiffness of the elastomer. These two aspects, in fact, cause the torque generated by the eccentric load to be absorbed in a minimum part of the web. However, having an alternating eccentricity along the same web (*case d* and *case e*) led to a slight increase in the value of F2 below the bearings having negative eccentricity Table 7.7, and to a slight decrease in the final value of F2 below the bearings having positive eccentricity (Table 7.6). This has been associated with the possibility that the upper plate that closes the elastomer has to rotate, in fact, allowing it only to rotate around the y-axis, the same values obtained in the absence of eccentricity would be obtained again.

TEST	F2 [MN]					
	no eccentricity	case a	case b	case c	case d	case e
1 (h_{stb} = 125mm)	1.345	1.336	-	1.339	1.316	1.317
2 (h_{stb} = 125mm)	1.364	1.366	-	1.364	1.345	1.345
3 (h_{stb} = 65mm)	0.924	0.925	-	0.924	0.918	0.919
3 (h_{stb} = 125mm)	0.975	0.972	-	0.975	0.961	0.961
4 (h_{stb} = 125mm)	0.951	0.951	-	0.956	0.939	0.939

Table 7.6: eccentricity influence in case of elastomeric bearings and pusher with simple discharge - reaction F2 under the bearings with positive eccentricity

TEST	F2 [MN]					
	no eccentricity	case a	case b	case c	case d	case e
1 (h_{stb} = 125mm)	1.345	-	1.346	1.347	1.370	1.375
2 (h_{stb} = 125mm)	1.364	-	1.367	1.379	1.402	1.402
3 (h_{stb} = 65mm)	0.924	-	0.925	0.926	0.934	0.935
3 (h_{stb} = 125mm)	0.975	-	0.978	0.976	0.992	0.991
4 (h_{stb} = 125mm)	0.951	-	0.954	0.951	0.969	0.969

Table 7.7: eccentricity influence in case of elastomeric bearings and pusher with simple discharge - reaction F2 under the bearings with negative eccentricity

Table 7.8 and Table 7.9 summarize the comparison between the various cases, in function of the pairs bearings-launching bearings (pair 1: steel bearings with a section HEM260, which rests on a spherical node pusher type GE80 − AW; pair 2: type B elastomeric bearings with three sheets of reinforcement, resting on a pusher with simple discharge).

	F2 [MN]											
	no eccentricity		case a		case b		case c		case d		case e	
TEST	pair 1	pair 2	pair 1	pair 2	pair 1	pair 2	pair 1	pair 2	pair 1	pair 2	pair 1	pair 2
1 (h_{stb} = 125mm)	1.367	1.345	1.342	1.336	-	-	1.336	1.339	1.240	1.316	1.241	1.317
2 (h_{stb} = 125mm)	1.390	1.364	1.351	1.366	-	-	1.342	1.364	1.252	1.345	1.252	1.345
3 (h_{stb} = 65mm)	0.947	0.924	0.934	0.925	-	-	0.940	0.924	0.878	0.918	0.877	0.919
3 (h_{stb} = 125mm)	0.996	0.975	0.976	0.972	-	-	0.973	0.975	0.902	0.961	0.902	0.961
4 (h_{stb} = 125mm)	0.981	0.951	0.953	0.951	-	-	0.950	0.956	0.879	0.939	0.880	0.939

Table 7.8: reaction F2 under the bearings with positive eccentricity in the different cases and bearings/launching bearings pairs

	F2 [MN]											
	no eccentricity		case a		case b		case c		case d		case e	
TEST	pair 1	pair 2	pair 1	pair 2	pair 1	pair 2	pair 1	pair 2	pair 1	pair 2	pair 1	pair 2
1 (h_{stb} = 125mm)	1.367	1.345	-	-	1.392	1.346	1.404	1.347	1.492	1.370	1.495	1.375
2 (h_{stb} = 125mm)	1.390	1.364	-	-	1.417	1.367	1.425	1.379	1.519	1.402	1.522	1.402
3 (h_{stb} = 65mm)	0.947	0.924	-	-	0.953	0.925	0.950	0.926	1.006	0.934	1.008	0.935
3 (h_{stb} = 125mm)	0.996	0.975	-	-	1.011	0.978	1.015	0.976	1.081	0.992	1.082	0.991
4 (h_{stb} = 125mm)	0.981	0.951	-	-	0.993	0.954	0.997	0.951	1.073	0.969	1.075	0.969

Table 7.9: reaction F2 under the bearings with negative eccentricity in the different cases and bearings/launching bearings pairs

At the end of the speech, the model created has allowed to investigate in a sufficiently accurate way the sectional behavior and to evaluate the influence of the two different types of pusher on the instability of the section.

Moreover, since the *Python Script* was created with the purpose of performing parametric calculations, such as optimization calculations, it would be interesting to investigate the overall behavior by changing only certain parameters, for example:

- Only change the thickness of the bottom plate or of the webs and check the trend of F2;
- Investigate more accurately the impact that the eccentricity has on the sectional behavior, such as how far negative eccentricity leads to an increase in the final value of F2;

- Change the sign of the imperfections, or make a combination of these, since their sign and magnitude greatly influence the sectional behavior;
- Reduce the stiffness value of the springs simulating the elastomer, as this would result in a rotation of the upper metal plate;
- Attribute an eccentricity also along the x direction, since it would involve a variation of the bending moment (moment around y);
- Investigate tests 5 and 6 more thoroughly;
- Only change the inclination of the web.

Acknowledgments

Ringraziamenti

Innanzitutto ritengo doveroso ringraziare il professor Ceravolo, il professor Mensinger e la mia supervisor Nadine Maier, per avermi dato l'opportunità di fare questa bellissima esperienza a Monaco di Baviera, dove ho avuto l'opportunità di conoscere persone straordinarie, sia in facoltà che al difuori. In particolare, ricorderò sempre l'aiuto offertomi da Giovanni Filomeno, un amico a cui devo molto, non solo per avermi offerto il suo aiuto, ma anche e soprattutto per avermi facilitato l'integrazione nella nuova realtà che stavo vivendo.

Naturalmente ciò non sarebbe stato possibile senza il supporto della mia famiglia, sempre presente e pronta a sostenermi in qualsiasi momento. Ringrazio inoltre la mia fidanzata, la quale da anni, con la sua comprensione, supporta ogni mia decisione e mi dà conforto nei momenti difficili.

Ringrazio amici come Simone, Desideria, Enrico, Giacomo, Erika, Ludovico, Pierpaolo, Luca Pennisi, Martina, Claudia, Giuseppe, Giovanni, Aurelio, Fabio, Arturo, Santina, Vittoria, Francesca, Veronika, Luca Conti, Humann a Alex, con i quali ho trascorso momenti indimenticabili e ai quali auguro una vita piena di gratificazioni.

Questo lavoro ha rappresento il coronamento del percorso universitario, spesso tortuoso e pieno di ostacoli, ma sempre con qualcuno pronto a tenderti la mano e a darti la forza di ripartire.

Bibliography

[1]   https://en.wikipedia.org/wiki/Incremental_launch [last edit 5/9/2018]

[2]   http://en.vsl.cz/incremental-launching-method/ [last edit 5/9/2018]

[3]   Seisenberger J., *Beuluntersuchungen an längsversteiften Platten unter realistischer Lasteinleitung aus dem Taktschiebeverfahren*, Munich, 2018

[4]   Maier N., Ndogmo J., Pourostad V., Mensinger M., Kuhlmann U., *Zwischenbericht zum Forschungsprojekt „Talbrücke Thulba",* Munich, 2018

[5]   DIN Deutsches Institut für Normung e.V., DIN EN 1993-1-5: Eurocode 3: Bemessung und Konstruktion von Stahlbauten Teil 1-5: Plattenförmige Bauteile; Deutsche Fassung EN 1993-1-5-2:2006 + AC:2009+Nationaler Anhang, 2009.

[6]   Johansson B., Maquoi R,. Sedlacek G., Müller C., Beg D., *Commentary and worked examples to EN 1993-1-5 "Plated Structura Elements", 2007*

[7]   Mensinger M., Ndogmo J., Both I., *Buckling behavior of stiffened plate under biaxial compression and shear*, 2016

[8]   https://support.ansys.com/staticassets/ANSYS/Conference/Boston/downloads/ Customizing%20ANSYS%20WB%20-%20Sudharshan%20Renganathan.pdf [last edit 5/9/2018]

[9]   https://www.ansys.com/-/media/ansys/corporate/resourcelibrary/article/aa-v2-i1-analyzing-buckling.pdf [last edit 5/9/2018]

[10]   https://www.simutechgroup.com/tips-and-tricks/fea-articles/94-fea-tips-tricks-buckling [last edit 5/9/2018]

[11]   https://www.sharcnet.ca/Software/Ansys/17.0/en-

         us/help/wb_sim/ds_buckling_analysis_type.html [last edit 5/9/2018]

[12]   https://support.esss.co/hc/en-us/articles/205250985-How-to-use-scripts-to-

         generate-a-plane-wing-using-ANSYS-Design-Modeler-15-0   [last   edit

         5/9/2018]

[13]   https://www.sharcnet.ca/Software/Ansys/16.2.3/en-

         us/help/ans_elem/Hlp_E_SHELL181.html [last edit 5/9/2018]

[14]   DIN Deutsches Institut für Normung e.V., DIN EN 1337-3: Lager im Bauwesen

         - Teil 3: Elastomerlager; Deutsche Fassung EN 1337-3:2005, 2005.

[15]   DIN Deutsches Institut für Normung e.V., DIN EN 1337-2: Lager im Bauwesen

         - Teil 2: Gleitteile; Deutsche Fassung EN 1337-2:2004, 2004.

[16]   https://www.sharcnet.ca/Software/Ansys/17.0/en-

         us/help/act_dev/act_dev_ironpython.html [last edit 5/9/2018]

[17]   https://medias.schaeffler.com/medias/de!hp.ec.br.dp/GE..-AW*GE80-AW [last

         edit 5/9/2018]

[18]   https://www.google.de/search?q=incremental+launching&source=lnms&tbm=i

         sch&sa=X&ved=0ahUKEwiJmqq3r8ndAhVrxYUKHbOUDmgQ_AUICigB&

         biw=1366&bih=657#imgrc=jG0D-z7ZFtCmnM: [last edit 20/9/2018]

[19]   https://www.google.de/search?q=incremental+launching+method&tbm=isch&

         tbo=u&source=univ&sa=X&ved=2ahUKEwi_wr2UssfdAhVRmYsKHZ_eBE

         AQsAR6BAgFEAE&biw=1366&bih=662#imgrc=aTVLsbgYQY7aEM: [last

         edit 20/9/2018]

[20]   https://www.google.de/search?q=incremental+launching+method&tbm=isch&

         tbo=u&source=univ&sa=X&ved=2ahUKEwi_wr2UssfdAhVRmYsKHZ_eBE

         AQsAR6BAgFEAE&biw=1366&bih=662#imgrc=V7gua789wwsE5M: [last

         edit 20/9/2018]

154

[21]   https://www.google.de/search?q=incremental+launching+method&tbm=isch&

tbo=u&source=univ&sa=X&ved=2ahUKEwi_wr2UssfdAhVRmYsKHZ_eBE

AQsAR6BAgFEAE&biw=1366&bih=662#imgrc=NITKakMTRST52M: [last

edit 20/9/2018]

[22]   https://www.google.de/search?biw=1242&bih=597&tbm=isch&sa=1&ei=c3qj

W_GzF4LIaKzvuIgI&q=clouds+and+bridges&oq=clouds+and+bridges&gs_l

=img.3...6213.8756.0.8928.7.7.0.0.0.0.100.393.6j1.7.0....0...1c.1.64.img..0.1.1

00...0i19k1.0.FjEzuF4KyOA#imgrc=ir7zGAan-fyH_M: [last edit 20/9/2018]

[23]   Zizza A., *Buckling Behaviour of Unstiffened and Stiffened Steel Plates Under

Multiaxial Stress States*, Stuttgart, 2016